

Nanostructured Multifunctional Materials for Control of Light Transport and Surface Wettability

by

Hyungryul Choi

B.S., Mechanical Engineering, Korea Advanced Institute of Science and Technology (2009)

M.S., Mechanical Engineering, Massachusetts Institute of Technology (2011)

Submitted to the Department of Mechanical Engineering in partial fulfillment of the requirements for the degree of

Doctor of Philosophy in Mechanical Engineering

at the

MASSACHUSETTS INSTITUTE OF TECHNOLOGY

June 2014

© Massachusetts Institute of Technology 2014. All rights reserved.


Signature redacted

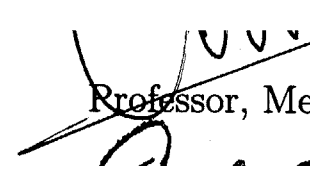
Author


Department of Mechanical Engineering

Signature redacted

May 19, 2014

Certified by


George Barbastathis
Professor, Mechanical Engineering

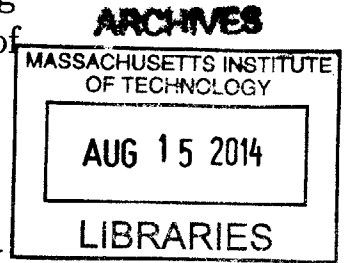
Thesis Supervisor

Signature redacted

Accepted by

David E. Hardt

Chairman, Department Committee on Graduate Theses



Nanostructured Multifunctional Materials for Control of Light Transport and Surface Wettability

by

Hyungryul Choi

Submitted to the Department of Mechanical Engineering
on May 19, 2014, in Partial Fulfillment of the
requirements for the Degree of
Doctor of Philosophy in Mechanical Engineering

ABSTRACT

Biological surfaces have evolved to optimize their structures and physical and chemical properties at the micro/nanoscale for adaptation to different environments, exhibiting a wide variety of beneficial functions, ranging from optical properties to wettability, such as anti-reflection coatings in moth eyes and self-cleaning surfaces of lotus leaves. Combining optical and wetting functions in multifunctional materials is critical for practical engineering applications such as energy harvesting, color generation, and operation of optical instrumentation in humid conditions. However, analyses of the functional design constraints of specified optical and wetting functions followed by integrative optimization have been rare, and limited to simple pairwise combinations from two distinct research disciplines. Furthermore, fabricating the desired multifunctional nanostructured materials remains a difficult engineering challenge due to the limitations of existing nanofabrication methods.

The work in this thesis focuses on the joint control of light transport and surface wettability. It starts with analysis and design, followed by implementation of new multifunctional nanostructured materials using novel nanolithographic fabrication techniques. We first consider multifunctional silica surfaces consisting of conical nanostructures (nanocones) for enhanced omnidirectional broadband transmissivity in conjunction with structural superhydrophilicity or robust superhydrophobicity. This is achieved through a systematic approach to concurrent design of nanostructures in both domains and an innovative fabrication procedure that achieves the desired aspect-ratios and periodicities in the nanocones with few defects, high feature repeatability, and large pattern area. Enhanced optical transmissivity exceeding 98% has been achieved over a broad bandwidth and range of incident angles independent of the polarization state. These nanotextured surfaces also demonstrate robust anti-fogging or self-cleaning properties, offering potential benefits for applications such as photovoltaic solar cells.

As an extended function of this silica nanocone surface, we propose the systematic design and development of nanostructured transparent anti-fingerprint surface coatings that degrade fingerprint oils using photocatalytic effects. The TiO₂-based porous nanoparticle surfaces exhibit short timescales for decomposition of fingerprint oils under ultraviolet light, plus they have transparency comparable to typical glass with low optical haze (< 1%), and are mechanically robust. These TiO₂ nanostructured surfaces are anti-fogging, anti-bacterial, compatible with flexible glass substrates, and remain photocatalytically active in natural sunlight.

Lastly, instead of eliminating *all reflections* over the broadband wavelengths of light for enhanced super-transmissivity, 2-dimensional (2D) periodic nanorod surfaces capable of generating vivid colors by *wavelength-selective reflection* have also been designed and developed. The geometry of the nanorod structures on top of a silicon substrate is optimized to obtain high contrast of colors while still allowing for scalable nanopatterning with the help of newly invented nanofabrication processes.

By developing an integrated understanding of optical and wetting properties of nanostructured materials, we have been able to realize novel functionalities using nanostructured surfaces conceived by concurrent design in the two domains and created by new nanofabrication techniques.

Thesis Supervisor: George Barbastathis
Title: Professor, Mechanical Engineering

Acknowledgments

First and foremost, I would like to thank my research advisor Professor George Barbastathis. He provided incredibly valuable advice and guidance during my PhD. He showed me how to become not only a great researcher but also an extraordinary advisor. Working with him at MIT had been a great pleasure in my life.

I also appreciate support from my committee members, Prof. Gareth H. McKinley, Prof. Nicholas X. Fang, and Prof. Karl Berggren. They gave me excellent suggestions and encouraged my research at every meeting. Prof. Robert E. Cohen also gave me many helpful comments on the research.

I am grateful to Professor Chih-Hao Chang. When he worked with me at MIT, he also suggested me the right direction for me to pursue in my research. At the beginning of my life at MIT, Dr. Se-Young Yang and Dr. Satoshi Takahashi also gave me valuable nanofabrication techniques which allowed me to fabricate various nanostructures.

Dr. Kyoo-Chul Park and Dr. Hyomin Lee are great collaborators, who allowed me to have fruitful results. Without their help, I couldn't have succeeded in finishing the research work. I also thank Dr. Christy Petruczuk, Dr. Yun Seog Lee, Dr. Thomas Crouzier, and Professor Asye Asatekin for their support.

I also would like to thank all the 3D Optical Systems Group members: Dr. Hanhong Gao, Dr. Seongkeun Cho, Justin Lee, Jason Ku, Max Hsieh, Yi Liu, Adam Pan, Nikhil Vadhavkar, Kelli Xu, Dr. Nader Shaar, Thomas Xu, Dr. Lei Tian, Dr. Se Baek Oh, Prof. Laura Waller, Prof. Jon Petrucci, Dr. Yongjin Sung, Dr. Yunhui Zhu, Dr. Hyun Jin In, Dr. Jose Dominguez-Caballero, Dr. Tony Nichol, Dr. Nick Loomis, Prof. Baile Zhang, Prof. Yuan Luo, Dr. Yen-Sheng Lu, Xiaogang Liu, Disi. A, Martin Deterre, Dr. Qin Miao, and all in Singapore. We had a great time talking about new ideas using white boards, and they were always willing to help me whenever I had difficulties on my research. Especially, I want to thank Jeong-Gil Kim. We have talked about many things

from the research to personal concerns. I cannot imagine going through this process without him sitting behind me.

I want to thank Ignacio Cornago and Sagrario Dominguez from Spain since they are great collaborators for creating Multifunctional-Glass and they helped me a lot. I also thank James Daley, Timothy Savas, Mark Mondol, and Kurt Broderick. They have provided technical support and valuable discussion regarding nanofabrication processes. I cannot count how many favors I owe them.

I also want to thank the Korean Graduate Society Association in Mechanical Engineering (KGSAME) friends and my friends in Korea who supported me all the time throughout my life at MIT. I also acknowledge the financial support of the STX Scholarship Foundation and Kwanjeong Educational Foundation.

Finally, I thank my amazing family for who always show their endless love on me and encourage me to try out my own life. Words cannot express my love and gratitude for them. I love you all dearly.

Contents

Chapter 1 Introduction.....	25
1.1 Importance of multifunctional materials for light transport and surface wettability	29
1.2 Lessons from nature: nanostructured multifunctional materials for control of light transport and surface wettability	30
1.3 Light transport at optical interfaces	33
1.4 Interfacial tension of materials and wetting phenomena on textured surfaces	40
1.5 Fabrication of nanostructures for multifunctionality	47
1.5.1 Interference lithography	50
1.5.2 Layer-by-Layer assembly	51
1.6 Outline of thesis	53
Chapter 2 Nanotextured Silica Surfaces with Omnidirectional Broadband Supertransmissivity and Robust Superhydrophobicity	55
2.1 Introduction.....	55
2.2 Fresnel reflection and anti-reflection coatings	57
2.3 Wetting characteristics on textured surfaces	63
2.4 Design and optimization	64
2.4.1 Optical design constraints	64
2.4.2 Wetting design constraints	74
2.5 Fabrication process	78
2.6 Results and discussion	79
2.6.1 Optical properties	80
2.6.2 Wetting properties	87
2.7 Conclusion	92
Chapter 3 Fabrication of Controllable-Aspect-Ratio Periodic Subwavelength Tapered Periodic Nanocone Structures	93
3.1 Introduction.....	93
3.2 Multiple shrinking mask etching	95
3.3 Fabrication of controllable-aspect-ratio subwavelength tapered periodic silica nanocone structures	99
3.3.1 Fabrication of high aspect-ratio (~ 5) tapered silica nanocone structures.....	99

3.3.2	Fabrication of ultra high aspect-ratio (> 6) tapered silica nanocone structures	101
3.4	Simple and low cost fabrication method of controllable-aspect-ratio silica nanocone structures	107
3.4.1	Simple and low cost fabrication of medium aspect-ratio (~ 3) tapered silica nanocone structures	107
3.4.2	Hardmask-free fabrication of low aspect-ratio (~ 2) tapered silica nanocone structures.....	110
3.4.3	Optical properties	112
3.5	Conclusion	116
Chapter 4	Transparent Anti-fingerprint Surfaces	117
4.1	Introduction.....	117
4.2	Transparent superoleophobic surfaces with periodic silica nanocone structures coated with nanoparticles and their limitations	120
4.2.1	Re-entrant structures for superoleophobic surfaces	121
4.2.2	Fabrication process and initial results	124
4.2.3	Limitations of transparent superoleophobic surfaces for transparent anti-fingerprint surfaces	128
4.3	Transparent fingerprint-eating (or <i>dactylovorous</i>) surfaces based on TiO ₂ nanoparticle coatings	131
4.3.1	Photocatalytic effect of titanium dioxide	131
4.3.2	Design.....	132
4.3.3	Fabrication process and optimization.....	136
4.4	Results and discussion	140
4.4.1	Optical properties and photocatalytic effects	140
4.4.2	Mechanical robustness	146
4.4.3	Multifunctionality.....	151
4.5	Conclusion	155
Chapter 5	Nanostructured Color Silicon Surfaces	157
5.1	Introduction.....	157
5.2	Color science	159
5.3	Optical interference and thin-film interference	162
5.4	Design and optimization	168
5.5	Fabrication process	178

5.6	Results and discussion	180
5.7	Conclusion	182
Chapter 6 Thesis Summary and Future Work		183
6.1	Thesis Summary	183
6.2	Future work.....	185
6.2.1	Grayscale Interference Lithography (GIL).....	185
6.2.2	Talbot lithography using aperiodic subwavelength structures	194
6.2.3	Fabrication of multifunctional inverted nanocone arrays.....	203
Appendix A Dimensionless measure of robustness $T^*(z/H)$ of the Cassie-Baxter state against an applied pressure difference across the water-air interfaces		205
Appendix B Transparent Anti-fingerprint Surfaces		209
B.1	Quantification of lateral capillary imbibition of sebum over a thin porous layer of TiO ₂ nanoparticles	209
B.2	Porosity of the TiO ₂ nanoparticle coating	214
B.3	Optical transmissivity and photocatalytic effect for the TiO ₂ nanoparticle coating (50 dipping cycles), a flat TiO ₂ film deposited by using electron beam deposition, and SunClean™ glass	216
B.4	Mechanical robustness test results of the TiO ₂ nanoparticle coating (50 dipping cycles) against repeated shear force	219
References		221

List of Figures

Figure 1-1. a) Scanning electron microscope (SEM) image of an anti-reflective nipple array on the *Attacus atlas* moth eye. Reproduced from Ref. [21] with permission from The Royal Society of Chemistry. b) Transmission electron microscope (TEM) image showing wing-scale cross-sections of *M. rhetenor*. Reproduced from Ref. [10] with permission from Nature Publishing Group. c) SEM image of the *Nelumbo mucifera* (Lotus) leaf surface. Reproduced from Ref. [14] with permission from Wiley-VCH, John Wiley & Sons, Inc. d) SEM image of the textured surface of the desert beetle *Stenocara* sp. Reproduced from Ref. [11] with permission from Nature Publishing Group31

Figure 1-2. Schematic drawing of the fundamental light interaction phenomena within two optically different media34

Figure 1-3. Wave vectors for light incident on a boundary separating two different optical media [27]35

Figure 1-4. Incoming wave whose electric field is normal to the plane-of-incidence [25]38

Figure 1-5. Incoming wave whose electric field is in the plane-of-incidence [25]39

Figure 1-6. Schematic illustration of forces on molecules of a liquid41

Figure 1-7. Schematic drawing of a liquid drop on a solid surface with the quantities in Young's equation42

Figure 1-8. Schematic drawings of liquid droplets on a flat surface and textured surface. The liquid penetrates into the texture and fully wets the surface. The apparent contact angle is determined by Eq. 1.22, and this state is known as the Wenzel state43

Figure 1-9. Wetting diagram for the Wenzel state [33, 36]. The slope of the plot represents r_w 44

Figure 1-10. Schematic drawings of liquid droplets on a flat surface and textured surface. The liquid sits partially on air, and the apparent contact angle can be determined by Eq. 1.23. This state is known as the Cassie-Baxter state45

Figure 1-11. Wetting diagram for the Cassie-Baxter state [33, 36]46

Figure 1-12. Schematic drawing of interference lithography (IL) configuration [54, 55]51

Figure 1-13. Schematic illustration of Layer-by-Layer (LbL) assembly through electrostatic interaction. Reproduced from Ref. [56] with permission from The Royal Society of Chemistry	52
Figure 2-1. Cross-section SEM image of graded-index coating with a modified-quintic-index profile. Reproduced from Ref. [18] with permission from Nature Publishing Group	59
Figure 2-2. a) Fresnel reflection at the optical interface of a flat surface. b) Principle of an anti-reflective surface, consisting of subwavelength nanocone structures whose period P is smaller than the wavelength of incident light. Subwavelength tapered nanostructures offer adiabatic impedance mismatch between the air (n_1) and the medium (n_2) and thus reduce reflection	60
Figure 2-3. SEM image of the subwavelength structured (SWS) surface. The grating period is 150 nm, and the grooves are 350 nm deep. Reproduced from Ref. [3] with permission from Optical Society of America	61
Figure 2-4. SEM image of anti-reflective structures on the PMMA substrate obtained through hot embossing process. Reproduced from Ref. [68] with permission from Wiley-VCH, John Wiley & Sons, Inc	61
Figure 2-5. Schematic of the nanocone structure geometry and incident light configuration	65
Figure 2-6. Optical transmissivity response (zeroth-order) of the transparent nanocone structured surface in Figure 2-5. The geometry of the structures determines the bandwidth of the perfect transmission region	66
Figure 2-7. Calculated optical transmissivity with respect to the wavelength and height of the nanocone structure with a refractive index (n_2) of a) 1.5, b) 2, and c) 3. The surrounding medium is air ($n_1 = 1$)	69
Figure 2-8. Upper limit wavelength (λ_{max}) values calculated by RCWA, and the values estimated from Eq. 2.12, with respect to the wavelength and height of the nanocone structure with a refractive index (n_2) of 1.5, 2, and 3. The surrounding medium is air ($n_1 = 1$), and the angle of incidence is 0°	71
Figure 2-9. Normalized maximum (λ_{max}/H) and minimum (λ_{min}/P) operating wavelengths plotted against incident angles with the substrate's refractive index (n_2) of 1.5. The surrounding medium is air ($n_1 = 1$)	72
Figure 2-10. The normalized operating bandwidth (B^*) with respect to structure aspect-ratio for different incident angles. For the structure to function at large angles (θ_1), high aspect-ratio structures are required	73

Figure 2-11. Transmission efficiency (zeroth-order) of the anti-reflective nanocone structure simulated using RCWA for a number of incident angles as functions of the wavelength of the incident illumination74

Figure 2-12. Schematic drawings of the three-phase (air-liquid-solid) contact line on hydrophobically-modified (left) and hydrophilic (right) nanocone structures [45]. The insets show corresponding goniometer images for 5 μl droplets with apparent contact angles of $\theta^* = 165 \pm 1^\circ$ (left) and $\theta^* \leq 5^\circ$ (right), respectively. The black thick arrows (γ_{LV}) represent directions of surface tensions at the three-phase (air-liquid-solid) contact lines75

Figure 2-13. SEM image of the fabricated nanocone structures [45]. The period of the structure P is 200 nm.....79

Figure 2-14. Transmissivity for both a) Transverse magnetic (TM) and b) Transverse electric (TE) polarized light through the single-sided and double-sided patterned surfaces with respect to incident angle. Transmissivity on the single-sided patterned surface and double-sided patterned surface are shown in red and in blue, respectively. Dots represent measured transmission data, and the solid lines are numerically calculated values by RCWA method80

Figure 2-15. Averaged broadband transmissivity with two measurements on both TE and TM polarizations at the four different incident angles ($\theta_I = 0^\circ, 30^\circ, 45^\circ, \text{ and } 60^\circ$) with a range of wavelength ($250 \text{ nm} \leq \lambda \leq 1700 \text{ nm}$) [45]. The black line represents the calculated transmissivity values of the flat fused silica surface at normal incident angle81

Figure 2-16. Broadband total transmissivity (blue solid line) and zeroth-order transmissivity (red solid line) through the double-sided patterned surface at normal incident angle ($\theta_I = 0^\circ$) with a range of wavelengths ($400 \text{ nm} \leq \lambda \leq 850 \text{ nm}$). Optical haze is shown in black line with respect to wavelength82

Figure 2-17. Measured external quantum efficiency (EQE) of a processed solar cell as a function of wavelength ($300 \text{ nm} \leq \lambda \leq 1100 \text{ nm}$) at normal incident angle ($\theta_I = 0^\circ$). Lines with light blue, blue, red, and yellow colors are measured EQE without any layer, with the double-sided patterned surface, with the single-sided patterned surface, and with a flat silica surface on top of the solar cell, respectively83

Figure 2-18. Measured optical transmissivity of the nanotaper structures and simulated transmissivity using RCWA for both transverse electric (TE) and transverse magnetic (TM) polarized lights as a function of the wavelength at 30° incident angle [45]84

Figure 2-19. Measured optical transmissivity of the nanotaper structures and simulated transmissivity using RCWA for both TE- and TM-polarized lights as a function of the wavelength at 45° incident angle [45]85

Figure 2-20. Measured optical transmissivity of the nanotaper structures and simulated transmissivity using RCWA for both TE- and TM-polarized lights as a function of the wavelength at 60° incident angle [45]85

Figure 2-21. Blue-dyed water droplets sitting on a transparent nanotaper surface (left) and on a flat glass (right), each placed on top of printed black letters [45]. The insets are top views of the same two surfaces. The very weak reflection and high contact angle of the tapered nanocone surface contrast strong reflection and a low contact angle of water on the flat glass87

Figure 2-22. Sequential images of a water droplet impact on an oblique (30° from the horizontal plane) nanotaper surface (taken through the use of a high speed camera; $V = 6.26$ m/s and $We \approx 1785$) [45]. The last image on the bottom right side demonstrates that no residual droplets remain on the nanotaper surface due to the high robustness of the Cassie-Baxter state to the dynamic pressure88

Figure 2-23. Optical transmissivity measurements for quantifying the self-cleaning property of the nanocone surfaces. Evolution of the transmissivity of a red laser ($\lambda = 632.8$ nm) through a) surface-contaminated tapered nanocone surface, and b) flat glass surfaces, respectively [45]89

Figure 2-24. Optical transmissivity measurements for quantifying the anti-fogging property of the nanocone surfaces [45]. a) Image of printed letters viewed through fogged nanocone (left) and flat glass (right) surfaces. b) Change of transmissivity due to fogging and defogging on double-sided nanotaper (blue), single-sided nanotaper (red) and flat cleaned glass (black) surfaces90

Figure 2-25. Principle of anti-fogging property on the nanotextured silica surface. a) light scattering due to microscopic water droplets on a hydrophilic flat glass surface. b) no light scattering because of rapid imbibition of the thin layer of water on the nanotextured surface. An inset shows the magnified view of the nanotextured surface. When $\theta_{adv} - \varphi < 90^\circ$, the net traction force on the liquid-vapor interface is directed downward; thus it promotes the imbibition of the liquid into the solid structure91

Figure 3-1. a) Schematic of conventional single hardmask etching process. b) Schematic of double-hardmask etching process. The numbered arrows denote reactive ion etching processes [54, 94]96

Figure 3-2. Schematic of the shrinking hardmask etching process, which is the equivalent process of arrow 3 presented in Figure 3-1b [54, 94]97

Figure 3-3. Successive SEM images of the process of shrinking mask etching process shown in Figure 3-2. All the scale bars represent 200 nm. The substrate is a fused silica wafer, and the material of the second hardmask is poly-silicon represented by white dotted lines98

Figure 3-4. a-f) Fabrication steps of subwavelength high aspect-ratio silica nanocone structures. f) Schematic of the fabricated surface by shrinking mask etching (see Figure 3-3). The height and the period of the fabricated nanocone structures are around 1.1 μm , and 200 nm, respectively101

Figure 3-5. Fabrication processes of subwavelength ultra high aspect-ratio (> 6) silica nanocone structures. a) Development of negative photoresist pattern. b) Transferring the nanohole pattern into the anti-reflective coating (ARC) layer through a 20-nm-thick SiO_2 layer. c) Enlargement of the size of the holes through O_2 reactive ion etching (RIE) process. d) Hydrogen silsequioxane (HSQ) filling the enlarged holes. e) HSQ posts. f) Silicon posts. g) Subwavelength periodic silica nanorods with ultra high aspect-ratio (> 6)104

Figure 3-6. Cross-section SEM micrograph of fabricated ultra high aspect-ratio subwavelength nanocone structures [93]105

Figure 3-7. Heights of the fabricated nanocone structures with respect to the width (or diameter) of the HSQ nanorods (the first hardmask)106

Figure 3-8. Cross-section SEM images of the fabricated silica nanocone structures marked by A, B, C and D in Figure 3-7106

Figure 3-9. Fabrication process of subwavelength medium aspect-ratio (~ 3) silica nanocone structures [97]108

Figure 3-10. Cross-section SEM micrograph of the fabricated silica nanocone structures with an aspect-ratio of ~ 3 [97]109

Figure 3-11. Fabrication process of subwavelength low aspect-ratio (~ 2) silica nanocone structures111

Figure 3-12. Cross-section scanning electron micrograph of the fabricated silica nanocone structures with an aspect-ratio of ~ 2 112

Figure 3-13. Measured optical transmissivity of the nanotaper structures as a function of the wavelength at normal incident angle. i) Double-sided patterned and ii) Single-sided patterned surfaces fabricated with the help of the hardmask (20-nm-thick SiO_2) described in Section 3.4.1. iii) Single-sided patterned surface fabricated without the hardmask. iv) Flat fused silica wafer113

Figure 3-14. SEM image of the subwavelength positive photoresist (PFi88-A2) post structures after development process depicted in Figure 3-11b115

Figure 4-1. Image of fingerprint oils deposited on a touchscreen display (iPhone 4S). The inset shows a magnified view of the fingerprint oils, which reveals micrometric liquid droplets117

Figure 4-2. Schematic of the square array of silica nanocones coated uniformly with nanoparticles	121
Figure 4-3. a) SEM micrographs for the micro-hoodoo surfaces having circular flat caps. b) Drop of octane on the silanized micro-hoodoo surface ($\theta_{adv} = 163^\circ$). Reproduced from Ref. [113] with permission from The American Association for the Advancement of Science	122
Figure 4-4. Schematic diagrams illustrating the expected liquid–vapor interface on two idealized surfaces with different values of the equilibrium contact angle (θ_E). Reproduced from Ref. [71] with permission from Materials Research Society	123
Figure 4-5 a) Schematic of a liquid drop deposited on the fractal-like composite interface made of 25-nanometer-thick silica shells. b) Drop of hexadecane deposited on the surface with a static contact angle of $156 \pm 1^\circ$. Reproduced from Ref. [107] with permission from The American Association for the Advancement of Science	124
Figure 4-6. Schematic illustration of the fabrication process for the transparent superoleophobic surfaces	125
Figure 4-7. SEM images of the fabricated subwavelength nanocone structures encrusted with LbL-deposited nanoparticles. a) Oblique view. b) Top view	126
Figure 4-8. Images of drops of a) Water, b) DMSO, c) Jojoba oil, and d) Hexadecane on the surfaces with the corresponding advancing contact angles	126
Figure 4-9. Defects on the fabricated surface. a) Aggregation. b) Defective surface areas lacking the nanocones	127
Figure 4-10. Schematic of change in the gap between the meniscus of liquid and solid surface with respect to the period (or spacing)	128
Figure 4-11. Schematic of a liquid drop on an array of pillars in the a) Cassie-Baxter and b) Wenzel state. Reproduced from Ref. [114] with permission from The Royal Society of Chemistry	129
Figure 4-12. Schematic of the superamphiphobic (or superoleophobic) layer consisting of pillars of sintered spheres from side and top view. The liquid is suspended on top in the Cassie state. If no pressure is applied, the liquid surface is planar. With pressure the contact line moves downwards and the interface starts to curve. Reproduced from Ref. [114] with permission from The Royal Society of Chemistry	129
Figure 4-13. Schematic illustration of photocatalytic effect on titanium dioxide (TiO_2)	132
Figure 4-14. Schematic illustration of the two-step mechanism that leads to degradation of the sebum: (step 1) capillary imbibition of low surface tension components into the	

permeable nanostructure and (step 2) photocatalytic decomposition of the imbibed liquids on TiO ₂ nanoparticles	133
Figure 4-15. Time-sequential images of the initial spreading and capillary imbibition of fingerprint oils by capillary force	134
Figure 4-16. Time-sequential images of fingerprint oils on the nanoparticle coated side (top side, thickness = 114.8 ± 6.2 nm) and a typical microscope slide (bottom side) for 0, 20, 40, and 60 minutes of UV exposure ($I = 1.5 \pm 0.1 \text{ mW/cm}^2$ at $300 \text{ nm} \leq \lambda \leq 400 \text{ nm}$)	135
Figure 4-17. Schematic illustration of Layer-by-Layer (LbL) coating process. The 8 steps of the figure including 6 rinsing steps will now be referred to as 1 dipping cycle	136
Figure 4-18. Schematic illustration and SEM image of the nanoparticle coated surface	138
Figure 4-19. Film thickness of TiO ₂ nanoparticle coating layer with respect to the number of coated dipping cycles, measured using profilometry (Dektak)	138
Figure 4-20. Measured optical transmissivity over the visible range ($400 \text{ nm} \leq \lambda \leq 800 \text{ nm}$) for four different thicknesses of TiO ₂ nanoparticle layers. The black line represents the transmissivity of a typical microscope (soda lime) glass slide that is used as the substrate for the TiO ₂ nanoparticle coatings	140
Figure 4-21. Illustration of the experimental process for quantifying the dactyloporous effect. The two microscope images correspond to the PDMS stamp (20 mm by 10 mm) with micrometric post array before depositing artificial sebum (left), and the same PDMS stamp with the absorbed sebum (right)	142
Figure 4-22. Time evolution of measured transmissivity (angle of incidence = 0°, $\lambda = 660 \text{ nm}$) through an artificial sebum-stamped spot of a 50 dipping cycle thick TiO ₂ nanoparticle coating under UV light ($1.5 \pm 0.1 \text{ mW/cm}^2$ at $300 \text{ nm} \leq \lambda \leq 400 \text{ nm}$). The insets show two images of a part of the resolution test chart viewed through the nanoparticle coated surfaces with the artificial sebum deposits at $t = 0 \text{ min}$ (left) and 150 min (right) of UV exposure time	143
Figure 4-23. Time evolution of measured apparent contact angle of water droplets (Volume $V = 5 \mu\text{L}$) deposited on a 50 dipping cycle coating under UV light exposure. The apparent contact angle values are reduced to less than 5° after $t = 120 \text{ min}$ demonstrating the recovery of superhydrophilicity of TiO ₂ nanoparticle surfaces	144
Figure 4-24. Longevity test of the 50 dipping cycle TiO ₂ nanoporous coating. The blue square dots clearly represent the full recovery (up to 10 cycles) with approximately no change in optical transmissivity ($\lambda = 660 \text{ nm}$) and consistent UV exposure time (3 hours) that takes to reach the initial transmissivity after repeated stamping the artificial sebum	

pattern. The hollow blue square dots indicate the transmissivity values right after the deposition of the artificial sebum. The blue lines with arrows represent the recovery of transmissivity. The red colored transparent box shows the single cycle of photocatalytic decomposition of the artificial sebum during 3 hours of UV exposure that is also shown in Figure 4-22146

Figure 4-25. Optical spectral responses and haze of the TiO₂ nanoparticle surface (blue) and the superoleophobic soot-based surface (red). Insets: (i) Micrograph of a superoleophobic soot-based surface; (ii), (iii) Goniometric images of a droplet of artificial sebum deposited on the surface before and after twice applying a contact force of 4 N in the normal direction of the surface, respectively147

Figure 4-26. Evolution of optical transmissivity (at $\lambda = 660$ nm) after repeatedly applying a normal contact force (4 N) on the dactyloporous surface through a latex rubber pad with area $A = 81$ mm². The four insets are images of the resolution test chart (with image quality greater than $\alpha = 0.92$) taken through the LbL-deposited nanoparticle surfaces after repeated mechanical loading148

Figure 4-27. Mechanical durability test results of the TiO₂ nanoparticle coating against shear stress emulating sliding gesture of human fingers. Evolution of optical transmissivity (at $\lambda = 660$ nm) after repeatedly applying a contact sliding of a latex rubber pad (contact area $A = 81$ mm²) with a normal contact force (0.254 N) which is equivalent to the minimum shear force applied by human fingers to operate capacitive touchscreen [131] on the TiO₂ nanoparticle coated surface (blue) and the superoleophobic soot-based surface (red). The inset on the left-hand side (i) represents the SEM image of the destroyed region of the transparent superoleophobic coating, and two insets on the right-hand side (ii, iii) are the SEM images of the TiO₂ nanoparticle coating150

Figure 4-28. Time evolution of transmissivity due to fogging and defogging on a freshly-prepared TiO₂ nanoparticle coated surface (blue), and a bare glass microscope slide (red). Insets show optical micrographs of a resolution test chart viewed through the nanoparticle coated glass (i) and the microscope glass slide (ii) taken at the moments marked by the green color bar (at time $t \sim 20$ s). Image distortion analysis using a standard resolution test target is used to quantify the anti-fogging performance in the same way as used in Figure 4-26 [129, 130]. The clear in-focus left inset image of the resolution test chart is transmitted through the TiO₂ nanoporous surface, which shows the antifogging property ($\alpha = 0.92$). The correlation coefficient ($\alpha = 0.58$) for the right inset image (a fogged glass microscope slide case) indicates unacceptably poor visual clarity152

Figure 4-29. Fraction of live *E. coli* on the TiO₂ nanoporous surface (blue) and a microscope slide (red) with respect to exposure time. Fluorescence images showing anti-bacterial activity of the TiO₂ nanoparticle-deposited surface under UV exposure (1.6 ± 0.1 mW/cm² at $300 \text{ nm} \leq \lambda \leq 400 \text{ nm}$) for 3 hours. Green and red colors represent live

and dead <i>E. coli</i> on both the nanoparticle coated side (lower image) and a typical microscope glass slide (upper image)	153
Figure 4-30. Flexible glass substrate deposited with a TiO ₂ nanoparticle film (lower half on the left) by the LbL fabrication method. The three sequential images on the right show that a fingerprint deposited on the flexible TiO ₂ nanoparticle coated surface progressively disappears under sunlight irradiation ($I_{solar} = 4 \pm 1 \text{ mW/cm}^2$ at $300 \text{ nm} \leq \lambda \leq 400 \text{ nm}$) for 3 hours	154
Figure 5-1. CIE standard observer color matching functions: $X(\lambda)$, $Y(\lambda)$ and $Z(\lambda)$ [144]	160
Figure 5-2. CIE 1931 color space chromaticity diagram and standard RGB color space [144]	161
Figure 5-3. Optical interference effects from an oil film on water	162
Figure 5-4. Schematic drawing of the thin film configuration. The surrounding medium is air whose refractive index is 1	163
Figure 5-5. Schematic of the thin layer (single-layer anti-reflection coating) structure geometry and incident light configuration. The surrounding medium is air. Electrical fields are calculated at the cross-section demonstrated by the pink colored shaded region (see Figure 5-7)	164
Figure 5-6. Calculated optical reflectance of normal incident light from the thin layer model schematically illustrated in Figure 5-5 with respect to the wavelengths ($400 \text{ nm} \leq \lambda \leq 2000 \text{ nm}$)	165
Figure 5-7. Electric field distributions calculated using finite domain time difference (FDTD) at ①, ②, and ③ in Figure 5-6 (destructive interference). All the white scale bars represent 100 nm	166
Figure 5-8. Electric field distributions calculated using FDTD at ④, ⑤, and ⑥ in Figure 5-6 (constructive interference). All the white scale bars represent 100 nm	167
Figure 5-9. Schematic diagram of the proposed nanostructured color coatings. Yellow beam represents incoming white light, and red, orange, and green colored beams indicate the reflected colored light from the nanorod structures	168
Figure 5-10. Optical reflectance spectrum against normal incident light calculated by finite difference time domain (FDTD) simulations with respect to different heights of the periodic nanorods and wavelengths with a fixed width of 160 nm and a period of 200 nm	170
Figure 5-11. Optical reflectance spectrum against normal incident light calculated by using the thin-film model and transfer matrix method with the same geometrical constraints used in Figure 5-10. A layer of the nanorod structures is considered a thin flat	

film with an effective refractive index that is determined to be that of the fundamental mode of the silicon waveguide. The dotted lines shown with the calculated C values represent the calculated local maximum and minimum reflectance values from the thin-film model. The upright triangle marks represent the local maximum reflectance values in Figure 5-10 calculated from FDTD; in contrast, the downward pointing triangle marks represent the local minimum reflectance values in Figure 5-10 calculated from FDTD. Both the dotted lines and the triangle marks show good agreements171

Figure 5-12. a) Calculated electric field distributions using FDTD at the cross-sections of the nanorod at the wavelength of (i) 617 nm with the height of 250 nm, (ii) 648 nm with the height of 300 nm, and (iii) 710 nm with the height of 350 nm. b) Electric field distributions at the cross-sections of the nanorod at the wavelength of (iv) 640 nm with the height of 200 nm, (v) 670 nm with the height of 250 nm, and (vi) 718 nm with the height of 300 nm. The inset between Figures 5-12a and 5-12b schematically shows the cross-section of the nanorod where the electric field distributions are calculated by FDTD. White dotted lines show the boundary of the nanorod structures. Note that all the scale bars represent 100 nm, and the circled numbers can be found in Figure 5-11173

Figure 5-13. Optical reflectance spectrum against normal incident light calculated by FDTD simulations with respect to different heights of the periodic nanorods with a period of 200 nm and a fixed diameter of a) 120 nm, b) 140 nm, c) 160 nm, and d) 180 nm ...174

Figure 5-14. Reflected colors from the nanorod structures with varying height from 200 nm to 400 nm with a 25 nm step increase (presented by blue arrows) mapped on top of the CIE 1931 chromaticity diagram, with a fixed diameter of 160 nm. For comparison, the inset shows the colors generated from the nanorod structures with a fixed diameter of 120 nm (green solid dots and dotted lines), 140 nm (orange solid dots and dotted lines), 160 nm (red solid dots and dotted lines), and 180 nm (purple solid dots and dotted lines), with respect to the varying heights (from 200 nm to 400 nm with a 25 nm incremental step)176

Figure 5-15. Schematic of the fabrication process and the corresponding SEM images. a) Development of negative photoresist pattern. b) Transferring the nanohole pattern into anti-reflective coating layer. c) Enlargement of the size of the holes through oxygen reactive ion etching (RIE). d) Hydrogen silsequioxane (HSQ) filling the fabricated holes. e) HSQ posts. f) Subwavelength periodic silicon nanorods for color coating. Note that all the scale bars represent 200 nm179

Figure 5-16. a) Colors theoretically calculated by FDTD simulations (red solid dots) and experimentally measured colors (black hollow dots) from the fabricated nanostructured color coatings placed on the CIE chromaticity diagram. b) The image of the fabricated sample and its corresponding colors181

Figure 6-1. Schematic of Grayscale Interference Lithography (GIL) processes for fabricating aperiodic subwavelength nanostructures. Aperiodic subwavelength nanostructures can be created by the conventional interference lithography combined with a moving aperture plate [96]186

Figure 6-2. Exposure dose distribution with respect to lateral position (x) over one period (P) in Grayscale Interference Lithography (GIL). The total exposure dose (D) is the sum of the dose exposed by the interfering beam (D_i) and the dose exposed by single beam under the shade region (D_s) [96]188

Figure 6-3. a) Image of the subwavelength 1D grating fabricated by GIL with the single exposure. During the exposure, the aperture plate moves to the left side of the sample (negative x -direction) at the constant speed. b) Cross-sectional micrographs of the grating with respect to the position from i region to $viii$ region marked in Figure 6-3a [96]191

Figure 6-4. Duty cycle of the 1D grating with respect to coordinate in the x -dimension in Figure 6-3a. Error bars represent the standard deviation values of the measured duty cycles [96]192

Figure 6-5. 2D aperiodic subwavelength gratings fabricated by GIL with the double exposures. a) schematic of the double exposures on a 2.5 cm by 2.5 cm sample. b) top-view micrographs of the grating on the i region (left) and on the ii region (right) [96] .193

Figure 6-6. Simulated intensity pattern generated by an aperiodic 1D phase mask with linearly varying duty-cycle under normal illumination [156]195

Figure 6-7. Diffraction orders and the Talbot distance (z_i) through the 1D phase grating with respect to the grating period (P)196

Figure 6-8. Transmitted efficiency of the diffraction orders and contrast values of the intensity profile at the Talbot plane with respect to the duty cycle (w/P) when $P = 390$ nm and $H = 220$ nm197

Figure 6-9. Simulated intensity pattern generated by the designed aperiodic 1D phase mask with linearly varying duty cycles198

Figure 6-10. Schematic of the processes for fabricating aperiodic diffracted intensity pattern from aperiodic grating phase mask199

Figure 6-11. Scanning electron micrographs of the fabricated 1D phase mask on a fused silica. The duty cycle (w/P) gradually varies from 0.1 to 0.75, which covers the perfect contrast region in Figure 6-8. The period P is 390 nm, and the height $H = 220 \pm 5$ nm .200

Figure 6-12. Cross-section scanning electron micrographs of the preliminarily fabricated 3D nanostructures with the simulated intensity profiles (exposure dose: 32.15 mJ/cm²).201

Figure 6-13. Cross-section scanning electron micrographs of the fabricated 3D nanostructures with the simulated intensity profiles (exposure dose: 56.16 mJ/cm²)202

List of Tables

Table 2-1. The structure geometry for rigorous coupled wave analysis (RCWA). 20 discrete layers are used for defining nanocone structures and the duty cycles of each layer are listed in the table. The duty cycle is the ratio of diameter to period of the nanocone [45]86

Table 4-1. Optical transmissivity and haze of the nanoporous titania coatings used for sebum digestion. a) Required exposure time until the moment that the optical transmissivity reaches 99% of the original transmissivity measured under UV illumination ($I = 1.5 \pm 0.1 \text{ mW/cm}^2$ at $300 \text{ nm} \leq \lambda \leq 400 \text{ nm}$) without the artificial sebum. b) See Appendices B.3 and B.4 for details145

Chapter 1 Introduction

Natural biological surfaces have evolved to optimize their structures and physical and chemical properties at the micro/nanoscale for a wide variety of functions, ranging from optical properties to wettability. For example, nanostructures discovered in moth eyes and cicada wings minimize reflectivity over a broad range of wavelengths and incident angles, which allows them to capture more light and hide from their predators at night. Layered periodic nanostructures on butterfly wings reflect only pure single colors to seduce their mates for breeding. Moreover, micro/nanostructures on lotus leaves exhibit a self-cleaning effect, using rain droplets to keep themselves pristine, and hence are able to capture more sunlight without dust.

These studies have in turn inspired development of biomimetic surfaces emulating the anti-reflective, self-cleaning, water-harvesting, and color-generating capabilities of functional surfaces found in nature. In photovoltaic industries, tapered subwavelength nanostructures on silicon surfaces have been fabricated in order to increase the light-collecting efficiency of solar cells, while reducing reflection of sunlight. Display industries recently have started seeking to adapt these structures to their panels so as to increase their viewing angles and enhance the brightness of the displays. In addition to the industrial applications in optics, superhydrophobic coatings, which are also known as lotus effects, have been used for windshields to prevent water droplets from clinging to the glass. As seen in the examples, these functions of the nanostructured surfaces inspired by natural biological surfaces have influenced not only academic researchers but also industrial practices. There is ample reason to seek to better understand these properties.

These useful phenomena in optics and wetting emerge from unique micro- and nanostructures on surfaces. When the length of the structures is on the order of the wavelength of light (or less), light behaves differently than it typically does at the optical interfaces of bulk materials. These nanostructures optically behave as homogeneous

media with effective optical properties, such as anti-reflectivity and selective-wavelength reflection of incoming light, that are much superior to those of natural bulk materials. Also, interfacial tension between a solid and a liquid at the micro/nanoscale is the dominant force; thus micro/nanoscale structures combined with surface chemistry enable control of the wetting properties.

Despite these structures' 1) beneficial functions, 2) their potential as industrial applications, and 3) their contributions to understanding physical phenomena in two different fields, however, analyses of the functional design constraints of specified optical and wetting functions followed by integrative design and optimization have been rare – and limited to simple pairwise combinations from two distinct research disciplines. Furthermore, fabricating the desired multifunctional nanostructured materials remains a difficult engineering challenge due to the limitations of existing nanofabrication methods. The current fabrication techniques are not optimized for scalable production of multifunctional nanostructured materials; therefore, a new scalable fabrication method needs to be developed.

Hence, the work in this thesis focuses on a joint consideration of controlling light transport and surface wettability, starting with analysis and design, followed by the implementation of new multifunctional nanotextured materials using novel nanolithographic fabrication techniques. We report development of three different nanostructured multifunctional materials optimized in the optical and fluidic domains and corresponding novel fabrication methods.

We first consider nanostructured multifunctional silica surfaces for enhanced omnidirectional broadband transmissivity with structural superhydrophilicity or robust superhydrophobicity. This is achieved through a systematic approach to concurrent design of optimal structures in both domains and an innovative fabrication procedure that achieves the desired aspect-ratios and periodicities with few defects, high feature repeatability, and large pattern area. The accomplishment of such high aspect-ratio structures on silica enables us to achieve enhanced anti-reflection and

superhydrophobicity/superhydrophilicity properties that provide self-cleaning and anti-fogging effects with excellent repeatability over large surfaces.

Next we investigate fingerprint oil-repellent surfaces, which is an extended approach of the superhydrophobic surfaces for keeping non-wettability with low surface tension liquids such as fingerprint oils. However, these superoleophobic surfaces are mechanically weak and optically hazy. We instead propose the systematic design and development of transparent nanostructured surface coatings that resist the deposition and accumulation of fingerprint oils using photocatalytic effects. The nanostructured coatings are based on a very thin (sub-micron) oleophilic TiO_2 nanoporous matrix that is deposited via Layer-by-Layer (LbL) assembly. The TiO_2 -based porous nanoparticle surfaces exhibit short time scales for decomposition of fingerprint oils under ultraviolet (UV) light, plus they are mechanically robust, with transparency comparable to typical glass. These TiO_2 nanostructured surfaces are anti-fogging, anti-bacterial, compatible with flexible glass substrates, and remain photocatalytically active in natural sunlight.

Lastly, we propose a 2-dimensional (2D) array of periodic subwavelength nanorod structures on top of a silicon surface to generate a wide variety of vivid colors using a scalable nanopatterning method. We develop a novel nanofabrication technique followed by interference lithography (IL) and reactive ion etching (RIE) to fabricate the designed silicon nanorod structures with a large duty cycle (~ 0.8 , which is practically difficult to achieve via typical interference lithography) for acquiring high contrast of colors. Strong interference effects inside these nanostructures allow control of selective-wavelength reflectance, and the fabricated silicon coating is readily observable even to the naked eye since the nanostructured color coating covers a surface area as large as 2 cm by 4 cm.

In summary, by developing an integrated understanding of optical and wetting properties of nanostructured materials, we have been able to realize novel functionalities using nanostructured surfaces conceived by concurrent design in the two domains and created by new nanofabrication techniques. Preliminary results of additional nanofabrication

methods developed for these nanostructured multifunctional materials will also be briefly introduced.

1.1 Importance of multifunctional materials for light transport and surface wettability

Multifunctionality for light transport and surface wettability is critical for fundamental understanding of physical interfacial properties of materials and for practical engineering applications such as energy harvesting, color generation, and operation of optical instrumentation in extreme climates or humid conditions where the optical reflectivity, transmittance, wetting and other physical interfacial properties must satisfy multiple design characteristics in order to fulfill system requirements [1, 2]. For example, the light collecting efficiency of a photovoltaic solar cell is highly influenced by both surface dust contamination and optical reflection losses over a broad range of wavelengths and incident angles [1-3]. The operational efficiency and longevity would benefit from both self-cleaning and anti-reflection surface properties. To achieve the high transmissivity required for operation of optical instrumentation under humid conditions in chemical and biological laboratories, antifogging and anti-reflection as well as enhanced transparency would convey critical advantages; these multifunctional material design strategies could also find practical utility in enhanced performance characteristics of common objects such as goggles and vehicle windshields [4]. These multiple functions can provide numerous opportunities for improving the environment in which we live, and also offer economic benefits [5].

Although natural bulk materials do not exhibit these beneficial interfacial properties, it has been discovered that these functions of biologically produced surfaces stem from nanostructures; hence many researchers have intensively sought fundamental understanding of the functions from those surfaces, and the connections to nanostructures [6-11]. In the next section, I will continue to discuss the lessons from nature and the connection between nanostructures and multifunctionality.

1.2 Lessons from nature: nanostructured multifunctional materials for control of light transport and surface wettability

Biologically produced surfaces take advantage of multiple beneficial functions originating from micro/nanostructures that cannot be observed in natural bulk materials. With the help of significant advances in micro- and nanotechnologies, the study of the structures, functions, and mechanisms of biologically produced surfaces at the micro/nanoscale has boomed for decades, in the effort to understand those properties and create artificial functional surfaces [6-12]. In particular, these functions in two different domains, optics and surface wettability, have been extensively investigated because of their technological potential and engineering applications [1, 6, 9, 12-14].

Studies on their physical phenomena and mechanisms have shown that the optical and wetting properties of those surfaces are closely related to the length scale of the surface structures. To achieve the optical properties such as anti-reflectivity and selective-wavelength reflection, the size of the structures needs to be on the order of the wavelength of light or less. When that is true, light behaves differently than it typically does at the optical interfaces of bulk materials. These nanostructures optically act as a homogeneous medium with effective refractive indices, showing superior optical functions, such as anti-reflectivity and selective reflection of incoming light, compared to those of natural bulk materials [1, 9, 15-18]. Figure 1-1 shows the multifunctional surfaces existing in nature mapped with respect to the length scale (or feature size). In order to obtain optical properties superior to those from bulk materials, the typical size of structures on butterflies' wings and moths' eyes is on the same order of visible wavelength ($400 \text{ nm} \leq \lambda \leq 800 \text{ nm}$) or less [10, 19-22]. Two scanning electron microscope (SEM) images on the left-hand side demonstrate the surface morphologies of moths' eyes and butterflies' wings, respectively.

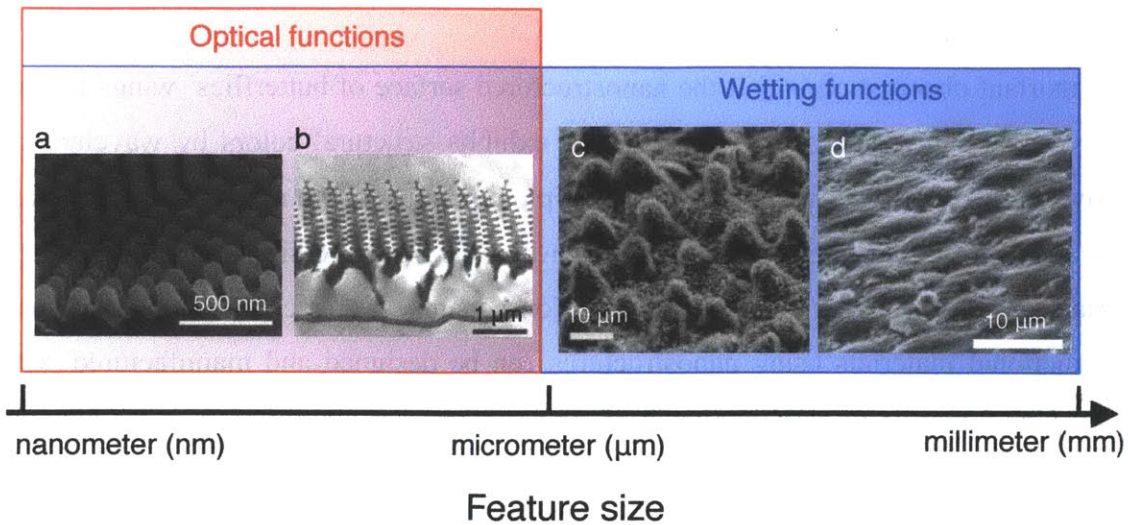


Figure 1-1. a) Scanning electron microscope (SEM) image of an anti-reflective nipple array on the *Attacus atlas* moth eye. Reproduced from Ref. [21] with permission from The Royal Society of Chemistry. b) Transmission electron microscope (TEM) image showing wing-scale cross-sections of *M. rhetenor*. Reproduced from Ref. [10] with permission from Nature Publishing Group. c) SEM image of the *Nelumbo nucifera* (Lotus) leaf surface. Reproduced from Ref. [14] with permission from Wiley-VCH, John Wiley & Sons, Inc. d) SEM image of the textured surface of the desert beetle *Stenocara sp.* Reproduced from Ref. [11] with permission from Nature Publishing Group.

In addition, surface wettability is the interfacial interaction between a solid and a liquid. For effective control of surface wettability by using interfacial tension, the size of structures should be on the order of micrometers (μm) or less, because interfacial tension (or surface tension) effects are dominant at these length scales [23]. Micro/nanostructures on lotus leaves exhibiting robust superhydrophobicity, and those on a desert beetle that collects water with the help of alternating hydrophobic and hydrophilic areas, are shown in Figure 1-1. The length scale of the structures of the leaves or of the beetle is on the order of micrometers or even smaller to make surface tension dominant, which leads to well controlled surface wettability that has also never existed in bulk materials. Again, these useful phenomena in optics and wetting emerge from unique micro- and nanostructures on surfaces.

One important observation is that the nanostructured surface of butterflies' wings fosters superhydrophobicity, and at the same time it exhibits structural colors by wavelength-selective reflection [24]. This proves that multiple functions in two major different fields, optics and wetting, can be mutually present when the structure size of the engineered materials is on the order of nanometers. Consequently, it is conceivable that new multifunctional materials using nanostructures can be designed and manufactured with the consideration of both requirements for both optics and wetting.

1.3 Light transport at optical interfaces

What we see is all about interactions between light and objects. Leaves are green, the skies are blue, and the moon is yellow at night. Light transport at optical interfaces had drawn much attention due to its fundamental importance to our visual perception and its unique properties. In classical physics, light interaction phenomena at optical interfaces consist of reflection, transmission, and refraction as well as absorption of light [25, 26]. These are fundamental elements for understanding light behavior on flat or rough surfaces, and are required to explain light transport with nanostructured materials later.

Figure 1-2 shows a schematic drawing of fundamental light interaction phenomena within two optically different media. When a light wave propagates from medium 1 to medium 2, some portion of the light wave will be reflected to the medium 1 and the remainder of the light wave is transmitted through the medium 2. These processes are called reflection and transmission. When the propagating light encounters a different medium with different optical properties such as refractive index, the propagation direction of transmitted light changes in order to conserve the momentum of the transmitted and reflected light waves. This is called refraction ($n_1 \sin \theta_1 = n_2 \sin \theta_2$, Snell's law), which is also a commonly observed phenomenon [25, 26]. Light absorption occurs when the energy of photons is converted to internal energy such as heat due to vibration of electrons when light propagates through a medium. Light intensity is attenuated by absorption of a part of its photons. These are the fundamental light interaction phenomena that will be discussed in this thesis.

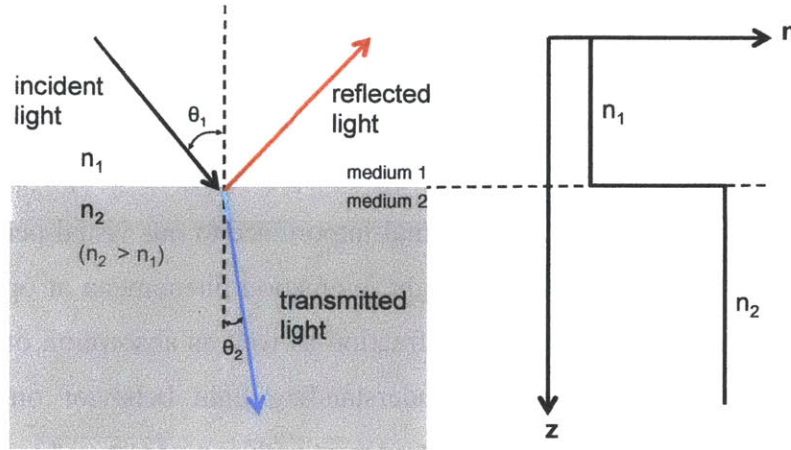


Figure 1-2. Schematic drawing of the fundamental light interaction phenomena within two optically different media.

These phenomena can be explained by electromagnetic theory. Light is an electromagnetic wave, and consists of orthogonally oscillating electrical fields \vec{E} and magnetic fields \vec{H} . Symbols with bars on top represent vector quantities. The connection between the two fields is explained by Maxwell's equations, which are

$$\nabla \times \vec{H} = \frac{\partial \vec{D}}{\partial t} + \vec{J} \quad (1.1)$$

$$\nabla \times \vec{E} = -\frac{\partial \vec{B}}{\partial t} \quad (1.2)$$

$$\nabla \cdot \vec{D} = \rho \quad (1.3)$$

$$\nabla \cdot \vec{B} = 0 \quad (1.4)$$

where \vec{E} is the electric field (volt/m), \vec{B} is the magnetic flux density (weber/m²), \vec{H} is the magnetic field, \vec{D} is the electric displacement (coulombs/m²), \vec{J} is the electric current density (amperes/m²), ρ is the electric charge density (coulombs/m³) [25, 26]. Eq. 1.1 is Ampere's law, Eq. 1.2 is Faraday's law, Eq. 1.3 is Gauss' law for electric

fields, and Eq. 1.4 is Gauss' law for magnetic fields [25, 26]. With Eqs. 1.1-1.4, Maxwell's theory of electromagnetic fields is completely expressed, and light transport phenomena at optical interfaces can be fully described by solving these equations with boundary conditions [25, 26].

Reflectance and transmittance coefficients can also be calculated at the optical interface. Consider a plane harmonic wave incident upon a boundary between two different homogeneous, isotropic media, as shown in Figure 1-3. There are incident, reflected, and transmitted waves. The space-time dependence of these three waves, aside from constant amplitude factors, is given by the following complex equations [27]:

$$\exp\left[i(\bar{k}_i \cdot \bar{r} - \omega t)\right]: \text{incident wave} \quad (1.5)$$

$$\exp\left[i(\bar{k}_r \cdot \bar{r} - \omega t)\right]: \text{reflected wave} \quad (1.6)$$

$$\exp\left[i(\bar{k}_t \cdot \bar{r} - \omega t)\right]: \text{transmitted wave} \quad (1.7)$$

where \bar{k} is a wave vector, and \bar{r} is a position vector.

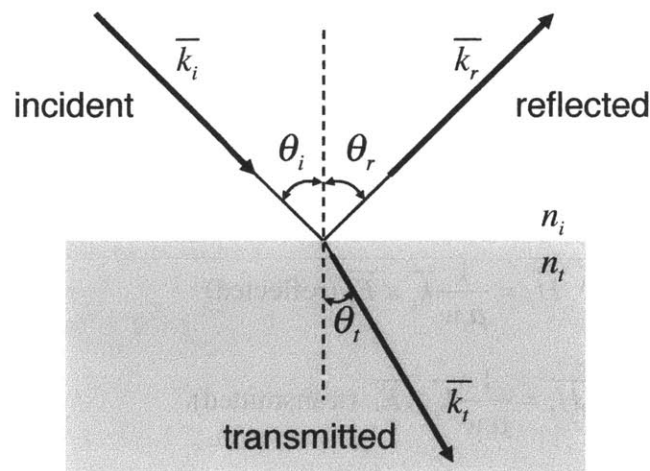


Figure 1-3. Wave vectors for light incident on a boundary separating two different optical media [27].

Since the time factors are equal, we will have the following equation [27],

$$\overline{k}_i \cdot \overline{r} = \overline{k}_r \cdot \overline{r} = \overline{k}_t \cdot \overline{r} \quad (1.8)$$

at the boundary in Figure 1-3. Eq. 1.8 becomes

$$k_i \sin \theta_i = k_r \sin \theta_r = k_t \sin \theta_t, \quad (1.9)$$

where k is a wave number [25-27]. Now in the space of the incident and reflected waves, the two waves are traveling in the same medium, hence the wave vectors have the same magnitude; that is $k_i = k_r$, and it also reduced to law of reflection, $\theta_i = \theta_r$ [25-27].

Let \overline{E}_i denote the electric field vector of a plane harmonic wave that is incident on the optical boundary in Figure 1-3, and let \overline{E}_r and \overline{E}_t denote the electric field vectors of the reflected and transmitted waves, respectively [27]. By Eqs. 1.1-1.4 and $\overline{H} = \mu^{-1} \nabla \times \overline{E}$, the magnetic field vectors are given by

$$\overline{H}_i = \frac{1}{\mu_i \omega} \overline{k}_i \times \overline{E}_i \quad (\text{incident}) \quad (1.10)$$

$$\overline{H}_r = \frac{1}{\mu_i \omega} \overline{k}_r \times \overline{E}_r \quad (\text{reflected}) \quad (1.11)$$

$$\overline{H}_t = \frac{1}{\mu_t \omega} \overline{k}_t \times \overline{E}_t \quad (\text{transmitted}). \quad (1.12)$$

Assume that \vec{E}_i is perpendicular to the plane-of-incidence (called TE polarization), as shown in Figure 1-4. Due to the continuity of the tangential components of the electric fields [25-27], we have at the boundary

$$E_i + E_r = E_t. \quad (1.13)$$

Using the continuity of the tangential components of the magnetic fields [25-27], we also have at the boundary

$$-H_i \cos \theta_i + H_r \cos \theta_r = -H_t \cos \theta_t. \quad (1.14)$$

Making use of Eqs. 1.10-1.14, $\vec{k} \cdot \vec{E} = 0$, and $\mu_i \approx \mu_t$, we can obtain

$$r_{TE} = \left(\frac{E_r}{E_i} \right) = \frac{n_i \cos \theta_i - n_t \cos \theta_t}{n_i \cos \theta_i + n_t \cos \theta_t} \quad (1.15)$$

$$t_{TE} = \left(\frac{E_t}{E_i} \right) = \frac{2n_i \cos \theta_i}{n_i \cos \theta_i + n_t \cos \theta_t} \quad (1.16)$$

where r_{TE} and t_{TE} denote the amplitude reflection and transmission coefficients, respectively [25-27].

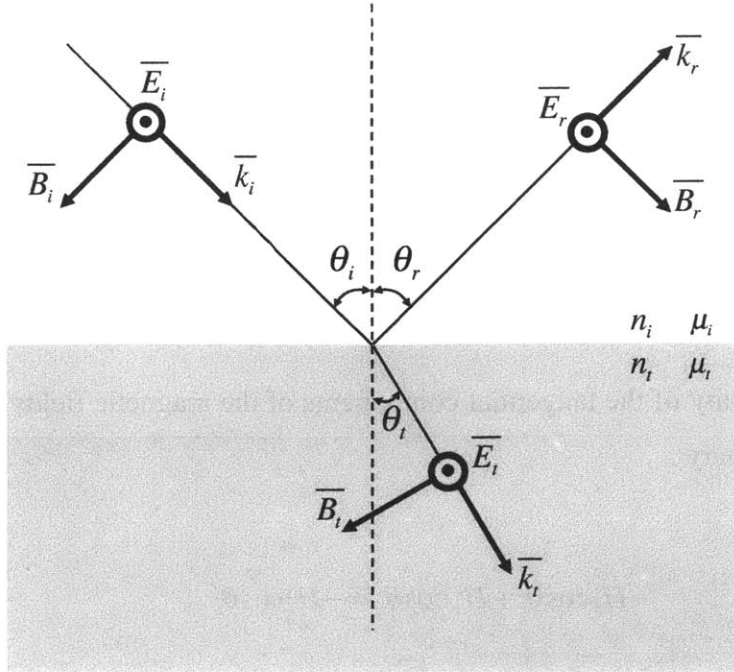


Figure 1-4. Incoming wave whose electric field is normal to the plane-of-incidence [25].

A similar pair of equations can be derived when \vec{E}_i lies in the plane-of-incidence (called TM polarization), as shown in Figure 1-5 [25]. Continuity of the tangential components of the electric and magnetic fields on both sides of the boundary lead to

$$E_i \cos\theta_i - E_r \cos\theta_r = E_t \cos\theta_t \quad (1.17)$$

$$H_i + H_r = H_t. \quad (1.18)$$

Making use of Eqs. 1.10-1.12, 1.17, and 1.18, we can also obtain

$$r_{TM} = \left(\frac{E_r}{E_i} \right) = \frac{n_t \cos \theta_i - n_i \cos \theta_t}{n_i \cos \theta_i + n_t \cos \theta_t} \quad (1.19)$$

$$t_{TM} = \left(\frac{E_t}{E_i} \right) = \frac{2n_i \cos \theta_i}{n_i \cos \theta_i + n_t \cos \theta_t} \quad (1.20)$$

where r_{TM} and t_{TM} denote the amplitude reflection and transmission coefficients, respectively [25-27]. Eqs. 1.15, 1.16, 1.19, and 1.20 are known as *Fresnel's equations*.

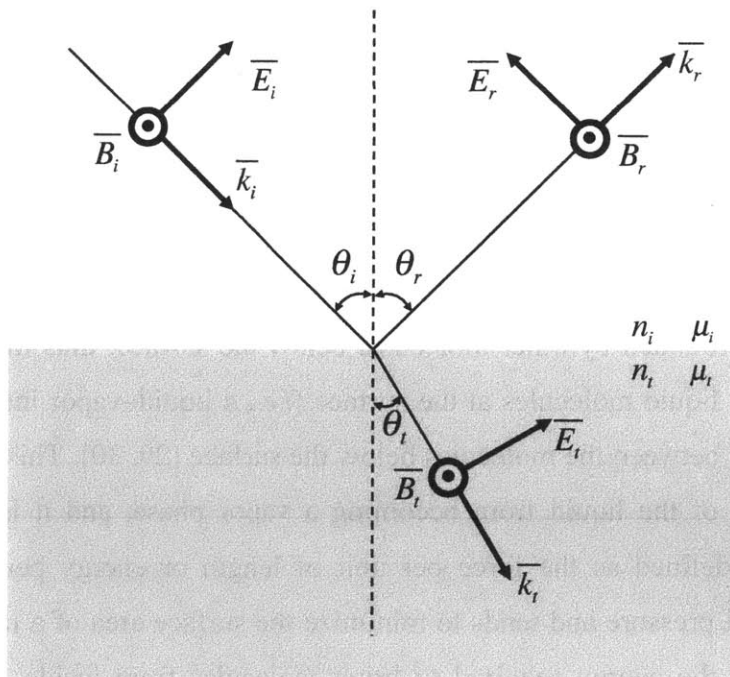


Figure 1-5. Incoming wave whose electric field is in the plane-of-incidence [25].

1.4 Interfacial tension of materials and wetting phenomena on textured surfaces

Lotus leaves are capable of repelling water droplets, but glass is not. What makes them different, and can we make glass water-repellent? To answer these two questions, we need to understand the interaction between a liquid and a solid. Wetting is the study of how a liquid interacts with another liquid or a solid (*i.e.*, how a liquid dropped on a solid surface spreads out), and surface tension and contact angle are the most fundamental factors in wetting.

Surface tension is an inherent interfacial characteristic of material interfaces, and is generated by intermolecular forces [28-30]. Molecules of a liquid are surrounded by other neighboring molecules below a surface (*i.e.*, a liquid–vapor interface), as shown in Figure 1-6, and the net forces acting on these molecules are going to be negligible because each molecule is drawn equally in all directions. At the surface, however, the molecules are only partially surrounded by other molecules below the surface; thus the cohesive force between adjacent liquid molecules at the surface (*i.e.*, a liquid–vapor interface) becomes stronger than that between the molecules below the surface [29, 30]. This force prevents a condensed phase of the liquid from becoming a vapor phase, and it is represented by surface tension, defined as the force per unit of length or energy per unit area. This generates internal pressure and tends to minimize the surface area of a liquid. It can also be interpreted as the energy required to bring molecules from inside the liquid to the surface and to create new surface area [29, 30].

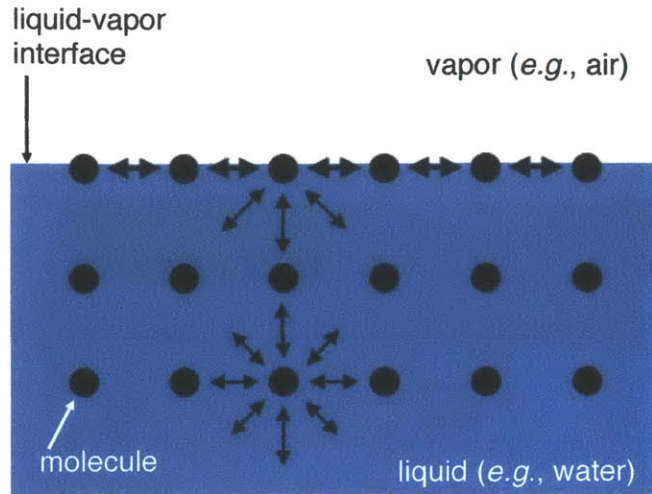


Figure 1-6. Schematic illustration of forces on molecules of a liquid.

The contact angle of a liquid is the angle between the leading edge of a liquid on a solid surface at the three-phase contact line (liquid-vapor-solid), and it plays an important role in wetting as an intuitive indicator of wettability of a liquid on a solid surface [29]. Figure 1-7 shows the contact angle, which is also the angle θ_E , at the equilibrium state created by the interfacial force balance between the three phases (liquid-vapor-solid) in the tangential direction of the flat solid surface. It is quantitatively defined as Young's equation,

$$\cos\theta_E = (\gamma_{SV} - \gamma_{SL}) / \gamma_{LV}, \quad (1.21)$$

where γ_{ij} is an interfacial tension between phases i and j , and S, L, V indicate solid, liquid, and air, respectively [29]. When the contact angle of water droplets is smaller than 90° on a substrate, it is called a hydrophilic surface. In contrast, when the water contact angle is greater than 90° , it is considered a hydrophobic surface. The most hydrophobic and common material is Teflon[®], which shows contact angles between 110° to 120° [31, 32]. Moreover, contact angles greater than 150° , a phenomenon called superhydrophobicity [33], have been demonstrated by texturing the solid surfaces.

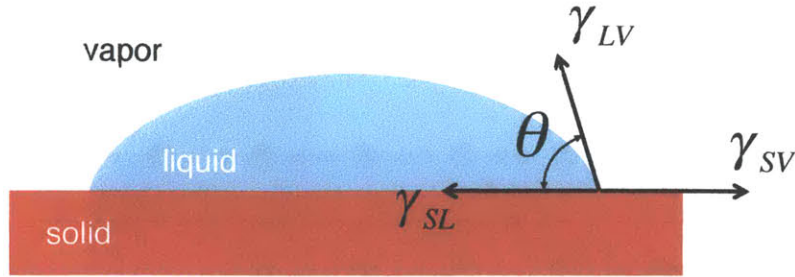


Figure 1-7. Schematic drawing of a liquid drop on a solid surface with the quantities in Young's equation.

In practice, the contact angle is not always the same as the value calculated from Eq. 1.21. At a given surface, the contact angle can vary from the advancing contact angle (measured when the solid/liquid contact area increases), θ_{adv} , to the receding contact angle (measured when the solid/liquid contact area decreases), θ_{rec} [34]. The equilibrium angle from Young's equation is always a value between the receding contact angle and the advancing contact angle. This difference between advancing and receding contact angles is called contact angle hysteresis (CAH). The contact angle hysteresis originates from heterogeneities in the topography and chemical composition of the solid surface, and this generates an adhesion force between the surface and a liquid [28, 31, 34]. This phenomenon can also be seen with a small water droplet at rest on a tilted surface. The contact angle at the front of the droplet is larger than that at the rear due to CAH; therefore, this creates a net adhesive force to the surface, and the water droplet is pinned at the surface [28, 32].

Through efforts at control of adhesive force between a liquid and a solid surface, it has been found that the contact angle and the contact angle hysteresis of a liquid can be modified by changes in the surface topography of the solid substrate and its surface chemistry; hence these can make the surfaces extremely non-adhesive or adhesive [32].

Wenzel first suggested the relationship between apparent contact angles and roughness of surfaces with the following equation [35]:

$$\cos \theta^* = r_w \cos \theta_E, \quad (1.22)$$

where r_w is the average roughness ratio, defined as the actual surface area divided by the projected surface area, θ^* is an apparent contact angle, and θ_E is the equilibrium contact angle of a liquid on a flat solid surface determined by Young's equation. This equation shows the fully-wetted state of liquid droplets on textured surfaces. Assuming that θ_E is 60° and r_w (called Wenzel roughness) is 1.9, the apparent contact angle becomes 18.2° , as schematically shown in Figure 1-8. Due to increase in surface roughness (r_w), the contact angle decreases and hydrophilicity is promoted. The correlation between the apparent contact angle and the equilibrium contact angle of the Wenzel state can also be plotted onto the wetting diagram shown in Figure 1-9 [33, 36].

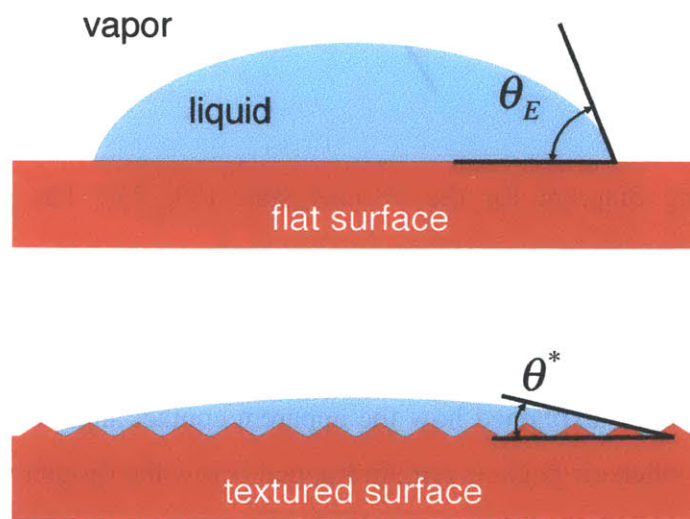


Figure 1-8. Schematic drawings of liquid droplets on a flat surface and textured surface. The liquid penetrates into the texture and fully wets the surface. The apparent contact angle is determined by Eq. 1.22, and this state is known as the Wenzel state.

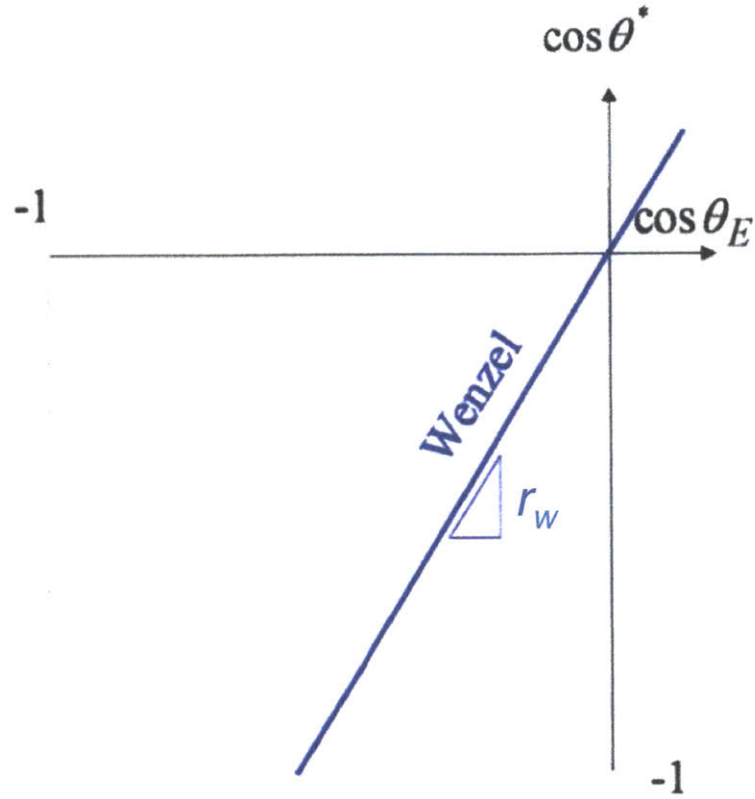


Figure 1-9. Wetting diagram for the Wenzel state [33, 36]. The slope of the plot represents r_w .

Later, Cassie and Baxter explained how the apparent contact angle of a droplet changes on a rough surface when air pockets remain trapped below the droplet with the following equation [37]:

$$\cos \theta^* = f_s \cos \theta_E + f_a \cos \pi = f_s \cos \theta_E - f_a, \quad (1.23)$$

where f_s is the fraction of solid remaining in contact with the droplet, and $f_a (= 1-f_s)$ is the fraction of air pockets remaining in contact with the droplet. A droplet on a flat solid shows the equilibrium contact angle θ_E , while it does not spread out on a film of air (contact angle of π). The cosine of the apparent angle (θ^*) becomes a sum of the cosines of the equilibrium contact angles of the liquid and air (θ_E and π , respectively), weighted

by the respective proportions of solid and air below the droplet [32]. This applies when the droplet is sufficiently large compared with the scale of roughness [38]. For example, when θ_E is 120° and f_s is 0.2, the apparent contact angle reaches a value of 154.2° . This wetting property is also schematically shown in Figure 1-10. As f_s decreases, the apparent contact angle increases and hydrophobicity is promoted. The correlation between the apparent contact angle and the equilibrium contact angle of the Cassie-Baxter state can also be plotted onto the wetting diagram shown in Figure 1-11 [33, 36].

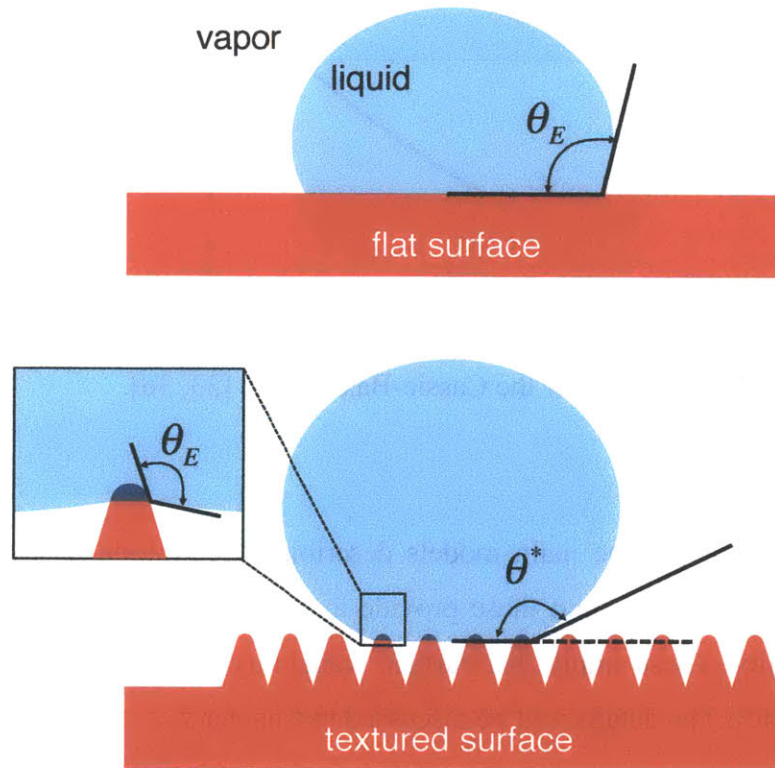


Figure 1-10. Schematic drawings of liquid droplets on a flat surface and textured surface. The liquid sits partially on air, and the apparent contact angle can be determined by Eq. 1.23. This state is known as the Cassie-Baxter state.

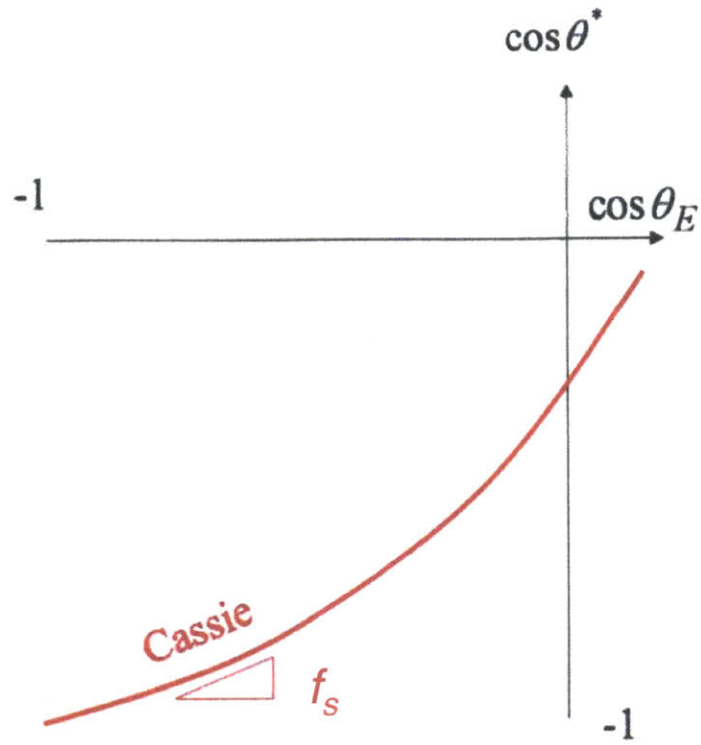


Figure 1-11. Wetting diagram for the Cassie-Baxter state [33, 36].

These two equations are the main models describing the wetting behavior of a liquid droplet on a rough surface, and these provide a fundamental framework for control of surface wettability. These imply that surface wettability can be enhanced by structured roughness [39, 40]. The details will be discussed in Chapter 2.

1.5 Fabrication of nanostructures for multifunctionality

In order for all these beneficial applications of the multifunctional surfaces to become reality, the major challenge is how to reliably create structures at the nanoscale. This also requires the development of engineering nanofabrication approaches with appropriate processing of materials with the desired structural, mechanical, optical, and wetting properties [41]. There are critical requirements that the candidates for nanofabrication methods for multifunctional materials must satisfy. The methods must be (1) cost-effective, (2) compatible with large-area nanofabrication, and (3) capable of creating precise and desired shapes of defect-free nanostructures optimized for multifunctionality. As discussed in Section 1.1, the multifunctional surfaces are beneficial for commercial products such as glasses, goggles, and displays. Since the sizes of these products are usually on the order of meters, the fabrication method for the multifunctional surfaces must be inexpensive to cover a large area with nanostructures and, at the same time, capable of precise fabrication of nanostructured materials with the desired mechanical geometries that are optimized for advanced functions and their applications in optics and wetting. In this section, current prominent fabrication methods for nanostructures, and their limitations, will be briefly introduced.

Significant advances in nanotechnology over the past few decades enable precise and scalable fabrication of nanostructures. One of the leading technologies in fabricating nanostructures is optical projection lithography, which also led to the industrial revolution in the semiconductor industry. Optical projection lithography, sometimes called photolithography, is a process to pattern shapes or parts of a thin film that is called photoresist, on a substrate using ultraviolet (UV) light. Photoresist is a material that can be chemically modified by light exposure; thus the exposed or unexposed photoresist, with the help of a photomask, is patterned. One shortcoming of photolithography is that the resolution of patterns is restricted to about half of the wavelength, due to diffraction of UV light. However, the optical lithographic process, through numerous techniques, such as immersion lithography, extreme UV exposure, and double patterning, has overcome the diffraction limit of light, and feature sizes as small as 32 nm are being

manufactured with the optical projection lithography. This is the most reliable and scalable lithographic technique for creating nanostructures; however, expensive instruments and facilities with huge investment are certainly required, and this violates the requirements for the nanofabrication of multifunctional surfaces.

Electron beam lithography (EBL) is also a promising technique to create nanostructures by directly drawing desired patterns on a resist layer with a focused electron beam. Since the wavelengths of electron beams are much smaller than those of UV light for photolithography, this technique is not restricted by the diffraction limit of light; hence the smallest feature size is on the order of a few nanometers – making it the most accurate lithographic method. Although EBL has this major advantage, it is mainly limited by low throughput and implementation difficulties for large-area nanofabrication. As a result, it has been popularly used for demonstrations in scientific studies and prototypes of relatively small nanoelectronic and nanophotonic devices that require high accuracy of the geometries (~ 1 nanometer accuracy).

In 1996, a cost-effective and scalable nanofabrication method, so-called nanoimprint lithography, was introduced based on mechanical embossing with a pre-shaped template [42]. This method is also compatible with large-area nanofabrication or roll-to-roll processes [43], offering potential advantages such as low cost and high throughput. In spite of many advantages compared to conventional lithography methods such as photolithography and EBL, a mold structure is certainly required in advance of the nanoimprint process, and defects can be readily produced by both incomplete filling of negative patterns and the shrinkage phenomenon of the imprinted materials [44].

The three promising candidates have been widely used for the development for new materials and devices in the semiconductor industry as well as academia. These are also useful for complex and multicomponent nanomaterials that are needed for advanced functional applications; however, many obstacles such as low throughput, high cost, and defects still have to be overcome in order to create nanostructured multifunctional surfaces optimized for effective control of light transport and surface wettability. In

addition, the nanofabrication method must satisfy the three requirements mentioned earlier: cost-effectiveness, large-area capability, and precise nanofabrication.

There is, however, one photolithographic method that produces periodic nanostructures without a mask, which can both overcome the difficulties mentioned previously and satisfy the requirements. Interference lithography (IL) is one of the most effective and low cost approaches for large-area nano-patterning and defect-free nanostructure fabrication of periodic subwavelength nanostructures, and it has also been utilized for years to build multifunctional surfaces [45], magnetic data storage media [46, 47], and photonic materials [48, 49]. Interference lithography is based on interference between two or more coherent laser beams, usually in a Lloyd's mirror interferometer [50] or a Mach-Zehnder interferometer [51]. Because of the nature of interference, periodicity is guaranteed if the beam wavefront quality and uniformity are sufficiently good over the required surface area of overlap. Thus, 1-dimensional (1D) gratings, 2-dimensional (2D) gratings, and hexagonal hole/dot arrays, which are ideally suited for multifunctionality, can be easily fabricated.

Furthermore, self-assembly, defined as the spontaneous organization of two (or more) components into larger aggregates using covalent and/or noncovalent bonds [52, 53], is one of the most appealing nanofabrication methods for the realization of advanced functions in optics and wetting because of low cost, simplicity, and scalability, allowing for the development of complex, multifunctional nanostructures. This method relies on cooperative interactions of small components such as nanoparticles that assemble spontaneously in a predefined way to produce a larger structure in two or three dimensions [52, 53].

The aim of this thesis includes development of an appropriate approach for the controlled fabrication of nanostructured materials on the nanometer scale and implementation of multiple functions in optics and wetting. Interference lithography and self-assembly, the most promising lithographic methods, will provide comprehensive platforms for development and building of nanostructured multifunctional surfaces; therefore, these

two methods, and how they are utilized with novel techniques to create multifunctional nanostructured materials, will be discussed in Chapters 2, 3, 4, and 5.

1.5.1 Interference lithography

Two spatially and temporally coherent beams (with a wavelength of λ) interfere and form a standing wave pattern in a region where they overlap. This sinusoidal standing intensity pattern is recorded on a layer of positive or negative photoresist [54, 55], and then desired grating is achieved, as shown in Figure 1-12. The intensity pattern is given by

$$I = |\overline{E}_r + \overline{E}_l|^2, \quad (1.24)$$

where \overline{E}_r is the electric field of the incoming beam on the right-hand side, and \overline{E}_l is the electric field of the incoming beam on the left-hand side. The two beams can be expressed by

$$\overline{E}_r = \overline{e}_r \cdot E_r \cdot \exp(nkz \cos \theta + kx \sin \theta) \cdot \exp(-j\omega t), \quad (1.25)$$

$$\overline{E}_l = \overline{e}_l \cdot E_l \cdot \exp(nkz \cos \theta - kx \sin \theta) \cdot \exp(-j\omega t), \quad (1.26)$$

where \overline{e}_r and \overline{e}_l are the unit vectors representing the polarization states of the two beams, E_r and E_l are the amplitudes of the right and left incoming beams, respectively, k is the wave number ($k = 2\pi/\lambda$), θ is the angle of incidence of the two laser beams, ω is the angular frequency ($\omega = 2\pi f$), f is the frequency of light, and n is the refractive index of the surrounding medium.

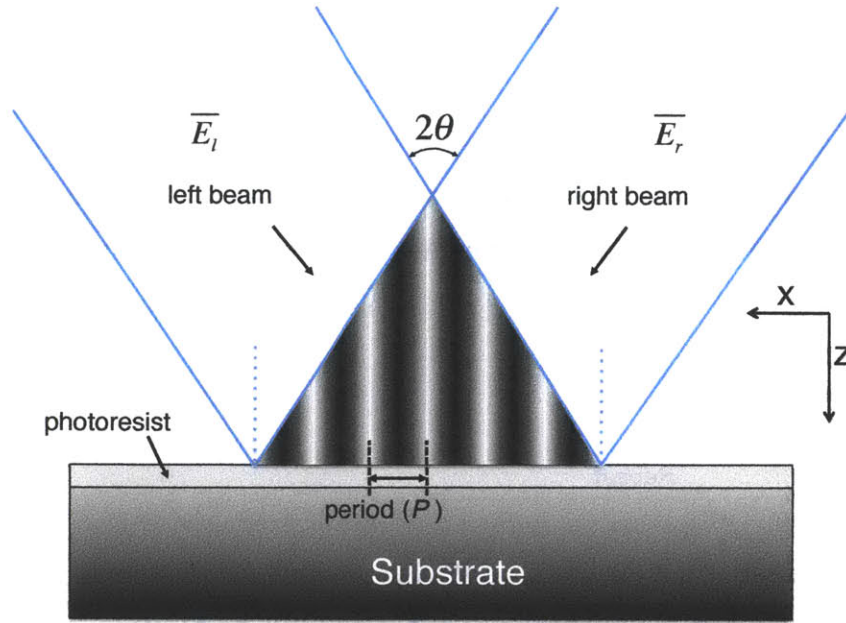


Figure 1-12. Schematic drawing of interference lithography (IL) configuration [54, 55].

The intensity profile along x-direction is

$$I(x) = (E_r)^2 + (E_i)^2 + 2E_r E_i (\overline{e}_r \cdot \overline{e}_i) \cos(2nkx \sin \theta). \quad (1.27)$$

The period (P) of the intensity pattern becomes

$$P = \frac{\lambda}{2n \sin \theta}. \quad (1.28)$$

1.5.2 Layer-by-Layer assembly

Among many self-assembly nanofabrication techniques, Layer-by-Layer (LbL) assembly is one of the easiest and most inexpensive processes for multilayer formation at the nanoscale, and it allows a variety of materials to be incorporated within the thin film structures [56-58]. LbL assembly is a technique to build a thin and conformal layer of

micro/nano-sized particles using alternate layers of positively and negatively charged colloidal particles [56-59], shown in Figure 1-13. Alternation of the surface charge enables an assembly between positively and negatively charged materials affording a great freedom in the number of layers and layering sequence [56]. This technique is also compatible with large-area nanofabrication, and capable of creating precise and desired shapes of defect-free nanostructures [56], which satisfies the three requirements introduced in Section 1.5.

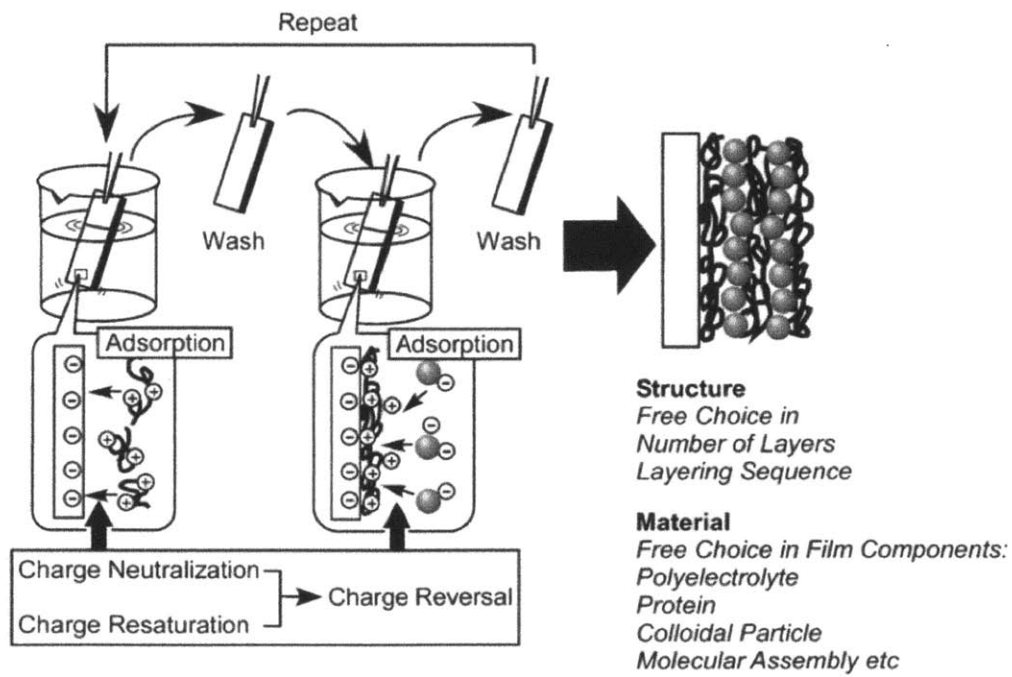


Figure 1-13. Schematic illustration of Layer-by-Layer (LbL) assembly through electrostatic interaction. Reproduced from Ref. [56] with permission from The Royal Society of Chemistry.

1.6 Outline of thesis

In this thesis I present nanostructured multifunctional materials for control of light transport and surface wettability, and newly developed nanofabrication methods for these new materials.

First of all, nanostructured multifunctional silica surfaces for enhanced omnidirectional broadband transmissivity with structural superhydrophilicity or robust superhydrophobicity will be covered in Chapter 2. This is achieved through a systematic approach to concurrent design of optimal nanostructures in two domains, optics and wetting, and an innovative fabrication procedure that achieves the desired aspect-ratios and periodicities with few defects, high feature repeatability, and large pattern area. This multifunctional material will be called “multifunctional glass.”

The multiple shrinking mask etching method (developed for creating the multifunctional glass introduced in Chapter 2) will be discussed further in Chapter 3. This method, combined with interference lithography and specific techniques, also enables successful fabrication of subwavelength periodic silica nanocone structures with controllable-aspect-ratio of 4.5 to 7. In addition, simple and low cost fabrication methods for silica nanocone structures with low aspect-ratios of 2 to 3 have been developed, *with* and even *without* the hardmask material that had been considered an essential for fabricating high aspect-ratio structures.

Although touch screen technologies have been popular and transparent anti-fingerprint surfaces have received much attention, the tapered silica nanocone structures (multifunctional glass introduced in Chapter 2) do not provide oil repellency. They can repel water (has relatively high surface energy), but not oil (has relatively low surface energy). At the beginning of Chapter 4, newly developed transparent superoleophobic surfaces, especially their limitations as transparent anti-fingerprint surfaces, will be discussed. In contrast to previous studies that have targeted an oil repellency mechanism, we have taken the counter-intuitive approach of constructing our surface from an

oleophilic material. Design, fabrication, and characterization of transparent fingerprint-eating surfaces, which are optimized for optical transparency and photocatalytic fingerprint removal, will be discussed in detail. This multifunctional material utilizes the combined favorable effects of rapid capillary imbibition (or hemi-wicking [60]) of fingerprint oils into a porous oleophilic titania nanoparticle structure and subsequent photocatalytic decomposition upon exposure to the ultraviolet (UV) component of natural sunlight. It achieves a practical degradation time (≤ 3 hours under sunlight) of fingerprints, while also retaining optical transparency comparable to ordinary glass.

Instead of eliminating all reflections over the broadband wavelengths of light with the tapered silica nanostructured materials (multifunctional glass introduced in Chapter 2), properly designed nanostructured surfaces are capable of generating vivid colors by selective-wavelength reflection. Chapter 5 introduces the design, optimization, and nanofabrication of 2-dimensional (2D) periodic subwavelength nanostructured silicon surfaces for effective reflective color generation. The geometry of the nanorod structures on top of the silicon substrate is designed and optimized to obtain high contrast of colors while still allowing for scalable nanopatterning with the help of newly invented nanofabrication processes.

Chapter 6 suggests possible future work expanding on the scope of this thesis. Preliminary results of new nanofabrication methods for these nanostructured multifunctional materials will be briefly introduced. Moreover, possible future applications of these nanostructured multifunctional materials developed in this thesis will also be discussed.

Chapter 2

Nanotextured Silica Surfaces with Omnidirectional Broadband Supertransmissivity and Robust Superhydrophobicity

2.1 Introduction

Specifying the interaction of a “multifunctional” surface with liquids and light has long been recognized as a topic of both fundamental and practical significance. Conical structures on a surface have been proposed for that purpose because they address both interactions: the cone apex angle controls the contact angle of liquid, as well as the effective refractive index gradient to achieve adiabatic matching between air and the substrate, thus minimizing reflection. The key design parameter is the nanocone aspect-ratio (*i.e.*, height over diameter), at the same time posing the tough fabrication challenge.

In this chapter, we report an approach to co-design the nanostructures in the optical and fluidic domains, and an experimental fabrication procedure that achieves the desired aspect-ratios with virtually no defects and with high repeatability. The fabricated structures demonstrate highly robust structural superhydrophilicity or, with the addition of a surface coating, superhydrophobicity. Optical transmissivity exceeding 98% is measured over a broad bandwidth and range of incident angles at both polarizations. We also demonstrate and optically quantify anti-fogging and self-cleaning behavior, both potentially beneficial for energy harvesting and utilization.

Note that this chapter is partially based on the following publications and patent applications.

•K.-C. Park*, H.J. Choi* et al., “Nanotextured Silica Surfaces with Robust Super-Hydrophobicity and Omnidirectional Broadband Super-Transmissivity,” ACS Nano, 2012 (*Equally contributed to this work, Reprinted with permission from [45]. Copyright 2012 American Chemical Society)

•H.J. Choi et al., “Bio-inspired Multifunctional Nanostructured Surface,” Micro and Nano Engineering 2011 conference, Germany, 2011

•H.J. Choi et al., “Fabrication of Subwavelength High Aspect-Ratio Tapered Fused Silica Nanostructures for Transparent Photophilic Material,” EIPBN 2011 conference, Las Vegas, USA, 2011

•H.J. Choi et al., “Inverted Nanocone Structures for Multifunctional Surfaces and its Fabrication Process,” US Patent, Application no. 61/669,240, July 2012

•H.J. Choi et al., “Process for Fabricating High Aspect-Ratio Tapered Nanocone Structures,” US Patent, Application no.61/477,792, April 2011

2.2 Fresnel reflection and anti-reflection coatings

Fresnel reflection (reflection of light) is the general optical phenomenon occurring at optical interfaces. Many researchers have investigated ways to remove the reflection from interfaces; hence it has been found that Fresnel reflection at optical interfaces can be successfully suppressed by using optical interference effects with a thin layer of coating.

When light travelling in medium 1 passes the optical interface between medium 1 and medium 2, as previously shown in Figure 1-2, the reflectance (or reflection coefficient) of light at the interface can be calculated by Fresnel's equations with respect to the polarization state of light:

$$R_{TE} = \left(\frac{n_1 \cos \theta_1 - n_2 \cos \theta_2}{n_1 \cos \theta_1 + n_2 \cos \theta_2} \right)^2 \quad (2.1)$$

for the TE polarization, and

$$R_{TM} = \left(\frac{n_2 \cos \theta_1 - n_1 \cos \theta_2}{n_1 \cos \theta_1 + n_2 \cos \theta_2} \right)^2 \quad (2.2)$$

for the TM polarization, respectively, where n_1 is the refractive index of the medium 1, n_2 is the refractive index of the medium 2, θ_1 is the angle of incidence of light, and θ_2 is the angle of transmitted light through the medium 2 [17, 25].

When a thin layer of coating with a refractive index of n_{AR} exists at the interface between the two media, and the multiple light rays reflected from this layer and reflected back to the medium 1 are perfectly out of phase (π phase difference), all the light beams reflected backwards can cancel each other due to destructive interference [17, 25]. This is called a single-layer anti-reflection coating, and the thickness of the single layer must be

$$t = \frac{\lambda}{4n_{AR}}, \quad (2.3)$$

where λ is the wavelength of light, and n_{AR} is the refractive index of the single layer existing at the optical interface between the medium 1 and medium 2, when the angle of incidence θ_1 is zero and the following equation holds:

$$n_{AR} = \sqrt{n_1 n_2}. \quad (2.4)$$

This provides perfect anti-reflection [17, 25]; however, this works only with a single wavelength and single incident angle.

To overcome the limitation of this anti-reflective coating, a novel way of using multilayer coatings has been developed. By tuning the thicknesses and refractive indices of the multilayers, such as alternating layers with high and low refractive indices, anti-reflection coatings can work over broad wavelength ranges and with a wide range of incident angles. Today, most frequently used anti-reflection coatings are based on these multilayer interference structures [17, 25]. These coatings, however, have limitations such as poor adhesion and thermal mismatch between the thin-film stack [3].

In addition to the single-layer and multilayer anti-reflection coatings offering anti-reflectivity, it was discovered by Lord Rayleigh in 1879 [61] that a gradient refractive index layer can be used to significantly improve anti-reflective performance of optical coatings. Although different coatings with different gradient refractive index profiles have been theoretically investigated for years for broadband anti-reflection properties [62, 63], finding optical materials with a low refractive index (~ 1) is a challenge to building the desired gradient-index profiles. Instead of finding low-refractive-index materials, a gradient refractive index anti-reflection coatings that eliminate Fresnel reflection at an AlN/air interface over a broad range of wavelengths have been fabricated

by using SiO₂ and TiO₂ layers grown by oblique-angle deposition, as shown in Figure 2-1 [18].

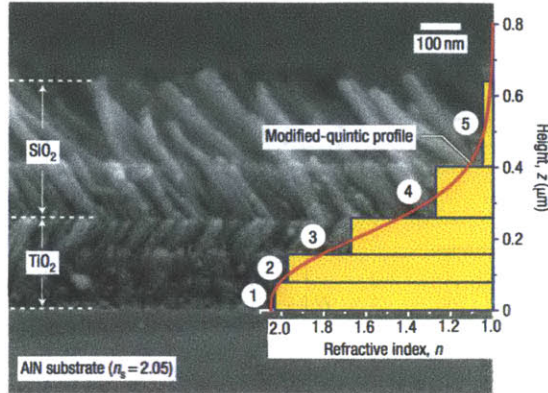


Figure 2-1. Cross-section SEM image of graded-index coating with a modified-quintic-index profile. Reproduced from Ref. [18] with permission from Nature Publishing Group.

This coating shows a nearly perfect anti-reflectivity with omnidirectional incidence of light over a broad wavelength range; however, this surface has a limitation on producing multifunctional properties because it is flat. The Wenzel (wetted state) or Cassie-Baxter (non-wetted state) states ($r_w \sim 1$ or $f_a \sim 0$: see Section 1.4) cannot be created on the surface with no roughness. Moreover, due to the possibility of the optical anisotropy arising from oblique-angle deposition [64], its refractive index can change with respect to angle of incidence or polarization of light, which is undesirable.

To overcome these limitations, subwavelength nanostructured materials have been studied, and have been considered to make a gradient-index layer with a certain level of surface roughness ($r_w > 1$) for effective control of both light transport and surface wettability. When the feature size of the structures, such as the period P , is smaller than the wavelength of light (λ), nanostructures behave as an effective medium with an effective refractive index [65, 66]. Tapered subwavelength nanostructures provide adiabatic impedance mismatch between the air and substrate (or gradient refractive index), and thus drastically reduce Fresnel reflection losses at the optical interface, as

schematically shown in Figure 2-2b. This phenomenon based on the nanostructures has been first observed on moth eyes [6, 8, 67], and these subwavelength structures have been developed for years in order to fabricate anti-reflective materials.

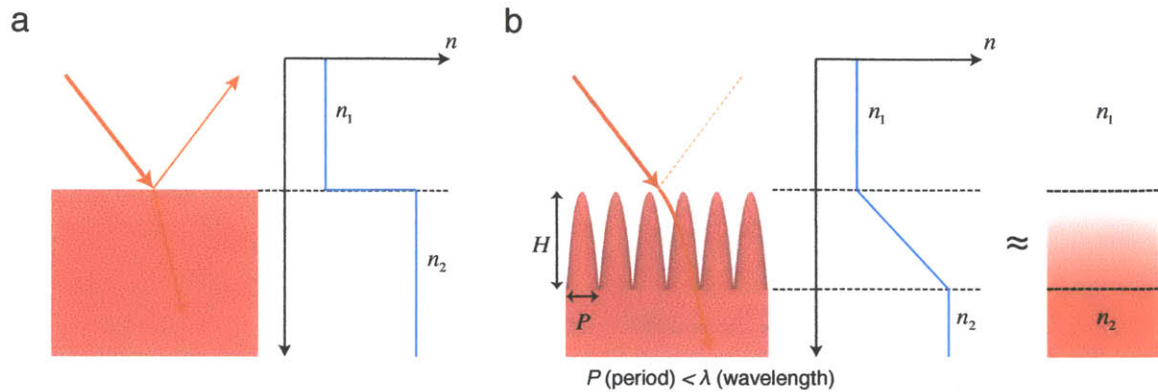


Figure 2-2. a) Fresnel reflection at the optical interface of a flat surface. b) Principle of an anti-reflective surface, consisting of subwavelength nanocone structures whose period P is smaller than the wavelength of incident light. Subwavelength tapered nanostructures offer adiabatic impedance mismatch between the air (n_1) and the medium (n_2) and thus reduce reflection.

These functional surfaces have been prepared by methods, such as electron beam lithography (EBL) [3], and nanoimprinting with replication from the mold [68]. Figure 2-3 shows an SEM image of the subwavelength structured surface upon a crystal silicon substrate fabricated through electron beam lithography [3]. At a wavelength of 400 nm the reflectivity decreased to 0.5% from the 54.7% of the silicon substrate [3]. An SEM image of polymethylmethacrylate (PMMA) nanospikes fabricated through nanoimprinting is also shown in Figure 2-4 [68].

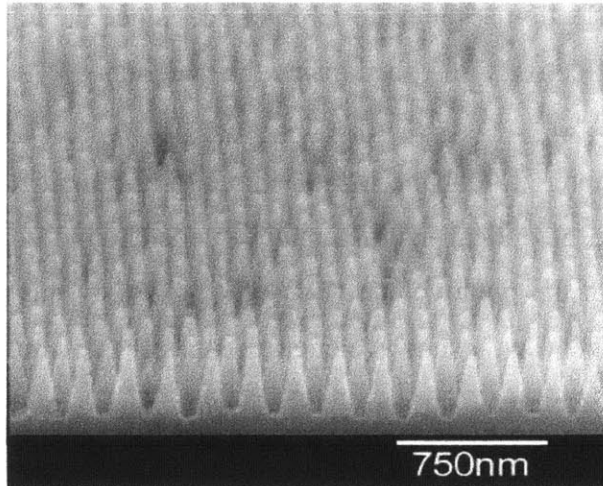


Figure 2-3. SEM image of the subwavelength structured (SWS) surface. The grating period is 150 nm, and the grooves are 350 nm deep. Reproduced from Ref. [3] with permission from Optical Society of America.

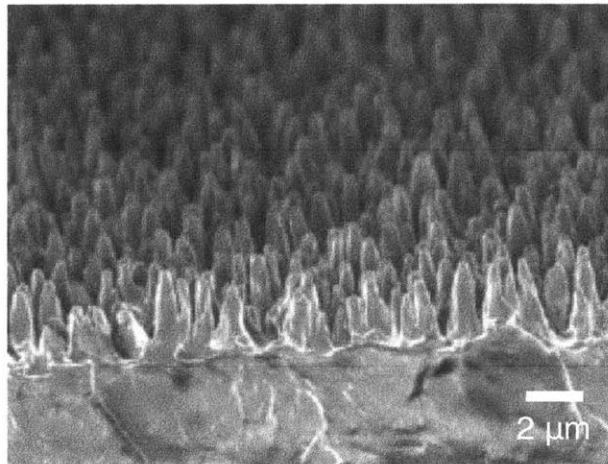


Figure 2-4. SEM image of anti-reflective structures on the PMMA substrate obtained through hot embossing process. Reproduced from Ref. [68] with permission from Wiley-VCH, John Wiley & Sons, Inc.

Most of the studies on anti-reflective structures are based on *absorptive* materials (*e.g.*, Si, GaAs, carbon nanotube, etc.) [2, 3, 15, 68, 69] because nanofabrication methods of these materials have been developed for years. However, these tapered nanostructures

only suppress light reflection at the material interfaces since the transmitted light without Fresnel reflection is effectively absorbed inside the materials.

As discussed in Chapter 1, enhanced transmissivity of multifunctional materials is essential for operation of optical instrumentation under humid conditions and the light collecting efficiency of the photovoltaic (PV) cell. To satisfy this requirement, we have taken this approach (i.e., subwavelength conical structures) of constructing nanostructured multifunctional surfaces with a *transparent* material, fused silica, for enhanced transmissivity and, at the same time, for control of surface wettability from superhydrophobicity to superhydrophilicity.

2.3 Wetting characteristics on textured surfaces

On rough surfaces, the wetting properties of water droplets can be explained through the Wenzel model (fully wetted state), and the Cassie-Baxter model (non-wetted state; water droplets sit partially on the solid texture and partially on air pockets entrapped within the texture) [36]. On superhydrophobic surfaces (or Cassie-Baxter surfaces), water droplets can easily roll or bounce off, leading to the removal of dust particles and contaminants [2, 7, 36, 70]. Increasing the aspect-ratio (H/P) of the texture, combined with a low surface energy coating, results in a great energy barrier for water droplets to transition from the composite Cassie-Baxter state to a fully-wetted Wenzel state, thus preserving the self-cleaning effect [71].

In addition to high aspect-ratio (H/P), several other geometrical properties, such as the feature density, characteristic geometric scale, and topography of the surface texture, play pivotal roles in creating robust superhydrophobic surfaces that can resist wetting under dynamic condition [72]. Studies have shown that an array of high aspect-ratio posts with a high number density (*e.g.*, carbon nanotube forest with a surface chemical treatment [73]) show superhydrophobicity with strong resistance against the transition of Cassie-Baxter state to the Wenzel state in water droplets on textured surfaces. This irreversible transition occurs when the applied pressure difference due to the curvature of liquid droplet or other dynamic external perturbations, for example, droplet impact between the liquid drop sitting on the surface and air reaches to a critical value. This critical value is defined as the breakthrough pressure, *i.e.*, the maximum pressure difference that the liquid-air interface (or Cassie-Baxter state) can maintain.

2.4 Design and optimization

The conical surface structures have been proposed for control of light transport (*i.e.*, elimination of Fresnel reflection) and control of surface wettability, such as superhydrophobicity and superhydrophilicity. In this section we identify the key design parameter to be the cone aspect-ratio (height over diameter), and the geometrical constraints of the nanostructured multifunctional material are designed for offering optimal performances in both optics and wetting domain.

2.4.1 Optical design constraints

An array of periodic subwavelength tapered structures behaves essentially like a transmissive band-pass filter, in which the band-pass range indicates the spectral regime with suppressed optical reflection (or enhanced transmittance) [45, 74]. A schematic of the geometric configuration is depicted in Figure 2-5, where light with a wavelength of λ illuminates the nanocone array (substrate index n_2) at an incident angle of θ_I .

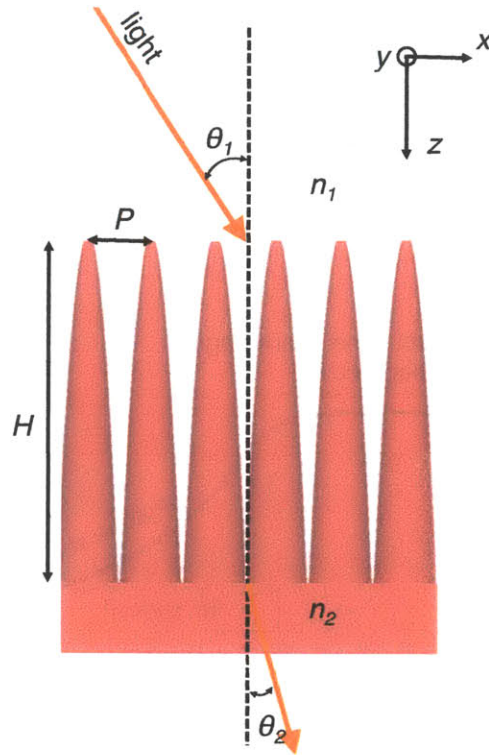


Figure 2-5. Schematic of the nanocone structure geometry and incident light configuration.

The lower and upper wavelength limits λ_{min} and λ_{max} for this band-pass are shown in Figure 2-6, and they can be tailored by controlling the geometry of the structure. Light with a wavelength in the region between the two wavelength limits (represented by the perfect transmissive region) can pass through the periodic subwavelength tapered structures without Fresnel reflection due to the adiabatic impedance matching at the optical interface. However, the optical transmissivity in the region with the wavelengths greater than the upper wavelength limit λ_{max} gradually decreases as the wavelength increases. This is because light with a relatively longer wavelength than the structure height does not consider the nanocone structure as a gradient effective refractive index medium; therefore the transmissivity reaches the same value as that of the flat surface as the wavelength increases. In contrast, the transmissivity at a wavelength smaller than the lower wavelength limit λ_{min} also decreases rapidly as the wavelength decreases, because the structure is considered as a periodic diffraction phase grating and incoming light

becomes diffractive. These phenomena are strongly related to the geometry of the nanocone structure: the lower wavelength limit λ_{min} is determined by the structure period P [25, 75, 76], and the upper wavelength λ_{max} is mainly determined by the structure height H .

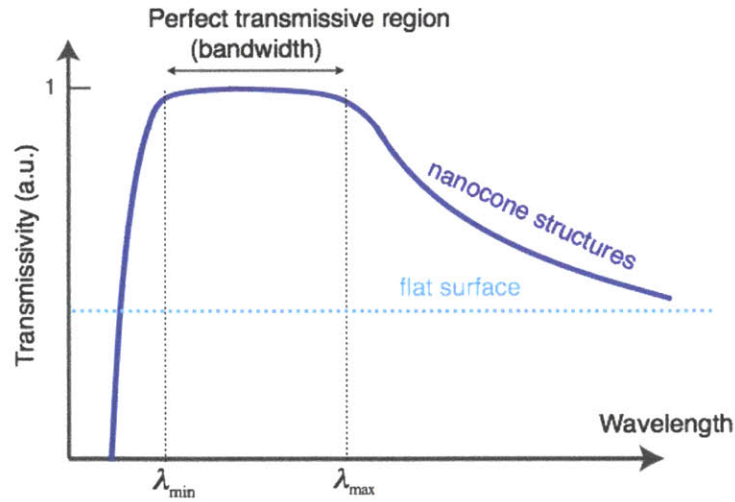


Figure 2-6. Optical transmissivity response (zeroth-order) of the transparent nanocone structured surface in Figure 2-5. The geometry of the structures determines the bandwidth of the perfect transmission region.

The structure period P governs the minimum wavelength cutoff (or the lower wavelength limit λ_{min}). This occurs when the structure is no longer subwavelength, and light becomes diffractive [17, 25, 74-76]. In Figure 2-6, the transmittance drops quickly below the lower wavelength limit λ_{min} because the first diffracted orders appear in this wavelength region. To examine this effect, the wave vector for the first diffracted order is given by,

$$\frac{2\pi}{\lambda} n_2 \sin \theta_{diff} = \frac{2\pi}{P} - \frac{2\pi}{\lambda} n_1 \sin \theta_1 . \quad (2.5)$$

Setting $\sin\theta_{diff} \rightarrow 1$ ensures the diffracted beam is evanescent, thus transferring all the energy in the transmitted zeroth-order. By reorganizing Eq. 2.5, the minimum operating wavelength (or the lower wavelength limit λ_{min}) can be approximated [25, 75, 76] as

$$\lambda_{min} = P \cdot (n_2 + n_1 \sin\theta_1). \quad (2.6)$$

This equation suggests that the lower wavelength limit (λ_{min}) is proportional to the structure period P , and this minimum operating wavelength increases with increasing incident angles and the structure period P .

In contrast, the upper wavelength limit λ_{max} is determined by the structure height H that is the thickness of effective medium consisting of the nanocones.

The z-component of the incident wave vector is

$$k_z = n_1 \frac{2\pi}{\lambda} \cos\theta_1. \quad (2.7)$$

Because the subwavelength tapered structures emulate an effective medium for adiabatic impedance matching (n_1 to n_2) to reduce the optical reflection, the structure height of the structures should be greater than a wavelength of incident light in the medium to ensure adiabatic impedance matching. To ensure the anti-reflectivity conditions through the tapered nanocone structures, the following condition (Eq. 2.8) must satisfy (As a first-order approximation, we set the constraint that H be sufficiently tall that the z-component of the incident wave can undergo a full 2π -phase cycle).

$$k_z H > 2\pi \quad (2.8)$$

Based on this first-order approximation, we can estimate the upper wavelength limit λ_{max} of the nanocone structures. Rearranging Eq. 2.8 leads to

$$\lambda_{\max} \sim Hn_1 \cos\theta_1, \quad (2.9)$$

predicting the maximum operating wavelength (or the upper wavelength limit λ_{\max}) for a given H , and incident angle θ_1 . It is important to note that the upper wavelength limit λ_{\max} decreases with decreasing height and increasing incident angles.

While the lower wavelength limit λ_{\min} is well defined from Eqs. 2.5 and 2.6 (or grating equation), an exact expression or explicit formula for estimating the upper wavelength limit λ_{\max} has not been achieved. For better estimation of the upper wavelength limit λ_{\max} , Eq. 2.9 becomes

$$\lambda_{\max} = \alpha \cdot Hn_1 \cos\theta_1, \quad (2.10)$$

where the factor of alpha (α) is empirically defined, and is based on rigorous coupled-wave analysis (RCWA) theoretical simulation work [75, 77].

To estimate the factor of alpha (α) for a given structure, transmissivity values of the nanocone structures are calculated, with respect to varying wavelengths from 0.25 μm to 10 μm and heights from 200 nm to 2000 nm, as shown in Figure 2-7. The structure has a linear profile with a square lattice and a fixed period of 200 nm, and is simulated by 20 discrete layers using RCWA [77]. A diffraction phenomenon related to the lower wavelength limit is not considered because the aim is to find the upper wavelength limit (λ_{\max}) through the RCWA simulations [77]. Generally, light reflection at an optical interface is governed by the Fresnel equation, and the transmittance of the flat substrate against normal incident light ($\theta_1 = 0^\circ$) is

$$T = 1 - \left(\frac{n_1 - n_2}{n_1 + n_2} \right)^2 \quad (2.11)$$

This is strong evidence that the upper wavelength limit is also related to the refractive indices of the two media. To see the effect of refractive indices of the nanostructures on optical transmissivity, especially on the upper wavelength limit λ_{max} , the refractive indices of the substrate (n_2) for Figures 2-7a, 2-7b, and 2-7c are set to be 1.5, 2, and 3, respectively. The surrounding medium is air, whose refractive index (n_1) is 1. The maximum value of the contour maps is set to be 1, representing perfect transmission without Fresnel reflection, and the minimum values are set to be the transmissivity values of the flat substrates with the specific refractive indices, which are determined by Eq. 2.11 due to Fresnel reflection.

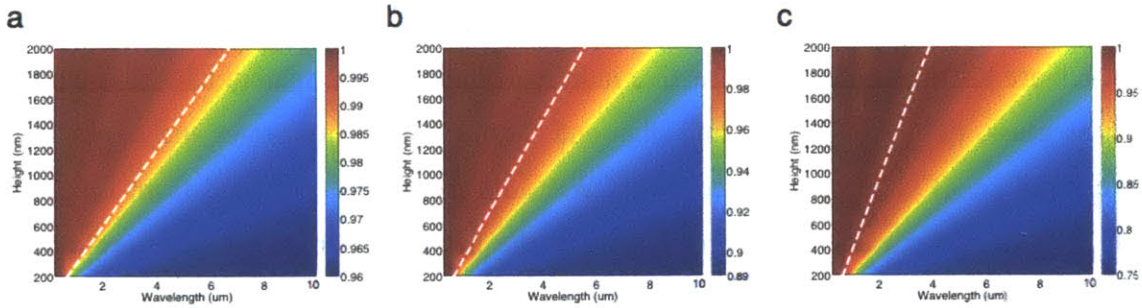


Figure 2-7. Calculated optical transmissivity with respect to the wavelength and height of the nanocone structure with a refractive index (n_2) of a) 1.5, b) 2, and c) 3. The surrounding medium is air ($n_1 = 1$).

It can be observed that the reflectivity is suppressed when the structure height H is relatively larger than the wavelength λ , represented by red colored regions on the figures. In addition, all the transmissivity behaviors in Figure 2-7 are very similar, and the same values of the transmissivity are proportional to the heights of the structures, which also verify both Eqs. 2.9 and 2.10. To find the factor of alpha values (α) with respect to the refractive indices (n_2) in Eq. 2.10, the threshold value for the upper wavelength limit is set to be 0.99 (or 99%), which is shown by the white dotted lines on the contour maps.

A representative refractive index of the effective medium (n_{rep}) where the nanocones are placed can be approximately determined to be $(n_1 + n_2)/2$, according to the first-order

approximation among the effective medium theories [65, 66]. Simply by calculating the slopes of the white dotted lines and correlating those values with the representative refractive indices, it is found that the alpha values (α) are inversely proportional to n_{rep} , and a factor of ~ 4 is also found to match the threshold value (0.99) for the upper wavelength limit; consequently, the upper wavelength limit λ_{max} can be defined by the following equation:

$$\lambda_{max} = \alpha \cdot H n_1 \cos \theta_1 \approx \frac{2}{n_1 + n_2} H n_1 \cos \theta_1 \cdot 4 = 8 \frac{n_1}{n_1 + n_2} H \cos \theta_1. \quad (2.12)$$

This equation still holds with all the cases with the different refractive indices from 1.5 to 3, which are the most common refractive indices of optically transparent natural materials such as glass, titanium dioxide, and diamond. Figure 2-8 demonstrates the upper limit wavelength (λ_{max}) values calculated by RCWA, and the values estimated from Eq. 2.12, with respect to the wavelength and height of the nanocone structure with a refractive index (n_2) of 1.5, 2, and 3. The proposed model (Eq. 2.12) for the upper limit wavelength (λ_{max}) values show a good match to the values calculated from RCWA simulations. The upper limit wavelength (λ_{max}) values ($n_2 = 3$) calculated from RCWA display nonlinear behavior (height $H \leq 1000$ nm) because the transmissivity value of the perfect transmissive region (depicted in Figure 2-6) is slightly lower than those with a medium of lower refractive indices ($n_2 < 3$). However, the upper limit wavelengths still follow the general trend predicted by Eq. 2.12, and these can also be seen in Figure 2-7c.

Note that a can be determined in a slightly different way with different profiles of nanocone structures and with different threshold values for the upper limit wavelength λ_{max} ; however, λ_{max} is always proportional to the structure height H .

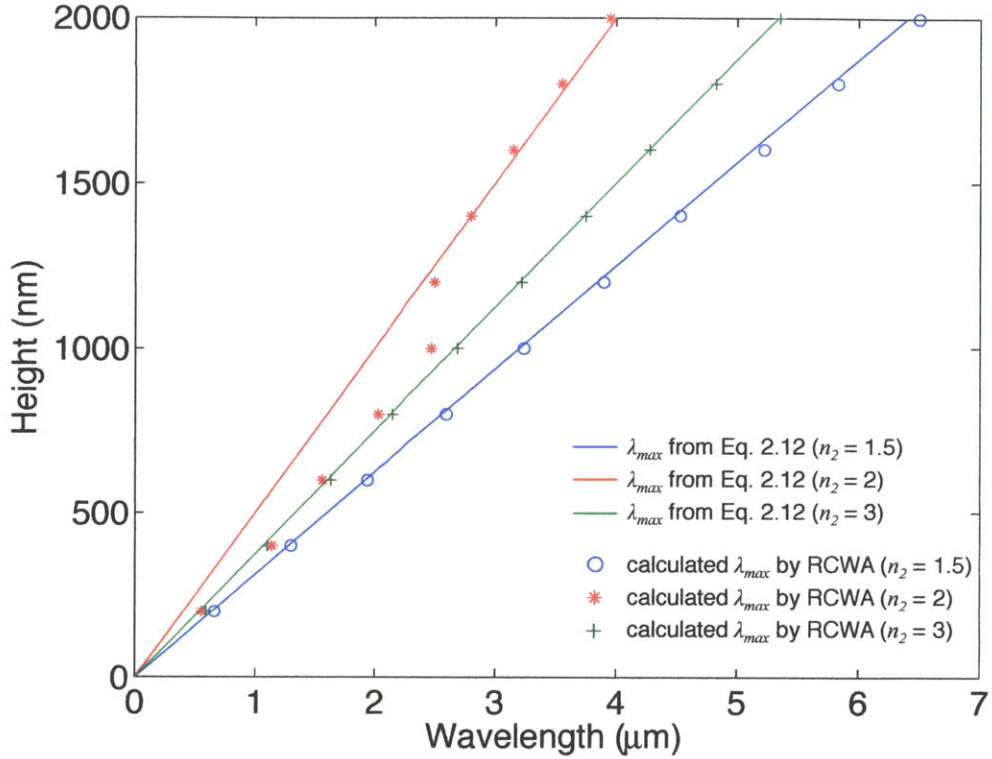


Figure 2-8. Upper limit wavelength (λ_{max}) values calculated by RCWA, and the values estimated from Eq. 2.12, with respect to the wavelength and height of the nanocone structure with a refractive index (n_2) of 1.5, 2, and 3. The surrounding medium is air ($n_1 = 1$), and the angle of incidence is 0° .

Figure 2-9 depicts the normalized maximum and minimum operating wavelengths (λ_{max}/H and λ_{min}/P) as functions of incident angles. To yield a larger operating bandwidth ($\Delta\lambda = \lambda_{max} - \lambda_{min}$), the height of the nanostructure needs to be maximized and the period of the nanostructure needs to be minimized, leading to the combined requirement of a high aspect-ratio nanocone structure.

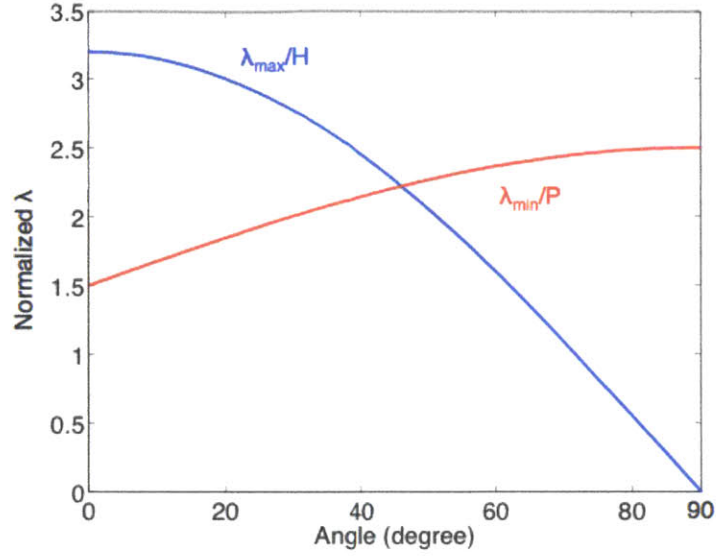


Figure 2-9. Normalized maximum (λ_{max}/H) and minimum (λ_{min}/P) operating wavelengths plotted against incident angles with the substrate's refractive index (n_2) of 1.5. The surrounding medium is air ($n_1 = 1$).

Using Eqs. 2.6 and 2.12, we define the normalized bandwidth as:

$$B^* = \frac{\Delta\lambda}{\lambda_{min}} = \frac{\lambda_{max} - \lambda_{min}}{\lambda_{min}} = \frac{8}{n_1 + n_2} \left(\frac{H}{P} \right) \frac{n_1 \cos\theta_1}{n_2 + n_1 \sin\theta_1} - 1 \quad (2.13)$$

where $\Delta\lambda = \lambda_{max} - \lambda_{min}$. This simple relationship can be used to approximately predict the operating bandwidth ($\Delta\lambda$) of the structure, which represents the optical parameter to maximize. When the normalized bandwidth becomes a negative value, there is no enhanced transmissive behavior of the nanocone structure (*i.e.*, no perfect transmissive region in Figure 2-6). Figure 2-10 depicts the normalized bandwidth (B^*) with respect to incident angles for various aspect-ratios. As expected, higher aspect-ratios lead to a larger operating bandwidth ($\Delta\lambda$) for all incident angles, whereas large incident angles lead to decreased bandwidth.

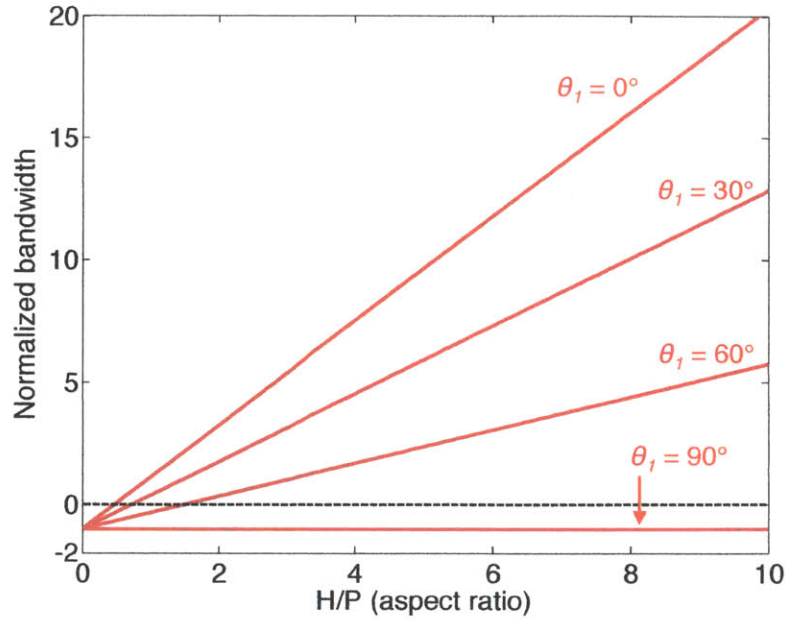


Figure 2-10. The normalized operating bandwidth (B^*) with respect to structure aspect-ratio for different incident angles. For the structure to function at large angles (θ_i), high aspect-ratio structures are required.

These first-principle models of the upper and lower wavelength limits (λ_{max} and λ_{min}) can be validated by comparing them to RCWA simulation results. The structure has a linear profile with a square lattice, and is simulated by 20 discrete layers using RCWA simulations [78, 79]. Figure 2-11 depicts the transmissivity simulated at an air/glass interface ($n_1 = 1$ and $n_2 = 1.5$) for incident angles of 0° , 30° , 45° , and 60° as a function of wavelengths of incident light. In this RCWA simulation, the nanocone structure has $P = 200$ nm and $H = 1000$ nm. The 99% transmissivity cut-off level is added to the figure, represented by the black dotted line, so that the operating bandwidths ($\Delta\lambda = \lambda_{max} - \lambda_{min}$) for each angle can be compared. This shows that the operating bandwidth ($\Delta\lambda$) for each angle follows the general trend predicted by Eq. 2.13 and Figure 2-9.

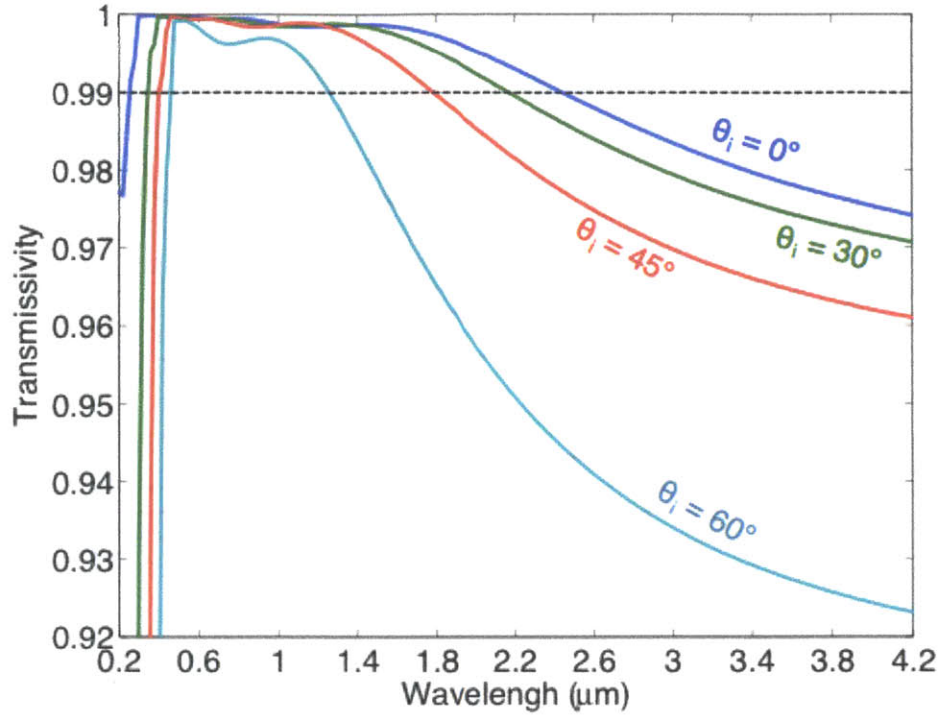


Figure 2-11. Transmission efficiency (zeroth-order) of the anti-reflective nanocone structure simulated using RCWA for a number of incident angles as functions of the wavelength of the incident illumination.

Using this analysis we can derive the approximate normalized operating bandwidth (B^*) and use it as the optical non-dimensional merit function. Clearly, then, to improve the bandwidth of anti-reflection on nanotextured surfaces, it is crucial to be able to obtain structures with high aspect-ratio.

2.4.2 Wetting design constraints

In parallel to these studies on control of light transport, anti-reflectivity, understanding of wetting behavior on rough surfaces is significant for design and optimization of the nanotextured multifunctional materials. Moving beyond simple cylindrical post arrays,

experiments and calculations on a wide range of surface topographies have suggested that enhanced superhydrophobicity can be obtained by high-density conical or pyramidal structures with small hemispherical caps on the tips [12]. Such structures promote a robust Cassie-Baxter state with higher apparent contact angles ($> 150^\circ$) and lower contact angle hysteresis (CAH), because of the very small liquid-solid area fraction $f_s = 2\pi(1 + \cos\theta_{adv})(r/P)^2$ (in the case of an advancing contact angle $\theta_{adv} \geq 90^\circ$ and a square array of conical structures with hemispherical tops, where r is the radius of the hemispherical top in Figure 2-12) and negligible effects of contact line pinning on the hemispherical tops of the features [12].

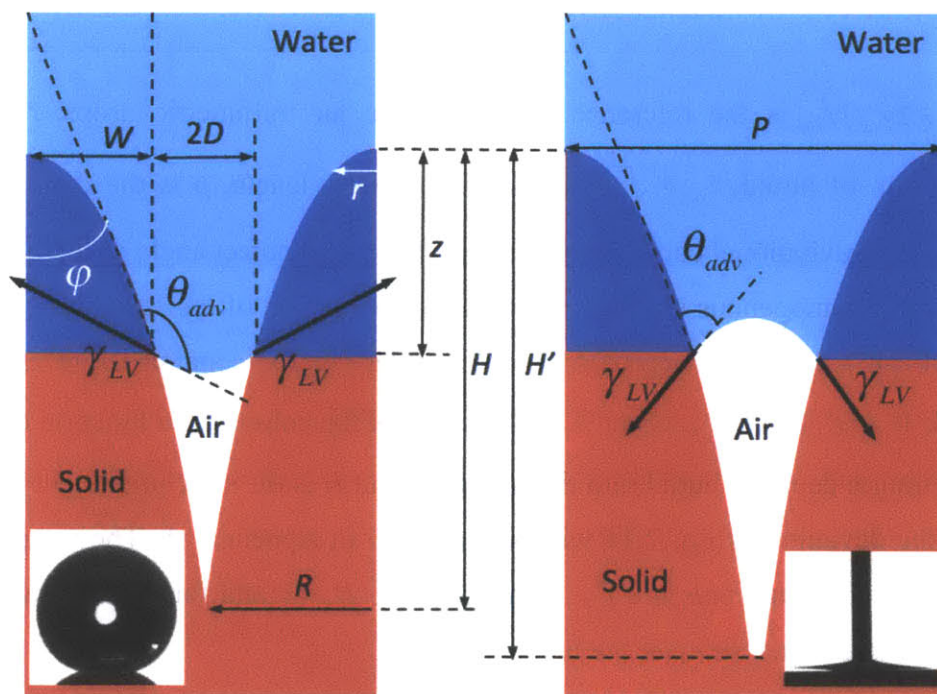


Figure 2-12. Schematic drawings of the three-phase (air-liquid-solid) contact line on hydrophobically-modified (left) and hydrophilic (right) nanocone structures [45]. The insets show corresponding goniometer images for $5 \mu\text{l}$ droplets with apparent contact angles of $\theta^* = 165 \pm 1^\circ$ (left) and $\theta^* \leq 5^\circ$ (right), respectively. The black thick arrows (γ_{LV}) represent directions of surface tensions at the three-phase (air-liquid-solid) contact lines.

The conical shape of the nanostructures developed in this study also plays an important role in providing greater resistance to loss of superhydrophobicity (or Cassie-Baxter to Wenzel transition). The structure is self-stabilizing and the critical breakthrough pressure increases progressively as the advancing liquid meniscus penetrates into the surface texture due to the continuously decreasing spacing between each cone. This self-stabilization [72] can be quantified by modifying the dimensionless robustness parameter introduced by Tuteja *et al.* based on the geometry of the cone structure. By considering the geometric features in Figure 2-12 that parameterize the high aspect-ratio taper structures, the relevant dimensionless parameter becomes

$$T^*(z/H) = P_{crit}/P_{ref} = \pi \ell_{cap} (z/H)^{\frac{3}{2}} \cos(\theta_{adv} - \varphi) / \left[2P \left(1 - (\pi/4)(z/H)^{\frac{3}{2}} \right) \right], \quad (2.14)$$

where $P_{ref} = 2\gamma_{LV} / \ell_{cap}$ is the reference pressure scale for millimetric drops, γ_{LV} is the surface tension of liquid, $\ell_{cap} = \sqrt{\gamma_{LV} / \rho g}$ is the capillary length, ρ is the density of the liquid, g is the gravitational constant, θ_{adv} is the advancing contact angle of the liquid on a flat chemically homogenous surface, and φ is the cone angle of the feature as shown in Figure 2-12 [45]. Here, we approximate the slender tapered cone structure as a cubic paraboloid, $W = (P/2)\sqrt{z/H}$, where W is the radius of the column as a function of z/H , z is the penetration depth of liquid into the structure, and H is the structure height [45]. The details of the derivation of Eq. 2.14 will be discussed in Appendix A. The magnitude of the critical breakthrough pressure P_{crit} increases as $z/H \rightarrow 1$ and for smaller values of P that leads to more structures over the unit area.

In contrast, the aspect-ratio and shape profile of the conical structure can also explain the principle of superhydrophilic surfaces such as *Calathea Zebrina*, which display apparent contact angles with water lower than 10° , simply by changing the surface chemistry [80]. By changing the direction of the net surface traction (represented in the black arrows) of the three-phase contact line on the hydrophilic conical structure ($\theta_{adv} - \varphi < 90^\circ$) shown in Figure 2-12, the liquid is strongly imbibed into the structure with a traction force that increases as the spacing (P) between features decreases. Higher values of the Wenzel

roughness (r_w) promote a smaller apparent contact angle by capillary imbibition [81], which has also been shown in Section 1.4. The rapid imbibition of water into the structure (or condensation) promotes formation of a continuous liquid film with strong antifogging characteristics [60, 82, 83].

2.5 Fabrication process

Fused silica (SiO_2) is chosen as the substrate material to ensure enhanced transmission at visible wavelengths, while most of the recent work on subwavelength anti-reflection structures is based on absorptive materials (*e.g.*, Si, GaAs, carbon nanotubes, etc.) [3, 15, 69, 84, 85] which only suppress Fresnel reflection but do not enhance transmission. The subwavelength high aspect-ratio silica nanostructures ($P \sim 200 \text{ nm} < \lambda$) are patterned over a large area of the fused silica substrate (45 mm by 45 mm) using two orthogonal laser exposures ($\lambda = 325 \text{ nm}$) through interference lithography to yield a defect-free periodic square array. A novel multi-step etching process using shrinking masks has been developed to achieve the high aspect-ratio silica nanocone structures. The fabricated structure exhibits structural superhydrophilicity due to inherent hydrophilicity of silicon oxide surface (fused silica). The structure needs to be silanized using a standard vapor deposition process for superhydrophobicity. The fabricated structure is treated by a chemical vapor deposition of 1H,1H,2H,2H-perfluorodecyltrichlorosilane (Alfa Aesar, 96%) in an oven at 110 °C for 10 hours [86]. The fabrication process will be discussed further in Chapter 3.

2.6 Results and discussion

To simultaneously meet the optical and fluidic requirements, a tapered nanocone structure with cone angle $\sim 4.8^\circ$, on a periodic spacing $P \sim 200$ nm and height $H \sim 1.1$ μm with $\sim 15 \pm 5$ nm radius of curvature at the tip is directly fabricated on the fused silica substrate, as shown in Figure 2-13. The aspect-ratio of the fabricated structure yields dimensionless design parameter values of $B^* \sim 10^1$ (with normal incident angle) and $T^* \sim 10^6$ [45]. The fabricated slender tapered nanocone structures (shown in Figure 2-13) exhibit enhanced optical transmissivity with unobservable reflection compared to a flat glass slide or the flat fused silica wafer. The achieved optical and wetting properties will be discussed further in this section.

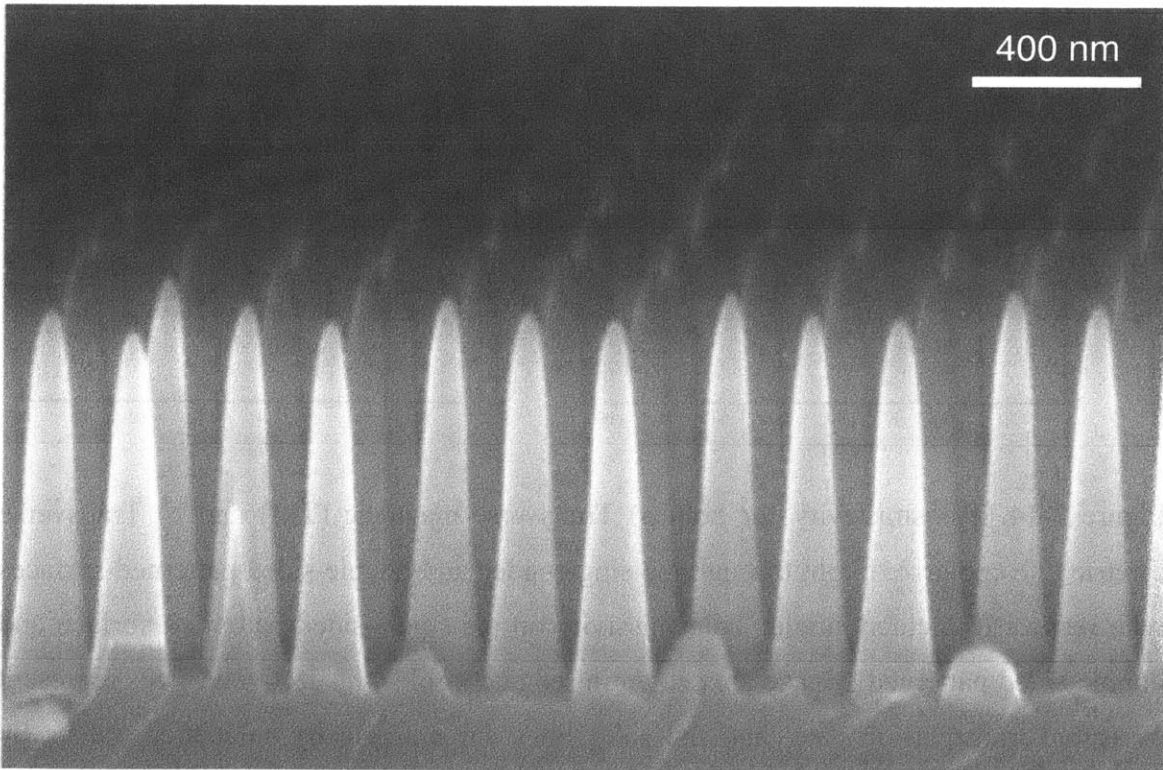


Figure 2-13. SEM image of the fabricated nanocone structures [45]. The period of the structure P is 200 nm.

2.6.1 Optical properties

To check enhanced transmissivity of the fabricated surfaces, angle dependent transmissivity measurements through the single-sided and double-sided patterned surfaces are performed using both transverse electric (TE) polarized and transverse magnetic (TM) polarized irradiation with a wavelength (λ) of 543 nm. As shown in Figure 2-14, transmissivity of the double-sided patterned surface is greater than 90% up to at 70° (angle of incidence) with both polarizations of the light, which has never been reported before to our knowledge. Numerically calculated transmissivity values by RCWA simulations are shown in solid lines (the single-sided patterned surface in red, and the double-sided patterned surface in blue), and these results have the same tendency with measured values.

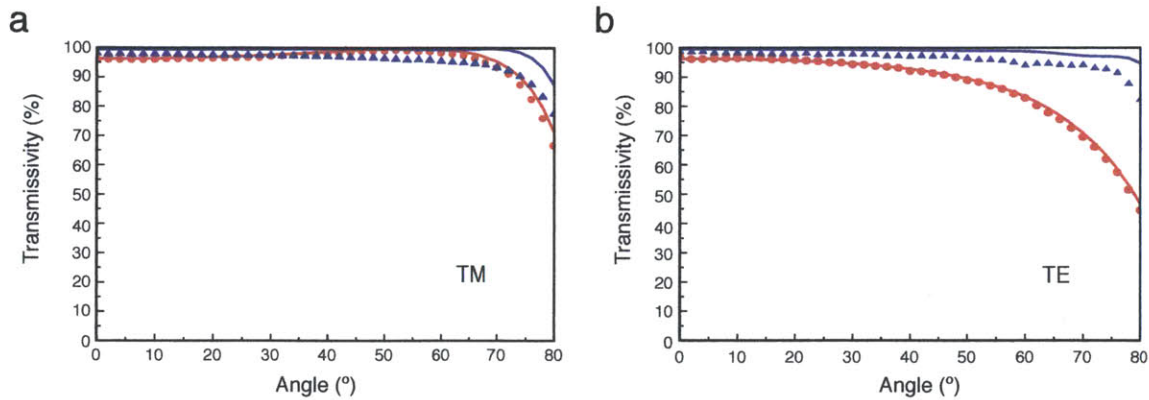


Figure 2-14. Transmissivity for both a) Transverse magnetic (TM) and b) Transverse electric (TE) polarized light through the single-sided and double-sided patterned surfaces with respect to incident angle. Transmissivity on the single-sided patterned surface and double-sided patterned surface are shown in red and in blue, respectively. Dots represent measured transmission data, and the solid lines are numerically calculated values by RCWA method.

The transmissivity measurements through the double-sided patterned surfaces are also carried out over a broad range of wavelength ($250 \text{ nm} \leq \lambda \leq 1700 \text{ nm}$) using TE-polarized

and TM-polarized irradiation at incident angles $\theta_I = 0^\circ, 30^\circ, 45^\circ,$ and 60° . The arithmetically averaged transmissivity values measured with two polarized lights are plotted in Figure 2-15. The double-sided surface exhibits transmissivity greater than 98% at $\theta_I = 0^\circ$ over a wide range of wavelengths. The measurements show a decrease in transmission ($\theta_I = 0^\circ$) at a lower wavelength bound of approximately 300 nm, because the 200-nm-period nanocone structure becomes increasingly diffractive (see Eq. 2.6). The transmissivity measurements at incident angles $\theta_I = 30^\circ, 45^\circ,$ and 60° demonstrate that the minimum wavelength bound (lower wavelength limit λ_{min}) increases with increasing the incident angle, which typically narrows the operational bandwidth for omnidirectional transmissivity, which have also been estimated by Eq. 2.6 and Figure 2-11 (see Section 2.4.1).

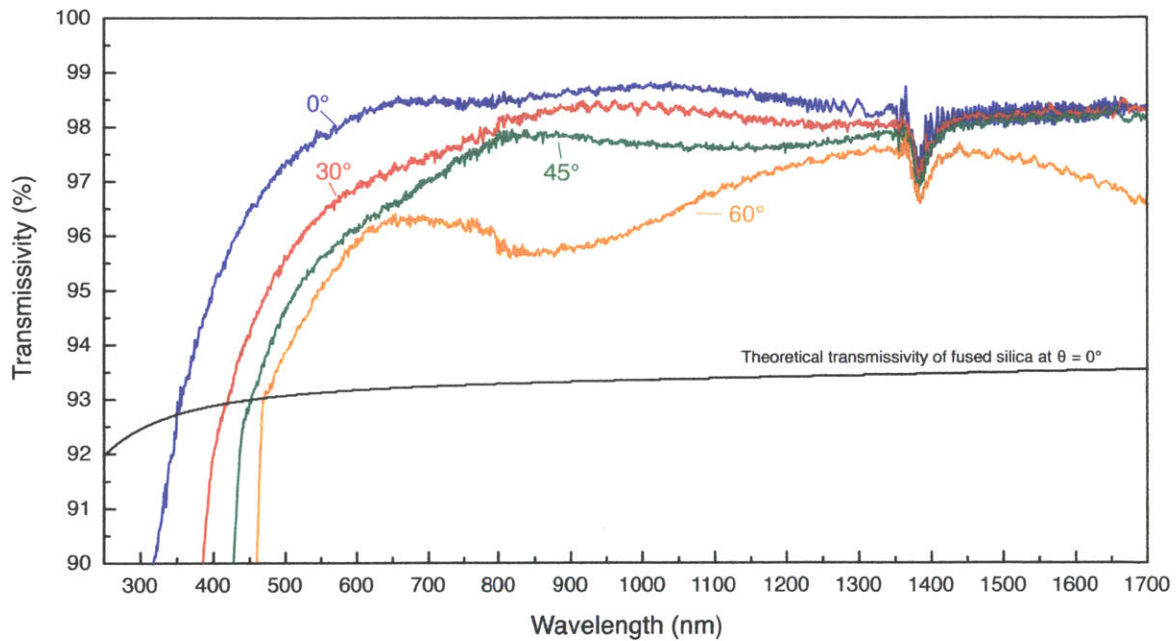


Figure 2-15. Averaged broadband transmissivity with two measurements on both TE and TM polarizations at the four different incident angles ($\theta_I = 0^\circ, 30^\circ, 45^\circ,$ and 60°) with a range of wavelength ($250 \text{ nm} \leq \lambda \leq 1700 \text{ nm}$) [45]. The black line represents the calculated transmissivity values of the flat fused silica surface at normal incident angle.

In order to calculate optical haze, the transmissivity measurements through the double-

sided patterned surfaces are also carried out over a broad range of visible wavelengths ($400 \text{ nm} \leq \lambda \leq 850 \text{ nm}$) at normal incident angle with and without an integrating sphere. According to ASTM D1003, optical haze is defined as a percentage of light diffusely scattered compared to the total light transmitted through the surface. In Figure 2-16, the blue and red curve represent the total transmissivity and the zeroth-order transmissivity, respectively, with respect to wavelength. The double-sided patterned surface exhibits optical haze, plotted by the black curve in Figure 2-16, smaller than 4% over the visible wavelength region. The optical haze increases at a small wavelength region because the light illuminating on the periodic nanocone structure becomes increasingly diffractive due to undesired defects during the fabrication steps. This will be discussed further in Chapter 3.

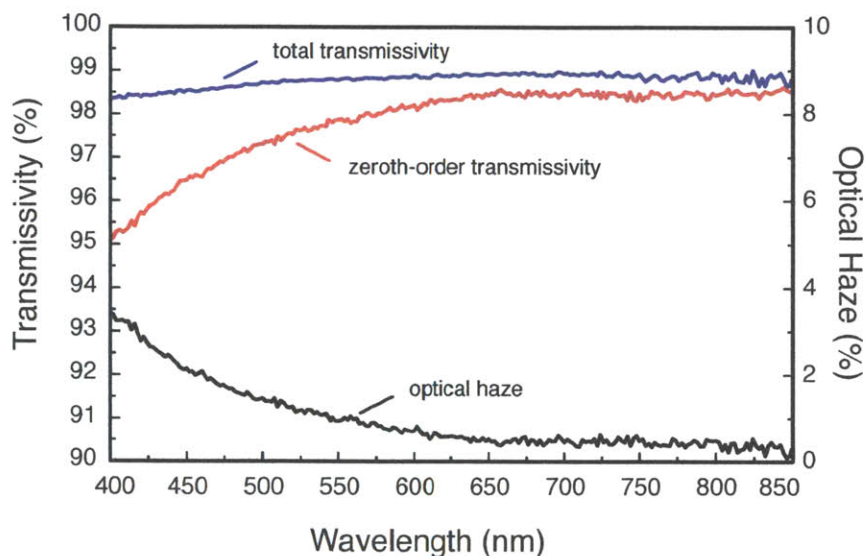


Figure 2-16. Broadband total transmissivity (blue solid line) and zeroth-order transmissivity (red solid line) through the double-sided patterned surface at normal incident angle ($\theta_i = 0^\circ$) with a range of wavelengths ($400 \text{ nm} \leq \lambda \leq 850 \text{ nm}$). Optical haze is shown in black line with respect to wavelength.

In order to examine optical performance of the fabricated silica surface as a protected glass for PV cells, the external quantum efficiency (EQE) is measured from the processed silicon solar cell with respect to wavelength ($300 \text{ nm} \leq \lambda \leq 1100 \text{ nm}$) in the cases that the

solar cell are covered by 3 different surfaces (flat fused silica, single-sided patterned silica surfaces, and double-sided patterned silica surfaces), as shown in Figure 2-17. Due to Fresnel reflection caused by optical impedance mismatch at the flat surface, the measured EQEs in the cases of the flat silica and single-side patterned silica surfaces show relatively large efficiency loss compared to that measured with the double-sided patterned surface. These EQE measurements verify that the double-sided patterned surface can improve around 8% in collecting-efficiency of solar energy that is wasted by Fresnel reflection of the flat surface within the wavelength region ($300 \text{ nm} \leq \lambda \leq 1100 \text{ nm}$).

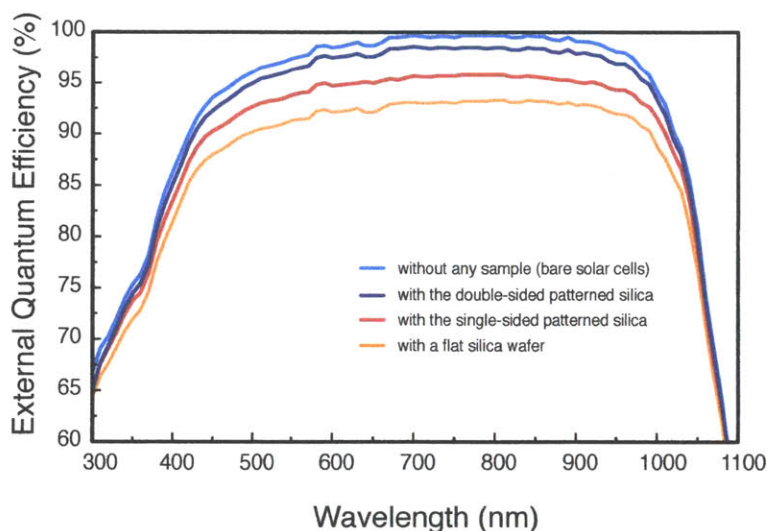


Figure 2-17. Measured external quantum efficiency (EQE) of a processed solar cell as a function of wavelength ($300 \text{ nm} \leq \lambda \leq 1100 \text{ nm}$) at normal incident angle ($\theta_i = 0^\circ$). Lines with light blue, blue, red, and yellow colors are measured EQE without any layer, with the double-sided patterned surface, with the single-sided patterned surface, and with a flat silica surface on top of the solar cell, respectively.

Figures 2-18, 2-19, and 2-20 show the measured optical transmissivity of the surface and simulated transmissivity using RCWA for both transverse electric (TE) and transverse magnetic (TM) polarized lights as a function of the wavelength from 300 nm to 1700 nm at the incident angles of 30° , 45° , and 60° , respectively. The measured optical

transmissivity with TM-polarized light is slightly higher than that with TE-polarized light because of the Brewster effect, which is also expected in the simulation results. In Figure 2-20, the transmissivity of TM-polarized light ($\theta_i = 60^\circ$) has the maximum value 99.5% at the wavelength of 1083 nm, while that of TE-polarized light ($\theta_i = 60^\circ$) has the minimum value 93.4% at the wavelength of 915 nm in the near infrared region, where the light is still not diffractive. In addition, all the transmissivity values drop as the incident angle increases, but those are still above 90% over a wavelength region from 465 nm to 1700 nm. The RCWA simulation results demonstrate a good agreement with the experimental data on the general efficiency trend. The measured experimental data show slightly lower transmissivity values than the calculated values due to defects and mechanical damage on the double-sided patterned surface, which will be discussed in Chapter 3. The optical transmissivity exhibits an abrupt drop at the wavelength of 1390 nm, since Si-OH band has an absorption band centered at this wavelength [87].

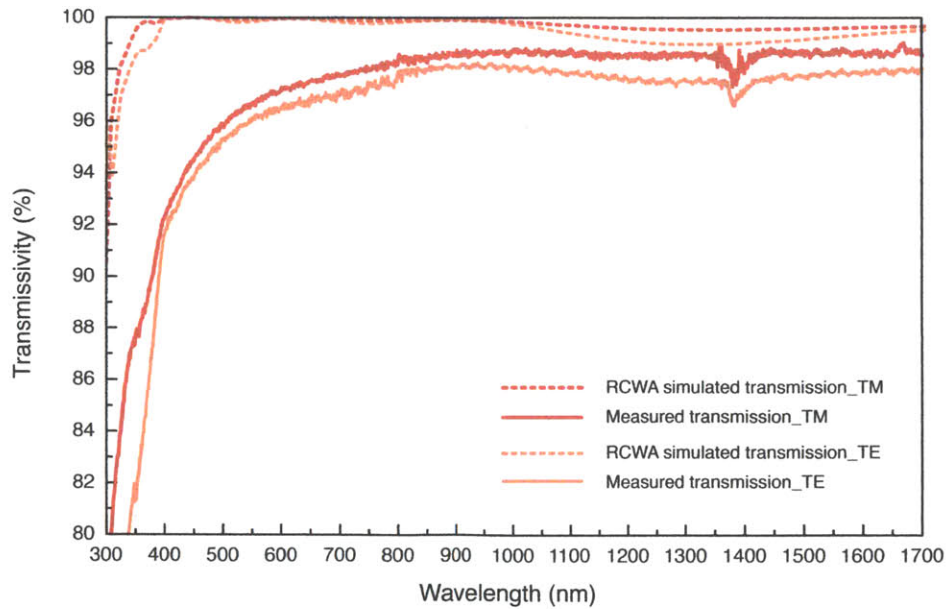


Figure 2-18. Measured optical transmissivity of the nanotaper structures and simulated transmissivity using RCWA for both transverse electric (TE) and transverse magnetic (TM) polarized lights as a function of the wavelength at 30° incident angle [45].

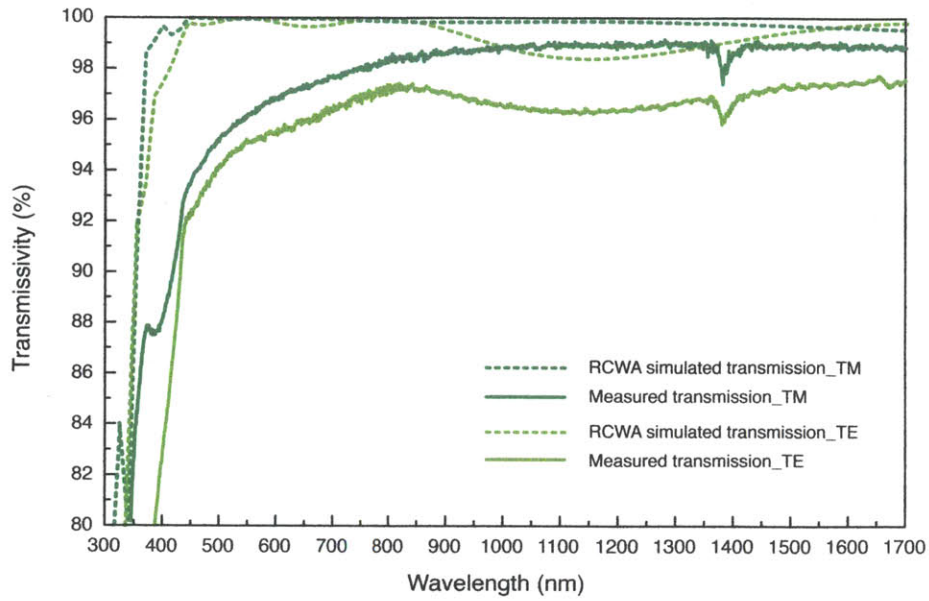


Figure 2-19. Measured optical transmissivity of the nanotaper structures and simulated transmissivity using RCWA for both TE- and TM-polarized lights as a function of the wavelength at 45° incident angle [45].

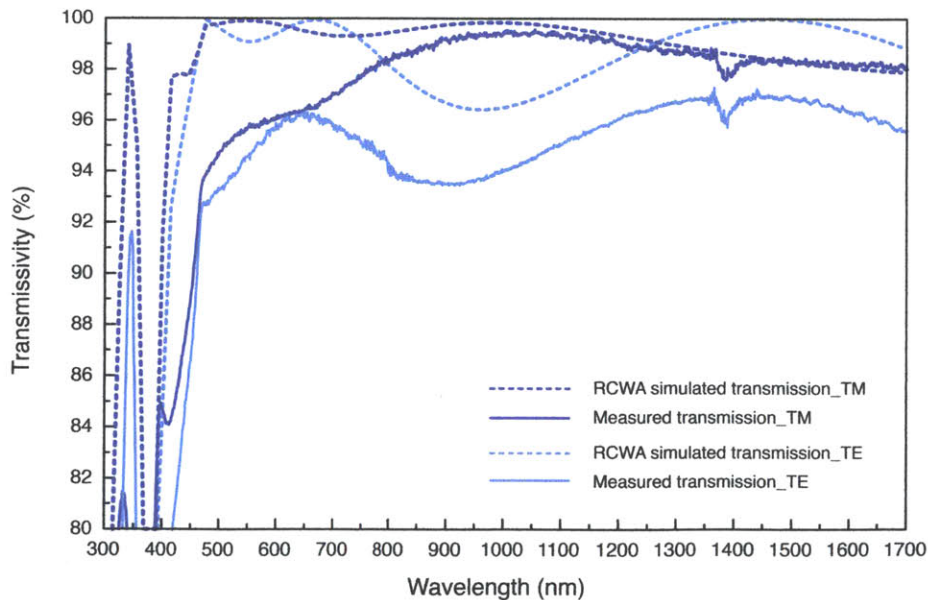


Figure 2-20. Measured optical transmissivity of the nanotaper structures and simulated transmissivity using RCWA for both TE- and TM-polarized lights as a function of the wavelength at 60° incident angle [45].

Note that the RCWA simulated results shown in Figures 2-14, 2-18, 2-19, and 2-20 are calculated by 20 discrete layers using 2D RCWA simulations with 121 spatial harmonics retained [78, 79]. The structure geometry is approximated and determined from the SEM images of the fabricated nanocones, and it is given in Table 2-1. A helium-neon (HeNe) laser ($\lambda = 543 \text{ nm}$) is used for angle-dependent transmissivity measurements.

Layer	Duty cycle	Layer	Duty cycle	Layer	Duty cycle
1	0.07	8	0.47	15	0.71
2	0.14	9	0.51	16	0.75
3	0.21	10	0.55	17	0.79
4	0.28	11	0.58	18	0.84
5	0.35	12	0.61	19	0.89
6	0.39	13	0.64	20	0.94
7	0.43	14	0.67		

Table 2-1. The structure geometry for rigorous coupled wave analysis (RCWA). 20 discrete layers are used for defining nanocone structures and the duty cycles of each layer are listed in the table. The duty cycle is the ratio of diameter to period of the nanocone [45]. Layer 1 is the top layer of the nanocone (tip).

A Cari-500 (UV-VIS-NIR) spectrophotometer is used for the polarization-dependent transmissivity measurements in the UV-VIS-NIR range with the Glan-Taylor polarizer (PGT-S1V) and is used for the haze measurement with an integrating sphere. It should be noted that some of the measurements by spectrophotometers in the range between visible to infrared wavelengths show discrete discontinuity in transmittance or reflectance values [15, 88]. This is because of the portions of TE- and TM-polarized light out of incident beams abruptly change at a specific wavelength ($\lambda \sim 800 \text{ nm}$ or 850 nm , depending on spectrophotometers). To avoid this discontinuity of the measurements, a linear polarizer should be applied.

2.6.2 Wetting properties

The high aspect-ratio nanostructures with a subwavelength spacing P of 200 nm are patterned over a large area ($> 1600 \text{ mm}^2$) of the substrate using two orthogonal interference lithography exposures to yield a defect-free periodic square array. The structure can be silanized using a standard vapor deposition process to achieve water repellency (or superhydrophobicity) [86]. The fabricated superhydrophobic and transparent anti-reflective surface enables a millimetric water droplet to form an almost perfect spherical bead (apparent advancing contact angle $\theta_{adv}^* = 165 \pm 1^\circ$, apparent receding contact angle $\theta_{rec}^* = 164 \pm 1^\circ$, and roll-off angle $\theta_{roll-off}^* \leq 2 \pm 1^\circ$), as shown in Figure 2-21.

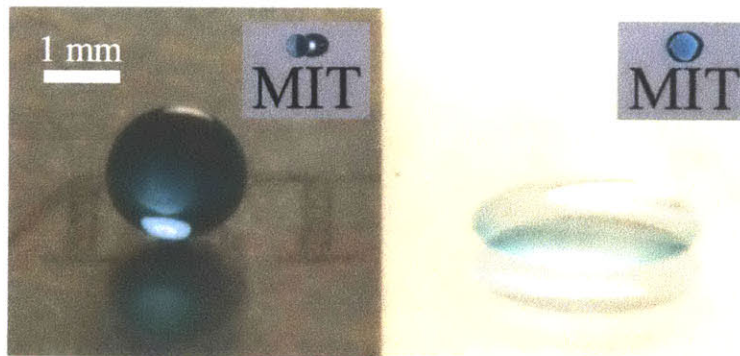


Figure 2-21. Blue-dyed water droplets sitting on a transparent nanotaper surface (left) and on a flat glass (right), each placed on top of printed black letters [45]. The insets are top views of the same two surfaces. The very weak reflection and high contact angle of the tapered nanocone surface contrast strong reflection and a low contact angle of water on the flat glass.

Evaluation of the modified design parameter T^* provides a simple analytic expression for the maximum pressure (assuming the liquid meniscus between four asperities forms a hemispherical liquid cap) $P_{crit} = T^*(z/H \rightarrow 1) \cdot P_{ref} \approx 2.3 \text{ MPa}$. This exceedingly high

value of critical breakthrough pressure and the concomitant self-stabilization effect [72] stem from the tapered conical structure which results in the minimum spacing on the order of tens of nanometers near the bottom of each valley ($z \rightarrow H$). The sequence of high-speed camera (Vision Research Phantom v5.0) images shown in Figure 2-22 following impact of a water droplet ($V \approx 6.26$ m/s, corresponding to Weber number $We \approx 1785$) clearly shows the consequences of this self-stabilization effect, with the complete droplet rebound and roll-off at higher impact velocities than previous dynamic studies [14, 40, 89].

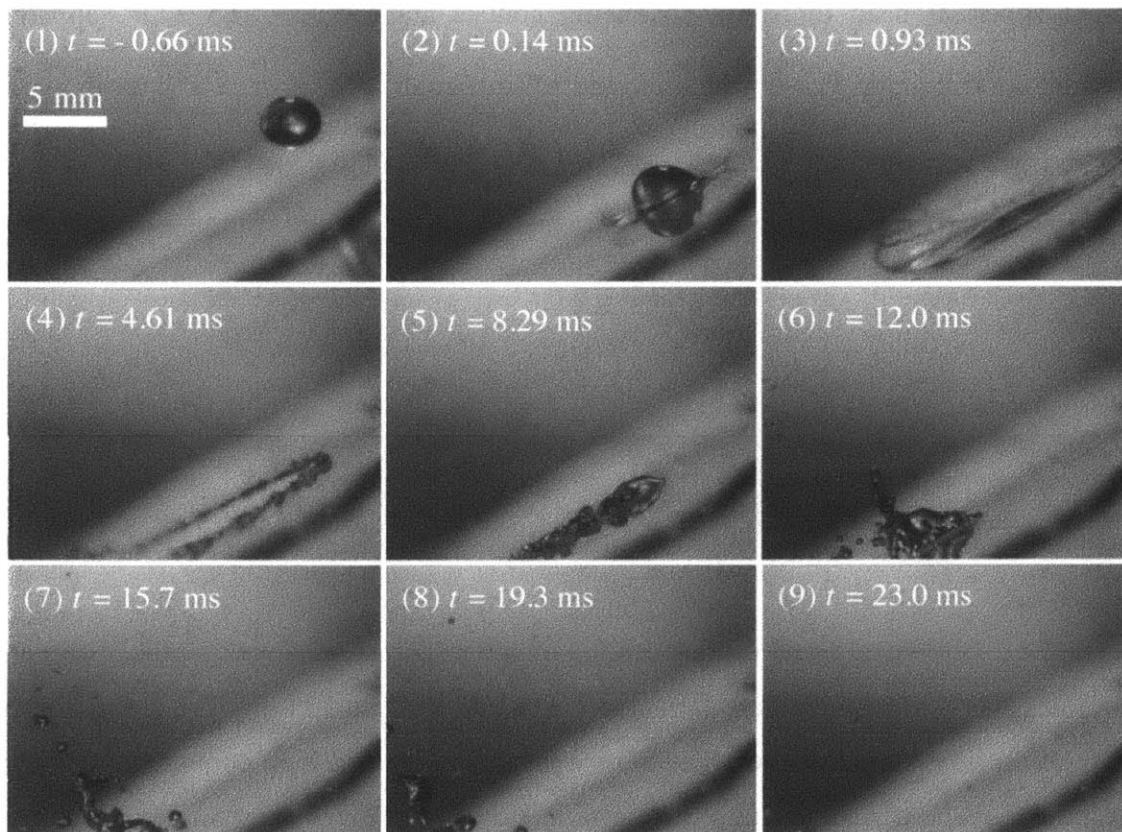


Figure 2-22. Sequential images of a water droplet impact on an oblique (30° from the horizontal plane) nanotaper surface (taken through the use of a high speed camera; $V \approx 6.26$ m/s and $We \approx 1785$) [45]. The last image on the bottom right side demonstrates that no residual droplets remain on the nanotaper surface due to the high robustness of the Cassie-Baxter state to the dynamic pressure.

In many practical applications, including solar panels, self-cleaning and prevention of contaminant fouling; or avoidance of fogging are also important to preserve high transmissivity. These deterrents are largely mitigated in the fabricated nanocone surfaces again due, respectively, to either superhydrophobicity or structural superhydrophilicity. To quantify, we compare changes in the transmissivity of the nanotextured surface and a flat silica surface after contaminant fouling using a red laser ($\lambda = 632.8 \text{ nm}$) at normal incidence. The transmissivity measurements are recorded while water droplets are released from a height of 10 mm (corresponding to impact velocity $V \approx 0.44 \text{ m/s}$; $We = 6.9$) from the inclined surfaces (30°) every five seconds. Figure 2-23 shows that the surfaces can be completely cleaned by at most three droplet impacts for three different common particulate contaminants (white sand, lycopodium, and silicon carbide) placed on the nanotextured surfaces, whereas water droplets are ineffective at cleaning the conventional flat glass surfaces due to the hysteretic pinning of residual water droplets. The apparent contact angles ($\theta^* > 160^\circ$) as well as contact angle hysteresis ($CAH < 3^\circ$) of the superhydrophobic nanostructured surface remain unaltered after more than 100 realizations of the self-cleaning tests carried out over a period of greater than 6 months.

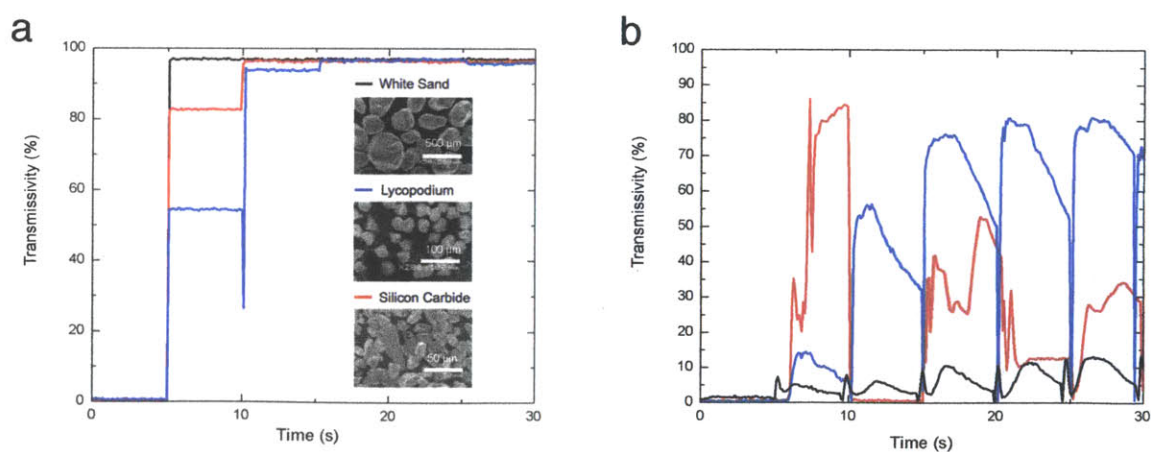


Figure 2-23. Optical transmissivity measurements for quantifying the self-cleaning property of the nanocone surfaces. Evolution of the transmissivity of a red laser ($\lambda = 632.8 \text{ nm}$) through a) surface-contaminated tapered nanocone surface, and b) flat glass surfaces, respectively [45].

As shown in Figure 2-24a, a clear in-focus image of the white letters transmitted through the nanotextured surface also demonstrates qualitatively the antifogging property conferred by structural superhydrophilicity. When viewed through a conventional hydrophilic flat glass surface placed adjacently, the image is much more blurry by comparison. We quantify this difference in Figure 2-24b by measuring the time evolution of transmissivity after exposing the nanotextured and conventional surfaces to a stream of saturated steam and then placing the surfaces (at $t = 5$ s) into the path of the laser beam ($\lambda = 632.8$ nm). Transmissivity through the fogged flat glass slide rapidly drops and then gradually increases to a constant value that still remains lower than that of the tapered nanocone surface. This loss of transmissivity on the flat hydrophilic surface is due to the deposition of microscopic droplets that remain pinned on the surface, as well as intrinsic reflection on the glass slide [90], as also schematically shown in Figure 2-25a. On the other hand, the measurements on the double-sided nanotextured surface shows an immediate recovery of transmissivity to a very high plateau value as a result of rapid imbibition of the thin layer of water followed by a uniform evaporation rate across the entire surface, as schematically shown in Figure 2-25b.

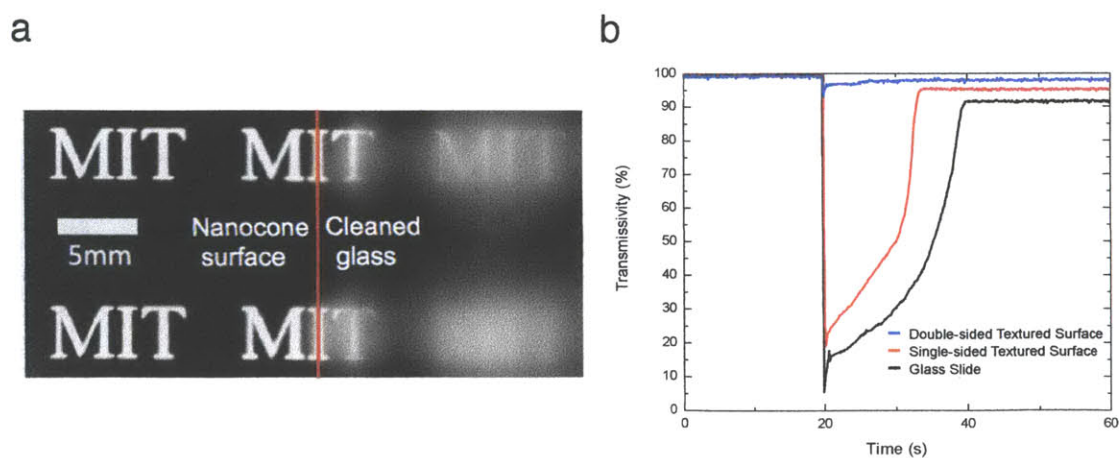


Figure 2-24. Optical transmissivity measurements for quantifying the anti-fogging property of the nanocone surfaces [45]. a) Image of printed letters viewed through fogged nanocone (left) and flat glass (right) surfaces. b) Change of transmissivity due to fogging

and defogging on double-sided nanotaper (blue), single-sided nanotaper (red) and flat cleaned glass (black) surfaces.

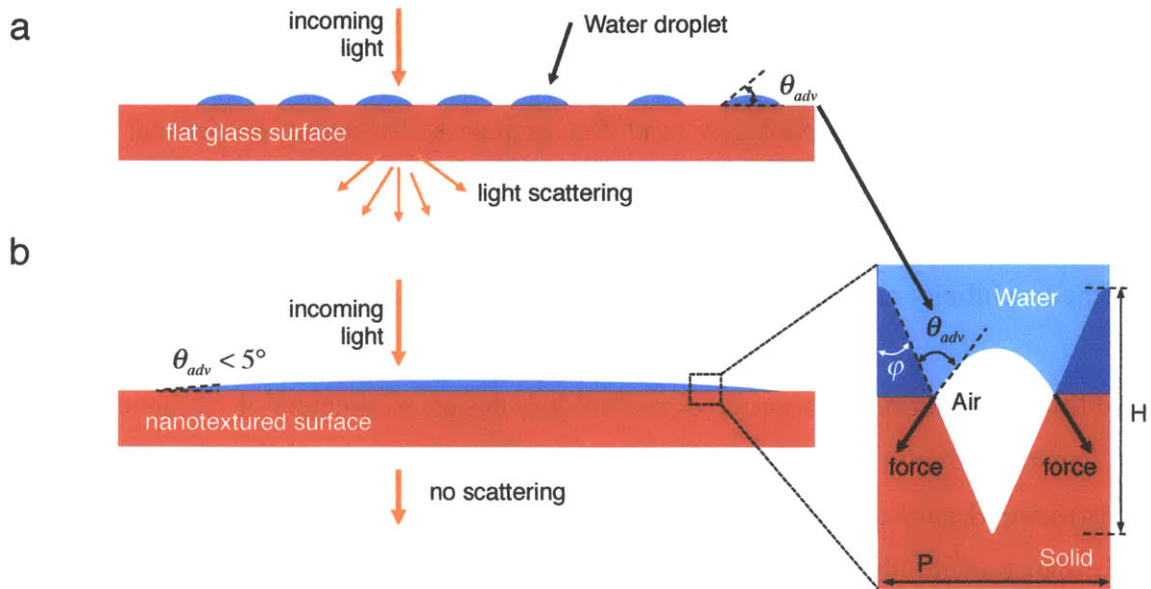


Figure 2-25. Principle of anti-fogging property on the nanotextured silica surface. a) light scattering due to microscopic water droplets on a hydrophilic flat glass surface. b) no light scattering because of rapid imbibition of the thin layer of water on the nanotextured surface. An inset shows the magnified view of the nanotextured surface. When $\theta_{adv} - \phi < 90^\circ$, the net traction force on the liquid–vapor interface is directed downward; thus it promotes the imbibition of the liquid into the solid structure.

2.7 Conclusion

The principal technological development described in this chapter is the design and fabrication of the nanostructured multifunctional material, a nanopatterned silica surface structure consisting of a periodic array of aligned tapered nanocones. This nanostructured surface enables us to simultaneously achieve omnidirectional broadband transmissivity as well as robust superhydrophobicity (and concomitant self-cleaning properties) by virtue of adiabatic impedance matching and promotion of the stable Cassie-Baxter composite surface state, respectively. The nanostructured surface also exhibits the strong structural superhydrophilicity arising from the large Wenzel roughness ($r_w > 1$).

In addition, we define appropriate dimensionless design parameters or ‘figures of merit’ that can objectively quantify the optical and wetting performance of these types of nanostructured surfaces. Using these design parameters (B^* and T^*), we show that the performance of the fabricated surface is superior, relative to what has been published in the literature to date, in terms of optical transmissivity over a bandwidth spanning from the ultraviolet (UV) to the near infrared. We also demonstrate anti-fogging and self-cleaning properties as well as dynamic resistance to high-speed droplet impact (*e.g.*, from a heavy rain).

The achievement of ultra high aspect-ratio nanostructures fabricated in glass (rather than silicon or polymeric substrates) is accomplished using novel fabrication processes, which will be described further in Chapter 3.

Chapter 3

Fabrication of Controllable-Aspect-Ratio Periodic Subwavelength Tapered Periodic Nanocone Structures

3.1 Introduction

Conical tapered nanostructures are known as suitable multifunctional structures that can be optimized for superior optical and wetting properties. The performance of the optical and wetting functions is determined by their geometrical constraints, such as height (H) and period (P), as explained in Chapter 2 [45]. In particular, high aspect-ratio (*i.e.*, the ratio of nanocone height to the base diameter) nanocone structures enable enhanced transmittance and robust superhydrophobicity and superhydrophilicity. For example, the higher the aspect-ratio of nanocone structures the surface has, the less reflectance it exhibits [45, 91]. Depending on the desired performances of specific applications, the aspect-ratio can be optimized.

However, fabricating perfect nanostructured surfaces with desired aspect-ratios remains a difficult engineering challenge due to limitation of existing nanofabrication methods [2, 16, 68, 92]. There have been a few efforts to produce such nanotextured structures with enhanced transmissivity and wetting properties, utilizing techniques such as replication method using polymer and reactive ion etching with colloidal lithography [2, 16, 68, 92]. However, it is difficult to make high aspect-ratio structures with replication, also known as the nanoimprint method [16, 42, 68], because the modulus of those polymers is not strong enough for high aspect-ratio structures to persist from detaching process compared

to crystal materials (*e.g.*, silicon and silicon oxide). Furthermore, colloidal lithography has limited spatial-phase coherence, resulting in non-perfect periodic/quasi-random structures that scatter light [2, 92].

Here, we propose a new fabrication technique to enable controllable-aspect-ratio nanocone fabrication by using a multi-step shrinking mask. By this novel manufacturing process, the multifunctional nanostructured surfaces, introduced in Chapter 2, have been successfully developed for their superior optical and wetting properties such as anti-reflection and superhydrophobicity/hydrophilicity. In addition, instead of using positive photoresist, negative photoresist is utilized to extend the capability of the multiple shrinking mask etching to increase the aspect-ratio up to 7 [93]. Additionally, simple and low cost fabrication methods for aspect-ratios of 2-3 silica nanocone structures have been developed *with* and even *without* the hardmask material that had been considered an essential for fabricating high aspect-ratio structures. These methods can be applied to large-scale, low cost, and high-throughput manufacturing of multifunctional nanostructured surfaces.

In this chapter I will introduce all the fabrication methods developed for controllable-aspect-ratio nanostructures in detail.

3.2 Multiple shrinking mask etching

A novel fabrication method for high aspect-ratio nanocone structures is based on multiple-step plasma etching using shrinking masks to get more flexible choices of materials and thicknesses for better control of the heights and profiles of nanocone structures [45, 54, 93, 94]. Conventional approaches of fabricating nanostructures using reactive ion etching [2, 3, 92] are based on a single hardmask, as represented in Figure 3-1a. Both the thickness of the hardmask (t_1) and the etch selectivity between the hardmask and the substrate would determine the height of the structures. However, this process is limited by the etch rate and thickness of the single hardmask. In other words, the final height is restricted to the material of the hardmask and its thickness, so that the height and profile of the nanocone structures cannot be effectively controlled.

In contrast, Figure 3-1b shows a schematic of the multiple mask etching process. Any desired nanoscale pattern of photoresist can be transferred to the first mask during the first etching process. The first mask is then used as another protective layer (or mask layer) to etch through the second etch mask. Here, the thickness of the hardmask (t_1) and the etch selectivity between the first hardmask and the second hardmask determine the maximum thickness of the second hardmask (t_2). The second hardmask with a thickness of t_2 is utilized as another protective layer to etch the substrate. This final etching process is the same as the final process of the conventional single hardmask etching process shown in Figure 3-1a; however, the major difference (and advantage) of the multiple mask etching is that the thickness of the last mask layer (t_2 in Figure 3-1b) through the multiple mask etching process can be thicker than the maximum thickness of the last mask layer (t_1 in Figure 3-1a) through the conventional etching process by introducing the additional hardmasks and etching processes, which also leads to the reliable fabrication of higher aspect-ratio nanostructures. The height of the structures can be designed and determined by etch selectivity and the thicknesses (t_1 and t_2) of the hardmask materials during the etching processes, which will be discussed later.

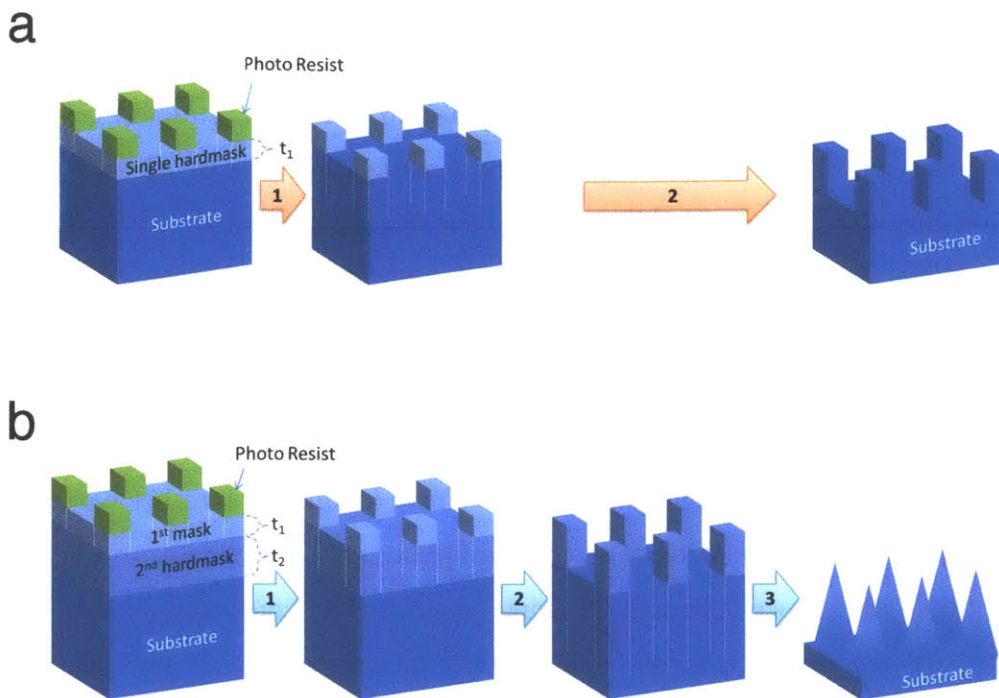


Figure 3-1. a) Schematic of conventional single hardmask etching process. b) Schematic of double-hardmask etching process. The numbered arrows denote reactive ion etching processes [54, 94].

Figure 3-2 illustrates the schematic cross-sections of the shrinking mask etching process, which corresponds to the arrow 3 shown in Figure 3-1b, for tapered nanocone structures. The desired aspect-ratio of nanocone structures results from not only the dimension of the width of the second mask (w_2) but also the thickness of the second mask (t_2). The key feature is utilizing material of the second mask that is etched during the last etching process (arrow 3 in Figure 3-1b), but at a much slower rate than that of a target material (substrate). The underlying layer (purple color) tends to be vertically etched away due to the reactive ion etching process; at the same time the second mask (dark blue) is shrinking. This allows the resulting profile to be tapered. The second mask covers the tip of the nanocone structures to provide a desired slope of nanocone structures, which is the aspect-ratio (H/P), until the moment that the second hardmask is fully removed. The final height (H) of the structure is determined by the etch rates of the materials during the

etching processes and the dimensions of the second hardmask, such as the width (w_2), according to the following equation:

$$H \approx \frac{e_{s_v}}{e_{2_h}} w_2 \quad (3.1)$$

where e_{s_v} is the vertical etch rate of the substrate, e_{2_h} is the horizontal etch rate of the second hardmask, and w_2 is the width of the second hardmask. Eq. 3.1 is valid when the following condition holds,

$$\frac{t_2}{e_{2_v}} > \frac{w_2}{e_{2_h}}, \quad (3.2)$$

where e_{2_v} is the vertical etch rate of the second hardmask and t_2 is the thickness of the second hardmask, because the second hardmask must remain and protect the substrate material until the tapered structure is created. If higher H is desirable, the etch process can also be repeated by using the tapered profile to etch into another material.

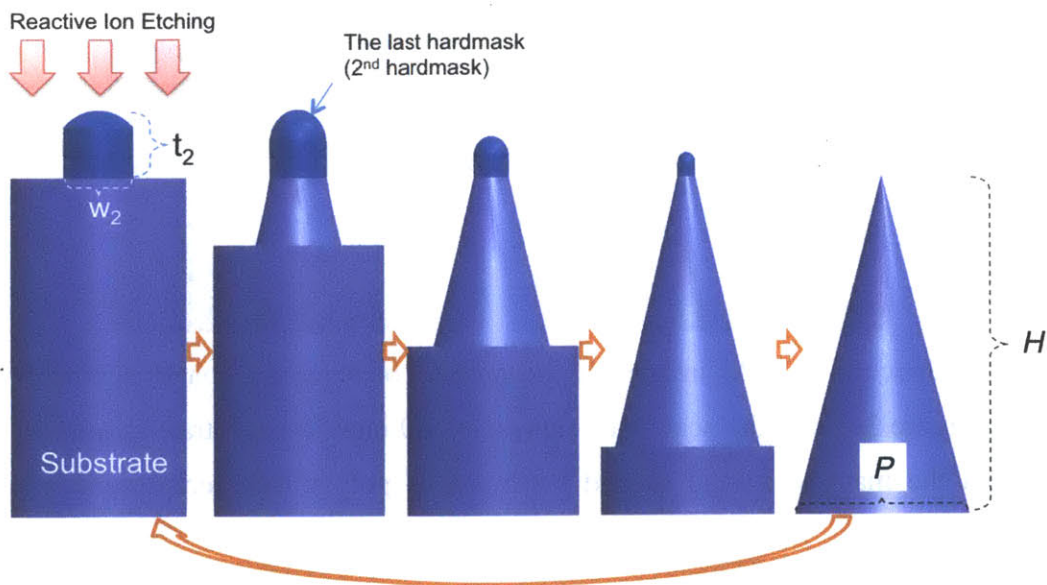


Figure 3-2. Schematic of the shrinking hardmask etching process, which is the equivalent process of arrow 3 presented in Figure 3-1b [54, 94].

Figure 3-3 demonstrates sequential SEM images of the process of shrinking mask etching, as shown in Figure 3-2. The significant benefit of multiple shrinking mask etching is that desired aspect-ratio silica nanocone structures can easily be obtained from successive conventional reactive ion etchings with additional hardmask layers. Note that since all of the processes are done in vacuum, structure collapse associated with surface tension in wet etches is avoided. Although this process is typically based on standard plasma etching, it is also compatible with, and can be adapted to, any lithographic techniques. Using this multiple shrinking mask etching process, the silica nanocones with an aspect-ratio in the range from 4.5 to 7 have been successfully fabricated directly on top of a fused silica wafer, which will be discussed further in the next sections.

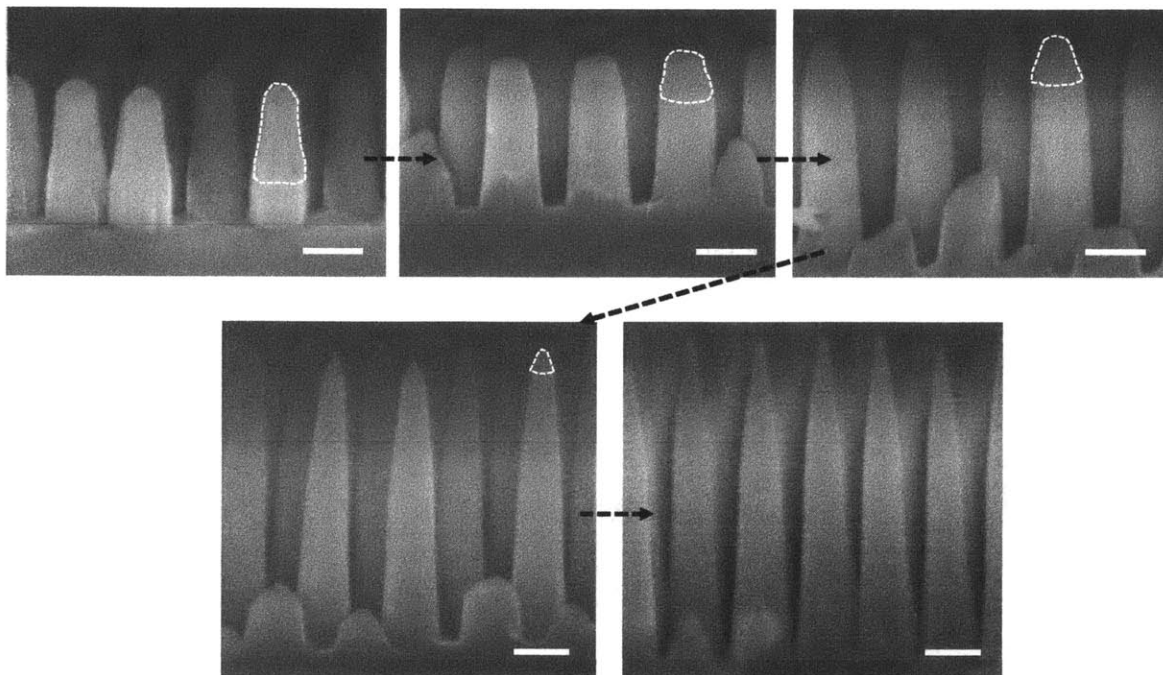


Figure 3-3. Successive SEM images of the process of shrinking mask etching process shown in Figure 3-2. All the scale bars represent 200 nm. The substrate is a fused silica wafer, and the material of the second hardmask is poly-silicon represented by white dotted lines.

3.3 Fabrication of controllable-aspect-ratio subwavelength tapered periodic silica nanocone structures

3.3.1 Fabrication of high aspect-ratio (~ 5) tapered silica nanocone structures

The detailed fabrication steps of high aspect-ratio (~ 5) silica nanocone structures introduced in Chapter 2 [45, 54] are shown in Figure 3-4. The multiple shrinking mask etching explained previously is utilized to enable high aspect-ratio of the nanocone structure. Poly-silicon films are deposited on both sides of a fused silica wafer with a chemical vapor deposition (CVD) technique for realizing high aspect-ratio silica structures, which is the shrinking mask layer and the second hardmask. Hydrogen silsequioxane (HSQ) films are then spun on both sides of the sample and hard-baked at 500 °C for 10 hours to be cured as the first hardmask because the cured HSQ layer acts similarly as a silicon oxide etch mask. To minimize scattering of light, interference lithography (IL) is used for creating the initial subwavelength perfectly periodic patterns. Interference lithography is typically performed with an anti-reflective coating layer deposited below a photoresist layer owing to maximize contrast of the sinusoidal intensity pattern by minimizing the reflection from the interface between the coating and the resist layer. Anti-reflective coating layers (I-con 7, Brewer Science) are spun on the both sides and baked at 180 °C in the oven for 1 hour, and positive photoresist (PFI-88A2, Sumitomo) is spun on one side of the sample, as shown in Figure 3-4a. All the thicknesses of multiple layers are also optimized for laser exposure of interference lithography. The period (P) is set to be 200 nm.

After fabricating a pattern of photoresist posts (200 nm period) with two separate orthogonal exposures of interference lithography (Lloyd's mirror interferometer lithography setup with $\lambda = 325$ nm) followed by development process with CD-26 in Figure 3-4b, it is transferred on the cured HSQ layer by reactive ion etching (O_2 and CHF_3 gas, respectively), and HSQ posts are created, as shown in Figures 3-4c and 3-4d. CHF_3 reactive ion etching is suitable for patterning SiO_2 layer including HSQ [95]. This

array of HSQ posts is the first hardmask layer, which enables creating an array of silicon posts. Using high etch selectivity ($\sim 10:1$) of hydrogen bromide (HBr) reactive ion etching between the poly-silicon and HSQ, the HSQ posts are transferred on the poly-silicon layer; thus the poly-silicon posts are created, as shown in Figure 3-4e. Depending on the thickness of the cured HSQ and HBr etch selectivity of reactive etching process, the height and width of the poly-silicon rods are determined, and even can be controlled. By the optimized reactive ion etching process with CHF_3 gas, a substrate, fused silica, is etched away vertically while the poly-silicon posts keep shrinking and protect silica nanocones. This is the critical feature of multiple shrinking mask etching method, as shown in Figure 3-3. This process keeps etching the fused silica substrate until all the poly-silicon posts disappear, and finally high aspect-ratio silica nanocone structures are formed directly on the fused silica, as also shown in Figures 3-4f. In order to maximize transmissivity through the fused silica, both sides are patterned because transmissivity is limited by Fresnel reflection due to the refractive index mismatch at the flat optical interface.

The multifunctional nanostructured surfaces fabricated by the newly developed multiple shrinking mask etching method exhibit superior optical and wetting properties such as anti-reflection and superhydrophobicity/hydrophilicity, as discussed in Chapter 2.

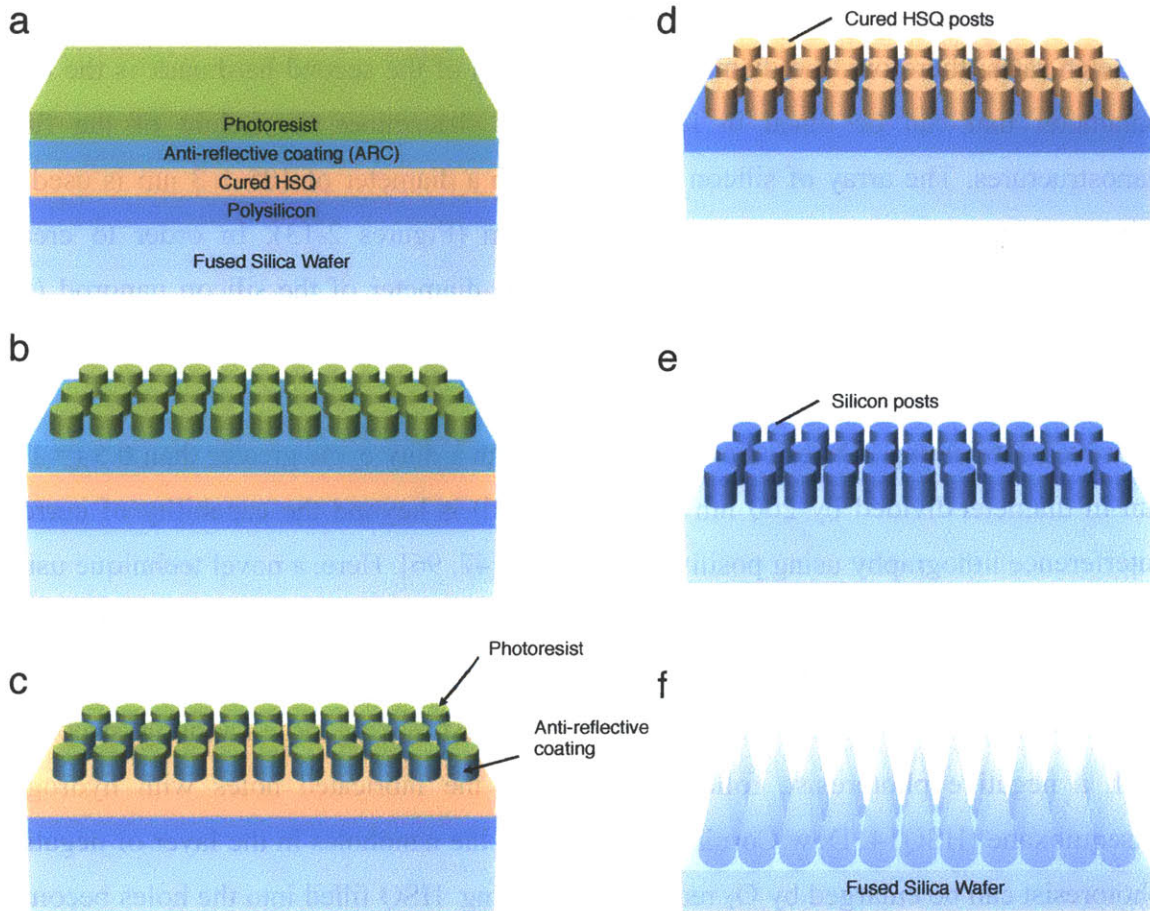


Figure 3-4. a-f) Fabrication steps of subwavelength high aspect-ratio silica nanocone structures. f) Schematic of the fabricated surface by shrinking mask etching (see Figure 3-3). The height and the period of the fabricated nanocone structures are around $1.1\ \mu\text{m}$, and $200\ \text{nm}$, respectively.

3.3.2 Fabrication of ultra high aspect-ratio (> 6) tapered silica nanocone structures

As previously explained in Chapter 2, it is crucial to be able to obtain nanocone structures with high aspect-ratio in order to improve the bandwidth of anti-reflection ($\Delta\lambda = \lambda_{max} - \lambda_{min}$). According to Eq. 3.1, the final height of the nanocone structure is directly proportional to the width (or diameter, in these structures) of the second hardmask structures. Since all the etching conditions, such as pressure and applied voltage, are

chosen to optimize the etch rates of the two different materials, it is challenging to change the etch rates; therefore, the diameter (or the width) of the second hardmask is the only parameter that can be tuned in Eq. 3.1, which determines the height of the final nanostructures. The array of silicon nanorods with a diameter of 105 ± 3 nm is used to fabricate the nanocone with a height of 1.1 μm (Figures 2-13). In order to create nanocones with a height greater than 1.1 μm , the diameter of the silicon nanorod (the second hardmask) must be enlarged.

However, fabricating 2D periodic rod structures with a duty cycle greater than 0.5 (= 100 nm in diameter divided by 200 nm in fixed period) is beyond the capability of current interference lithography using positive photoresist [47, 96]. Here, a novel technique using negative photoresist is developed and utilized to overcome this limitation and make large duty cycle (greater than 0.5) gratings with interference lithography, which leads to ultra high aspect-ratio (> 6) nanocones [93]. The key is first making large nanohole structures with a negative photoresist, followed by filling the fabricated holes with hydrogen silsequioxane (HSQ14, Dow Corning). The size of the nanoholes in the layer of negative photoresist can be enlarged by O_2 reactive ion etching. HSQ filled into the holes becomes an array of HSQ posts with a controllable duty cycle greater than 0.5, which is the first hardmask for etching the silicon layer (the second hardmask). These HSQ posts are transferred to the silicon layer, and the fabricated silicon rod structures become a shrinking hardmask for etching the fused silica wafer. This new approach enables creating 2D rod structures with a duty cycle greater than 0.5 because the duty cycle of the nanorods can be easily controlled by enlarging the diameter of the nanoholes in the negative photoresist layer.

Figure 3-5 illustrates the detailed fabrication process. In this experiment, the incident angle of the laser ($\lambda = 325$ nm) is optimized for the spatial period, which is 200 nm. A multi-layered coating is first created on top of the fused silica wafer. The coating consists of a negative photoresist layer (PS4, Tokyo Ohka), a 20-nm-thick SiO_2 interlayer, an anti-reflective coating layer (ARC, AZ Barli II, Microchemicals), and amorphous silicon. The thickness of each layer is optimized for interference lithography (IL). Two orthogonal

laser exposures are projected onto the photoresist by using a Mach Zehnder interferometer lithography setup, and the exposed photoresist is developed to leave a pattern of holes, as shown in Figure 3-5a. CF_4 and O_2 reactive ion etching processes are then used to transfer the pattern of holes to the SiO_2 interlayer and ARC layer, respectively. After the etching, the array of the nanoholes of the ARC layer is fabricated, as shown in Figure 3-5b. To enlarge the diameter of the nanoholes for a large duty cycle (> 0.5), O_2 reactive ion etching can be further used because the ARC is only laterally etched, while it is not etched vertically, due to the 20-nm-thick SiO_2 interlayer. This process (depicted in Figure 3-5b to 3-5c) is critical for creating large duty cycle nanorods via interference lithography. Hydrogen silsequioxane (HSQ14, Dow Corning) is filled into the fabricated holes, and then baked at 200 °C for 1.5 hours, as shown in Figure 3-5d. The excess layer of HSQ is first removed by CF_4 reactive ion etching. After removal of the remaining ARC layer using CF_4 and O_2 reactive ion etching, only the cured HSQ posts remain, as shown in Figure 5e. The pattern of HSQ posts is transferred to the amorphous silicon layer with hydrogen bromide (HBr) gas reactive ion etching, as shown in Figure 5f. Finally through CHF_3 gas reactive ion etching process, the fused silica substrate is etched away vertically while the silicon posts keep shrinking and protect silica nanocones; consequently, ultra high aspect-ratio silica nanocones are created, as shown in Figure 3-5g.

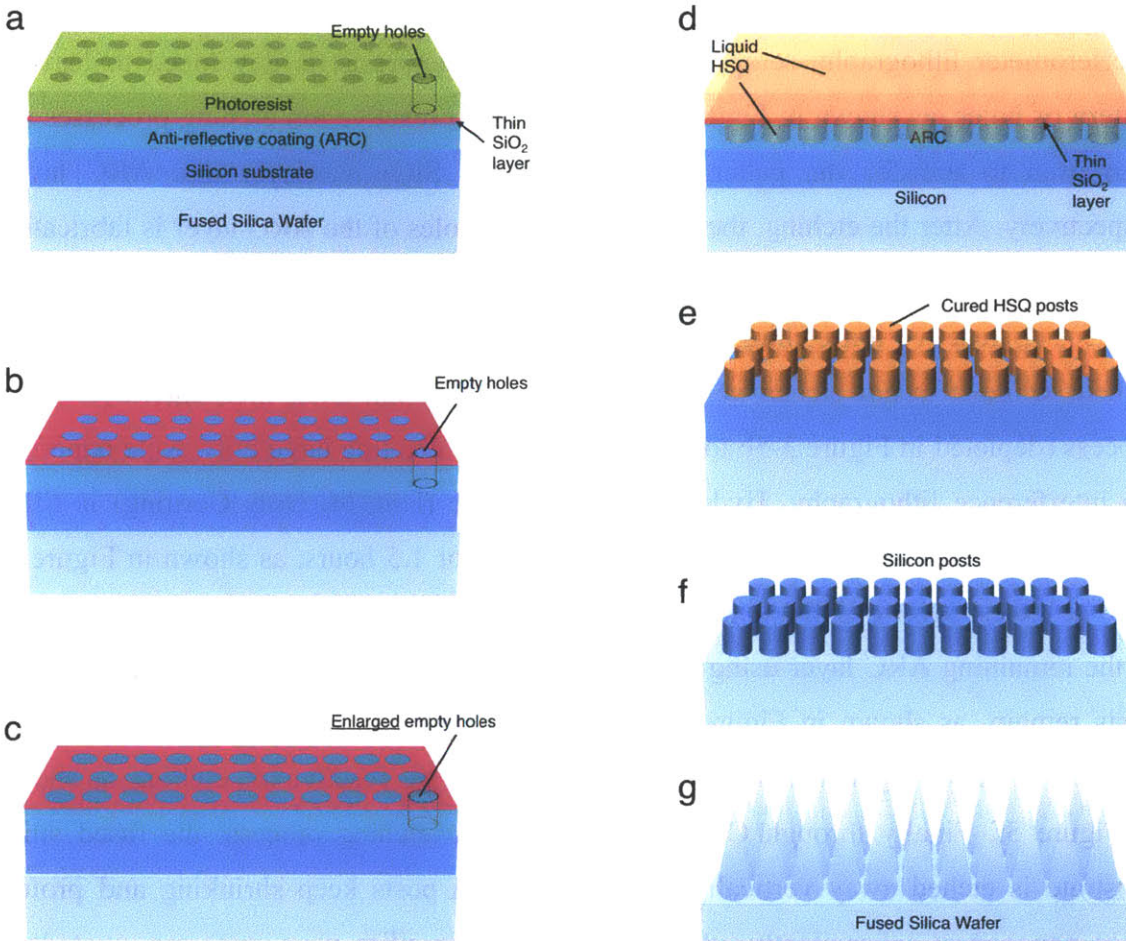


Figure 3-5. Fabrication processes of subwavelength ultra high aspect-ratio (> 6) silica nanocone structures. a) Development of negative photoresist pattern. b) Transferring the nanohole pattern into the anti-reflective coating (ARC) layer through a 20-nm-thick SiO_2 layer. c) Enlargement of the size of the holes through O_2 reactive ion etching (RIE) process. d) Hydrogen silsequioxane (HSQ) filling the enlarged holes. e) HSQ posts. f) Silicon posts. g) Subwavelength periodic silica nanorods with ultra high aspect-ratio (> 6).

Figure 3-6 displays a cross-section scanning electron micrograph of the fabricated surfaces patterned with 200-nm-period subwavelength tapered nanocone structures over $1.4 \mu\text{m}$ tall with sharp tips directly on the fused silica substrate [93]. The silica nanocone structures with an ultra high aspect-ratio of ~ 7 have also been fabricated using the proposed multiple shrinking mask etching process with the help of negative photoresist [93].

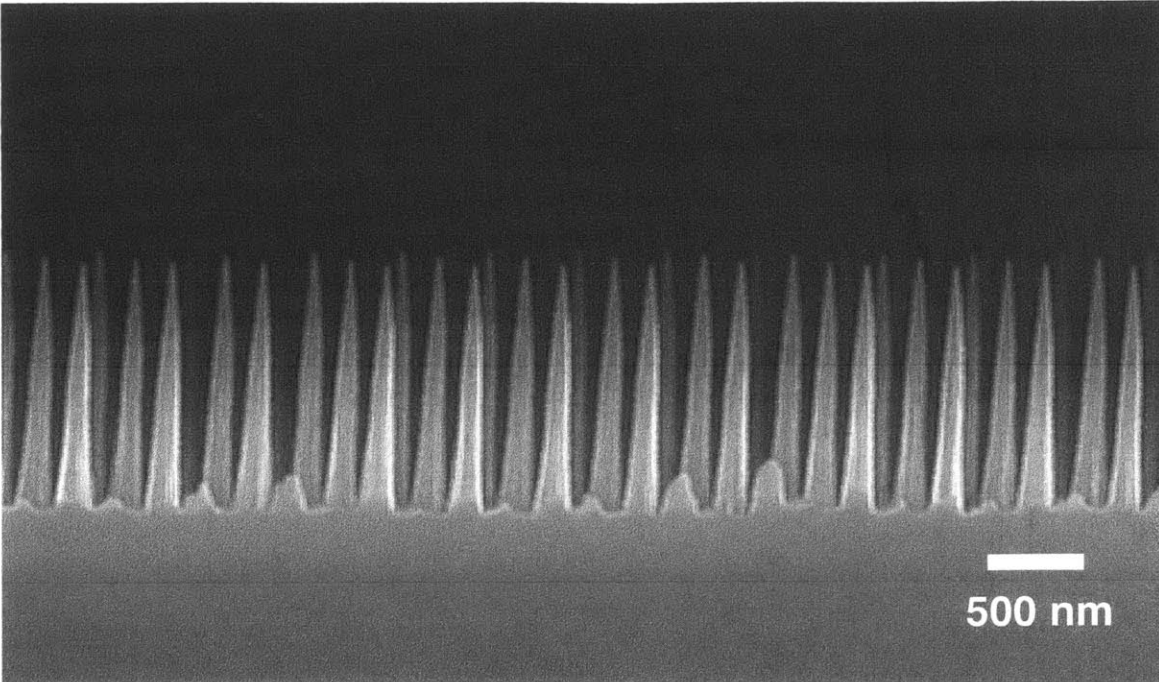


Figure 3-6. Cross-section SEM micrograph of fabricated ultra high aspect-ratio subwavelength nanocone structures [93].

Figure 3-7 shows the height of the fabricated nanocone structures with respect to the width (or diameter) of the silicon nanorods. The experimental results validate that the height linearly increases as the width of the silicon mask nanorod increases (also expected from Eq. 3.1). When the desired height of the nanocone is located under the light blue region in the graph, the multiple shrinking mask etching process with positive photoresist can be utilized. In contrast, the negative photoresist used for the multiple shrinking mask etching is required to achieve the desired structure height in the light red region of the graph. A and B in Figure 3-7 are fabricated by the method described in Section 3.3.1. In contrast, C and D are manufactured by the method described in Section 3.3.2.

Figure 3-8 shows the corresponding cross-section SEM micrographs of the fabricated nanocone structures marked by A, B, C, and D in Figure 3-7.

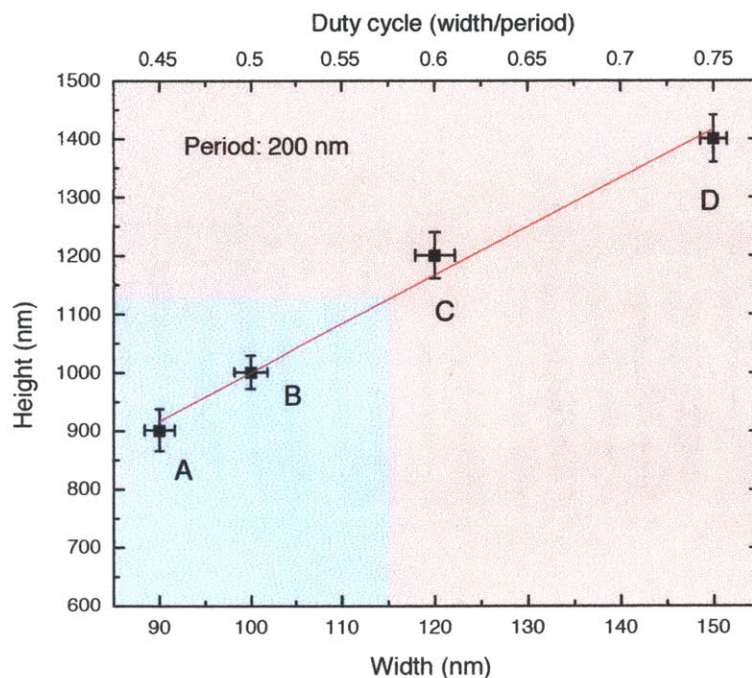


Figure 3-7. Heights of the fabricated nanocone structures with respect to the width (or diameter) of the HSQ nanorods (the first hardmask).

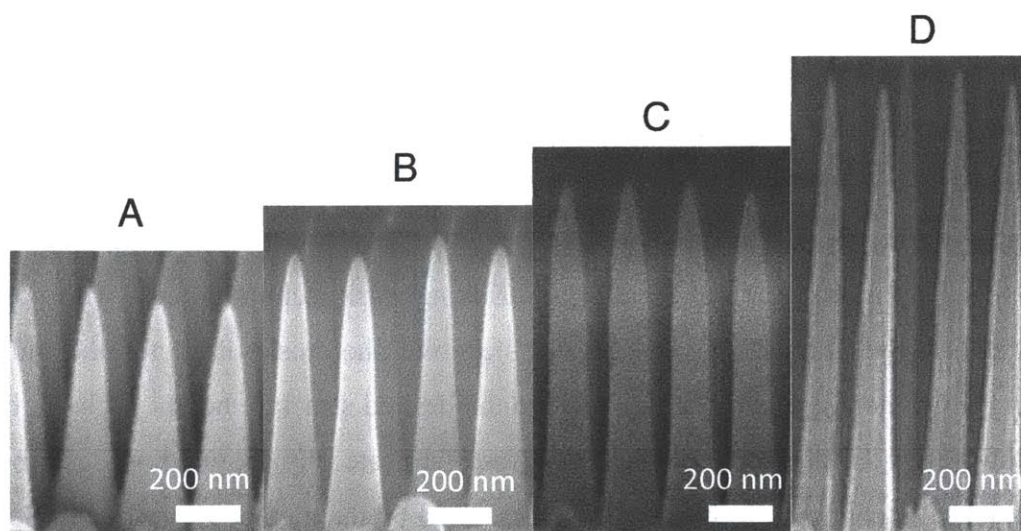


Figure 3-8. Cross-section SEM images of the fabricated silica nanocone structures marked by A, B, C, and D in Figure 3-7.

3.4 Simple and low cost fabrication method of controllable-aspect-ratio silica nanocone structures

3.4.1 Simple and low cost fabrication of medium aspect-ratio (~ 3) tapered silica nanocone structures

By using interference lithography and multiple shrinking mask etching, the desired aspect-ratio (from 4.5 to 7) silica nanocone structures can be created for optimizing the multifunctionality of the fabricated surfaces, as described in Section 3.3. Although controlling the aspect-ratio of the nanostructures by changing the thickness of each hardmask layer and the etch selectivity is easy [45, 93], it requires several uniform hardmask layers on top of a glass substrate and a number of dry etching processes, leading to high cost and long fabrication time. Commercialization of those fabrication methods has also been delayed by the costs of the thin film deposition and reactive ion etching processes. Thus, a new large-scale, low cost, and high-throughput manufacturing process of the multifunctional nanocone surfaces is needed.

Here, we propose a simple and low cost fabrication process for medium aspect-ratio (~ 3) periodic nanocone structures on a fused silica substrate without using a thick silicon layer (thickness > 100 nm) [97]. This fabrication method requires only a 20-nm-thick SiO_2 layer as a hardmask; thus periodic nanocone structures with an aspect-ratio of ~ 3 can be simply and easily manufactured, compared to those with high aspect-ratios of 4.5 to 7 (fabricated through the multiple shrinking mask method that are introduced in Sections 3.3.1 and 3.3.2). This is a trade-off between simplicity of the fabrication process and optical and wetting performance determined by the aspect-ratio of the nanocone; however, the enhanced transmissivity of the silica nanocones with the medium aspect-ratio (~ 3) is still achieved over the visible wavelengths.

The new fabrication process is combined with interference lithography, as depicted in Figure 3-9. A typical interference lithography trilayer is deposited on top of a fused silica

substrate for medium aspect-ratio nanocone structures: an anti-reflective coating (ARC, XHRiC-16, Brewer Science, Inc.) to minimize the reflection of the laser beam ($\lambda = 325$ nm) during exposure, a 20-nm-thick SiO_2 layer for improving the pattern transfer to the ARC layer, and a positive photoresist (PFI-88A2, Sumitomo) where the pattern is initially recorded. Two orthogonal laser ($\lambda = 325$ nm) exposures are projected onto the photoresist by using the Mach Zehnder interferometer lithography setup and the exposed photoresist is developed using CD-26 to leave a periodic pattern of posts. This pattern is transferred to the SiO_2 interlayer and the ARC layer through CF_4 and O_2 reactive ion etching, respectively. Finally, the pattern of ARC posts is transferred to the fused silica wafer while it also shrinks during CHF_3 reactive ion etching. The different etch rate between the ARC and fused silica enables realization of the medium aspect-ratio (~ 3) silica nanocone structures. The ARC posts protected by the thin SiO_2 interlayer play a vital role as the hardmask during CHF_3 reactive ion etching while being etched away as the shrinking mask that creates the tapered silica nanocone structure.

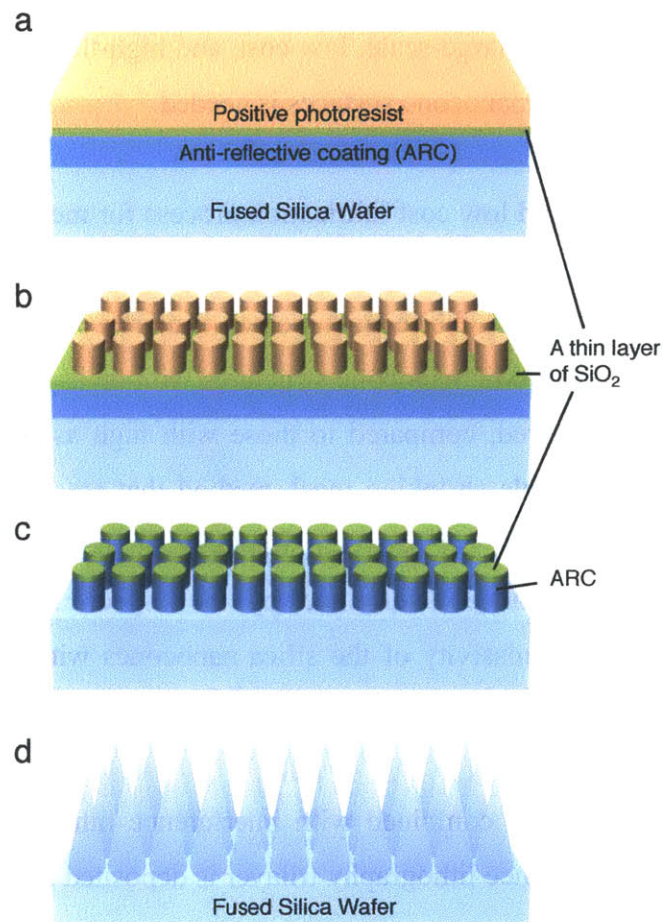


Figure 3-9. Fabrication process of subwavelength medium aspect-ratio (~ 3) silica nanocone structures [97].

A cross-section scanning electron micrograph of the surfaces patterned with 200 nm period tapered nanostructures over 600 ± 10 nm tall with ~ 20 nm radius of curvature at the tips directly on the fused silica substrate is shown in Figure 3-10.

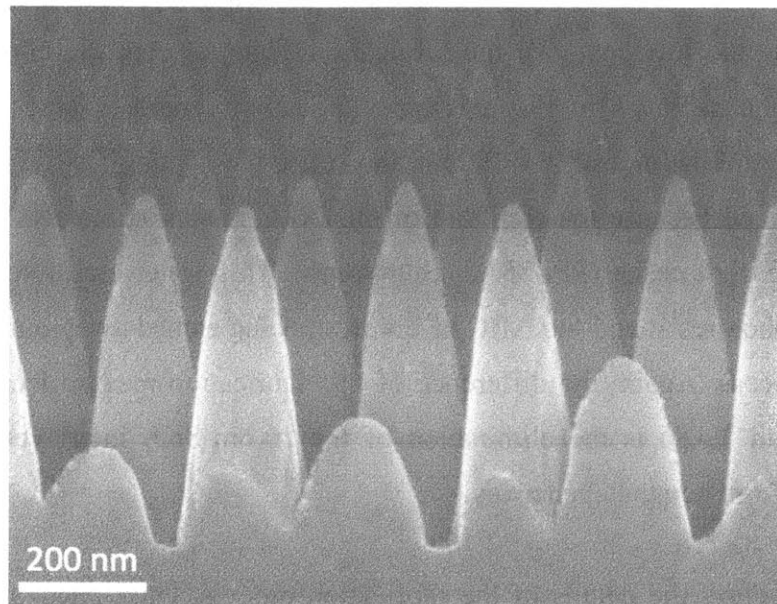


Figure 3-10. Cross-section SEM micrograph of the fabricated silica nanocone structures with an aspect-ratio of ~ 3 [97].

The 20-nm-thick layer of SiO_2 is deposited on top of the anti-reflective coating (ARC) during the fabrication process (demonstrated in Figure 3-9), and this SiO_2 layer improves the etch selectivity between the fused silica (SiO_2) and ARC coating as a hardmask material, which allows successful creation of defect-free medium aspect-ratio (~ 3) nanocone structures.

3.4.2 Hardmask-free fabrication of low aspect-ratio (~ 2) tapered silica nanocone structures

To further enhance the throughput of the fabrication process, a novel fabrication process without using the hardmask layer (the 20-nm-thick layer of SiO₂, shown in Figure 2-4) is developed to create low aspect-ratio (~ 2) tapered nanocone structures on a fused silica substrate. Although nanocones with medium aspect-ratios (> 2) cannot be fabricated without a hardmask, this fabrication process does not require reactive ion etching and deposition processes for hardmask materials; consequently, this leads to reduced fabrication time and low cost. All the fabrication details except the elimination of the hardmask are the same as in the previous fabrication processes (see Section 3.4.1). Instead of using the hardmask, a different anti-reflective coating (ARC, I-con7, Brewer Science) is utilized because the etch rate of this ARC is approximately 1.4 times faster than that of the photoresist (PFI-88A2, Sumitomo). This faster etch rate of ARC layer prevents both photoresist and the ARC layers from being etched away during O₂ reactive ion etching process. Again, the difference of this fabrication method from the previous one (see Section 3.4.1) is the elimination of the 20-nm-SiO₂ interlayer that perfectly prevents ARC from being etched away.

Figure 3-11 displays the details of the fabrication process. Only ARC and the positive photoresist layers are deposited on top of a fused silica substrate. Two orthogonal laser ($\lambda = 325$ nm) exposures are projected onto the photoresist by using a Lloyd's mirror interferometer lithography setup, and the exposed photoresist is developed to leave a periodic pattern of posts. This pattern is transferred directly to the ARC layer with O₂ reactive ion etching. Finally, the pattern of ARC posts is transferred to the fused silica wafer while it shrinks during CHF₃ reactive ion etching due to the different etch rates between ARC and fused silica that creates the low aspect-ratio (~ 2) nanocone structures.

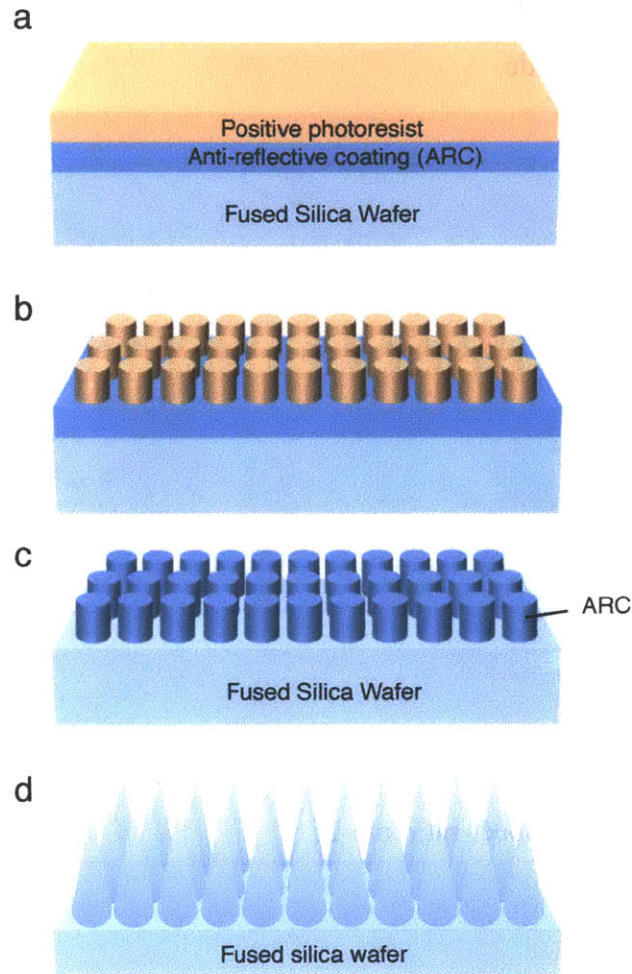


Figure 3-11. Fabrication process of subwavelength low aspect-ratio (~ 2) silica nanocone structures.

Figure 3-12 shows a cross-section scanning electron micrograph of the surfaces patterned with 200 nm periodic tapered nanostructures over 400 ± 25 nm tall with ~ 30 nm radius of curvature directly on a fused silica substrate. The heights of the nanocone structures have some variation since no hardmask material is used for creating the nanocones. The ARC and photoresist are only used as the mask layer to create the silica nanocone structures; thus the height of the nanocone is less than those of the structures fabricated with the help of the single hardmask or multiple hardmasks described in the previous sections. However, the fabrication process requires no toxic gas during the reactive ion

etching process and no deposition of the typical hardmask materials such as silicon, silicon oxide, and silicon nitride.

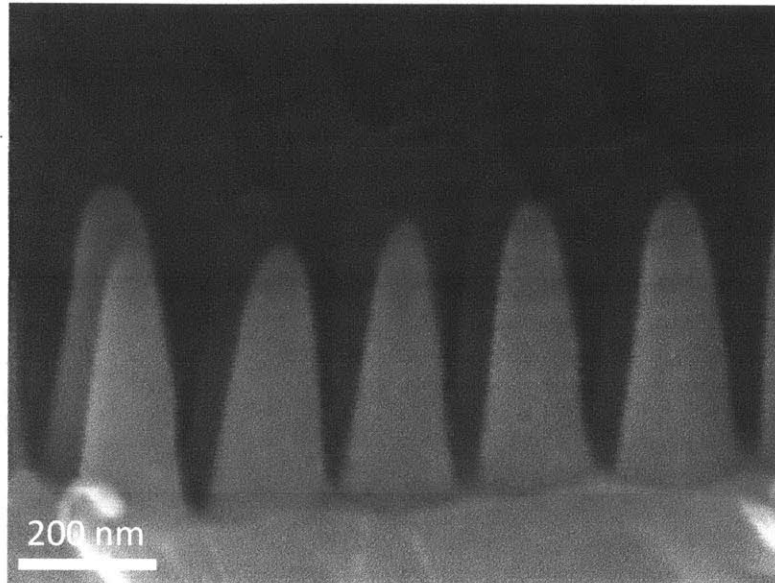


Figure 3-12. Cross-section scanning electron micrograph of the fabricated silica nanocone structures with an aspect-ratio of ~ 2 .

3.4.3 Optical properties

The transmissivity measurements through i) the double-sided patterned surface and ii) single-sided patterned surface (both fabricated with the help of the hardmask that is the 20-nm-thick SiO_2 described in Section 3.4.1), iii) single-sided patterned surface fabricated without the hardmask (demonstrated in Section 3.4.2), and iv) a flat fused silica wafer are carried out over a broad range of visible wavelengths ($400 \text{ nm} \leq \lambda \leq 800 \text{ nm}$) at normal incident angle, as shown in Figure 3-13. The i) red and ii) blue curves represent the transmissivity of the fabricated surfaces with the help of the 20-nm-thick SiO_2 layer during the RIE process. The iii) green curve shows the transmissivity of the single-sided nanostructured surface fabricated without the hardmask (shown in Figure 3-12). As seen in Figure 3-13, the measurements of the three nanostructured surfaces exhibit enhanced transmissivity (or anti-reflectivity), compared to that of the flat fused

silica surface. The transmissivity of i) the double-sided patterned silica surface increases up to 99.12%, and the averaged transmissivity is also greater than that of the single-sided patterned surfaces or the flat fused silica surface. The transmissivity of the two single-sided nanocone surfaces (represented by blue and green curves) is limited by Fresnel reflection arising from the step discontinuity in refractive index at the flat rear surfaces.

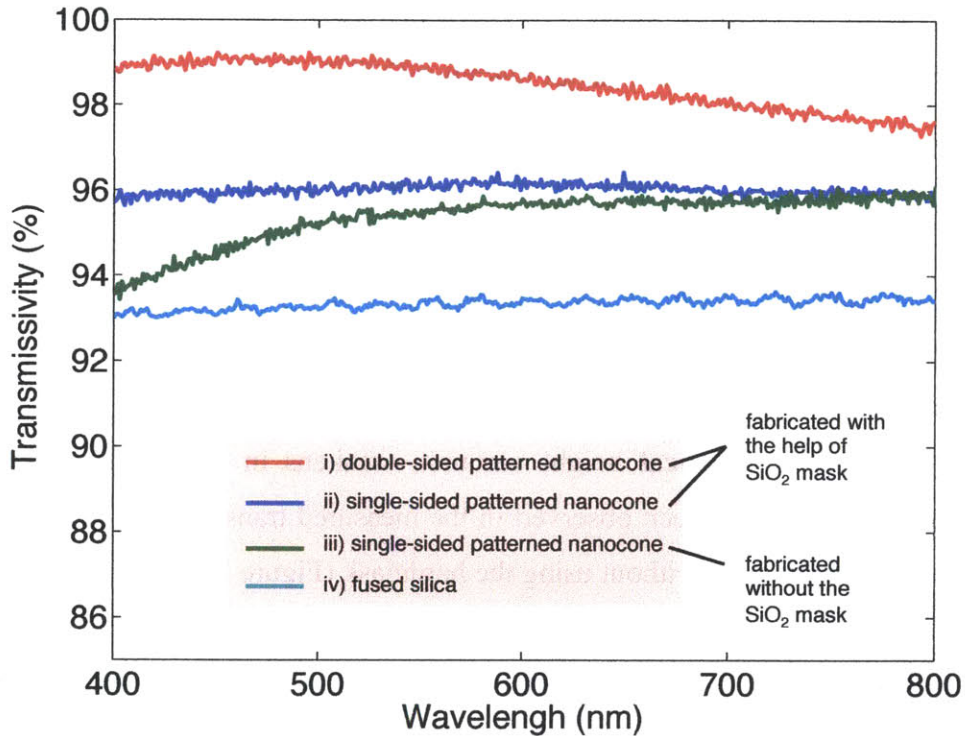


Figure 3-13. Measured optical transmissivity of the nanotaper structures as a function of the wavelength at normal incident angle. i) Double-sided patterned and ii) Single-sided patterned surfaces fabricated with the help of the hardmask (20-nm-thick SiO₂) described in Section 3.4.1. iii) Single-sided patterned surface fabricated without the hardmask. iv) Flat fused silica wafer.

The transmissivity value of the single-sided patterned surface *without* the hardmask (green curve) decreases as the wavelength decreases, while that of the single-sided patterned surface *with* the hardmask (blue curve) shows no change in transmissivity. All the periods of the fabricated silica structures are 200 nm; however, the height of the

single-sided patterned surface fabricated *without* the hardmask (green curve) is around 400 ± 25 nm, which is approximately 200 nm less than that of the single-sided patterned surface fabricated *with* the hardmask (blue curve). As discussed in Section 2.3, the optical transmissivity behavior of the periodic nanocone structure is governed by geometrical constraints such as the structure height H and period P . The height of the nanocone only determines the upper wavelength limit λ_{max} , and the upper wavelength limits of these nanocone structures with heights of 400 ± 25 nm are greater than 1 μm . This shows the transmissivity drop is not related to smaller heights, but to the defects and variation of the heights.

Lehr *et al.* simulated the influence of the imperfection of the subwavelength grating structures on the transmittance of an anti-reflective structure, such as a statistical height variation [17, 98]. They concluded that the transmittance losses due to scattering effects become dominant, and anti-reflective behavior of the subwavelength periodic tapered nanostructures having a statistical height variation weakens in the short wavelength region [17, 98]. This has also been observed in the measured transmissivity of the silica nanocone structures fabricated without using the hardmask (Figure 3-12).

The transmissivity drop in the small wavelength range, therefore, is due to the defects introduced in the fabrication process and the large variation of the heights. As shown in Figure 3-11, the positive photoresist and ARC layer are only the material that protects the tip of the nanocone structures for a desired slope of nanocone structures, until the moment that they are fully removed. If there are a few nanometer variations in diameters or heights of the developed photoresist nanorod structures, which can be easily introduced during the interference lithography and development process, those errors are easily transferred to the silica nanocone structures. Figure 3-14 shows a cross-section SEM micrograph of the positive photoresist nanorods after the development (also corresponding to the schematic of Figure 3-11b), and there are a few nanometers' differences in their rods' geometries, such as heights and diameters ($\alpha \neq \beta$). These variations are hardly seen in the silica nanocone structures fabricated with the help of the hardmasks because these errors become negligible due to the presence of hardmask that

typically has high etch selectivity to ARC and photoresist materials. These engineering drawbacks can result in non-perfect periodic/quasi-random structures, and scatter incoming light [17, 98]. Regardless of these defects, this newly developed fabrication process without using the hardmask demonstrates enhanced optical transmissivity (or anti-reflectivity) with other benefits, such as ease of fabrication, reduced fabrication time, and low cost.

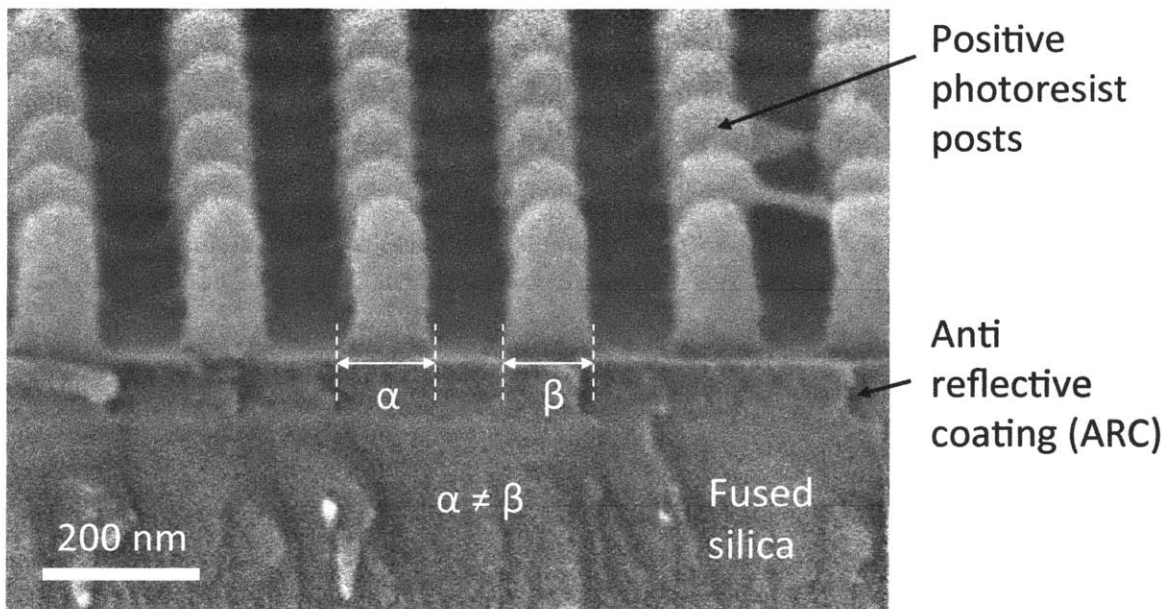


Figure 3-14. SEM image of the subwavelength positive photoresist (PFi88-A2) post structures after development process depicted in Figure 3-11b.

3.5 Conclusion

By developing a novel multiple shrinking mask etching process, we have demonstrated that subwavelength tapered conical structures with high aspect-ratio (~ 5) enhance transparency across a broad spectrum of visible wavelength and change surface wettability from superhydrophobicity to superhydrophilicity. The height of the nanocone structures, which is the key parameter of control of optical and wetting properties, can be effectively controlled by tuning the diameter of the nanorods used for the hardmask during the dry etching process. In addition, simple and low cost fabrication methods for medium and low aspect-ratios of 2 to 3 silica nanocone structures have even been developed with and without the hardmask material, which can be applied to large-scale and high-throughput manufacturing of multifunctional nanostructured materials.

Chapter 4

Transparent Anti-fingerprint Surfaces

4.1 Introduction

Undesired fingerprint oils (sebum) deposited on transparent surfaces such as the touchscreens of mobile phones and glass displays significantly lower optical transmissivity, hamper visibility, and contaminate flat clean surfaces with dirt and bacteria. As shown in Figure 4-1, the micrometric pattern of a fingerprint results in reflection and scattering of incident light, and contaminants can easily adhere to the oil-wetted surfaces [99-104]. Fingerprint oils are secreted from sebaceous glands located on top of the friction ridges that cover the tips of human fingers. The deposited print is predominantly water, but also contains a mixture of organic chemicals such as urea, uric acid, amino acid, ammonia, lipids, glucose and lactic acid resulting in an oily liquid with surface tension $23 < \gamma_{LV} < 60$ mN/m [99, 100, 105, 106].

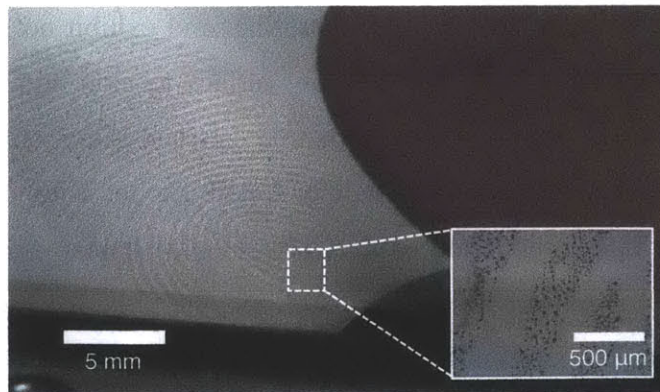


Figure 4-1. Image of fingerprint oils deposited on a touchscreen display (iPhone 4S). The inset shows a magnified view of the fingerprint oils, which reveals micrometric liquid droplets.

There have been several attempts to prevent formation of these fingerprints (*i.e.*, *dactylograms*) on transparent materials, such as glass and polymer, by employing oil-repellent textured surfaces. In recent years, transparent superoleophobic surfaces (*i.e.*, oil-repellent textured surfaces) with “re-entrant” structures have been developed by using deposition of candle soot with a thin silicon dioxide layer, followed by subsequent thermal heat treatment and application of suitable chemical coatings [107] or through polymer micromolding methods [108].

Inspired by the oil repellency mechanism with re-entrant structures, we also have attempted to develop robust superoleophobic and super-transmissive silica surfaces with a square array of subwavelength silica nanocones [45] coated uniformly with nanoparticles. This transparent superoleophobic surface has been developed in order to extend the beneficial functions of the superhydrophobic silica surfaces discussed in Chapter 2 to repellency of fingerprint oils. The subwavelength periodic silica nanocones [45] are chosen to suppress optical reflection, and the coated silica nanoparticles prepared by Layer-by-Layer (LbL) assembly [57, 109, 110] form the silica re-entrant nanostructures for superoleophobicity.

However, these textured superoleophobic coatings with the re-entrant structures reduce transmissivity of visible light due to light scattering, and exhibit no superoleophobicity that promotes the super-repellent state with low surface tension liquids. Moreover, it is discovered that the intrinsic thermodynamic metastability of the composite superoleophobic state (*i.e.*, a non-wetted state or Cassie-Baxter state) can result in failure of the oil repellency under moderate contact pressures of human fingers [60, 72, 111-114]. Susceptibility to mechanical damage also limits the utility of such microstructured coatings for preventing fingerprint deposition in practical applications [60, 72, 107, 108, 111-114]. The experimental results and their limitations will also be introduced in Section 4.2.

Here, we develop and quantitatively characterize transparent fingerprint-eating (or *dactylovorous*) surfaces. In contrast to previous studies that have targeted an oil

repellency mechanism, we have taken the counter-intuitive approach of constructing our surfaces from *oleophilic* material, titanium dioxide (TiO_2). In this chapter, design, fabrication, and characterization of the transparent fingerprint-eating surfaces, which are optimized for optical transparency and anti-fingerprint properties, are discussed in detail.

4.2 Transparent superoleophobic surfaces with periodic silica nanocone structures coated with nanoparticles and their limitations

A major challenge in surface engineering is the creation of transparent surfaces that repel low surface tension liquids, such as fingerprint oils. In recent years, transparent superoleophobic surfaces have been developed by several methods [107, 108, 115]; however, it is challenging to maintain optical transparency in the visible wavelength range and resistance to wetting by low surface tension liquids due to scattering of light and wetting failure of the superoleophobic state by external perturbations such as human finger touches, vibrations, and high-velocity droplet impact. Fractal-like soot structures deposited on glass surfaces [107] and micro-molded structures [108, 115] can induce optical scattering that results in haze and low transmissivity.

In this section, I will discuss the initially proposed re-entrant subwavelength nanocone structures for enhanced transparency and superoleophobicity, which can be used for anti-fingerprint surfaces, and their limitations. The re-entrant texture is first created using a square array of silica nanocones coated uniformly with nanoparticles, as shown in Figure 4-2. In Figure 4-2c, the uniformly deposited nanoparticles (red spheres) on top of the fabricated silica nanocones create re-entrant structures that can support a pressure difference across the air-liquid interface. To overcome low transmissivity of the existing work, the nanocone structure is used to minimize optical reflection losses over a broad range of wavelengths and a wide range of angles of incidence due to adiabatic impedance matching between the air and the glass, as discussed in Chapter 2. The feature size of the nanoparticle is much smaller than the wavelength of visible light; thus haze and light scattering can be minimized [18].

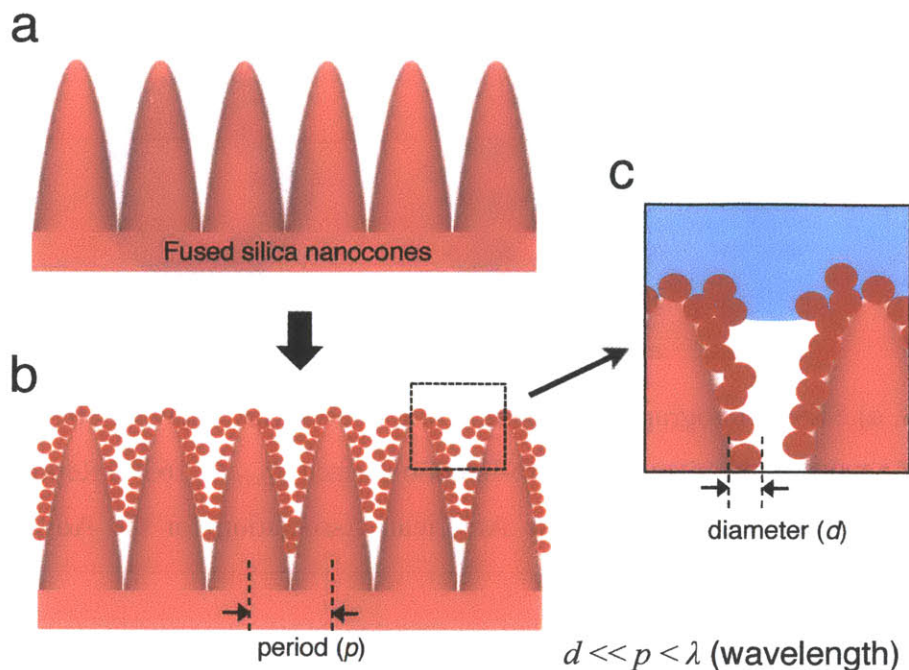


Figure 4-2. Schematic of the square array of silica nanocones coated uniformly with nanoparticles.

4.2.1 Re-entrant structures for superoleophobic surfaces

What are the “re-entrant structures” and why do we need them? Superhydrophobic surfaces have been developed for years by creating roughness on the surfaces with the help of surface chemistry, which shows water contact angles greater than 150° with low contact angle hysteresis [60, 116]. They repel high surface tension liquids such as water, but not low surface tension liquids such as oils. This limitation has generated extensive academic and industrial interest in oil-repellent surfaces, and Tuteja *et al.* first developed superoleophobic (or omniphobic) surfaces by patterning “re-entrant structures” on a silicon surface combined with surface chemistry, as shown Figure 4-3 [113]. These designed microtextured surfaces exhibit resistance to wetting from low surface tension liquids, including alkanes such as decane and octane.

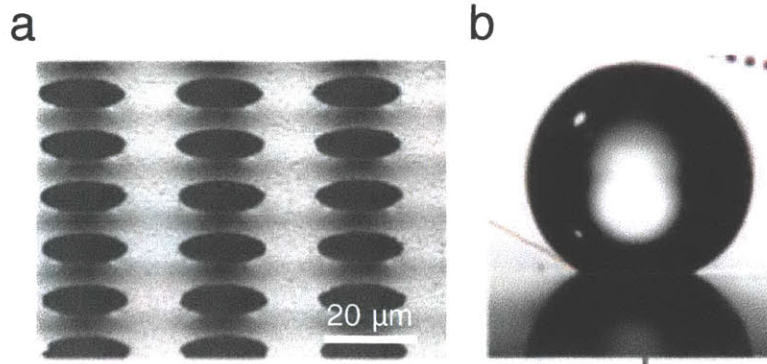


Figure 4-3. a) SEM micrographs for the micro-hoodoo surfaces having circular flat caps. b) Drop of octane on the silanized micro-hoodoo surface ($\theta_{adv} \approx 163^\circ$). Reproduced from Ref. [113] with permission from The American Association for the Advancement of Science.

The main idea of the re-entrant structures is to change the direction of the net surface traction of the three-phase (air-liquid-vapor) contact line on the textured structure upward, and support a pressure difference across the air-liquid interface [71, 72, 113]. Figure 4-4 schematically shows the concept of the re-entrant structures [71, 72]. The equilibrium angle (θ_E) is determined by Young's equation (also discussed in Chapter 1), and ψ represents the local texture angle. The liquid is light blue, and air is white. The dark blue surface is wetted, while the red surface is nonwetted. The arrows marked "F" represent the traction forces (*i.e.*, surface tensions of the liquid) at the air-liquid-vapor interface. When an equilibrium angle (θ_E) is smaller than the local texture angle (ψ), the net traction force on the liquid-vapor interface is directed downward; thus it promotes the imbibition of the liquid into the solid structure, leading to a fully wetted interface, as shown in Figure 4-4a [71, 72]. In contrast, when the equilibrium angle (θ_E) is greater than the local texture angle (ψ), the net traction force is pointing upward; this net force maintains non-wetted state (*i.e.*, a Cassie-Baxter state) by supporting a pressure difference on the air-liquid interface, as shown in Figure 4-4b [71].

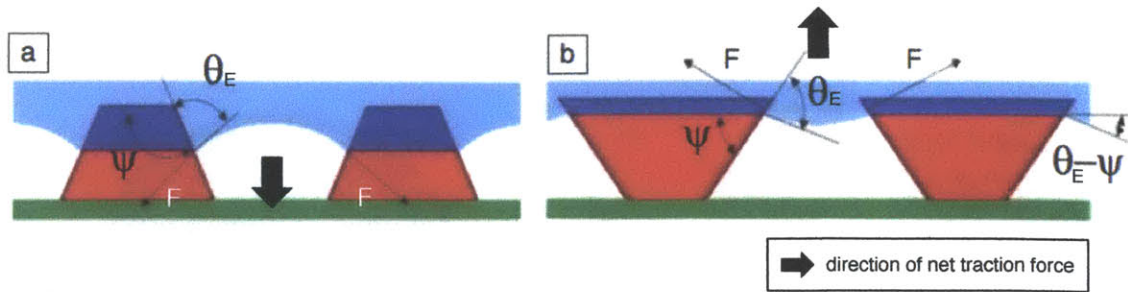


Figure 4-4. Schematic diagrams illustrating the expected liquid–vapor interface on two idealized surfaces with different values of the equilibrium contact angle (θ_E). Reproduced from Ref. [71] with permission from Materials Research Society.

Most superhydrophobic surfaces demonstrate superhydrophobicity with the local texture angle (ψ) greater than 90° [71, 72]. However, the maximum equilibrium angle (θ_E) of low surface tension liquids such as oil is still smaller than 90° [71]. To develop superoleophobic surfaces, structures with the local texture angle (ψ) smaller than 90° are required, and these structures are called re-entrant structures, as shown in Figure 4-4b. Recently, Deng *et al.* have demonstrated transparent and oil-repelling superamphiphobic coatings fabricated with a porous deposit of 25-nanometer-thick silica shells, as shown in Figure 4-5 [107]. Randomly deposited 25-nanometer-thick silica shells with an average diameter of 100 nm are utilized to create the re-entrant nanostructures with the local texture angle (ψ) smaller than 90° , which enables robust superoleophobicity.

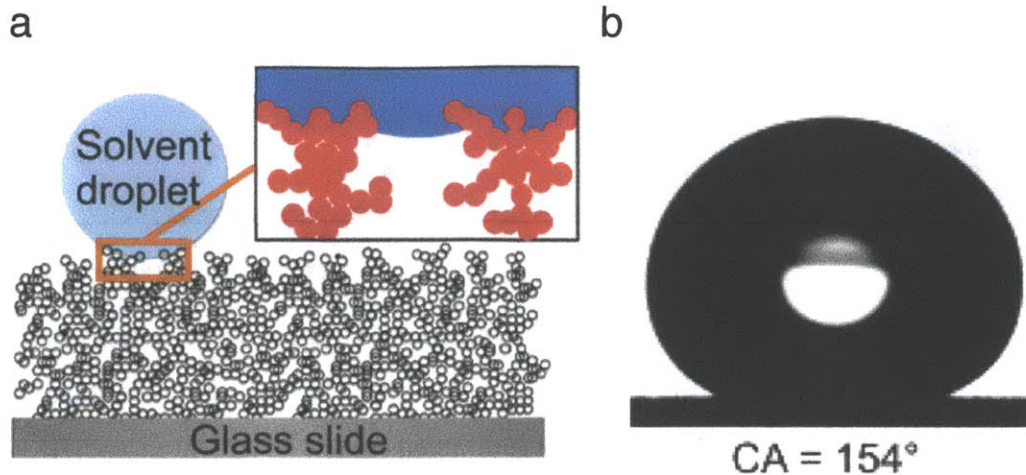


Figure 4-5 a) Schematic of a liquid drop deposited on the fractal-like composite interface made of 25-nanometer-thick silica shells. b) Drop of hexadecane deposited on the surface with a static contact angle of $156 \pm 1^\circ$. Reproduced from Ref. [107] with permission from The American Association for the Advancement of Science.

4.2.2 Fabrication process and initial results

To fabricate the proposed nanostructured surfaces, we combine top-down and bottom-up fabrication processes: interference lithography and multiple shrinking mask etching to pattern the primary nanocone structure [45]; and Layer-by-Layer (LbL) assembly [57, 109, 110, 117, 118] to add the secondary structure that consists of a nanoparticle coating that gives rise to re-entrant textures. Figure 4-6 is a schematic illustration of the fabrication process for the proposed transparent superoleophobic surfaces. The silica nanocone fabrication method has been described in Chapter 2, and LbL assembly process was introduced in Chapter 1. The resulting encrusted structures are calcinated and then coated with a low-energy chemical coating (see Section 2.5) [86]. LbL assembly provides uniform deposition of nanoparticles and precise control of thickness via the number of assembly steps. LbL assembly and the details of the fabrication process will be discussed further in the next sections because this LbL assembly is the main fabrication process of the transparent anti-fingerprint surfaces based on titania-based porous nanoparticle coatings.

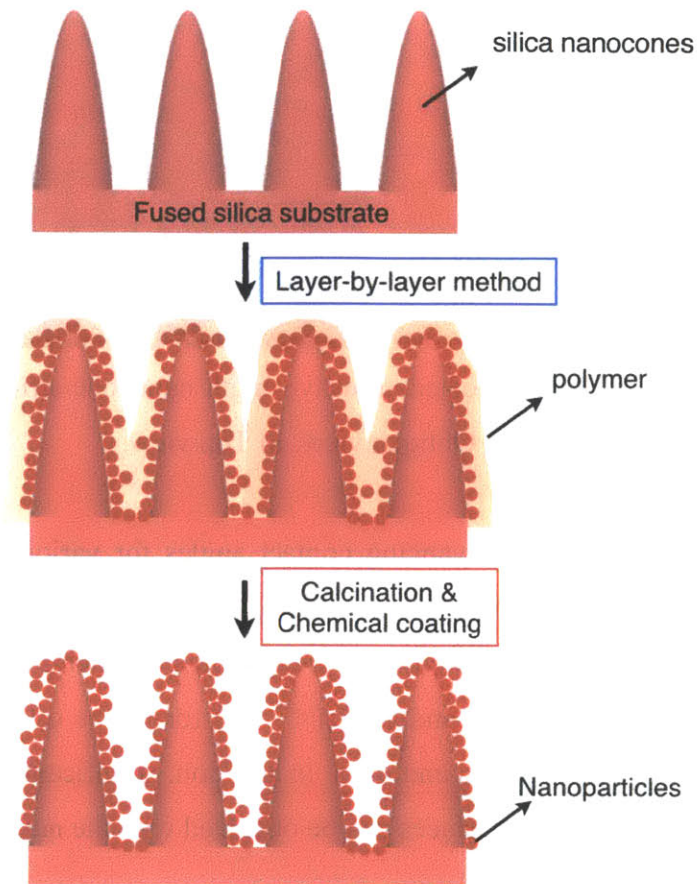


Figure 4-6. Schematic illustration of the fabrication process for the transparent superoleophobic surfaces.

SEM images of the fabricated surfaces through 4 dipping cycles of LbL assembly process are shown in Figure 4-7. The silica nanoparticles with a diameter of 20 ± 5 nm (Svaya Inc.) are uniformly deposited on top of the silica nanocones. The images show the presence of re-entrant structures created by the silica nanoparticles.

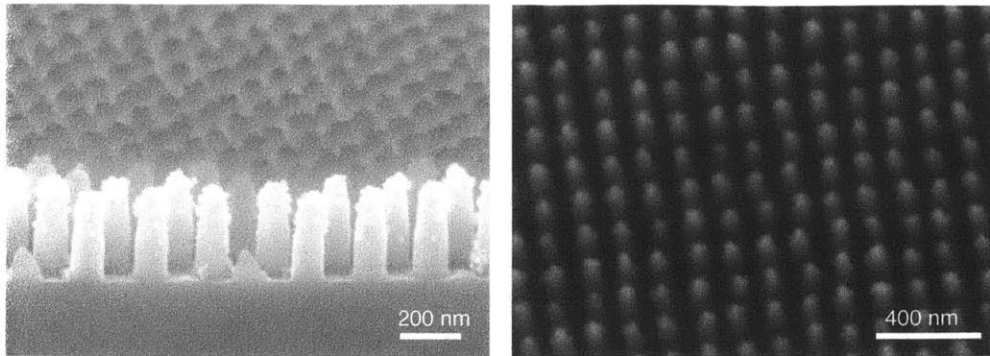


Figure 4-7. SEM images of the fabricated subwavelength nanocone structures encrusted with LbL-deposited nanoparticles. a) Oblique view. b) Top view.

Figure 4-8 displays the measured advancing contact angles for various liquids (water, DMSO, jojoba oil, and hexadecane) on the fabricated surfaces. The interesting result is that the fabricated surfaces do not exhibit superoleophobicity, which is demonstrated by the advancing contact angles of 127° and 121° ($< 150^\circ$) for jojoba oil and hexadecane, respectively, as shown in Figures 4-8c and 4-8d. In addition, significant optical haze and light scattering from the fabricated surfaces can be observed with the naked eye.

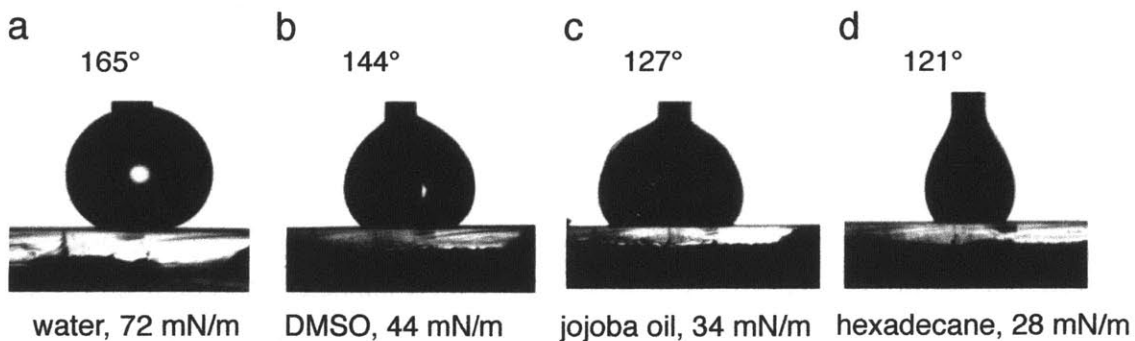


Figure 4-8. Images of drops of a) Water, b) DMSO, c) Jojoba oil, and d) Hexadecane on the surfaces with the corresponding advancing contact angles.

Figure 4-9 shows an SEM image of the area with structural defects of the fabricated surfaces. This image displays the undesired aggregation (Figure 4-9a) and defective surface areas without the nanocones that break the periodicity of the nanostructured surface (Figure 4-9b). These randomly deposited nanoparticles due to aggregation shown

in Figure 4-9a trigger undesired scattering of light and destroy the re-entrant structures constructed with the silica nanocones coated with the nanoparticles. DeRocher *et al.* have also observed the non-uniform deposition of the nanoparticles, and formation of large aggregates during LbL assembly in high aspect-ratio nanochannels, and they found these occur because of surface charge-induced electrostatic depletion of the depositing species [119]. Our work is also based on high aspect-ratio nanocone structures that are likely to result in aggregation and bridging of the nanocones.

The defective surface area without the nanocones shown in Figure 4-9b makes a larger spacing with the neighboring structures than the period of the nanocone structures ($P \approx 200$ nm). This phenomenon is also schematically depicted in Figure 4-10. The enlarged spacing due to the defects causes lowering the meniscus of low surface tension liquid; thus it weakens the robustness of superoleophobicity (or the breakthrough pressure) [71, 72]. Small perturbations, such as vibrations and impacts, can cause the Cassie-to-Wenzel transition of low surface tension liquid that will be discussed in the next section.

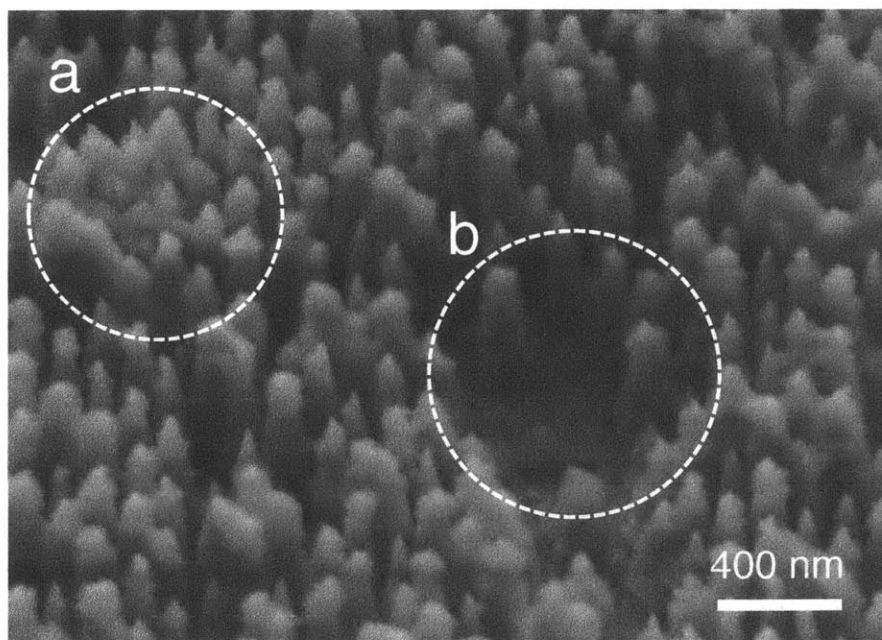


Figure 4-9. Defects on the fabricated surface. a) Aggregation. b) Defective surface areas lacking the nanocones

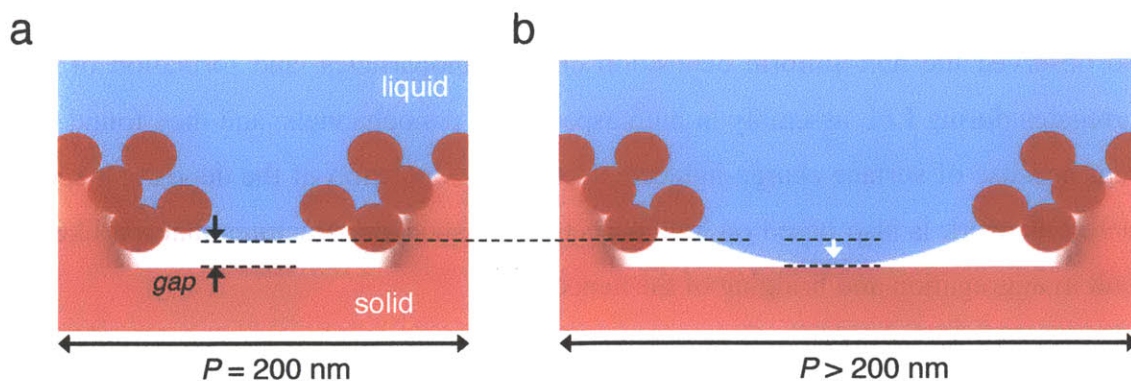


Figure 4-10. Schematic of change in the gap between the meniscus of liquid and solid surface with respect to the period (or spacing).

We strove to develop robust superoleophobic and super-transmissive silica surfaces with defect-free nanostructures which can be used for transparent fingerprint-resistant surfaces; however, the fabricated surfaces exhibit no superoleophobicity, and their transparency is not comparable to that of typical glass. Moreover, the recent theoretical research proposed by Butt et al. also suggests that the superoleophobicity raised from the fabricated nanostructures is not robust to the typical contact pressures of human fingers [114]. The details of this limitation will be discussed in the following section.

4.2.3 Limitations of transparent superoleophobic surfaces for transparent anti-fingerprint surfaces

When the liquid penetrates between the pillars, and touches the bottom of the surface, it remains there. This process from a) to b) of Figure 4-11 is called Cassie-to-Wenzel or impalement transition, and this transition must be avoided to obtain robust superoleophobicity [114].

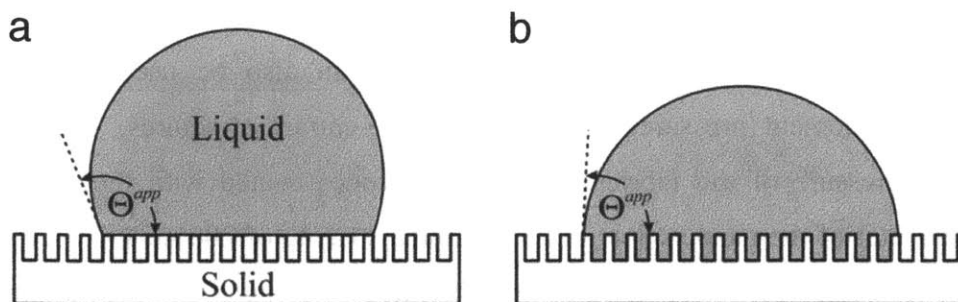


Figure 4-11. Schematic of a liquid drop on an array of pillars in the a) Cassie-Baxter and b) Wenzel state. Reproduced from Ref. [114] with permission from The Royal Society of Chemistry.

The maximum pressure difference that the air-liquid interface in an array of pillars (or cone structures) can sustain without going to the Wenzel state is called the breakthrough pressure (or impalement pressure), and this can be calculated from the geometrical constraints of the re-entrant structures [72, 114]. Butt et al. analytically calculated the impalement pressure of a surface with the pillars of sintered spheres, as shown in Figure 4-12 [114].

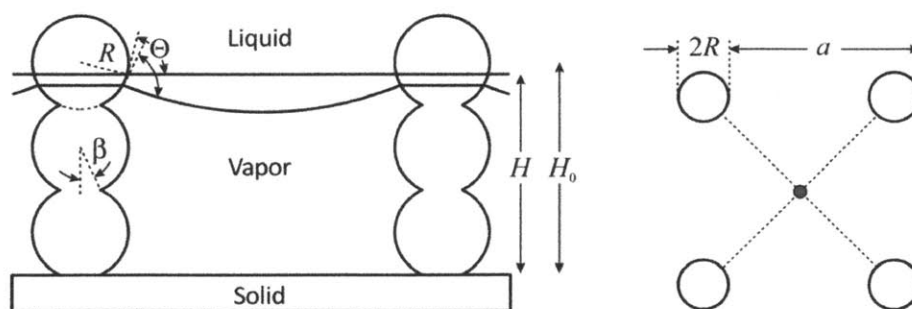


Figure 4-12. Schematic of the superamphiphobic (or superoleophobic) layer consisting of pillars of sintered spheres from side and top view. The liquid is suspended on top in the Cassie state. If no pressure is applied, the liquid surface is planar. With pressure the contact line moves downwards and the interface starts to curve. Reproduced from Ref. [114] with permission from The Royal Society of Chemistry.

The proposed analytical equations in their work can also be used for estimating theoretical impalement pressures of the existing re-entrant structures. The calculated impalement pressure of the fabricated silica nanocones coated with the nanoparticles (with a diameter of the nanoparticle of 25 nm and a spacing of 200 nm) is ~7.1 kPa, and that of the randomly deposited silica shells fabricated by Deng *et al.* (with a diameter of the silica shells of 100 nm and a spacing of 200 nm) is ~29 kPa [114]. However, these breakthrough pressures (or impalement pressures) are lower than moderate contact pressures by human fingers (~50 kPa) [111, 112], and that limits their extended use for anti-fingerprint surfaces because the typical human fingers' contact pressures break the non-wetting state, which leads to the fully wetted state with low surface tension liquids. This signifies that oil repellency mechanisms with re-entrant structures are not ideal for transparent anti-fingerprint surfaces, and a new approach must be developed. In the next section, a novel approach for transparent anti-fingerprint surfaces will be discussed in detail.

4.3 Transparent fingerprint-eating (or *dactylovorous*) surfaces based on TiO₂ nanoparticle coatings

To overcome the limitations mentioned in Section 4.2 for transparent anti-fingerprint surfaces, we develop titania-based porous nanoparticle coatings that are mechanically robust, with low haze, which exhibit short time scales for decomposition of fingerprint oils under ultraviolet (UV) light. Again, instead of previous studies that have targeted an oil repellency mechanism, we have taken the counter-intuitive approach of constructing our surfaces from *oleophilic* materials. The mechanism by which a typical dactylogram is consumed combines wicking of the sebum into the nanoporous titania structure followed by photocatalytic degradation. These TiO₂ nanostructured surfaces are also anti-fogging, anti-bacterial, and compatible with flexible glass substrates and remain photocatalytically active in natural sunlight.

4.3.1 Photocatalytic effect of titanium dioxide

Photocatalysis of titanium dioxide (TiO₂) is a well-known phenomenon for strong oxidation and reduction reactions, and has been widely used due to chemical stability and safety for the human body [101, 120-122]. These reactions activate decomposition of organic matter when TiO₂ is illuminated by UV light, thus allowing a surface of TiO₂ to remain clean [101, 120-122].

The mechanism of TiO₂ photocatalysis in presence of UV illumination is schematically shown in Figure 4-13. When TiO₂ is irradiated by light with energy equal to or greater than its band-gap energy, the valence band electrons are excited to the conduction band, while generating positive holes in the valence band [101, 120-122]. If the electrons and holes migrate to the surface of TiO₂ without recombination, and they can participate in various oxidation and reduction reactions with neighboring material such as water, oxygen, and other organic or inorganic species [101, 120-122]. The positive holes in the

balance band react with water (*i.e.*, hydroxide ion, OH⁻) in the atmosphere to produce the hydroxyl radical (•OH). In contrast, the excited electrons in the conduction band react with oxygen in the atmosphere, which form superoxide anions (•O₂⁻). These active oxygen species, hydroxyl radical and superoxide anions, are very powerful oxidants and extremely reactive; thus they can oxidize and decompose organic materials, and even mineralize them into CO₂, H₂O, etc [101, 120-122].

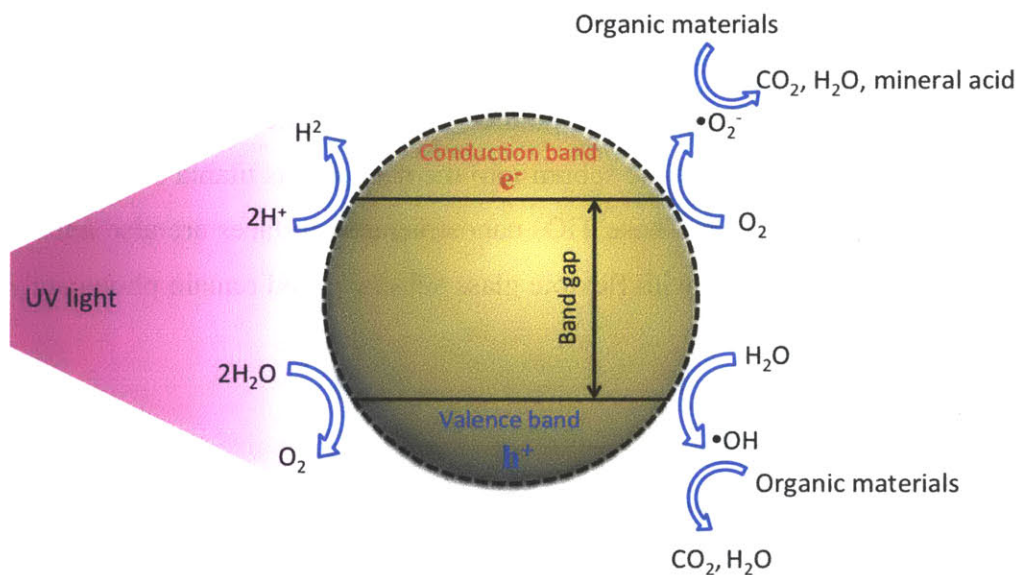


Figure 4-13. Schematic illustration of photocatalytic effect on titanium dioxide (TiO₂).

4.3.2 Design

We rely on the combined favorable effects of rapid capillary imbibition (or hemi-wicking [60, 82]) of fingerprint oils into a porous oleophilic titania nanoparticle structure and subsequent photocatalytic decomposition upon exposure to the ultraviolet (UV) component of natural sunlight. Although photocatalytic decomposition using titanium dioxide (TiO₂) films has been intensively studied for degrading low molecular weight organic materials into volatile components [101, 120-122], studies on multifunctional titania coatings that can achieve practical degradation times (≤ 3 hours under sunlight)

whilst also retaining optical transparency in the range of visible light are rare [101, 120-123].

To reduce the characteristic time required for photocatalytic degradation of fingerprint oils, we have designed nanoporous TiO_2 structures that reduce the thickness of the deposited sebaceous film and increase the interfacial contact area with the photocatalytic TiO_2 nanoparticles based on the mechanism illustrated in Figure 4-14. Rapid wicking of the low surface tension organic liquids that compose the sebum results in imbibition into the porous nanostructure. The creation of a very large surface area between the oil and the photocatalytic titania nanoparticles that constitute the transparent nanoporous coating helps accelerate the ensuing photocatalytic decomposition. The smaller the size of nanoparticles, the greater the surface area, leading to a shorter time required for photocatalytic decomposition of fingerprint oils.

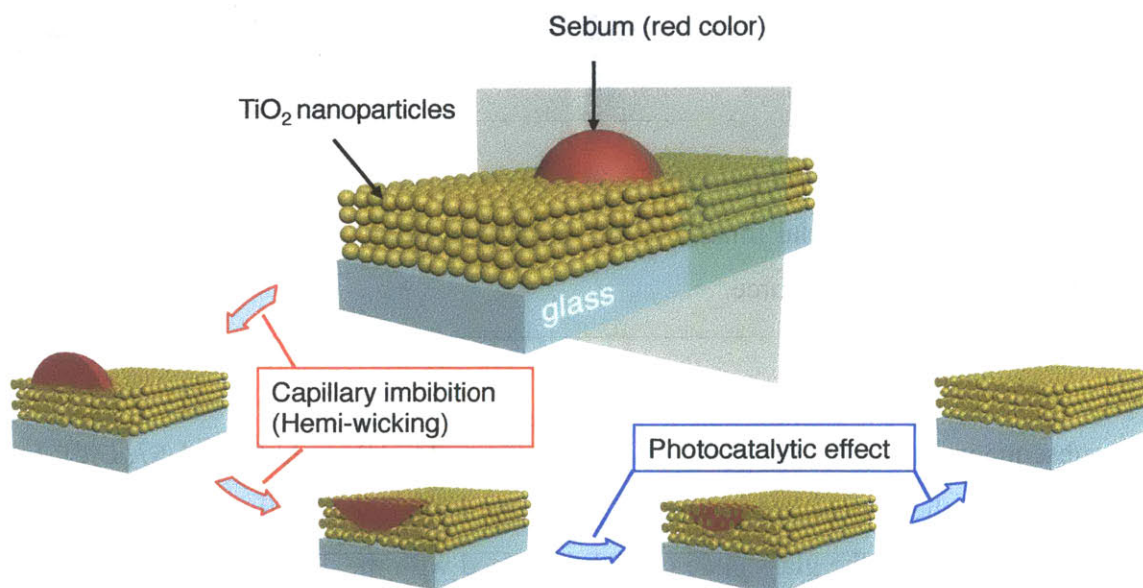


Figure 4-14. Schematic illustration of the two-step mechanism that leads to degradation of the sebum: (step 1) capillary imbibition of low surface tension components into the permeable nanostructure and (step 2) photocatalytic decomposition of the imbibed liquids on TiO_2 nanoparticles.

The spreading and imbibition of the viscous fingerprint oils shown in the microscopic images presented in Figure 4-15 can be quantified using bright field microscopy. Analysis of wicking into a nanoporous medium results in a Washburn-like spreading law with the front position of the sebum given by $l_{front} - l_0 \approx \sqrt{Dt}$ [124, 125]. Experiments and modeling (see Appendix B.1 for details) both give a characteristic diffusion coefficient of $D = 2K_p P_c / \mu \sim 10^{-10} \text{ m}^2/\text{s}$, where K_p is the permeability of the porous layer, P_c is the capillary pressure inside a pore, and μ is the viscosity of sebum. The time required for complete lateral capillary spreading over the characteristic distance between two friction ridges ($\Delta L \sim 10^2 \text{ }\mu\text{m}$) is therefore only $\Delta t \sim 10^2$ seconds.

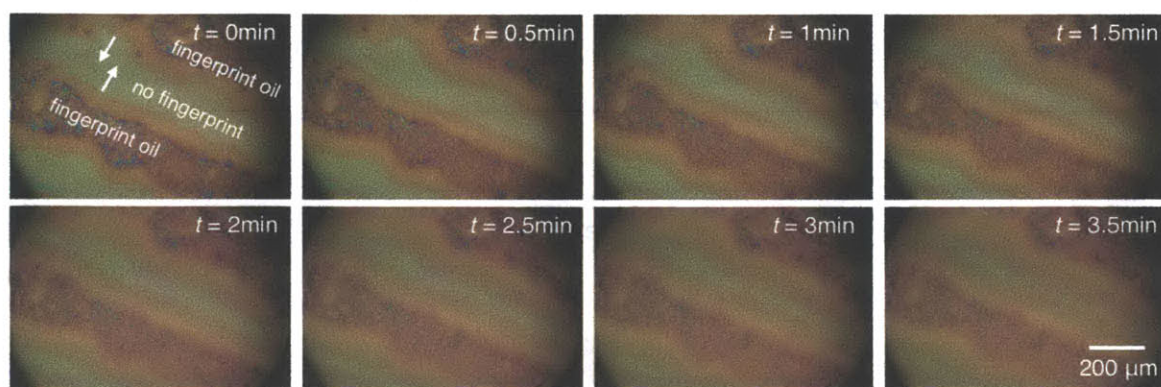


Figure 4-15. Time-sequential images of the initial spreading and capillary imbibition of fingerprint oils by capillary force.

The subsequent decomposition of the oils when exposed to UV light (UVM-57, UVP Inc.) is visualized in the optical images shown in Figure 4-16. The dactylogram deposited on the right-hand side of the glass slide (which is coated with the TiO_2 nanoparticle film) is first imbibed and then photocatalytically degraded. By contrast, an identical print deposited on a typical uncoated microscope glass slide (left side) remains unchanged even though both surfaces are continuously exposed to UV light ($1.5 \pm 0.1 \text{ mW}/\text{cm}^2$ at $300 \text{ nm} \leq \lambda \leq 400 \text{ nm}$) for the same period of 1 hour.

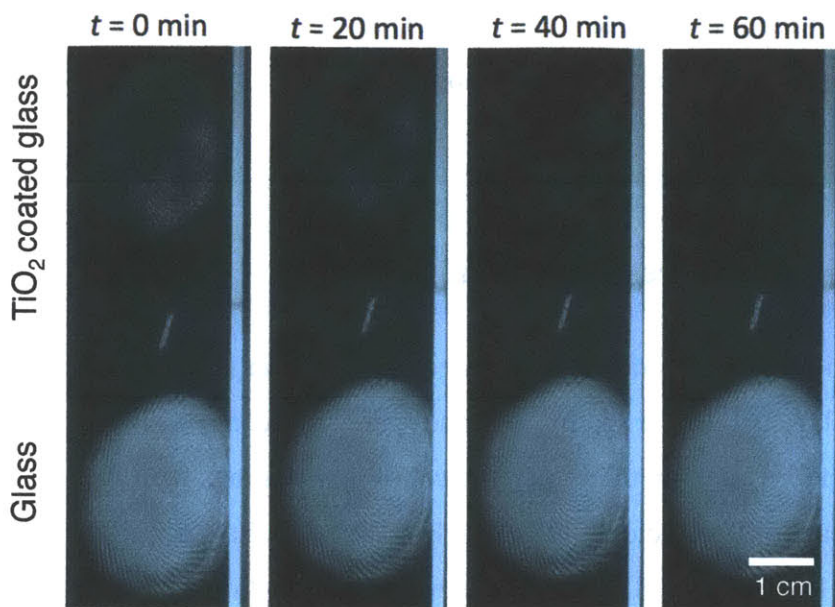


Figure 4-16. Time-sequential images of fingerprint oils on the nanoparticle coated side (top side, thickness = 114.8 ± 6.2 nm) and a typical microscope slide (bottom side) for 0, 20, 40, and 60 minutes of UV exposure ($I = 1.5 \pm 0.1$ mW/cm² at $300 \text{ nm} \leq \lambda \leq 400 \text{ nm}$).

In addition to enhancing the photocatalytic effect, maximizing light transmissivity and minimizing the optical haze are also important requirements for the design of practical transparent anti-fingerprint surfaces. When the wavelength of incident light is more than an order of magnitude greater than the components that constitute the nanostructured material, we can successfully model a representative volume element as a homogeneous medium with the refractive index determined by the volumetric ratio of the individual materials, according to effective medium theory [65, 66, 126, 127]. Designing the nanostructured coating to have a high porosity $p = (1-\phi)$, (where ϕ is the packing density of TiO₂ nanoparticles) leads to a smaller effective refractive index than the value for flat silicate glass, thus reducing reflection and increasing transmissivity within a specific wavelength region when compared to flat TiO₂ film with the same overall thickness [109, 127]. Moreover, the small length scale of the nanoparticle constituents ($< \lambda/10$) also leads to reduced haze generation with the incident light. We have considered these design constraints, the diameter of the particles needs to be less than ~ 40 nm, when we chose a

commercially available TiO₂ nanoparticle dispersion (Svaya Inc.) with average diameter of 22 nm to develop the nanoporous coating.

4.3.3 Fabrication process and optimization

In addition to design constraints on the size of the titania nanoparticles, the thickness of the coating layer must be optimized and precisely controlled using a reliable and reproducible fabrication method to create conformal coatings with low optical haze (*i.e.*, minimized scattering of incident visible light). We select Layer-by-Layer (LbL) assembly [57, 109, 110, 117, 118] using alternating depositions of a positively-charged poly(allylamine hydrochloride) (PAH) and negatively-charged titania nanoparticle dispersion, as schematically shown in Figure 4-17, to ensure uniform deposition of nanoparticles and precise control of thickness via the number of assembly steps. LbL assembly leads to conformal coatings with low optical haze when compared to other thin-film coating methods such as dip-coating, spray-coating or sol-gel processes. To remove the polymeric binder and to reinforce the structural durability of the nanoparticle coating, the LbL-coated glass slides are calcinated for 3 hours at temperatures not exceeding 350 °C (to ensure that the photocatalytic anatase structure of the titania was not transformed to a rutile form), resulting in a highly porous and sintered titania film.

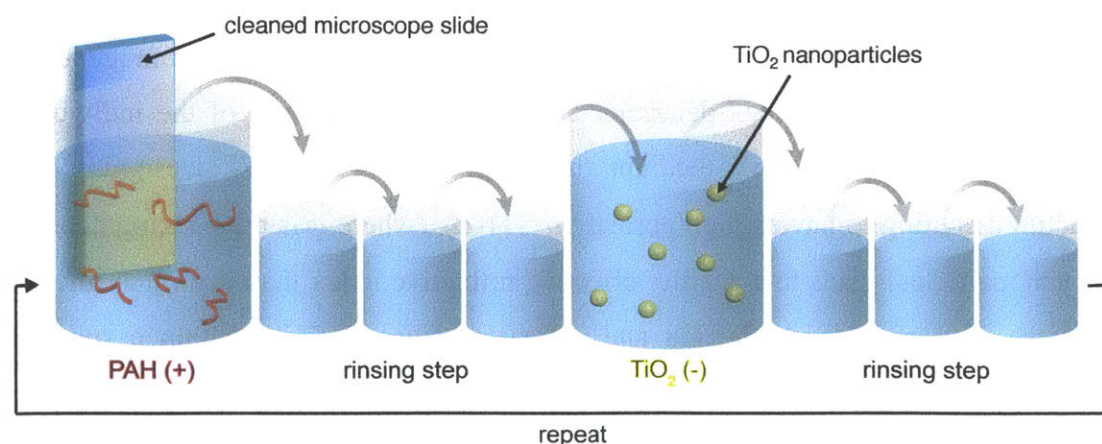


Figure 4-17. Schematic illustration of Layer-by-Layer (LbL) coating process. The 8 steps of the figure including 6 rinsing steps will now be referred to as 1 dipping cycle.

Here are the details of the fabrication process shown in Figure 4-17. Glass substrates are first degreased by sonication in a 4% (v/v) solution of Micro-90 cleaner (International Products Co.) for 15 min, subsequently sonicated twice in MQ water for 15 min. The substrates are blow-dried with dry air and treated for 2 min with an oxygen plasma (PDC-32G, Harrick Scientific Products, Inc.) at 150 mTorr before the LbL assembly to clean the surfaces. Sequential adsorption of polymer and nanoparticle layers is performed using a StratoSequence VI spin dipper (nanoStrata Inc.), controlled by StratoSmart v6.2 software, at 120-130 rpm. The concentrations of poly(allylamine hydrochloride) (PAH, $M_w = 58,000$ g/mol) and TiO₂ nanoparticle dispersions (Svaya Nanotechnologies, with mean diameter = 22 nm) in the dipping solutions are 1 mg/mL and 0.03 wt% respectively. Distilled water (>18 MΩ•m, Millipore Milli-Q™) water (MQ water) is used in formulating the polymer solution, nanoparticle dispersion, and in all rinsing procedures. The dipping time in the PAH solutions and TiO₂ dispersions are each 10 min followed by three sequential rinse steps (of 2, 1, and 1 min). The PAH solutions and TiO₂ dispersions and their respective rinse solutions are adjusted to pH 7.0 and pH 9.0 with either NaOH or HCl, respectively. These 8 steps including 6 rinsing steps shown in Figure 4-17 will now be referred to as 1 dipping cycle.

After the LbL assembly process, the coated substrate is calcinated for 3 hours at 350 °C. This temperature is sufficient to remove the PAH and to sinter the particle together into a nanoporous coating but ensures we retain the desired TiO₂ crystal structure (anatase) that maximizes photocatalytic activity and prevents it from being converted to the rutile structure. A schematic drawing of the nanoporous TiO₂ nanoparticle coating after calcination and a corresponding SEM image are shown in Figure 4-18. Figure 4-19 shows the growth behavior, and the measured thickness of the TiO₂ nanoparticle coating both before and after calcination. The coating thickness increases smoothly and monotonically, which enables accurate control of the thickness as the number of deposited PAH/TiO₂ dipping cycles is increased.

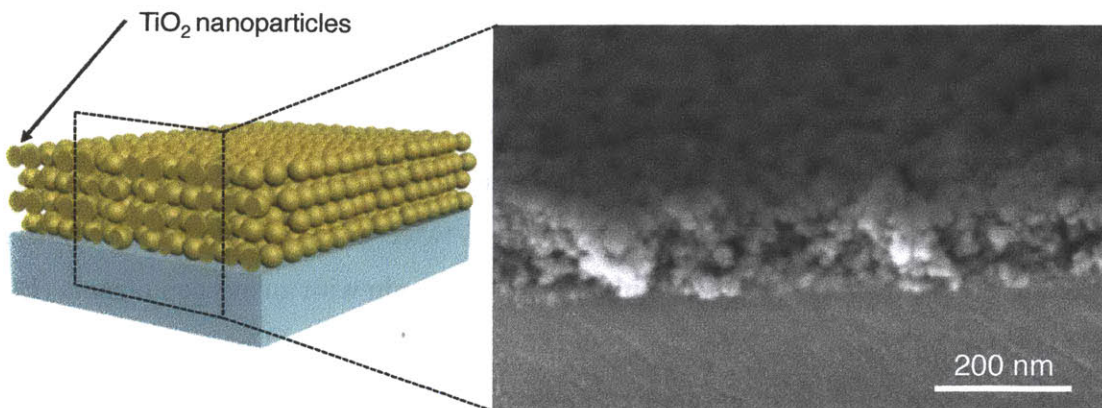


Figure 4-18. Schematic illustration and SEM image of the nanoparticle coated surface

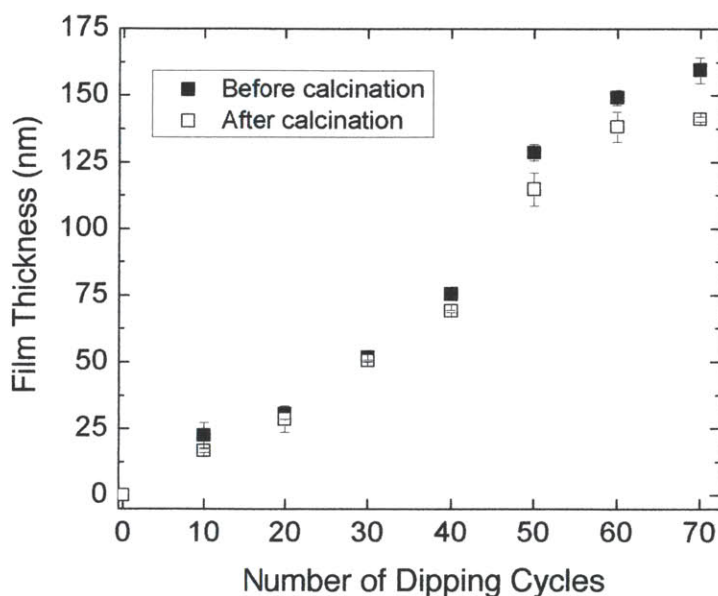


Figure 4-19. Film thickness of TiO₂ nanoparticle coating layer with respect to the number of coated dipping cycles, measured using profilometry (Dektak).

The porosity of the coating after calcination is determined by using ellipsometry to measure the values of the effective refractive index of the nanoporous film when two different fluids of known refractive index are imbedded into the porous structure (see Appendix B.2 for detailed schematics and experimental setup) [109]. After calcination the porosity of our LbL titania nanoparticle coatings is determined to be $p = (1-\phi) =$

0.496. This relatively large porosity lowers the effective refractive index of the final dry titania coating to $n_{\text{eff}} = 1.478$ ($\lambda = 633$ nm), which leads to suppression of reflections from the surface and enhances capillary imbibition of fingerprint oils into the nanoporous surfaces. Taking a representative coating thickness of 100 nm after calcination, the accessible surface area of this photocatalytic nanostructure corresponds to approximately 14 cm^2 per square centimeter of the coated glass, and increases linearly with the number of LbL deposition steps.

4.4 Results and discussion

4.4.1 Optical properties and photocatalytic effects

To guide our selection of the optimal thickness of this transparent photocatalytic TiO_2 coating, the optical transmissivity value over the wavelength range of visible light are measured, as shown in Figure 4-20. As the number of PAH/ TiO_2 dipping cycles deposited on the glass slides is increased, progressively lower optical transmissivity is measured over the spectral region of interest ($400 \text{ nm} \leq \lambda \leq 800 \text{ nm}$). However the layered nanoparticle structures with $N = 40$ ($d_{40} = 69.0 \pm 0.4 \text{ nm}$) and 50 dipping cycles ($d_{50} = 114.8 \pm 6.2 \text{ nm}$) still have greater average transmissivity (over wavelengths $550 \text{ nm} \leq \lambda \leq 800 \text{ nm}$), compared to a bare glass slide without a TiO_2 nanoparticle coating. This reduced reflectivity arises because of destructive thin-film interference at the air-nanoparticle-glass interfaces [109, 110, 117].

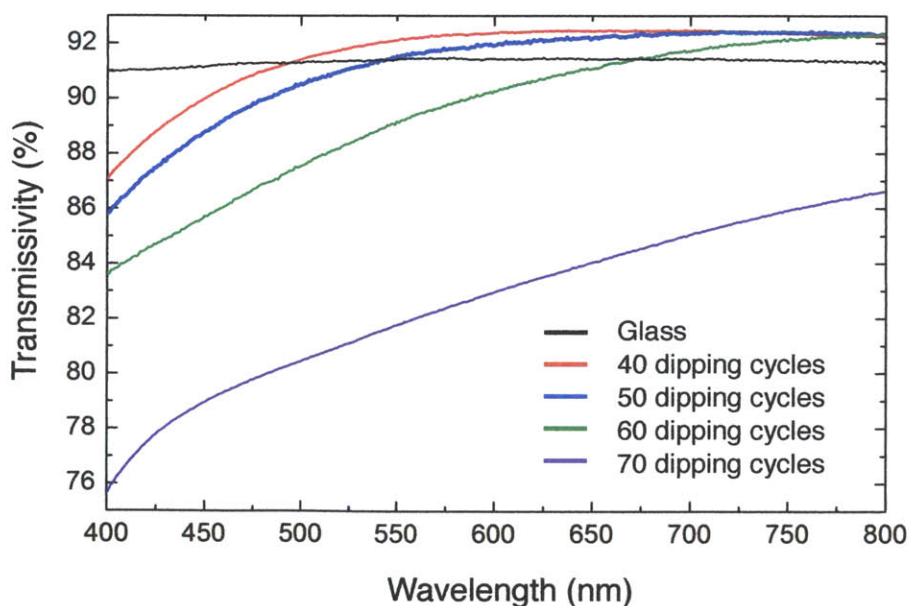


Figure 4-20. Measured optical transmissivity over the visible range ($400 \text{ nm} \leq \lambda \leq 800 \text{ nm}$) for four different thicknesses of TiO_2 nanoparticle layers. The black line represents the transmissivity of a typical microscope (soda lime) glass slide that is used as the substrate for the TiO_2 nanoparticle coatings.

Since optical haze induced by the nanoporous coating is also an important factor in selecting an optimal thickness, we also measure the haze (according to ASTM D1003, Standard Test Method for Haze and Luminous Transmittance of Transparent Plastics) as the number of deposited layers was increased. The average haze remains less than 2% over the spectral range of visible light ($400 \text{ nm} \leq \lambda \leq 800 \text{ nm}$) but increases steadily as the coating thickness increases as shown in Table 4-1. Note that a spectrophotometer (Cary-500) is used for spectral transmissivity and haze measurements (with an integrating sphere) in the visible range ($400 \text{ nm} \leq \lambda \leq 800 \text{ nm}$). A stabilized diode laser ($\lambda = 660 \text{ nm}$) is also used to measure the transmissivity at normal incidence angle.

To determine an optimal thickness which balances the trade-off between optical properties (optical transmissivity and haze) and the increased pore surface area for fingerprint decomposition, we quantify the dactylovoracity for different coated thicknesses of the porous TiO_2 nanostructure using a polydimethylsiloxane (PDMS) - based stamp that consists of a square array of periodic posts (period = $200 \mu\text{m}$) 'inked' with an artificial sebum ($\gamma_{LV} = 33.4 \pm 0.7 \text{ mN/m}$, measured by Krüss K10), as shown in Figure 4-21. At room temperature, 16 wt% oleic acid (Sigma-Aldrich, 99%), 12 wt% squalene (Alfa Aesar, 98%), 25 wt% jojoba oil (Sigma-Aldrich), and 41 wt% vegetable oil (Mazola) [106] are first introduced into a 200 mL glass bottle and then gently mixed using a vortex mixer for 1 hour. We use this mixture as the artificial sebum after storing it at room temperature for 24 hours. To minimize variability in successive dactylograms, we constructed a stamp-based method for depositing representative micro-droplet arrays of sebum. Polydimethylsiloxane (PDMS) posts are fabricated using an SU-8 mold. The artificial sebum is spread over the backside of a silicon wafer by spin-coating at 7000 rpm for 60 seconds. The stamp is then pressed against the oil film with a contact force of 4 N and held in contact for 3 seconds. When the stamp is removed, a small amount of artificial sebum remains on the tops of the wetted PDMS posts as shown in the inset of Figure 4-21. After having 'inked' the PDMS posts with artificial sebum, the stamp is first pressed into contact with a cleaned microscope slide (to ensure a uniform sebaceous coating on the microposts), and then used to stamp an array of sebum microdroplets onto the LbL-assembled and calcinated nanoparticle surface using a normal force of 4 N.

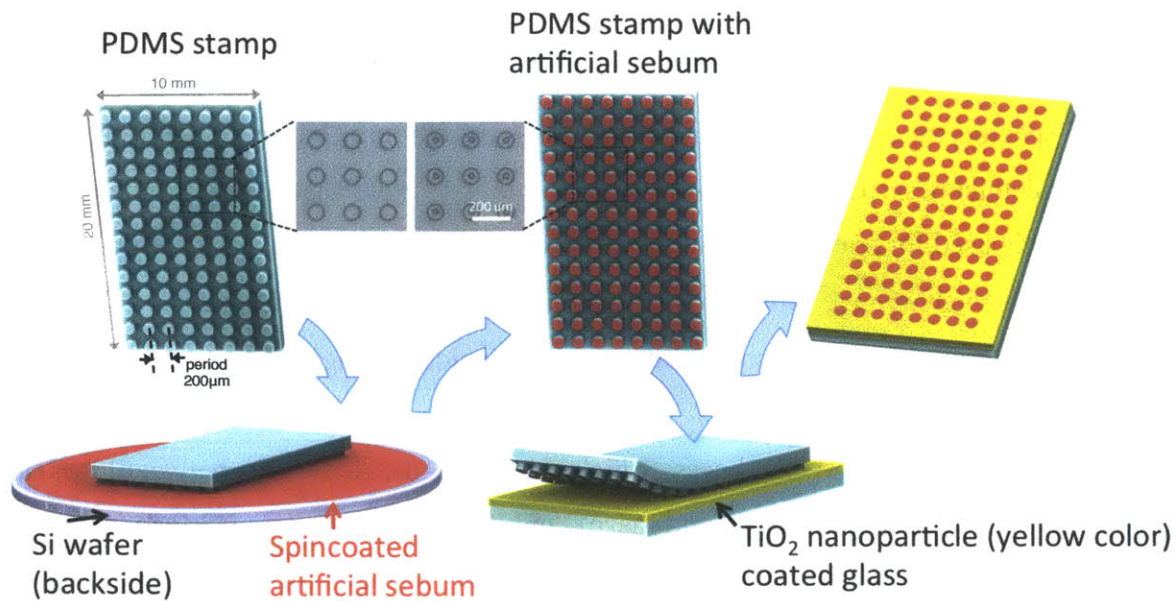


Figure 4-21. Illustration of the experimental process for quantifying the dactyloporous effect. The two microscope images correspond to the PDMS stamp (20 mm by 10 mm) with micrometric post array before depositing artificial sebum (left), and the same PDMS stamp with the absorbed sebum (right).

Figure 4-22 shows the measured transmissivity of monochromatic light ($\lambda = 660$ nm from a diode laser) for a 50 dipping cycle film ($d_{50} = 114.8 \pm 6.2$ nm) with respect to UV exposure time. The sebum deposited on the surface triggers optical reflection and scattering, and the transmissivity initially drops to 85.5% from the original value of 92.6%. As the surface is exposed to UV light (with an average intensity of 1.5 ± 0.1 mW/cm² averaged over the range $300 \text{ nm} \leq \lambda \leq 400 \text{ nm}$) the transmissivity gradually recovers to this initial, sebum-free value, and the distortional effects of the sebum disappear after 150 minutes of UV exposure. The inset images of the standard rest resolution targets further illustrate that image visibility through the 50 dipping cycle film ($d_{50} = 114.8 \pm 6.2$ nm) is fully recovered after 150 minutes of UV light exposure.

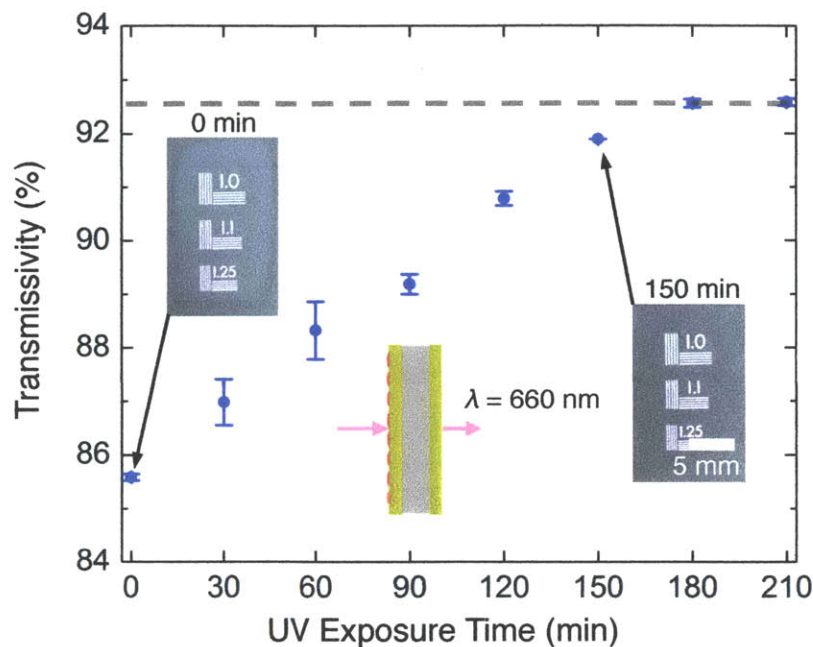


Figure 4-22. Time evolution of measured transmissivity (angle of incidence = 0° , $\lambda = 660$ nm) through an artificial sebum-stamped spot of a 50 dipping cycle thick TiO_2 nanoparticle coating under UV light (1.5 ± 0.1 mW/cm² at $300 \text{ nm} \leq \lambda \leq 400$ nm). The insets show two images of a part of the resolution test chart viewed through the nanoparticle coated surfaces with the artificial sebum deposits at $t = 0$ min (left) and 150 min (right) of UV exposure time.

The photocatalytic degradation of the artificial sebum stamped on the TiO_2 nanoparticle coating can also be examined by measuring change of the apparent contact angle of water droplets deposited on the TiO_2 nanoparticle coating with respect to UV light exposure time. As shown in Figure 4-23, the apparent contact angle of a 5 μL water droplet deposited on the 50 dipping cycle coating ($d_{50} = 114.8 \pm 6.2$ nm) decreases monotonically as the exposure time increases, and approaches a value below 5° after $t = 120$ minutes, because the intrinsic superhydrophilicity arising from the porosity of the nanoparticle coating is recovered.

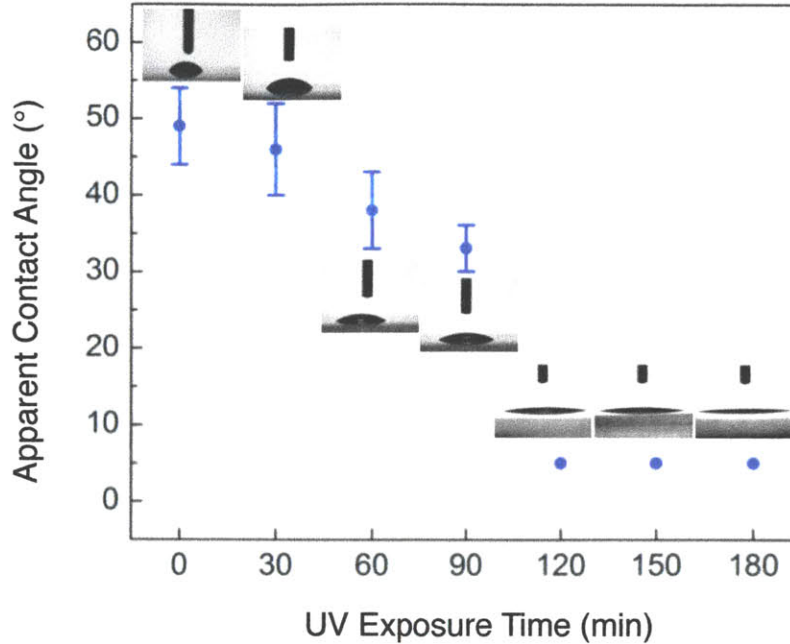


Figure 4-23. Time evolution of measured apparent contact angle of water droplets (Volume $V \approx 5 \mu\text{L}$) deposited on a 50 dipping cycle coating under UV light exposure. The apparent contact angle values are reduced to less than 5° after $t = 120$ min demonstrating the recovery of superhydrophilicity of TiO_2 nanoparticle surfaces.

The average values of transmissivity and haze as well as the time required for degrading the stamped artificial sebum are summarized in Table 4-1. Although the sebum film deposited on top of a thicker 60 dipping cycle TiO_2 nanoparticle coating ($d_{60} = 138.2 \pm 5.7$ nm) disappears more rapidly (within 30 minutes of the same UV light exposure), the average optical transmissivity remains below that of a flat uncoated microscope glass slide. Conversely, transmissivity tests with artificial sebum deposited on a thinner, 40 dipping cycle TiO_2 nanoparticle coating ($d_{40} = 69.0 \pm 0.4$ nm) shows that the oils do not completely vanish even after 270 minutes of UV light exposure because of the lower pore area available for photocatalytic digestion of the sebum. A 70 dipping cycle coating shows the fastest photocatalytic effect, however, the average haze value of this coating is greater than 1%, which exceeds the standard threshold desired in the touch screen industry [128]. It should be noted that in comparison with a commercially available glass

coated with TiO₂, SunClean™ glass (see Appendices B.3 and B.4 for details), the 60 dipping cycle coating which has an averaged transmissivity 16% greater than that of the SunClean™ glass shows 30 times shorter time to degrade the stamped artificial sebum under the same UV exposure condition.

	Average Thickness	Average transmissivity	Average haze	Photocatalytic effect ^{a)}
SunClean™ glass ^{b)}	-	72.5%	-	~ 15 hours
40 dipping cycles	69 nm	91.63%	0.34%	> 270 minutes
50 dipping cycles	115 nm	91.13%	0.79%	~ 150 minutes
60 dipping cycles	138 nm	89.46%	1.08%	~ 30 minutes
70 dipping cycles	141 nm	82.58%	1.77%	< 30 minutes

Table 4-1. Optical transmissivity and haze of the nanoporous titania coatings used for sebum digestion. a) Required exposure time until the moment that the optical transmissivity reaches 99% of the original transmissivity measured under UV illumination ($I = 1.5 \pm 0.1 \text{ mW/cm}^2$ at $300 \text{ nm} \leq \lambda \leq 400 \text{ nm}$) without the artificial sebum. b) See Appendices B.3 and B.4 for details.

Based on the results summarized in Table 4-1, the thickness of the coating can be chosen depending on specific applications and their requirements. Here, we select a 50 dipping cycle coating (with thickness $d_{50} = 114.8 \pm 6.2 \text{ nm}$) as the optimal thickness for constructing our transparent fingerprint-eating surfaces because it successfully suppresses reflectivity with comparably low haze whilst also realizing practically reasonable degradation times (< 150 minutes). In addition, the longevity test of the TiO₂ nanoparticle coatings that measures transmissivity of the coating ($\lambda = 660 \text{ nm}$) before and after the ten successive depositions of artificial sebum pattern followed by 3-hour UV exposure shows full recovery of transmissivity value on top of the 50 dipping cycle TiO₂ nanoparticle coating. As shown in Figure 4-24, the optical transmissivity ($\lambda = 660 \text{ nm}$) immediately drops to the values less than 86% after the artificial sebum is deposited on the

nanoporous coating, and it recovers to the initial transmissivity value after 3-hour UV exposure.

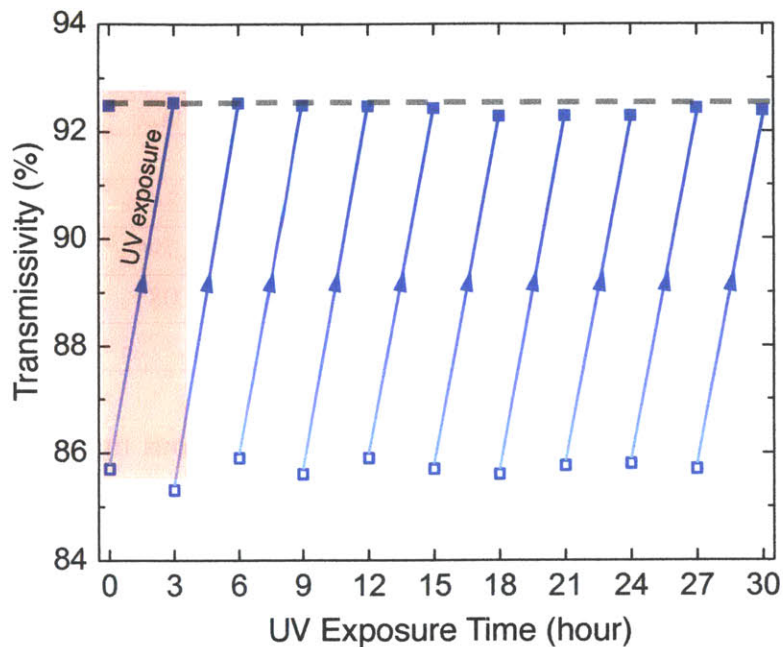


Figure 4-24. Longevity test of the 50 dipping cycle TiO₂ nanoporous coating. The blue square dots clearly represent the full recovery (up to 10 cycles) with approximately no change in optical transmissivity ($\lambda = 660$ nm) and consistent UV exposure time (3 hours) that takes to reach the initial transmissivity after repeated stamping the artificial sebum pattern. The hollow blue square dots indicate the transmissivity values right after the deposition of the artificial sebum. The blue lines with arrows represent the recovery of transmissivity. The red colored transparent box shows the single cycle of photocatalytic decomposition of the artificial sebum during 3 hours of UV exposure that is also shown in Figure 4-22.

4.4.2 Mechanical robustness

To compare the optical properties and mechanical durability of the TiO₂ nanoporous coating with an alternate anti-fingerprint coating approach consisting of a transparent superoleophobic coating [107], we investigate surfaces prepared by deposition of candle soot, followed by SiO₂ vapor deposition, calcination, and a chemical vapor deposition of perfluorodecyltrichlorosilane [107] as shown in Figure 4-25. When compared to the equivalent responses of the 50 dipping cycle nanoporous coating ($d_{50} = 114.8 \pm 6.2$ nm), the optical properties of this soot-templated superoleophobic surface (red) show an undesirable scattering of light and substantial haze that arise from the larger size of the soot nanoparticles (~ 100 nm) shown in the micrograph (i). Although goniometer tests (ii) show that the soot-templated surface is indeed superoleophobic with an advancing contact angle of $162 \pm 2^\circ$ for a droplet of artificial sebum ($\gamma_{LV} = 33.4 \pm 0.7$ mN/m), these re-entrant nanostructures are damaged irreversibly after a single application of a normal force of 4N (corresponding to a characteristic digital pressure of $4 \text{ N}/81 \text{ mm}^2 \sim 49 \text{ kPa}$). This results in the rapid loss of superoleophobicity shown in inset (iii) of Figure 4-25.

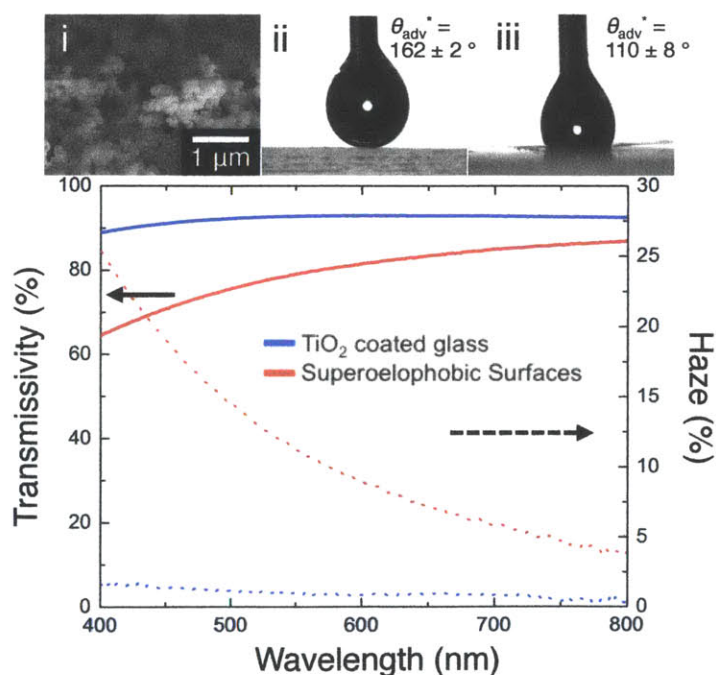


Figure 4-25. Optical spectral responses and haze of the TiO₂ nanoparticle surface (blue) and the superoleophobic soot-based surface (red). Insets: (i) Micrograph of a superoleophobic soot-based surface; (ii), (iii) Goniometric images of a droplet of artificial

sebum deposited on the surface before and after twice applying a contact force of 4 N in the normal direction of the surface, respectively.

In contrast, the same tapping force of 4 N (equivalent to a contact pressure of 49 kPa, representative of a typical finger stroke pressure [111, 112]) is repeatedly applied normal to the 50 dipping cycle nanoporous coating through the same latex rubber pad (9 mm by 9 mm). Figure 4-26 shows that there is no drop in optical transmissivity after repeated contact loading of up to 500 times. Image distortion analysis [129, 130] using a standard resolution test target is used to quantify the mechanical durability in a different way. The correlation coefficient ($0 \leq \alpha \leq 1$) indicates the level of image distortion due to repeated contact loading, compared to a reference image that is a part of the resolution test chart viewed through the nanoparticle coated surfaces. The value of zero represents no correlation between the two images due to poor optical clarity whilst the value of unity means complete matching among the images. The four insets of Figure 4-26 illustrate sharp in-focus images of the resolution test chart (with correlation coefficient α greater than 0.92) taken through the LbL-deposited nanoparticle surfaces after repeated contact loadings.

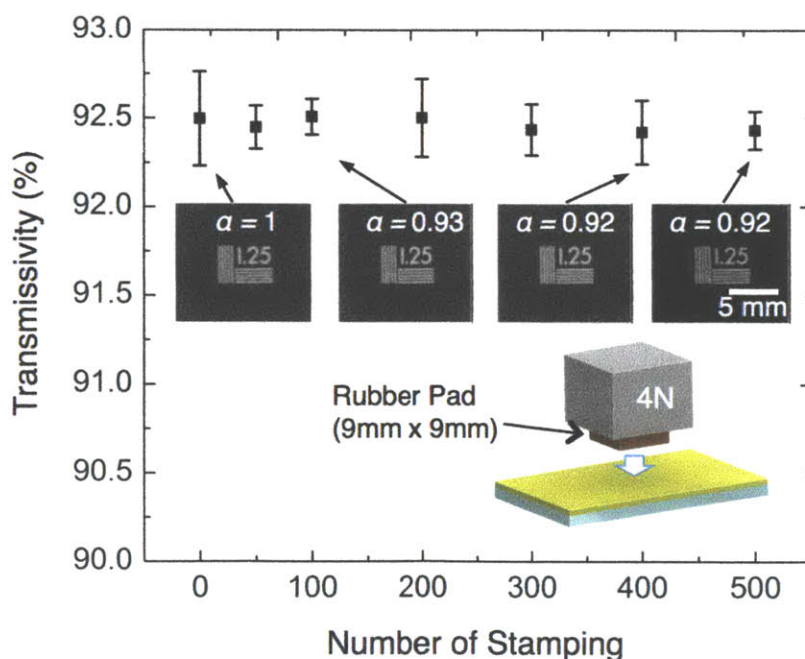


Figure 4-26. Evolution of optical transmissivity (at $\lambda = 660$ nm) after repeatedly applying a normal contact force (4 N) on the dactyloporous surface through a latex rubber pad with area $A = 81$ mm². The four insets are images of the resolution test chart (with image quality greater than $\alpha = 0.92$) taken through the LbL-deposited nanoparticle surfaces after repeated mechanical loading.

Moreover, mechanical durability of the LbL-deposited nanoparticle surfaces is also confirmed with contact sliding test in comparison with the transparent superoleophobic coating fabricated with candle soot as a template [107]. A latex rubber pad (9 mm by 9 mm) with a applied normal force of 0.254 N repeatedly slides against the horizontally mounted nanotextured surfaces (see the inset of Figure 4-27), which is equivalent to the minimum shear force applied by human fingers to operate capacitive touchscreen [131]. The measured kinetic friction coefficient between the rubber pad and the nanoporous coating is greater 0.5 (see Appendix B.4 for details), which leads that the shear force applied to the dactyloporous surface is approximately 0.1 N that is greater than the minimum lateral frictional force on a fingertip against capacitive touchscreen [131]. Figure 4-27 shows approximately no change in optical transmissivity of the TiO₂ nanoparticle coating even after 50 times repeated contact sliding test. In contrast, optical transmissivity of the transparent superoleophobic coating is changed to that of a flat microscope glass slide because the transparent superoleophobic coating is destroyed during the single sliding of the rubber pad on the coating. The inset on the left-hand side (i) represents the SEM image of the destroyed region of the transparent superoleophobic coating, and two insets (ii, iii) on the right-hand side are the SEM images of the TiO₂ nanoparticle coating. The nanoporous TiO₂ surfaces also passes a standard cross-hatch test (ASTM D3359, Standard Test Methods for Measuring Adhesion by Tape Test) and shows excellent adhesion.

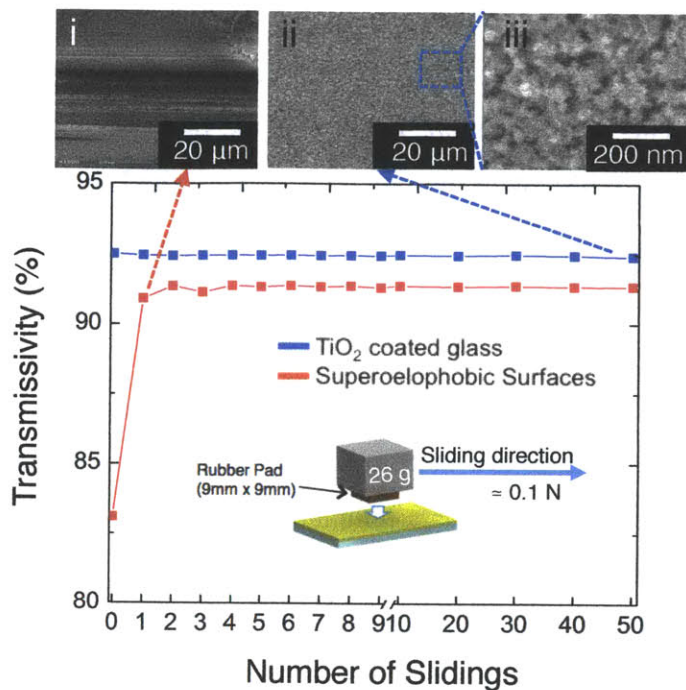


Figure 4-27. Mechanical durability test results of the TiO₂ nanoparticle coating against shear stress emulating sliding gesture of human fingers. Evolution of optical transmissivity (at $\lambda = 660$ nm) after repeatedly applying a contact sliding of a latex rubber pad (contact area $A = 81$ mm²) with a normal contact force (0.254 N) which is equivalent to the minimum shear force applied by human fingers to operate capacitive touchscreen [131] on the TiO₂ nanoparticle coated surface (blue) and the superoleophobic soot-based surface (red). The inset on the left-hand side (i) represents the SEM image of the destroyed region of the transparent superoleophobic coating, and two insets on the right-hand side (ii, iii) are the SEM images of the TiO₂ nanoparticle coating.

4.4.3 Multifunctionality

In addition to the superior optical transmissivity and enhanced mechanical robustness of the TiO₂ nanoporous surfaces as compared to the re-entrant superoleophobic surfaces, we have also explored other benefits compared to typical flat glass surfaces, conferred by structural superhydrophilicity and photocatalytic activity such as anti-fogging property and anti-microbial efficacy, which can both be important in keeping a textured and porous surface clean. Note that because of the intrinsic superhydrophilicity arising from the porosity of the nanoparticle coating (Figure 4-23), we can readily achieve the anti-fogging performance that is important for retaining optical transmissivity under moderate fogging conditions such as very humid warm environments. In Figure 4-28 we show the time evolution of optical transmissivity after exposing the 50 dipping cycle nanoporous coating (at $T = 5.2 \pm 0.2$ °C) and a bare glass slide at the same temperature (as control) to a stream of saturated steam followed by placing the surfaces (at time $t = 5$ s) into the path of a laser beam ($\lambda = 660$ nm from a diode laser). Transmissivity through the fogged uncoated glass surface rapidly drops to 5% and then gradually increases to a constant value that remains lower than the initial value measured with the TiO₂ nanoparticle-coated surface. This loss of transmissivity on the flat hydrophilic surface is due to the scattering from the deposited microscopic water droplets that remain pinned at chemical and physical heterogeneities on the substrate, as well as intrinsic reflection at each air-glass interface. On the other hand, the measurement on the nanoporous coating shows a small initial drop in the transmitted intensity as a result of rapid imbibition of the deposited airborne water droplets into the porous structure, followed by a uniform and rapid evaporation rate across the entire surface. The periodic fluctuations in transmissivity arise from constructive and destructive interference of the light (Newton's rings) [132] that is characteristically observed on a uniformly thinning film of liquid. As shown in the insets of Figure 4-28, a clear in-focus image of the resolution test chart is transmitted through the nanoporous surface, which also illustrates the antifogging property conferred by structural superhydrophilicity. Conversely, when the target is viewed through the conventional fogged microscope glass slide placed adjacently, the target image is unresolvable.

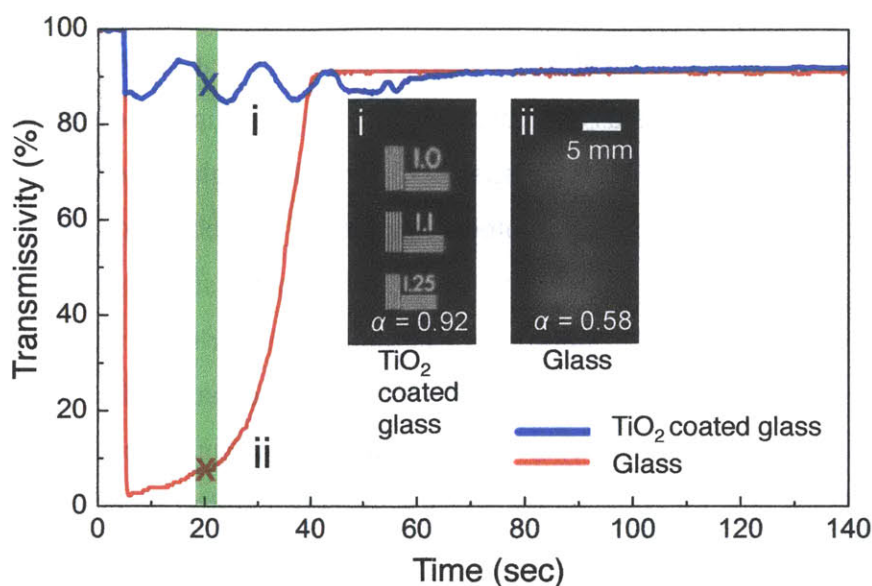


Figure 4-28. Time evolution of transmissivity due to fogging and defogging on a freshly-prepared TiO₂ nanoparticle coated surface (blue), and a bare glass microscope slide (red). Insets show optical micrographs of a resolution test chart viewed through the nanoparticle coated glass (i) and the microscope glass slide (ii) taken at the moments marked by the green color bar (at time $t \sim 20$ s). Image distortion analysis using a standard resolution test target is used to quantify the anti-fogging performance in the same way as used in Figure 4-26 [129, 130]. The clear in-focus left inset image of the resolution test chart is transmitted through the TiO₂ nanoporous surface, which shows the antifogging property ($\alpha = 0.92$). The correlation coefficient ($\alpha = 0.58$) for the right inset image (a fogged glass microscope slide case) indicates unacceptably poor visual clarity.

Moreover, we have explored the anti-bacterial properties of these photocatalytic coatings. Figure 4-29 shows the time evolution of the percentage of live (green) and dead (red) bacteria on glass substrate (left) and the TiO₂ nanoparticle coated surfaces (right). The dominant red coloration (99%) on the right-hand image signifies dead bacteria (*E. coli*) whose membranes are destroyed by the free radicals generated from the photocatalytic effect of TiO₂ nanoparticles [121, 133].

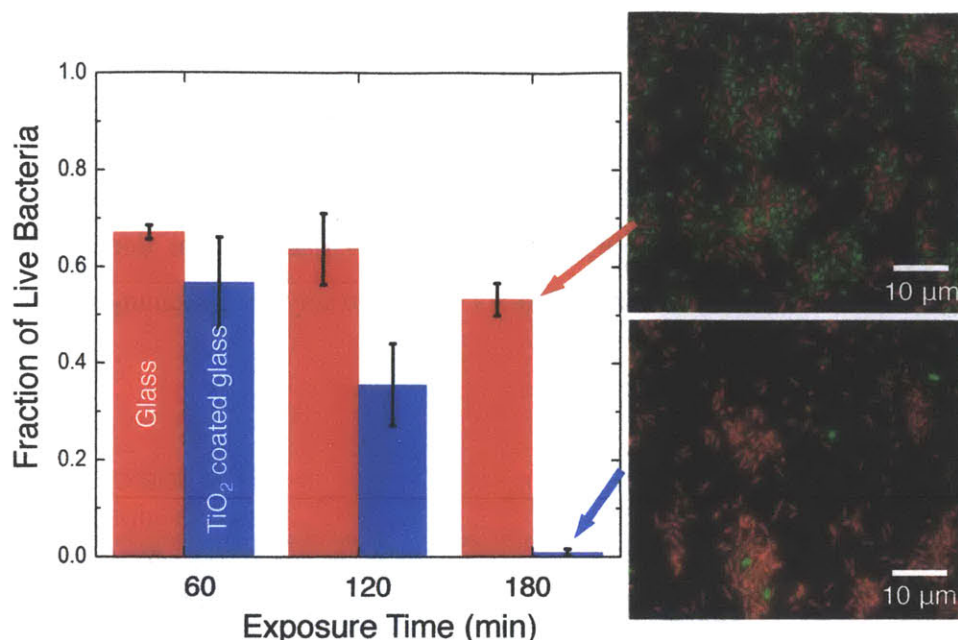


Figure 4-29. Fraction of live *E. coli* on the TiO₂ nanoporous surface (blue) and a microscope slide (red) with respect to exposure time. Fluorescence images showing antibacterial activity of the TiO₂ nanoparticle-deposited surface under UV exposure ($1.6 \pm 0.1 \text{ mW/cm}^2$ at $300 \text{ nm} \leq \lambda \leq 400 \text{ nm}$) for 3 hours. Green and red colors represent live and dead *E. coli* on both the nanoparticle coated side (lower image) and a typical microscope glass slide (upper image).

To facilitate future applications such as flexible touch screens, we have also demonstrated that the LbL fabrication method can be used to apply these TiO₂ nanoporous coatings to flexible glass substrates and secondly that the deposited sebum can also be degraded by direct exposure to natural sunlight within reasonable time durations. As shown in Figure 4-30, a flexible glass substrate (thickness = 0.1 mm, VWR) with 50 dipping cycles of PAH/TiO₂ deposited by LbL assembly followed by calcination can bend without damage (with a radius of curvature down to approximately 59 mm). In Figure 4-30 we also show three sequential images indicating that when fingerprint sebum is deposited on the flexible coating the dactylogram progressively disappears even under natural solar irradiation (with an averaged intensity over the wavelength range $300 \text{ nm} \leq \lambda \leq 400 \text{ nm}$, $I_{\text{solar}} = 4 \pm 1 \text{ mW/cm}^2$). The TiO₂ nanoparticle

coated side on the right (constructed from 50 dipping cycles of PAH/TiO₂ followed by calcination) exhibits a similar photocatalytic effect to that observed under the UV lamp (with a power of $1.5 \pm 0.1 \text{ mW/cm}^2$ at $300 \text{ nm} \leq \lambda \leq 400 \text{ nm}$). The nanoporous coating again shows an initial imbibition of the oil followed by complete photocatalytic removal of fingerprint sebum within 3 hours. By contrast the dactylogram deposited on the uncoated glass surface (left-hand image) does not show any visual changes at all upon solar irradiation.

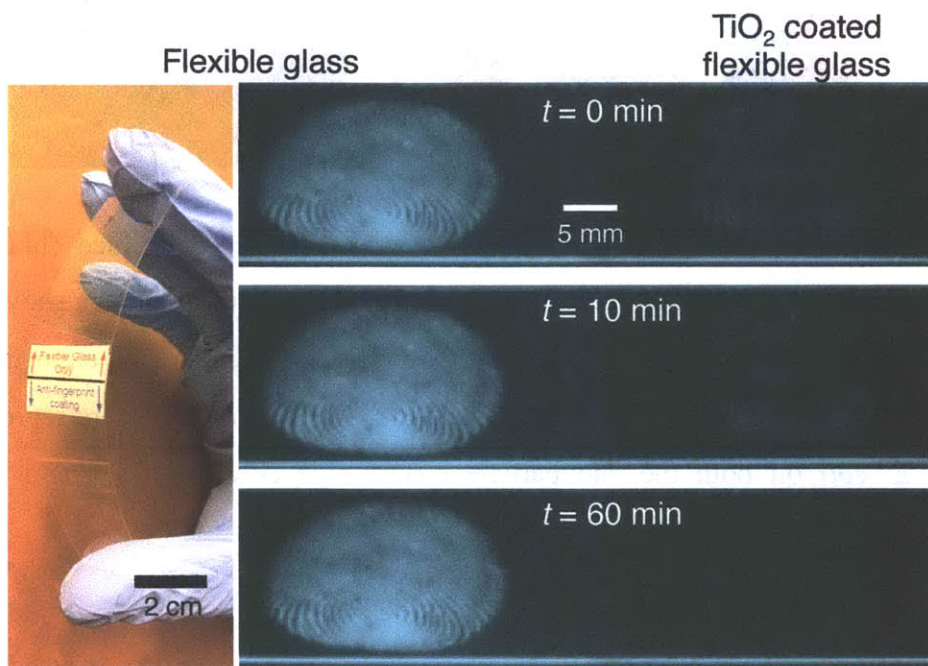


Figure 4-30. Flexible glass substrate deposited with a TiO₂ nanoparticle film (lower half on the left) by the LbL fabrication method. The three sequential images on the right show that a fingerprint deposited on the flexible TiO₂ nanoparticle coated surface progressively disappears under sunlight irradiation ($I_{\text{solar}} = 4 \pm 1 \text{ mW/cm}^2$ at $300 \text{ nm} \leq \lambda \leq 400 \text{ nm}$) for 3 hours.

4.5 Conclusion

In this work, we have designed and fabricated a nanoporous TiO₂ coating using LbL assembly techniques and subsequent calcination that results in superoleophilic capillary imbibition when an oily liquid such as fingerprint sebum is deposited on the surface. The nanoporous TiO₂ coating exhibits unique *dactylovorous* properties but also has superior optical transmissivity, lower haze and increased mechanical durability compared to a re-entrant superoleophobic surface. Finally, we have also demonstrated that the superhydrophilic and photocatalytic properties of the TiO₂ nanoporous coating result in additional anti-fogging and anti-bacterial properties as well as operational compatibility with flexible glass substrates and natural sunlight exposure, respectively.

Chapter 5

Nanostructured Color Silicon Surfaces

5.1 Introduction

Light interaction with nanostructures is of great interest due to their ability to control the flow of light as well as their promising functions such as eliminating reflection of light [15, 45, 54, 68, 92], enhancing optical fields for biomaterial detection and lithography [134-137], and increasing the light-collecting efficiency of photovoltaic devices [2, 17]. Also, nanostructured color filters based on wavelength-selective reflectance have also drawn much attention as an alternative to pigment-based color technologies, due to their distinctive optical properties such as reliability and bright color generation [137-140]. They have been developed for years in many ways, and recently, color filters with silicon nanowires have been studied extensively because of their unique mechanism of color tunability that utilizes light interaction only with the controllable geometry of silicon structures [138, 139]. These silicon color filters are relatively simple to be fabricated as they consist of a single material [138, 139], silicon, whose fabrication processes have been developed for decades, compared to other color filters such as plasmonic color filters that require metal and dielectric materials [137, 140, 141].

Although there are various advantages to silicon nanostructured color filters such as their unique mechanism and ease of fabrication, the reflected output color of the filters is too sensitive to the geometry of the nanowires [138, 139]. Colors generated from these filters are adjusted by mostly fine-tuning the diameter of silicon nanowire structures, and the variation of the diameter allowing a full range of colors is on the order of the range of tolerance of the most accurate nanofabrication technique such as electron beam lithography (EBL). Even a few nanometers' error in the size of the fabricated silicon structures can cause a large variation of colors [138, 139]. Furthermore, most of these

silicon nanowire color filters have been fabricated via EBL [139-141]; consequently, it is practically impossible to create nanostructured color filters on even as large a surface area as a square centimeter (1 cm^2).

Here, we propose a 2-dimensional (2D) array of periodic subwavelength nanorod structures on top of a silicon surface to generate a wide variety of vivid colors using a scalable nanopatterning method. The silicon surfaces with the nanorod structures result in different reflective spectral responses with respect to their heights, which is a more reliable mechanism for color generation compared to the existing work relying upon the diameters of the rods for color generation [138, 139]. Moreover, we also develop novel nanofabrication techniques combined with interference lithography (IL) and reactive ion etching (RIE) to fabricate designed silicon nanorod structures with a large duty cycle (~ 0.8) for acquiring high contrast of colors [142]. Nanorod structures with a large duty cycle (> 0.5) are practically difficult to achieve via typical interference lithography [47, 96]. Strong interference effects inside these nanostructures allow control of selective-wavelength reflectance, and the fabricated silicon coating is readily observable even to the naked eye since the nanostructured color coating can cover a surface area as large as 2 cm by 4 cm. These nanostructured color filters fabricated by the newly developed techniques can be employed further in reflective color displays and environmental sensors for monitoring changes in the refractive indices of liquids.

5.2 Color science

Color is “that aspect of visual perception by which an observer may distinguish differences between two structure-free fields of view of the same size and shape, such as may be caused by differences in the spectral composition of the radiant energy concerned in the observation” [143]. Color originates from a power distribution of light with respect to wavelength that stimulates light receptors in the eye with spectral sensitivities [143, 144]. Consequently, color science, which provides a connection between perception of color by the human eye and the spectrum of light, has been widely studied due to its industrial importance and possible applications such as display products [143, 144].

In 1931, the International Commission on Illumination defined a standard observer for colorimetry, based on 2° color matching [143, 144]. This, called CIE 1931 color space or 1931 CIE standard observer, incorporates both colorimetric and photometric behaviors. Although revision and evaluation of the standard observer are still required, it has been widely used for color specification in industry [143, 144]. In this thesis, it is used to identify colors generated from spectral response of light reflected from the nanostructured color filters. This is important because the geometry of the nanostructures is designed and optimized to exhibit the high contrast of colors that can be generated from the nanostructures.

Figure 5-1 shows the CIE 1931 color matching functions. Three functions with respect to wavelength, $X(\lambda)$, $Y(\lambda)$ and $Z(\lambda)$, define the color-matching properties of the CIE 1931 standard colorimetric observer [143, 144]. Figure 5-2 displays the CIE 1931 chromaticity diagram together with CIE RGB color space, and the chromaticity coordinates (x, y) can be calculated for light of any spectral power distribution $I(\lambda)$ based on Figure 5-1 [143, 144].

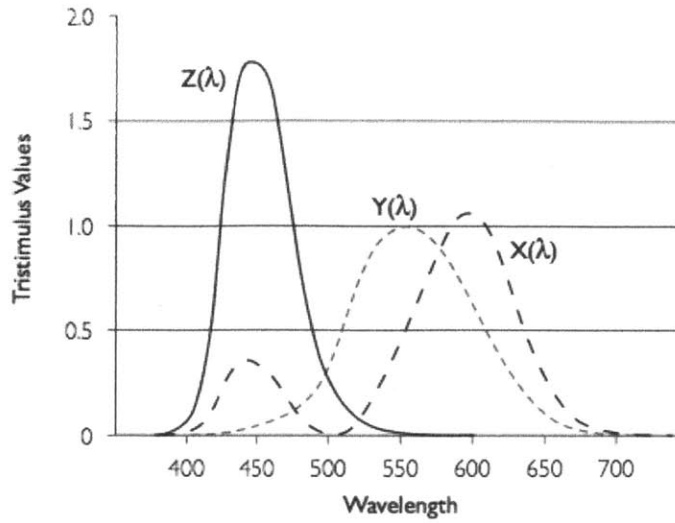


Figure 5-1. CIE standard observer color matching functions: $X(\lambda)$, $Y(\lambda)$ and $Z(\lambda)$ [144].

$$X = \int_{\lambda=380nm}^{\lambda=780nm} I(\lambda)\bar{x}(\lambda)d\lambda \quad (5.1)$$

$$Y = \int_{\lambda=380nm}^{\lambda=780nm} I(\lambda)\bar{y}(\lambda)d\lambda \quad (5.2)$$

$$Z = \int_{\lambda=380nm}^{\lambda=780nm} I(\lambda)\bar{z}(\lambda)d\lambda \quad (5.3)$$

$$x = \frac{X}{X+Y+Z} \quad (5.4)$$

$$y = \frac{Y}{X+Y+Z} \quad (5.5)$$

$$z = \frac{Z}{X+Y+Z} \quad (5.6)$$

The coordinates (x, y) calculated from Eqs. 5.1-5.6 conclusively indicate a specific color on the RGB color space (Figure 5-2) that we will perceive through the vision system of the eye based on the spectral power distribution $I(\lambda)$. The boundary of the color space indicates the colors generated from a single monochromatic wavelength, and the colors outside of the boundary cannot be seen [143, 144]. This chromaticity diagram with the

CIE RGB color space is mainly used to estimate generated colors of the spectral power distribution $I(\lambda)$.

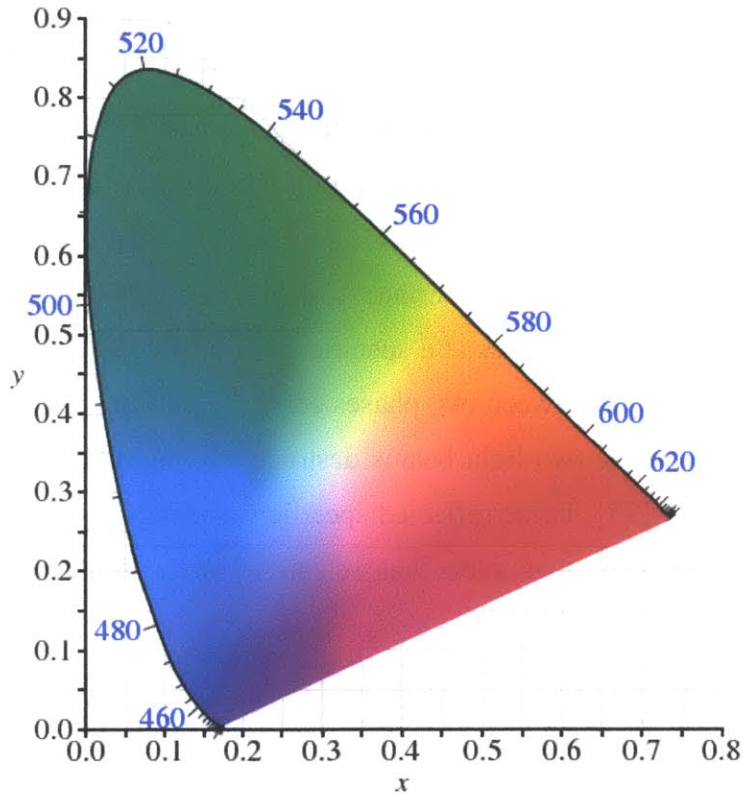


Figure 5-2. CIE 1931 color space chromaticity diagram and standard RGB color space [144].

5.3 Optical interference and thin-film interference

Optical interference is one of the most fundamental properties of light. This is also the principle of interference lithography (IL), which is utilized for fabricating the periodic subwavelength nanocone surfaces shown in Chapters 2 and 3. This phenomenon is often seen in a thin film of oil floating on top of water, as shown in Figure 5-3. The oil film reflects multiple rainbow colors, which depend on the thickness of the oil film. When a phase of the reflected light at an optical interface between air and oil is the same as that of the reflected light at the oil/water interface, two reflected beams of light constructively interfere and the reflection increases at a specific wavelength and incident angle [25]. In contrast, when a difference between two phases of the light beams reflected from the two interfaces is half of 2π , the two light beams destructively interfere and the reflection of light becomes reduced [25]. These reflected specific wavelengths of light (due to optical interference) create the variety of colors that we can see on the thin layer of oil.

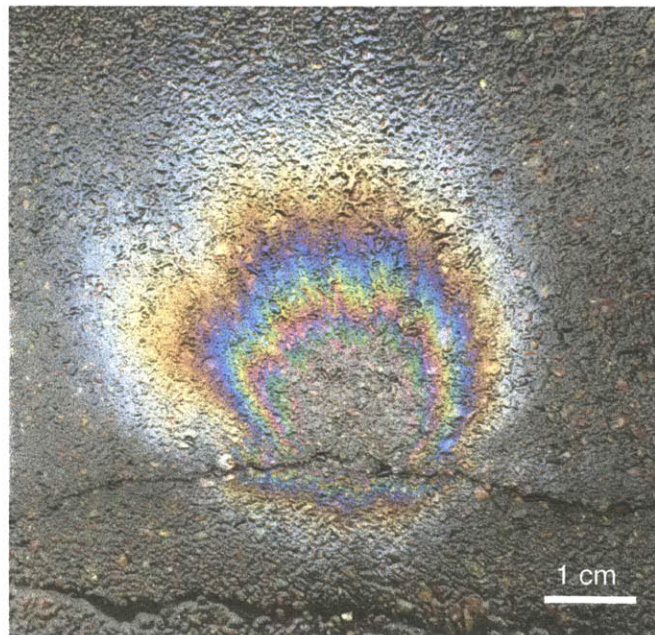


Figure 5-3. Optical interference effects from an oil film on water.

Using this phenomenon, a single quarter-wavelength coating of material whose refractive index is the square root of the substrate's refractive index is widely used to suppress reflection at a specific wavelength [25], which has also been discussed in Chapter 2. It causes zero reflection only at a specific wavelength and a specific incident angle. To overcome this limited anti-reflectivity, multilayer coatings that work at multiple wavelengths and wide incident angles have also been proposed and broadly utilized in the optics industry, as described in Chapter 2.

In this section, I will discuss how constructive and destructive interferences of incident light occur within a single layer consisting of periodic silicon nanorods, and how these optical phenomena yield vivid colors. Assuming that a thin layer (material 1) with a thickness t is deposited on top of a substrate (material 2) and that its refractive index, n , is lower than that of the substrate, as shown in Figure 5-4, the thickness of the film at which constructive interference against normal incident light occurs is

$$t = \frac{\lambda}{2n(\lambda)}C, \quad (5.7)$$

where λ is the wavelength of light, $n(\lambda)$ is the refractive index of the film that is a function of λ , and C is a constant which must be a positive integer. Local maximum reflectance occurs because of constructive interference when the optical path length from the start to the end of a thin film is an integer multiple of the wavelength [25].

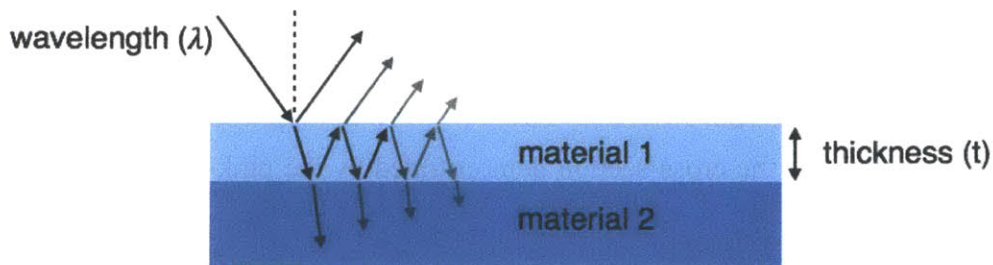


Figure 5-4. Schematic drawing of the thin film configuration. The surrounding medium is air whose refractive index is 1.

In contrast, local minimum reflectance occurs due to destructive interference when the optical path length is a positive integer multiple of the wavelength minus one half wavelength [25]. The thickness of the film at which destructive interference with normal incident light occurs is the same as Eq. 5.7, except with a constant C which is 0.5, 1.5, 2.5... and so on. Simply by evaluating C 's value at a specific wavelength with a refractive index of optical thin film, we can estimate optical interference effects under the film, which exhibit local maximum or minimum reflectance. As an example of interference effects on a thin film, Figure 5-5 shows a single-layer anti-reflection coating, with a thickness of 600 nm and a refractive index of 1.22 (see Section 2.2), deposited on top of a substrate (*e.g.*, glass) with a refractive index of 1.5.

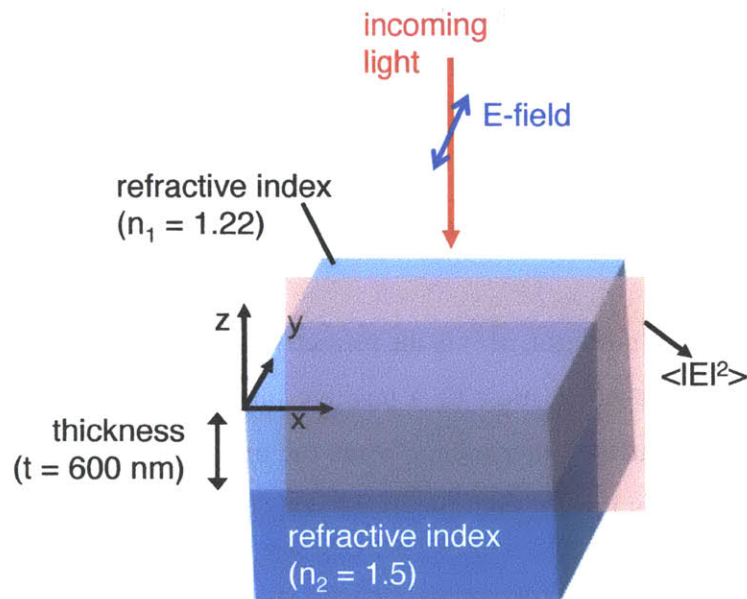


Figure 5-5. Schematic of the thin layer (single-layer anti-reflection coating) structure geometry and incident light configuration. The surrounding medium is air. Electrical fields are calculated at the cross-section demonstrated by the pink-colored shaded region (see Figure 5-7).

Figure 5-6 shows the calculated optical reflectance of normal incident light from the surface in Figure 5-5 with respect to the wavelength ($400 \text{ nm} \leq \lambda \leq 2000 \text{ nm}$). The

maximum reflectance is 4%, which is the reflectance value without the thin layer on the substrate. With the thin layer causing destructive interference, the reflectance becomes $\sim 0\%$ at certain wavelengths that are represented by the circled numbers, (i), (ii), and (iii) in Figure 5-6. In contrast, constructive interference occurs at three wavelengths, indicated by the circled numbers, (iv), (v), and (vi), which results in the maximum reflectance, 4%. As mentioned previously, we can also estimate constructive and destructive interference phenomena by calculating C values in Eq. 5.7. The calculated C values at (i), (ii), and (iii) are 3.5, 2.5, and 1.5, respectively, which represent the conditions for destructive interference. The C values at (iv), (v), and (vi) are 3, 2, and 1, respectively, which are the conditions for constructive interference.

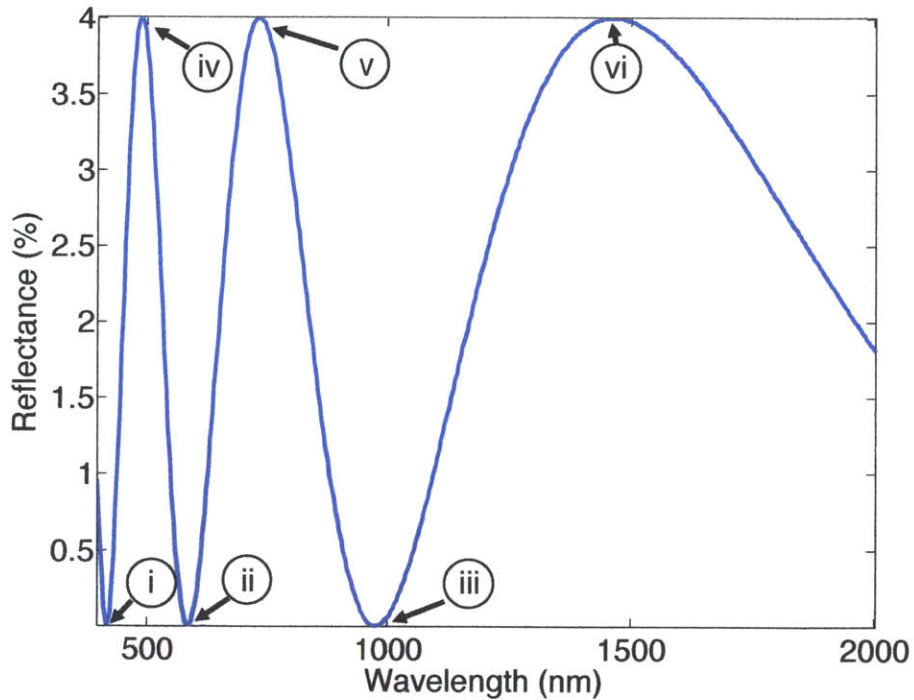


Figure 5-6. Calculated optical reflectance of normal incident light from the thin layer model schematically illustrated in Figure 5-5 with respect to the wavelengths ($400 \text{ nm} \leq \lambda \leq 2000 \text{ nm}$).

The physical mechanisms of constructive and destructive interference are also investigated by the electric field distributions calculated from finite domain time

difference (FDTD), as shown in Figures 5-7 and 5-8. The constructive and destructive interference phenomena are observed in the electrical field distributions calculated at the cross-section of the thin layer (represented in the pink-shaded region in Figure 5-5 and the schematic drawings on the left-hand side of Figures 5-7 and 5-8) where the local peak and dip reflectance values are located in Figure 5-6. Notice that the amplitudes of the electric field distributions in Figure 5-7 and 5-8 oscillate along the z -axis, which are the same behaviors as harmonic plane waves. The zero reflectance values appear at (i), (ii), and (iii) with the conditions for destructive interference in Figure 5-6, while having C values 3.5, 2.5, and 1.5, respectively. Figure 5-7 shows that the numbers of the wavelengths inside the thin layer at (i), (ii), and (iii) (represented in pink lines next to the electric field distribution maps) are 3.5, 2.5, and 1.5, respectively, as identified by the electric field distributions calculated inside the 600-nm-thick anti-reflection coating. These values (the number of the wavelengths inside the anti-reflection coating) are the same as the C values calculated previously.

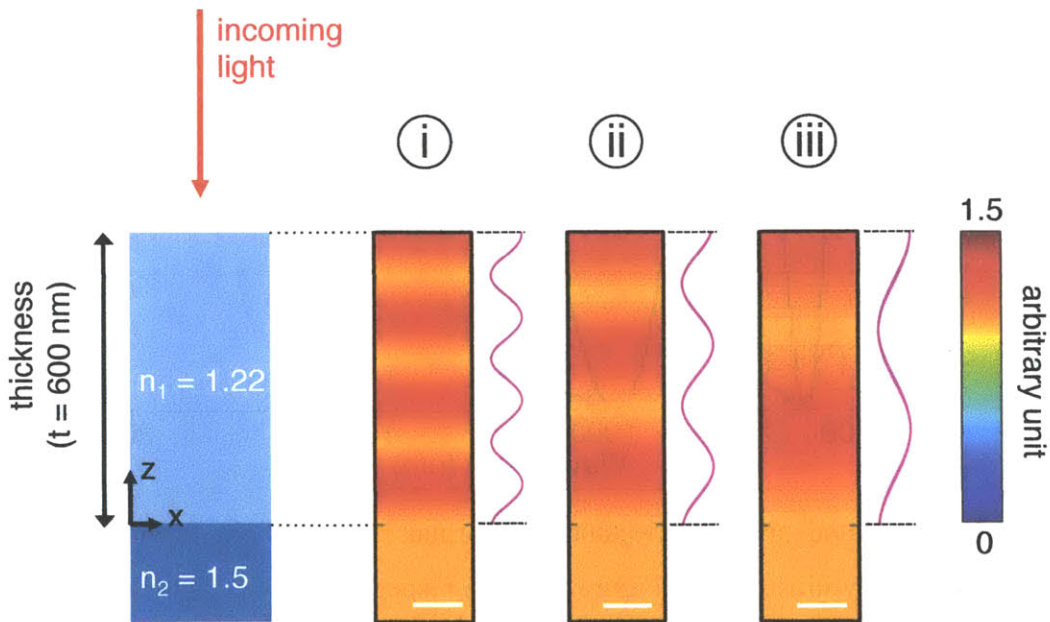


Figure 5-7. Electric field distributions calculated using finite domain time difference (FDTD) at (i), (ii), and (iii) in Figure 5-6 (destructive interference). All the white scale bars represent 100 nm.

In contrast, the maximum reflectance values appear at (iv), (v), and (vi) with the conditions for constructive interference in Figure 5-6, while having C values 3, 2, and 1, respectively. Figure 5-8 also demonstrates that the numbers of the wavelengths inside the anti-reflection coating layer at (iv), (v), and (vi) (represented in pink lines) are 3, 2, and 1, respectively. Again, these results are the same as the C values calculated previously. These show that the calculated electric field distributions can also reveal the occurrence of constructive or destructive interference within the thin layer. Note that all the scale bars in Figures 5-7 and 5-8 represent 100 nm. In Section 5.3, I will discuss how these interferences occur inside the silicon nanostructures, and the physical mechanisms of the nanostructured silicon color filters.

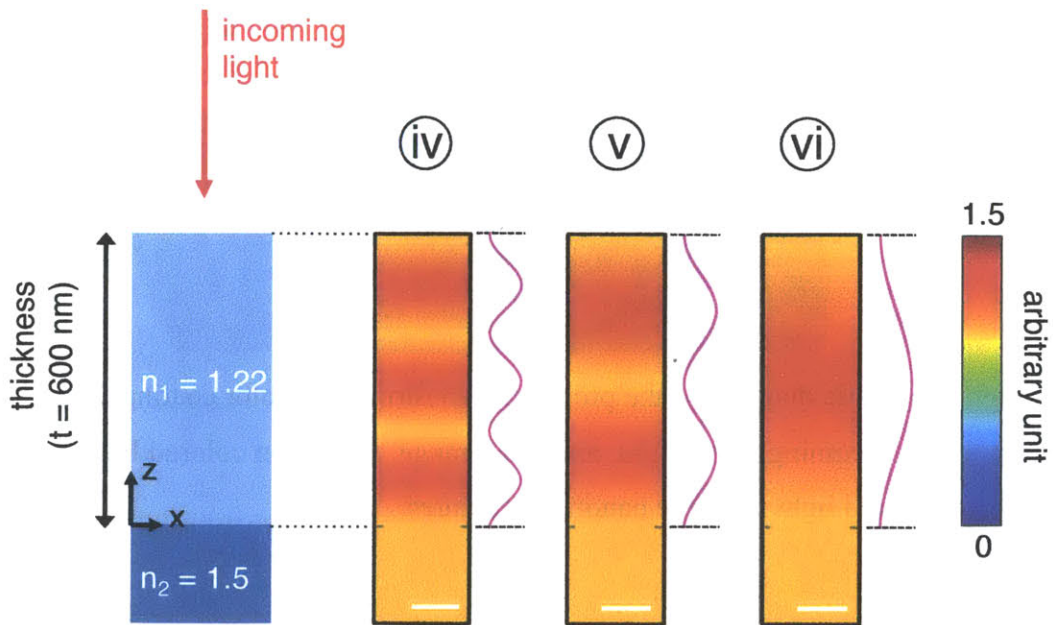


Figure 5-8. Electric field distributions calculated using FDTD at (iv), (v), and (vi) in Figure 5-6 (constructive interference). All the white scale bars represent 100 nm.

5.4 Design and optimization

The proposed nanostructured color coating on a silicon surface is presented in Figure 5-9, which consists of 2D arrays of silicon nanorod structures with different heights. There is no additional material required, which leads to ease of fabrication, and the output reflected color can be tuned by changing the height of the silicon nanorod structures.

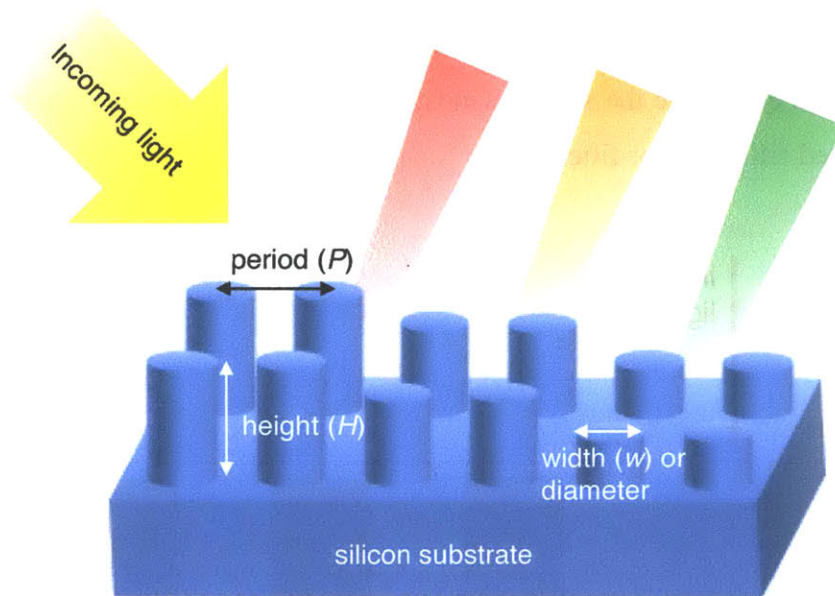


Figure 5-9. Schematic diagram of the proposed nanostructured color coatings. The yellow beam represents incoming white light, and red, orange, and green colored beams indicate the reflected colored light from the nanorod structures.

We first design the geometry of 2D periodic nanostructures for vivid color generation. Interference lithography (IL) is employed since it is one of the most effective and low-cost approaches for large-area nano-patterning of periodic nanostructures, as discussed in Chapter 1. As schematically shown in Figure 5-9, periodic nanorod structures can be fabricated by IL with 3 geometrical parameters: a certain period (P) that is determined by an exposure angle of interference lithography (see Eq. 1.28), a width (w) or a diameter of the nanorod that is controlled by exposure time and different kinds of photoresist, and a

height (H) that can be adjusted via reactive ion etching time. Among the three design parameters, we fix the period of the nanorods (P) because it is extremely difficult to adjust the exposure angle from time to time for creating different periodicity of the structures on a single substrate. The period P should be less than 400 nm because visible light through the periodic structures must not be diffractive due to its periodicity. This smaller period ($P < 400$ nm) leads that the nanostructured layer consisting of periodic structures can be considered as a homogeneous medium with an effective refractive index. The reliable and practical range of the periodicity that can be fabricated with a Lloyd's mirror system ($\lambda = 325$ nm) is ~ 170 nm to ~ 2000 nm. We choose the period (P) to be 200 nm for the design, optimization, and fabrication of the nanostructures.

Before determining the optimal geometrical constraints of the nanorods, the physical principle of wavelength-selective reflectance phenomena on the subwavelength periodic silicon nanorods is investigated through optical simulations and modeling. As shown in Figure 5-10, the reflectance spectra against normal incident light are calculated by FDTD simulations with respect to different heights of the periodic nanorods with a fixed width of 160 nm and a period of 200 nm. Each reflection spectrum has dips and peaks. As the height of the nanorods increases, these peaks and dips observed in the spectra shift to the right side, which results in positive slopes (represented by red dotted lines) in Figure 5-10. The optical path length through the medium consisting of subwavelength nanorods on the silicon surface increases while the height increases; thus the peaks and dips of the spectral response of reflected light shift to the right side of the x-axis in the graph, which is strong evidence that the layer of subwavelength nanorods acts as a homogeneous medium with effective optical properties. This phenomenon can be explained by effective medium theory [65, 66]. This is also seen that as a thickness of a homogeneous thin film on top of a silicon substrate increases, the specific wavelengths (where constructive and destructive interferences occur) change due to the variation of optical path length.

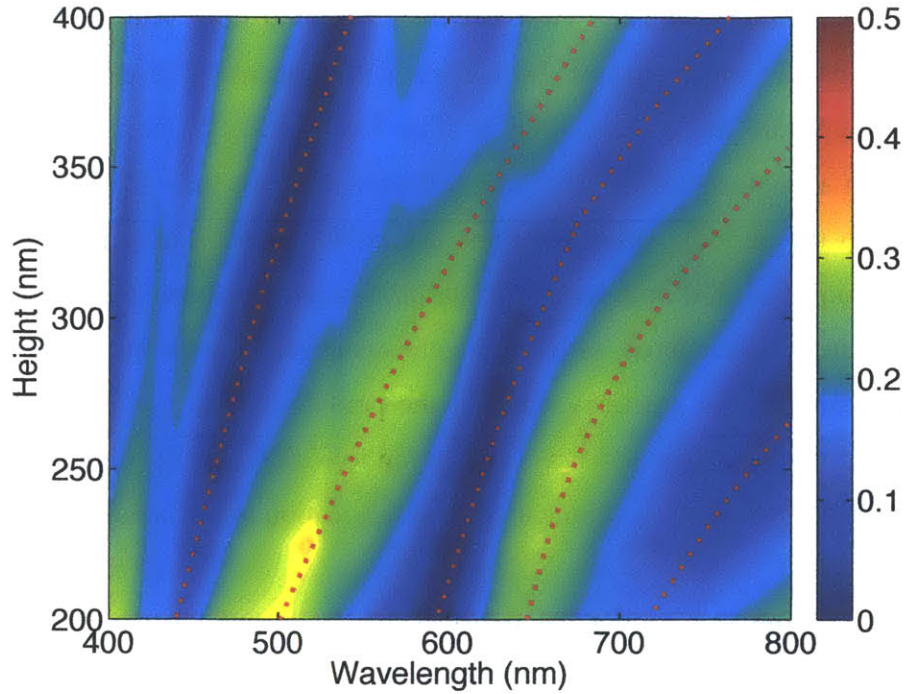


Figure 5-10. Optical reflectance spectrum against normal incident light calculated by finite difference time domain (FDTD) simulations with respect to different heights of the periodic nanorods and wavelengths with a fixed width of 160 nm and a period of 200 nm.

To validate the proposed model, the layer of the nanostructured rods is modeled as a homogeneous thin film on top of a silicon surface with effective refractive indices, which can be determined from the effective indices of the fundamental mode of waveguides of infinite silicon rod structures [139]. Mode Solver (MODE Solution 6.6, Lumerical Solutions Inc.) is used for calculating the effective indices of the fundamental mode of silicon rod structures. Based on this thin-film model, we can calculate reflective spectral responses from multiple reflections and transmissions at the optical interfaces by using transfer matrix method [145], and also estimate local minimum and maximum reflectance values, which correspond to the wavelengths where constructive and destructive interferences occur, with respect to different heights of the structures. Figure 5-11 shows the reflectance spectra against normal incident light based on the thin-film model with respect to different heights of the periodic nanorods with a fixed width of 160 nm and a period of 200 nm, which are the same conditions used in Figure 5-10. As expected from

thin-film interference, each spectrum with a fixed height also has multiple local dip and peak values.

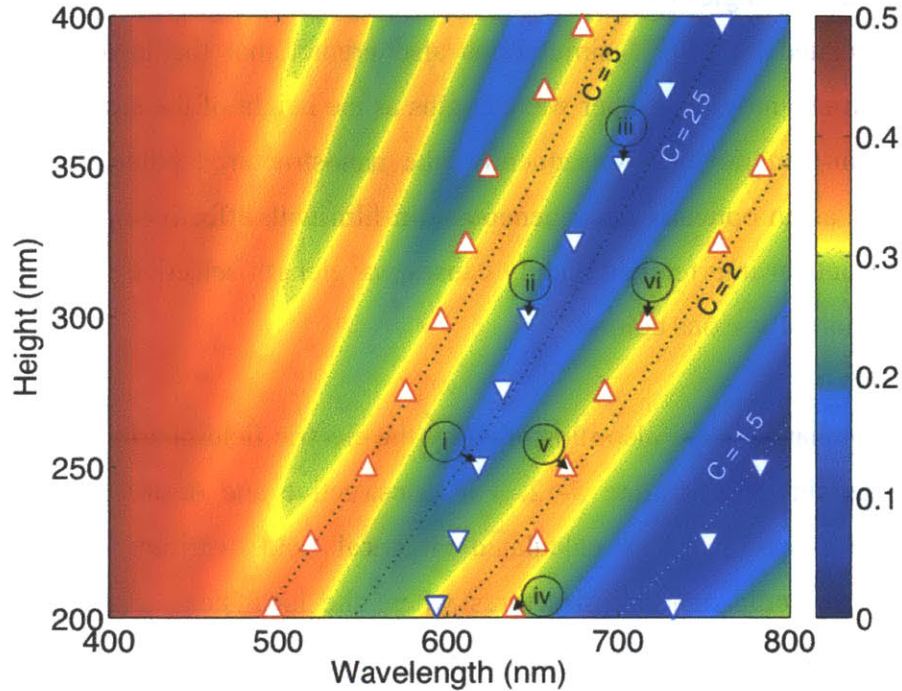


Figure 5-11. Optical reflectance spectrum against normal incident light calculated by using the thin-film model and transfer matrix method with the same geometrical constraints used in Figure 5-10. A layer of the nanorod structures is considered a thin flat film with an effective refractive index that is determined to be that of the fundamental mode of the silicon waveguide. The dotted lines shown with the calculated C values represent the calculated local maximum and minimum reflectance values from the thin-film model. The upright triangle marks represent the local maximum reflectance values in Figure 5-10 calculated from FDTD; in contrast, the downward pointing triangle marks represent the local minimum reflectance values in Figure 5-10 calculated from FDTD. Both the dotted lines and the triangle marks show good agreement.

The dotted lines in Figure 5-11 indicate the local maximum and minimum reflectance values calculated from the thin-film model with the effective refractive indices, having

the same C values with varying the height from 200 nm to 400 nm. The local maximum and minimum reflectance values, calculated from FDTD simulations (Figure 5-10), are also represented with triangle marks in Figure 5-11. It can be seen that the results from the thin-film model demonstrated by the dotted lines and those from FDTD simulations presented by the triangle marks match well. As expected, theoretical reflectance spectrums calculated by FDTD simulations also predict that the local peak and dip reflectance positions move to longer wavelengths as the height of the structures increase, as with the thin-film model. Consequently, the nanostructured color coating can be simply modeled as an optically homogeneous thin film with effective optical properties, and the strong optical interference mainly causes wavelength-selective reflection, which leads to generation of various colors.

The physical mechanisms are also illustrated by the electric field distributions calculated from FDTD, as shown in Figure 5-12. The constructive and destructive interference phenomena are observed in the calculated electrical field distributions at the cross-sections of the periodic nanorod structures where the local peak and dip reflectance values are located in Figure 5-11. Along the line passing through through (i), (ii), and (iii) in Figure 5-11 (exhibiting the local minimum reflection values), the two-and-one-half wavelengths of light are trapped inside of the nanorods in Figure 5-12a, which is the condition for destructive interference. In contrast, the local maximum reflection appears along the line passing through (iv), (v), and (vi) in Figure 5-11, showing that the two wavelengths of light exist inside of the nanorods in Figure 5-12b, which corresponds to the condition for constructive interference. Incoming light is tightly confined to the core of the silicon nanowires in both cases. The purple-colored waves on the right-hand side of Figures 5-12a and 5-12b represent the waves trapped inside of the silicon nanorods. Again, these electrical field distributions verify that the wavelength-selective reflectance is based on the interference effects inside silicon nanorod waveguides where the incoming beam is localized due to the guided mode of the nanorods. The physical mechanism of the wavelength-selective reflectance for producing color changes is the constructive and destructive interferences from coupled light inside the nanorod structure, which can simply be considered Fabry-Perot interference in the effective medium.

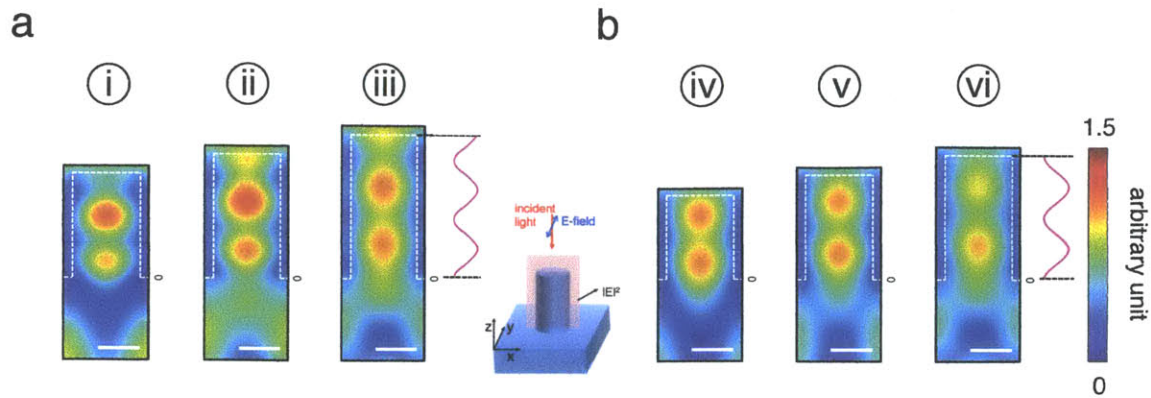


Figure 5-12. a) Calculated electric field distributions using FDTD at the cross-sections of the nanorod at the wavelength of (i) 617 nm with the height of 250 nm, (ii) 648 nm with the height of 300 nm, and (iii) 710 nm with the height of 350 nm. b) Electric field distributions at the cross-sections of the nanorod at the wavelength of (iv) 640 nm with the height of 200 nm, (v) 670 nm with the height of 250 nm, and (vi) 718 nm with the height of 300 nm. The inset between Figures 5-12a and 5-12b schematically shows the cross-section of the nanorod where the electric field distributions are calculated by FDTD. White dotted lines show the boundary of the nanorod structures. Note that all the scale bars represent 100 nm, and the circled numbers can be found in Figure 5-11.

Based on the mechanism of the wavelength-selective reflectance, the geometry of the color filter is optimized in order to generate vivid colors from the nanostructured silicon surface. Figure 5-13 demonstrates spectral reflectance responses of 4 different diameters (or widths w) of nanorods (120 nm, 140 nm, 160 nm, and 180 nm for Figures 5-13a, 5-13b, 5-13c, and 5-13d, respectively) against normal incident incoming light, calculated by FDTD simulations. In all the graphs, the height of the nanorod structures varies from 200 nm to 400 nm (y-axis) with a fixed period of 200 nm. It is expected that the slopes of the local reflectance dips and peaks get decreased as the diameter increases. The bigger diameter of the nanorods (contributing to a higher effective refractive index of the medium and a higher effective index of the fundamental mode of propagating light inside the silicon nanorod) lengthens the optical path length across the medium consisting of the nanorods, which results in less steep slopes of the dips and peaks in the reflective spectral

response contour map. To produce a variety of colors from reflection of light, local peak values of reflectance spectral response should shift from the beginning ($\lambda \sim 400$ nm) to the end ($\lambda \sim 800$ nm) of the visible wavelength range. However, we cannot estimate observable colors only from the reflected spectrum responses demonstrated in Figure 5-13.

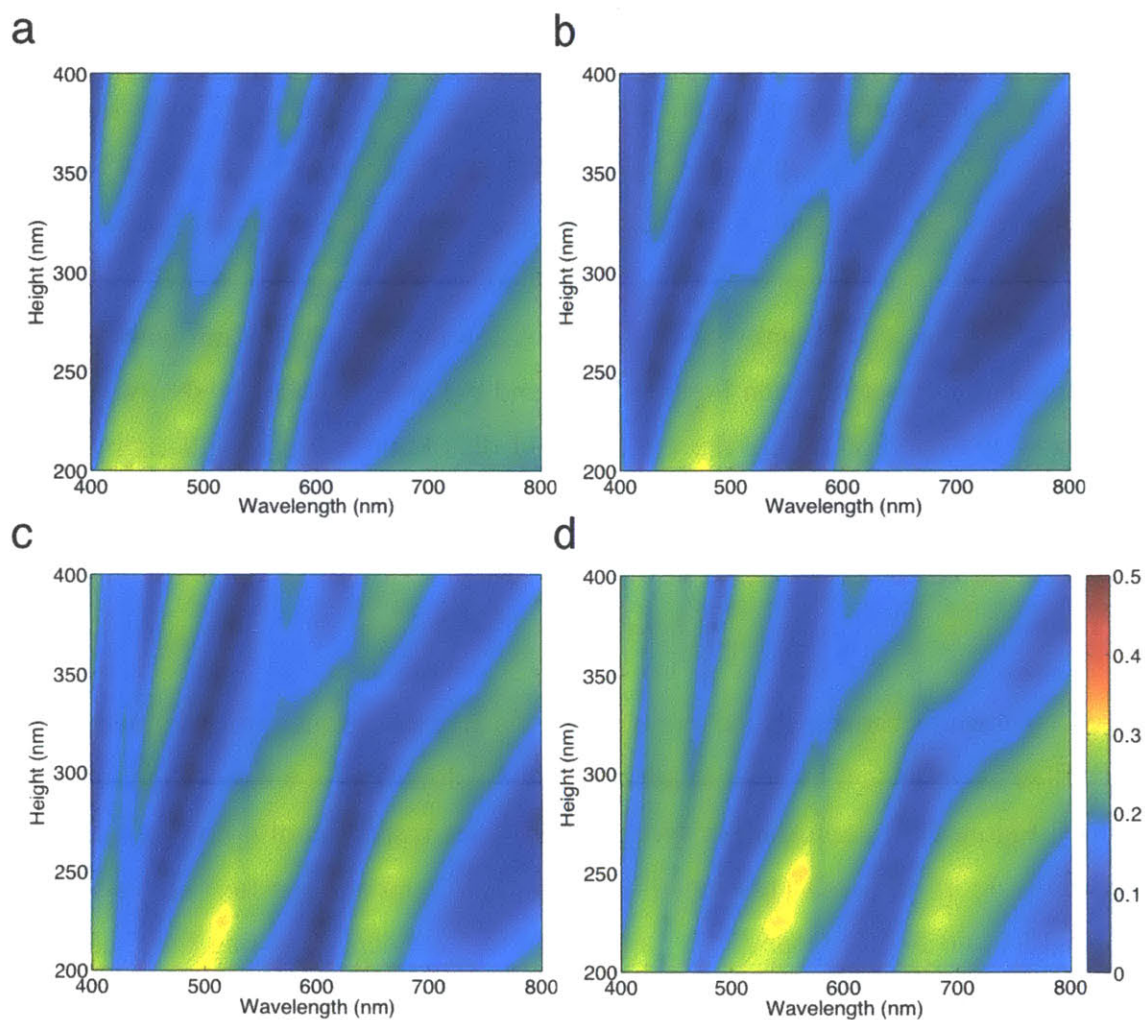


Figure 5-13. Optical reflectance spectrum against normal incident light calculated by FDTD simulations with respect to different heights of the periodic nanorods with a period of 200 nm and a fixed diameter of a) 120 nm, b) 140 nm, c) 160 nm, and d) 180 nm.

In order to represent colors from the spectral responses, each color from the specific geometry of nanostructures is mapped on top of the CIE 1931 chromaticity diagram [143, 144] in Figure 5-14. Chromaticity coordinates (x , y) in the diagram are calculated for light of any spectral power distribution, and the x and y coordinates indicate the color on the diagram we can see. When a spectral power response indicates a point near the white region located in the center of the diagram, white is observed. In contrast, single wavelengths of the spectral responses are located along the edge of the diagram, emitting the most distinct colors. Colored dots on the chromaticity diagram indicate colors that will be produced from the reflectance spectral responses with respect to different heights. Therefore, these dots should be placed near the edge of the chromaticity diagram, so as to create vivid colors from the nanostructured surfaces. The surface consisting of nanorods with a diameter of 160 nm and with varying heights (from 200 nm to 400 nm with a 25 nm incremental step) generates the most vivid colors compared to the colors from other sizes of the diameters, which are highlighted by red dots. For comparison, the upper right-hand side inset is the magnified diagram of the part surrounded by the black dotted box, which demonstrates the colors generated from the nanorod structures with a diameter of 120 nm (presented by green solid dots and dotted lines), 140 nm (presented by orange solid dots and dotted lines), 160 nm (presented by red solid dots and dotted lines), and 180 nm (presented by purple solid dots and dotted lines), with respect to the varying heights from 200 nm to 400 nm with a 25 nm incremental step.

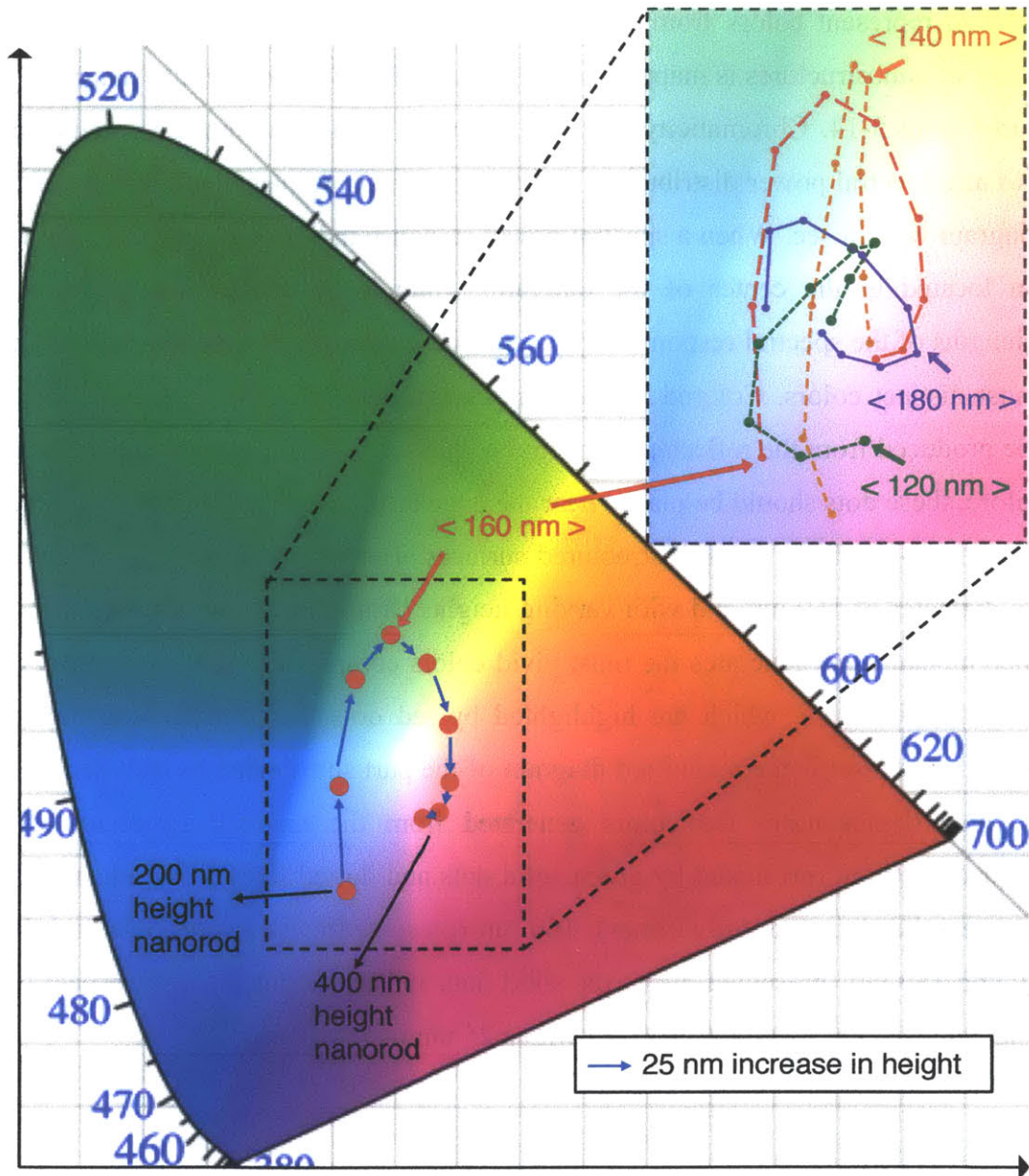


Figure 5-14. Reflected colors from the nanorod structures with varying height from 200 nm to 400 nm with a 25 nm step increase (presented by blue arrows) mapped on top of the CIE 1931 chromaticity diagram, with a fixed diameter of 160 nm. For comparison, the inset shows the colors generated from the nanorod structures with a fixed diameter of 120 nm (green solid dots and dotted lines), 140 nm (orange solid dots and dotted lines), 160 nm (red solid dots and dotted lines), and 180 nm (purple solid dots and dotted lines), with respect to the varying heights (from 200 nm to 400 nm with a 25 nm incremental step).

The rate of change in color with respect to size of nanostructures is much less than that of existing silicon color filters; consequently, the fabrication process of the nanostructured color filter that we propose is more stable than those of the color filters previously developed [138, 139]. Here, a 25 nm change in the height of the proposed structures can suffice to achieve generation of different colors. In contrast, with the existing silicon nanowire color filters [138, 139], a deviation of only 5-10 nm in the diameter of the nanostructures changes the output colors. This relative instability means that reliable color production is dependent on exceptionally accurate fabrication methods such as electron beam lithography.

5.5 Fabrication process

The nanostructured color filter is fabricated by interference lithography followed by reactive ion etching (RIE) for the geometry determined by the analysis and optimization on the three different design parameters based on the optical properties. The duty cycle of the optimized structures, which is defined as the ratio of the width (or diameter) to the period of the grating, is 0.8 (= 160 nm / 200 nm). Generally, fabricating nanostructures with a large duty cycle (> 0.5) is extremely challenging via conventional interference lithography [47, 96]; however, in the thesis a novel lithographic technique using negative photoresist has been developed and utilized for ultra high aspect-ratio nanocone structures, as discussed in Chapter 3 (see Section 3.3.2). This developed method allows making large duty cycle (> 0.5) 2D nanorod structures with interference lithography [93, 142]; therefore it is utilized to create the designed nanostructured color filters. Note that the shrinking mask etching for creating tapered structures is not needed in this process because the nanorod structures with sharp vertical side walls have to be created.

Figure 5-15 illustrates the detailed fabrication processes and corresponding SEM images. A multi-layered coating is first created on top of a crystalline silicon wafer. The coating consists of a negative photoresist layer (PS4, Tokyo Ohka), a 20-nm-thick layer of SiO₂, and an anti-reflective coating layer (XHRiC-16, Brewer Science). The thickness of each layer is optimized for interference lithography (IL) and the incident angle of the laser ($\lambda = 325$ nm) in IL is adjusted for the spatial period of 200 nm (see Eq. 1.28). Two orthogonal laser exposures are projected onto the photoresist by using the Lloyd's mirror setup and the exposed photoresist is developed to create an array of holes, as shown in Figure 5-15a.

CF₄ and O₂ reactive ion etching processes are then used to transfer the pattern of holes to the SiO₂ interlayer and ARC layer, to open the silicon surface, and to enlarge the size of the holes, as shown in Figures 5-15b and 5-15c, respectively. This process is critical for creating large duty cycle rods (or gratings) via IL. Hydrogen silsequioxane (HSQ14, Dow Corning) is filled into the fabricated holes, and then baked at 200 °C, as shown in Figure

5-15d. After removal of the SiO₂ and ARC layers using CF₄ and O₂ reactive ion etching, only the cured HSQ posts survive, as shown in Figure 5-15e. The pattern of HSQ posts is finally transferred to the silicon substrates after reactive ion etching with hydrogen bromide (HBr) gas, as shown in Figure 5-15f. The fabrication steps are almost identical to those introduced in Chapter 3; however, the shrinking mask etching process is not required for fabricating the nanorod structures. The different etch rates between the HSQ and silicon, and the thickness of the HSQ post, enable realization of the silicon nanorod structures. Note that all the scale bars represent 200 nm.

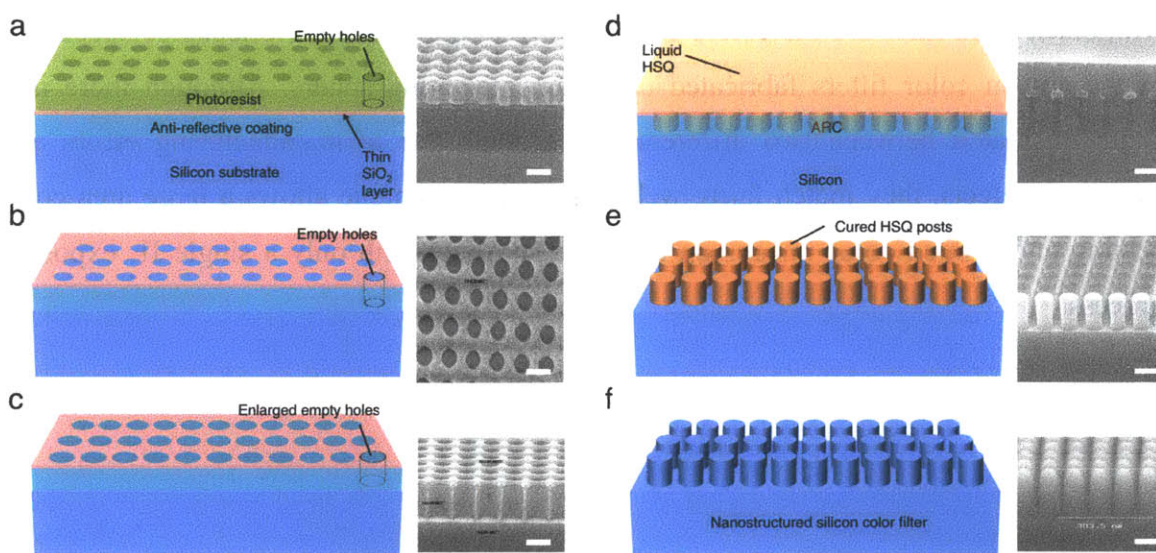


Figure 5-15. Schematic of the fabrication process and the corresponding SEM images. a) Development of negative photoresist pattern. b) Transferring the area of the nanohole pattern into anti-reflective coating layer. c) Enlargement of the size of the holes through oxygen reactive ion etching (RIE). d) Hydrogen silsequioxane (HSQ) filling the fabricated holes. e) HSQ posts. f) Subwavelength periodic silicon nanorods for color coating. Note that all the scale bars represent 200 nm.

5.6 Results and discussion

An image of the fabricated sample and its corresponding colors marked on the CIE chromaticity diagram is shown in Figure 5-16. The surface area of the fabricated silicon substrate is as large as 2 cm by 4 cm, and it has multiple colors depending on the height of the nanorods, which is determined by controlling the etching time in the final RIE step. The periodic subwavelength silicon rods exhibit vivid reflective colors that can be tuned by controlling their height. The red solid circles represent the calculated colors from the reflectance spectrum from the designed and optimized nanostructures, and the circles with black solid lines are the colors calculated from the measured reflectance spectrums of the silicon color filters fabricated using an integrating sphere. Although there is a slight mismatch between two different sets of dots due to manufacturing errors and structural defects, they match fairly well. This color technique allows a large area color coating and printed color images on a silicon substrate with only a single IL exposure process.

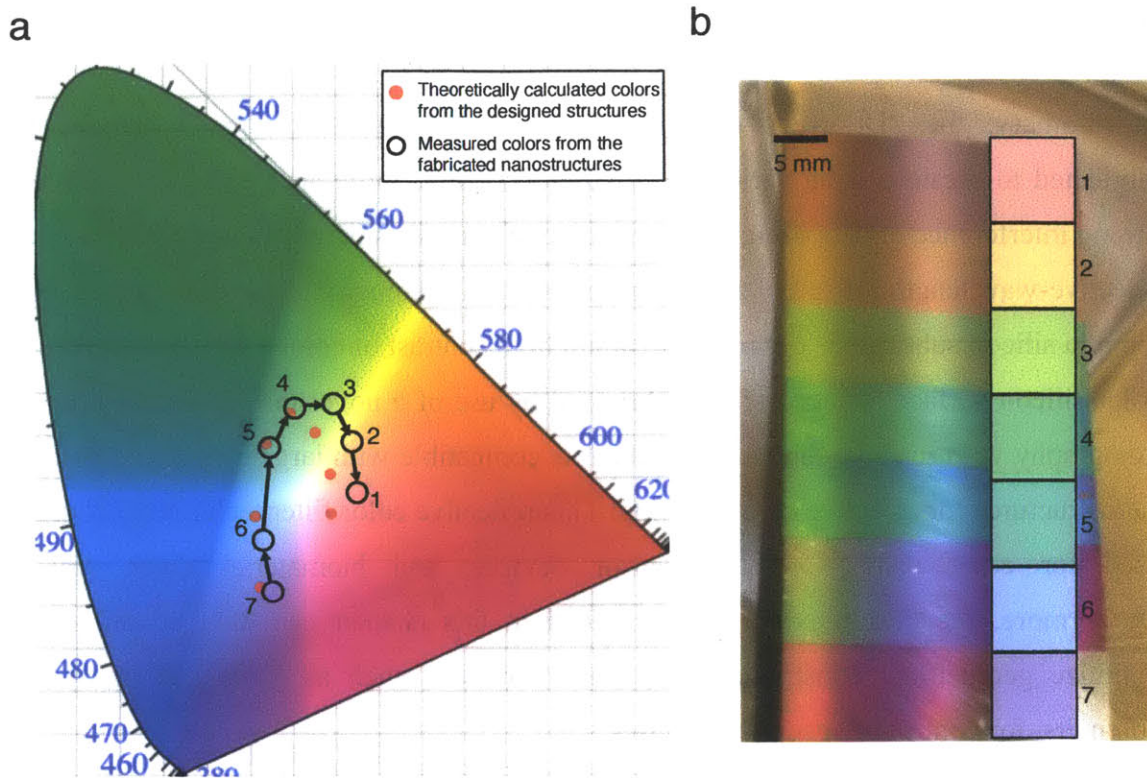


Figure 5-16. a) Colors theoretically calculated by FDTD simulations (red solid dots) and experimentally measured colors (black hollow dots) from the fabricated nanostructured color coatings placed on the CIE chromaticity diagram. b) The image of the fabricated sample and its corresponding colors.

5.7 Conclusion

In summary, the 2D arrays of periodic subwavelength silicon nanostructures are fabricated to create a wide variety of vivid colors on as large an area as 2cm by 4cm. Strong interference effects occur inside a lattice of periodic silicon nanorods, which allow selective-wavelength reflective spectral responses. The geometry of the nanostructures on top of a silicon substrate is optimized to attain high contrast of colors. The nanostructured color silicon surface is successfully fabricated by use of a novel method of interference lithography with reactive ion etching, which is compatible with large duty cycle periodic nanostructures for effective color filtering. This reflective color filter technology could be used for color displays, image sensor devices, and biomaterial color sensors. Furthermore, the design principle introduced in this chapter can also be utilized to optimize geometrical constraints with other materials, such as glass and transparent polymers, for control of spectral responses.

Chapter 6

Thesis Summary and Future Work

6.1 Thesis Summary

In this thesis I present nanostructured multifunctional materials for control of light transport and surface wettability, and newly developed nanofabrication methods for these new materials. First, the nanostructured multifunctional silica surfaces for enhanced omnidirectional broadband transmissivity with structural superhydrophilicity or robust superhydrophobicity have been successfully designed and fabricated through a systematic approach to concurrent design of optimal nanostructures in two domains, optics and wetting, and novel fabrication procedures that achieves the desired aspect-ratios. To fabricate this nanostructured multifunctional surface, the multiple shrinking mask etching method has been successfully invented and implemented. This method has also been utilized for successful fabrication of subwavelength periodic silica nanocone structures with controllable-aspect-ratio of 4.5 to 7. In addition, simple and low cost fabrication methods for silica nanocone structures with low aspect-ratio of 2 to 3 have been developed, with and even without the hardmask material that had been considered an essential for fabricating high aspect-ratio structures.

For transparent anti-fingerprint surfaces, in contrast to previous studies that have targeted an oil repellency mechanism, the counter-intuitive approach of constructing our surface from an *oleophilic* material has been taken; consequently, transparent fingerprint-eating surfaces, which are optimized for optical transparency and photocatalytic fingerprint removal, have been constructed based on oleophilic titania nanoparticle structure using LbL assembly. It achieves a practical degradation time (≤ 3 hours under sunlight) of fingerprints, while also retaining optical transparency comparable to ordinary glass and also being compatible with flexible glasses.

While eliminating all reflections over the broadband wavelengths of light with the tapered silica nanocone structures introduced in Chapter 2, 2-dimensional (2D) periodic silicon nanorod structures capable of generating vivid colors based on selective-wavelength reflection have also been designed, and created. The newly invented nanofabrication processes combined with interference lithography allow scalable nanopatterning of the colored silicon nanostructures.

6.2 Future work

Preliminary results of new nanofabrication methods for the nanostructured multifunctional materials will be briefly introduced. Moreover, possible future work and applications of these nanostructured multifunctional materials developed in this thesis will also be discussed.

6.2.1 Grayscale Interference Lithography (GIL)

Interference lithography has been used for creating the nanostructured multifunctional materials throughout this thesis. Although it enables the large-scale fabrication of perfectly periodic nanostructures with rapid patterning, most of the work have been limited to creating only periodic nanostructures. In other words, aperiodic nanostructures cannot be achieved by conventional interference lithography system such as Lloyd's mirror interferometer [50] and Mach-Zehnder interferometer [51]. Scanning beam interference lithography continuously varies the pattern period and orientation, but it's not a simple and low cost setup and it also requires complex control devices [146].

Here, I propose a novel and simple method to fabricate aperiodic subwavelength nanostructures by Grayscale Interference Lithography (GIL) with the conventional Lloyd's mirror interferometer and a movable aperture plate, which allows spatially varying duty cycle of gratings with a single exposure [96]. The key requirement for being able to successfully switch the duty cycle of the grating is the movable aperture plate, which modulates exposure dose on a photoresist layer [96].

The advantage of the proposed process is that it employs additional aperture plate with the interference lithography system, consequently presenting itself as a practical fabrication process of aperiodic subwavelength nanostructures with significantly lower manufacturing time and cost than existing approaches such as electron beam lithography (EBL) system.

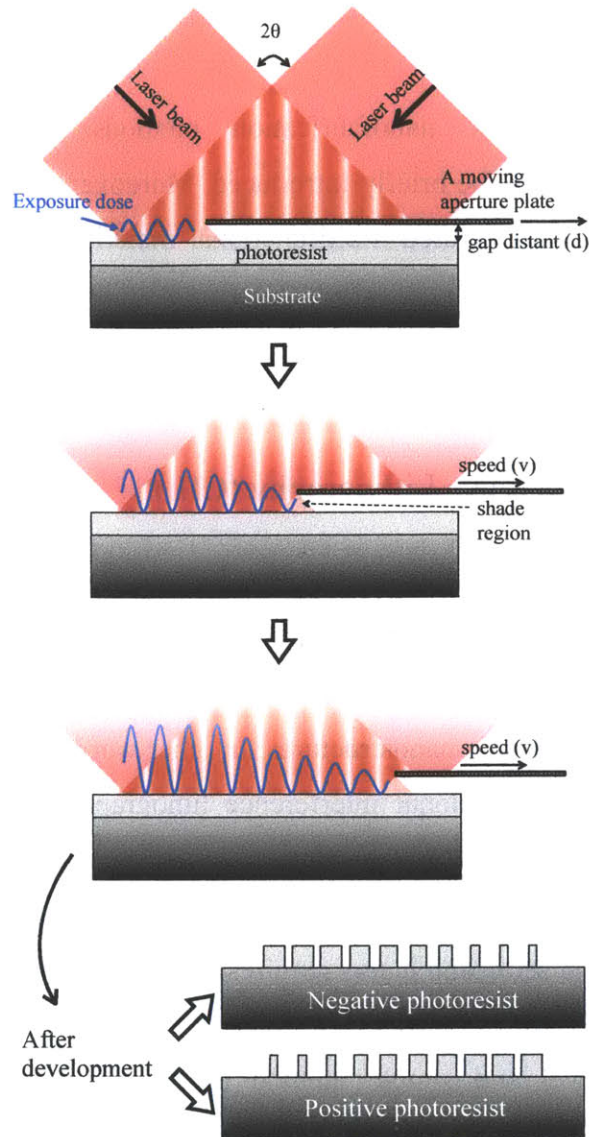


Figure 6-1. Schematic of Grayscale Interference Lithography (GIL) processes for fabricating aperiodic subwavelength nanostructures. Aperiodic subwavelength nanostructures can be created by the conventional interference lithography combined with a moving aperture plate [96].

The proposed fabrication process for GIL is illustrated in Figure 6-1. The process is based on the conventional interference lithography with exposure dose modulation by the moving aperture plate. The aperture plate can move at a speed (v) as a function of time,

and exposure dose will be mainly determined by intensity of the interfering laser beams and exposure time with the movement of the plate.

In order to fabricate aperiodic subwavelength nanostructures by GIL, the conventional Lloyd's mirror interferometer is used. When two coherent plane waves propagate with the angle (2θ), there is a sinusoidal intensity pattern with the spatial period P , which is given by

$$P = \frac{\lambda}{2n\sin\theta}, \quad (6.1)$$

where λ is the wavelength of the laser, and n is the refractive index of the surrounding medium (air). Interference lithography is typically performed with an anti-reflective coating layer deposited below a photoresist layer owing to maximize contrast of the sinusoidal intensity pattern by minimizing the reflection from the interface between the coating and the resist layer, as mentioned in Chapter 3. In the case of no reflection from the interface by introducing the anti-reflective coating, a sinusoidal exposure dose recorded by the interfering laser beams has perfect contrast, which leads to improvement of the photoresist sidewall.

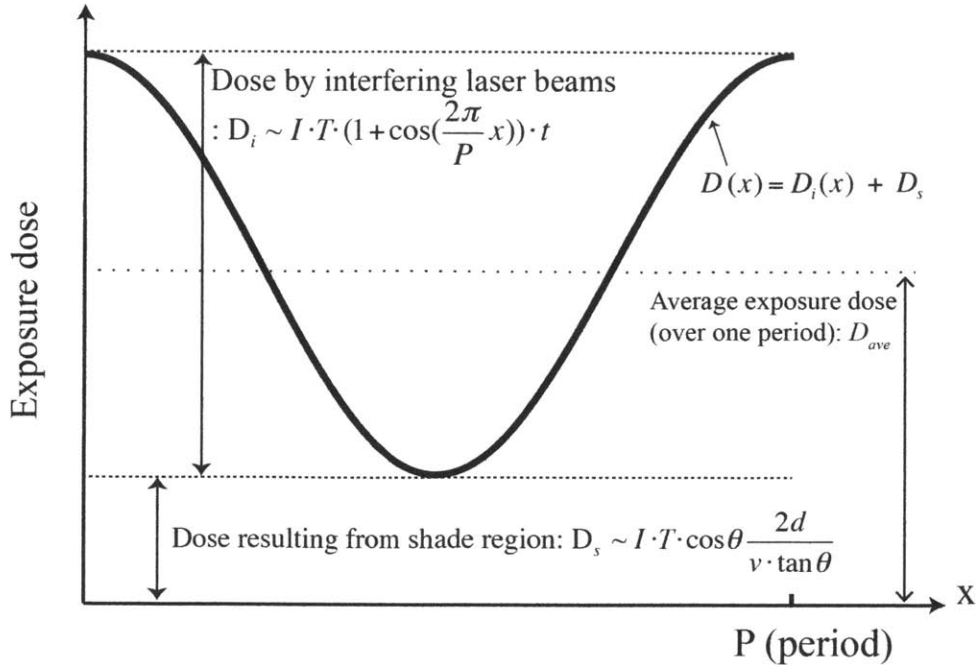


Figure 6-2. Exposure dose distribution with respect to lateral position (x) over one period (P) in Grayscale Interference Lithography (GIL). The total exposure dose (D) is the sum of the dose exposed by the interfering beam (D_i) and the dose exposed by single beam under the shade region (D_s) [96].

GIL, however, has one difference feature from the normal interference lithography, which is that a gap between the photoresist and the aperture plate creates shade region, depicted in Figure 6-1, exposed by only one beam instead of two laser beams that generate a sinusoidal intensity pattern. This region results in lowering the contrast of the exposure dose distribution, which is plotted in Figure 6-2. Since the dose exposed by the single beam under the shade region (D_s) is proportional to intensity times dwell times, it is estimated as follows:

$$D_s \sim I \cdot T \cdot \cos\theta \frac{2d}{v \tan\theta}, \quad (6.2)$$

where I is the incident intensity normal to the propagation direction of the light (measured with a power meter), θ is the incident angle, T is the fraction of the incident light that is transmitted into the resist (transmission coefficient of Fresnel equations), d is the gap distance between the aperture plate and resist layer, and v is the speed of the aperture plate at a specific position. The dose exposed by interfering laser beams is given by

$$D_i \sim I \cdot T \cdot \left(1 + \cos\left(\frac{2\pi}{P}x\right) \right) \cdot t, \quad (6.3)$$

where t is the time exposed by the interfering lasers.

The total exposure dose (D) should be the sum of the dose exposed by the interfering beam (D_i) and the dose exposed by single beam under the shade region (D_s). Due to the existence of the gap in GID, the minimum value of the total dose is the same as the dose exposed by the single beam (D_s). It lowers the contrast of the exposure dose distribution, which is given by

$$C = \frac{D_{\max} - D_{\min}}{D_{\max} + D_{\min}}. \quad (6.4)$$

In practice, the values of C should be greater than 0.9 to fabricate good profile of gratings [147]. To maximize the contrast C , the minimum value of the total dose, which is the dose exposed by the single beam (D_s) on the shade region, should be minimized by controlling the gap distance (d) and velocity (v).

In this experiment, the incident angle of the laser ($\lambda = 325$ nm) is optimized for the spatial period P , which is 200 nm. First, hydrogen silsequioxane (HSQ14, Dow Corning, 310 nm) films are then spun on a silicon wafer and hard-baked at 500°C in an oven for 4 hours to

be cured, because a cured HSQ layer is optically similar to SiO₂ layer. After RCA cleaning, sonication, and plasma oxygen etching for 30 seconds in order to remove organic particulates, an anti-reflective coating layer (I-con 7, Brewer Science, 105 nm) is spun on top of the HSQ layer and baked at 180°C in a hot plate for 1 minute. Each of the thicknesses of the multiple coated layers on the wafer is optimized for interference lithography in order to remove reflected beams from the interfaces between the stacked films below a photoresist layer, as well as increase contrast of the sinusoidal intensity pattern [148], as mentioned previously. A positive photoresist (PFI-88A2, Sumitomo, 240 nm) is spun on the stacked layers in the end, and baked on the hot plate at 90 °C for 90 seconds. Using Lloyd's mirror, the two laser beams make an interference pattern with a 200 nm period standing wave projected onto the photoresist for 1D grating. Two separate orthogonal laser exposures are projected onto the photoresist to fabricate 2D grating, with an interval time of 1 minute. During the exposure, a motorized linear stage (Zaber Technologies) is utilized to control the speed of the aperture plate and modulate exposure dose. The gap distance (d) is fixed with 1 mm to maximize the contrast of the exposure dose distribution (C). After exposure, the exposed photoresist is developed to leave a pattern of lines and posts.

By using the conventional Lloyd's mirror system with the moving aperture plate, the 1D and 2D aperiodic subwavelength gratings with varying duty cycles are successfully fabricated by single and double exposure methods. The duty cycle of the grating is defined as the ratio of the width to the period of the grating. Figures 6-3a and 6-3b show the image of the fabricated 1D grating sample, and cross-sectional micrographs of the 200 nm period 1D grating fabricated by GID with the single exposure, respectively. The moving aperture is moved from *viii* region to *i* region at a 31.25 $\mu\text{m/s}$ constant speed for 16 minutes to fabricate the 1D grating. Before the exposure, the aperture plate covers the whole prepared sample. After the exposure begins, it starts to move away from the sample to the left side of Figure 6-3a. As shown in Figure 6-3b, the duty cycle of the aperiodic 1D grating keeps decreasing from *i* region to *viii* region since the average value of the total exposure dose over one period (D_{ave}) increases from 4.4 mJ/cm^2 (*i* region) to 76.4 mJ/cm^2 (*viii* region) due to the linear movement of the aperture.

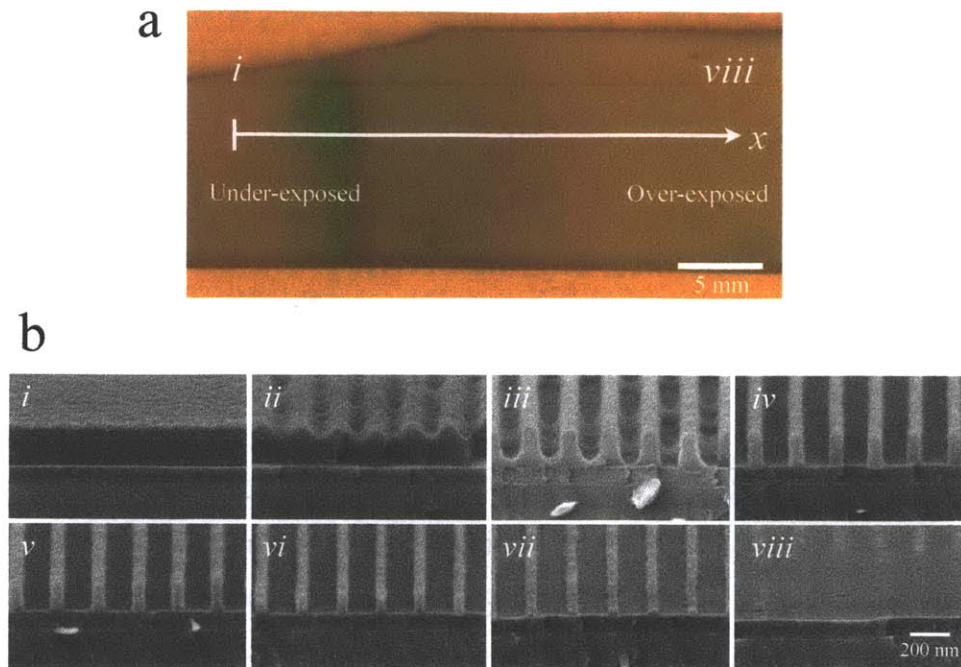


Figure 6-3. a) Image of the subwavelength 1D grating fabricated by GIL with the single exposure. During the exposure, the aperture plate moves to the left side of the sample (negative x -direction) at the constant speed. b) Cross-sectional micrographs of the grating with respect to the position from i region to $viii$ region marked in Figure 6-3a [96].

The duty cycle of the fabricated 1D grating (Figure 6-4) with respect to the coordinate in the x -dimension is plotted in Figure 6-4. Since the speed of the aperture is fixed during the experiment, the coordinate in the x -dimension is directly proportional to the average exposure dose over one period (D_{ave}). The width of the grating appears after 10 mm distance away from the starting point, because the photoresist is under exposed due to the low dose. The behavior of the duty cycle for the 1D grating fabricated by GID is found to well match the experimental results previously described in the literature [147, 148], because the dose exposed by the single beam (D_s) is much smaller than the average total dose over the whole area by controlling the gap distance. The minimum width size of the 1D grating fabricated by GID is 20 nm.

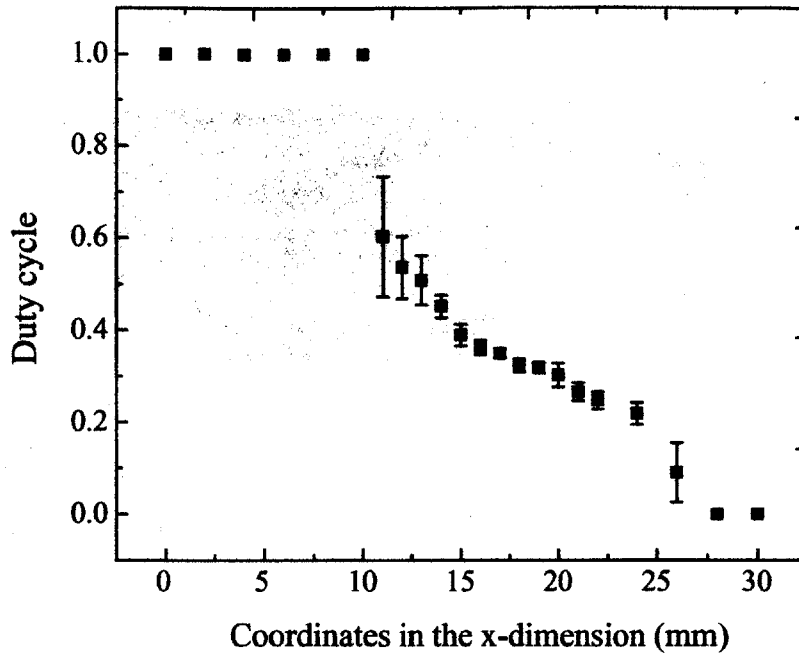


Figure 6-4. Duty cycle of the 1D grating with respect to coordinate in the x-dimension in Figure 6-3a. Error bars represent the standard deviation values of the measured duty cycles [96].

To conduct the feasibility test of 2D aperiodic gratings, two separate orthogonal laser exposures (double exposure) are projected onto the photoresist layer, as shown in Fig. 5a. The average exposure dose (D_{ave}) of the single exposure varies linearly from 22 mJ/cm² to 31 mJ/cm² with the aperture plate travelling 2.5 cm long at the constant speed 0.208 mm/s. The lowest total average exposure dose (D_{ave}) is 44 mJ/cm² on the top left region (i) and the highest total average exposure dose (D_{ave}) is 62 mJ/cm² on the bottom right region (ii), as presented in Figure 6-5a.

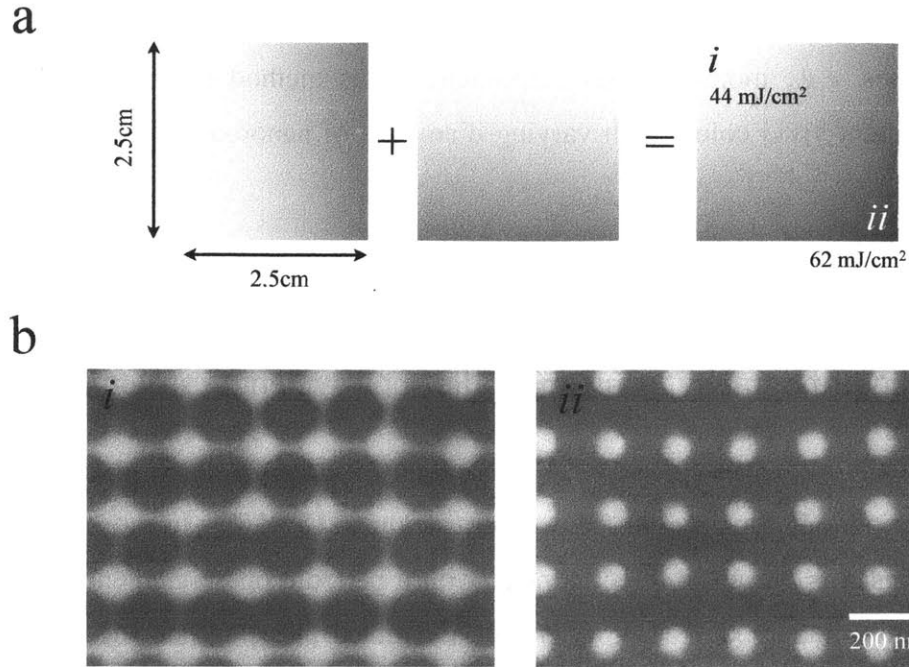


Figure 6-5. 2D aperiodic subwavelength gratings fabricated by GIL with the double exposures. a) schematic of the double exposures on a 2.5 cm by 2.5 cm sample. b) top-view micrographs of the grating on the *i* region (left) and on the *ii* region (right) [96].

Figure 6-5b shows two top-view SEM images of the 2D grating on two regions (*i*, *ii*) of Figure 6-5a. Due to the characteristic of the positive photoresist, the duty cycle of the 2D grating with lower exposure dose on the *i* region is greater than that with higher exposure dose on the *ii* region. This demonstrates that the duty cycle of the aperiodic 2D grating also can be well controlled by the modulation of the exposure dose with the moving aperture plate.

Grayscale Interference Lithography (GIL), for aperiodic subwavelength nanostructures, has been first developed. The 1D and 2D aperiodic gratings with the varying duty cycles are successfully created by GIL. The proposed process consists of the conventional interference lithography and moving aperture plate, and it delivers simple ways not only to make subwavelength gradient-index (GRIN) optical elements such as Luneburg lens [149, 150], but also to characterize and understand the behavior of a photoresist to changes in exposure dose. Future work will be to fabricate other periodic gratings with different

exposure dose modulations and different materials, and extend this process with different aperture plates, *e.g.*, motorized iris diaphragms. This method can also be utilized for creating gradient vivid colors with varying diameters of nanorod structures, as discussed in Chapter 5.

6.2.2 Talbot lithography using aperiodic subwavelength structures

In recent years, numerous phase-mask lithography techniques have been developed to fabricate periodic 3 dimensional (3D) nanostructures [151-155]. In these approaches, a thick photoresist is placed in direct contact with a periodic phase element, which can be lithographically patterned [151-154] or self-assembled [155]. When the phase mask is illuminated, the periodic structure generates a volumetric intensity distribution as governed by the Talbot effect, cross-linking (or de-crosslinking) the underlying photoresist to fabricate complex 3D nanostructures.

However, most of the work done have been limited to using periodic phase elements, which results in fabricated structures that are also periodic. Here, we explore the Talbot field generated from an aperiodic 1D grating with slowly spatially varying duty cycle while maintaining constant period [156]. Allowing the duty cycle of the phase mask to be varied enables control of the duty cycle of the resulting 3D structure [156]. We analyze the proposed lithography technique using both analytical and numerical methods, and compare the simulated results to the fabricated structures [156].

In the preliminary design we focus on a 1D phase grating with a constant period and linearly varying duty cycle. The aperiodic phase mask overlaid with the Talbot intensity pattern simulated using FDTD method is illustrated in Figure 6-6, where the mask material is a fused silica ($n = 1.48$) and the underlying material is photoresist (Sumitomo PFi88A8, $n = 1.60$). The grating is composed of eleven periods with constant period ($P = 300$ nm) and linearly increasing duty cycles from 0.2 to 0.8 with an interval 0.06. A periodic boundary condition is used in the horizontal direction, and a perfectly matching

layer is used at the bottom boundary to ensure no reflection. A transverse electric (TE) plane wave with free space wavelength ($\lambda = 325 \text{ nm}$) is illuminating from the top, and simulated intensity pattern is shown with contour color fill plot.

The simulation illustrate that the Talbot field generated from the aperiodic grating also exhibits spatially varying characteristics. It is important to note that the Talbot distance (z_t) is constant, since the period P of the phase element does not change. The variations in duty cycle lead to changes in the amplitude and phase of the diffracted orders while maintaining the spatial frequency, resulting in a spatially varying intensity contours, as observed in Figure 6-6. The Talbot distance (*i.e.*, neighboring z -distance between replicas of the original intensity pattern after the grating) is given by $2P^2/\lambda$, matching our simulation results. Upon exposure, the resulting 3D photoresist will yield variations in duty cycle due to the binary response of photoresist.

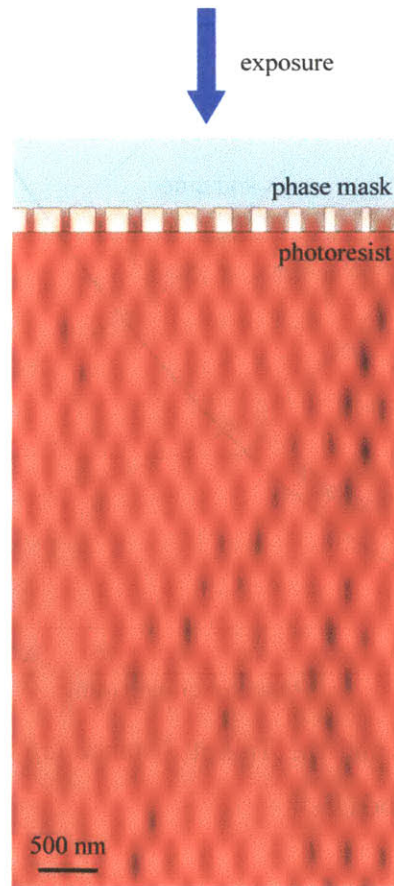


Figure 6-6. Simulated intensity pattern generated by an aperiodic 1D phase mask with linearly varying duty-cycle under normal illumination [156].

To maximize the contrast of intensity pattern of Talbot field, the geometrical constraints of the 1D phase grating, such as the period (P), height (H), and width (w), must be designed and optimized. Talbot effect is based on interference of the transmitted light waves (*i.e.*, diffracted orders), and Talbot field is not created without light diffraction. Figure 6-7 shows the diffraction orders and the Talbot distance (z_t) considering interference between the zeroth-order and the first-order diffracted lights through the 1D phase grating with respect to the period (P). This discovers that the grating period P should be greater than 220 nm to ensure Talbot fields created by interference between the zeroth-order and first-order diffracted light.

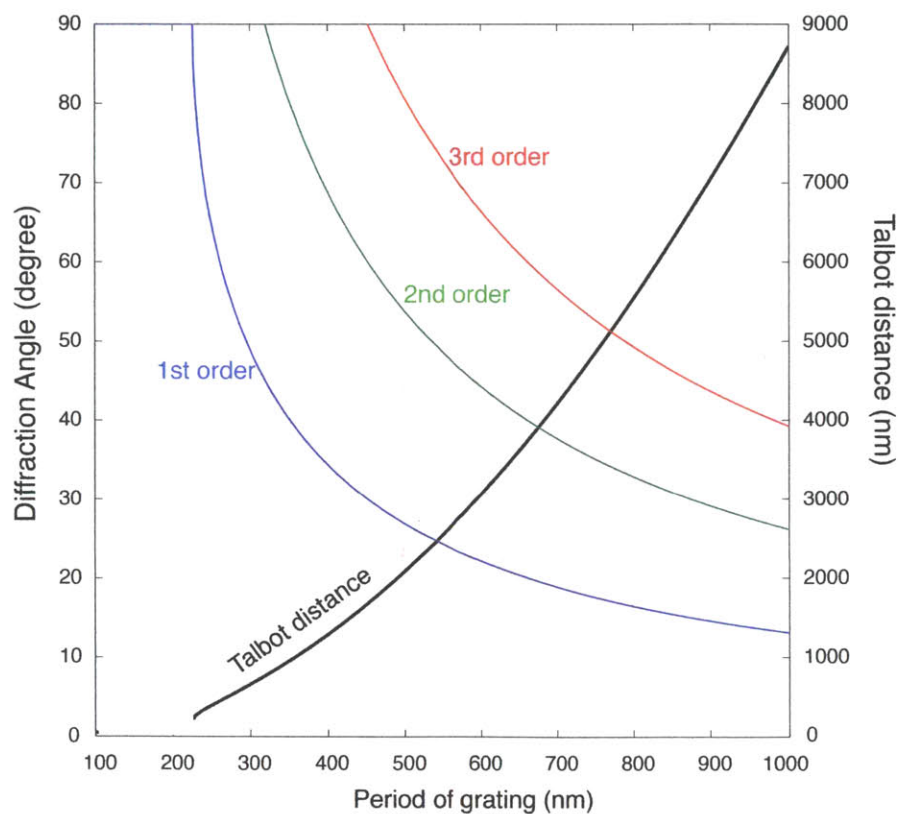


Figure 6-7. Diffraction orders and the Talbot distance (z_t) through the 1D phase grating with respect to the grating period (P).

To find the optical 1D phase mask geometry, the contrast values (C) of the intensity profile at the Talbot plane are examined. Note that the contrast of the exposure dose distribution is defined in Eq. 6.4, and in practice, the contrast values should be greater than 0.9 to fabricate good profile of gratings [147] (see Section 6.2.1). Transmitted efficiencies of the diffraction orders through the 1D grating with a period with 390 nm and a height of 220 nm as a function of the duty cycle are calculated using RCWA simulations, and plotted in Figure 6-8. Based on the calculated transmitted efficiencies, the contrast values (C) of the intensity profile at the Talbot plane can also be calculated with respect to the duty cycle, as also shown in Figure 6-8. Wider range of the duty cycle exhibiting perfect contrast values ($C = 1$) is certainly required to fabricate high contrast and sharp nanostructures; thus the optimal geometry of the phase mask that exhibit the widest range of the perfect contrast values can be found by tuning the three design parameters (period, height, and duty cycle) through RCWA simulations. The 1D phase grating ($P = 390$ nm, $H = 220$ nm) demonstrates the widest range of the perfect contrast values over duty cycles between 0.13 and 0.7, as shown in Figure 6-8; thus this has been chosen for the fabrication of the 1D phase mask.

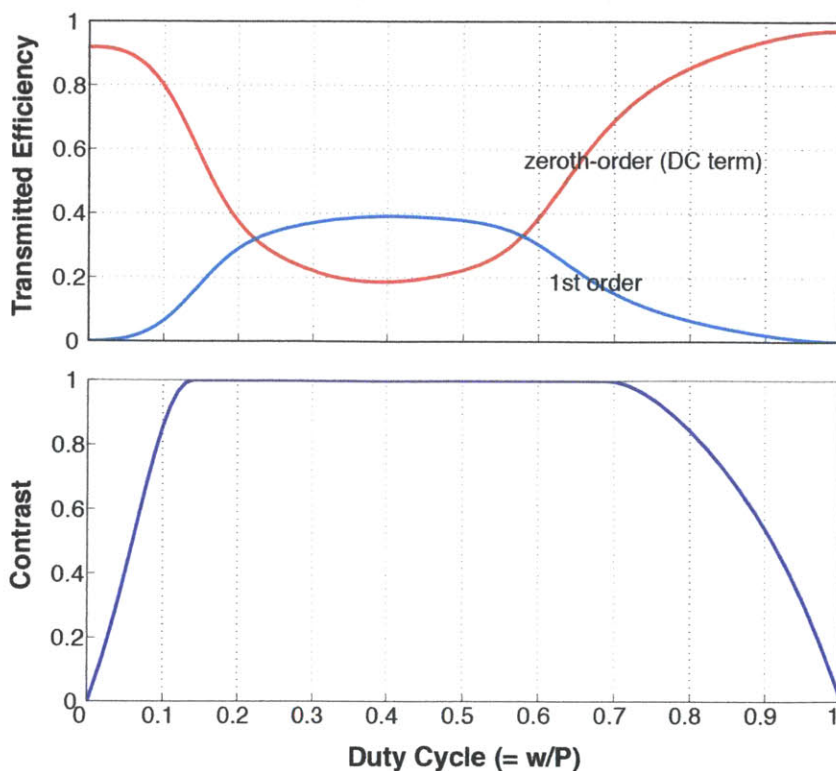


Figure 6-8. Transmitted efficiency of the diffraction orders and contrast values of the intensity profile at the Talbot plane with respect to the duty cycle (w/P) when $P = 390$ nm and $H = 220$ nm.

A simulated volumetric intensity pattern generated by the designed aperiodic 1D phase mask ($P = 390$ nm, $H = 220$ nm) with linearly varying duty cycles of 0.1 to 0.75 is shown in Figure 6-9. The phase mask creates an aperiodic array of focal spots, and the intensity pattern is repeated with the Talbot distance z_t . As expected in Figure 6-8, the contrast of the intensity profiles at the Talbot plane decreases as the duty cycle of the 1D grating decreases (left-hand side).

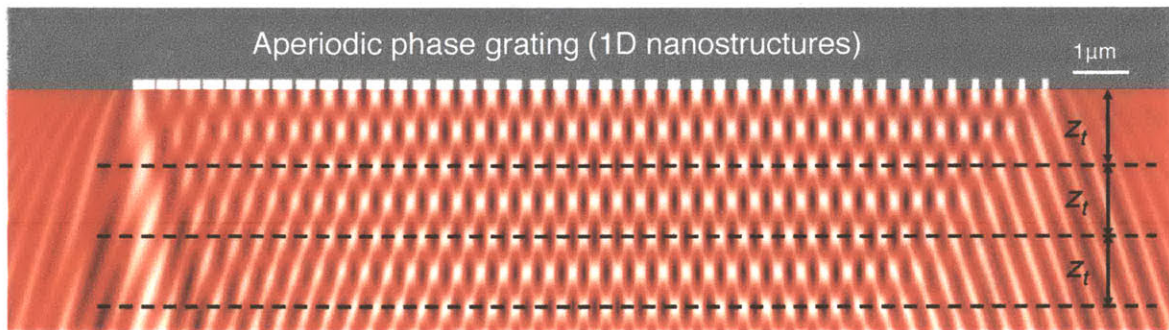


Figure 6-9. Simulated intensity pattern generated by the designed aperiodic 1D phase mask with linearly varying duty cycles.

The fabrication process for the optimized 1D phase grating is illustrated in Figure 6-10. To fabricate the aperiodic phase mask, poly(methyl methacrylate) (PMMA) is spincoated on a fused silica substrate coated with a 10-nm-thick Cr layer. Aperiodic grating with designed duty cycle profile are patterned using electron beam lithography (EBL). After electron beam exposure, the unexposed PMMA is developed, and the Cr layer is removed using chromium etchant (wet process) that does not attack SiO_2 and the residual PMMA. The pattern of PMMA grating is transferred into the fused silica substrate by CHF_3 reactive ion etching. The residual PMMA can be removed by N-methyl pyrrolidinone

(NMP) solution, resulting in a monolithic fused silica phase mask, as shown in Figure 6-11.

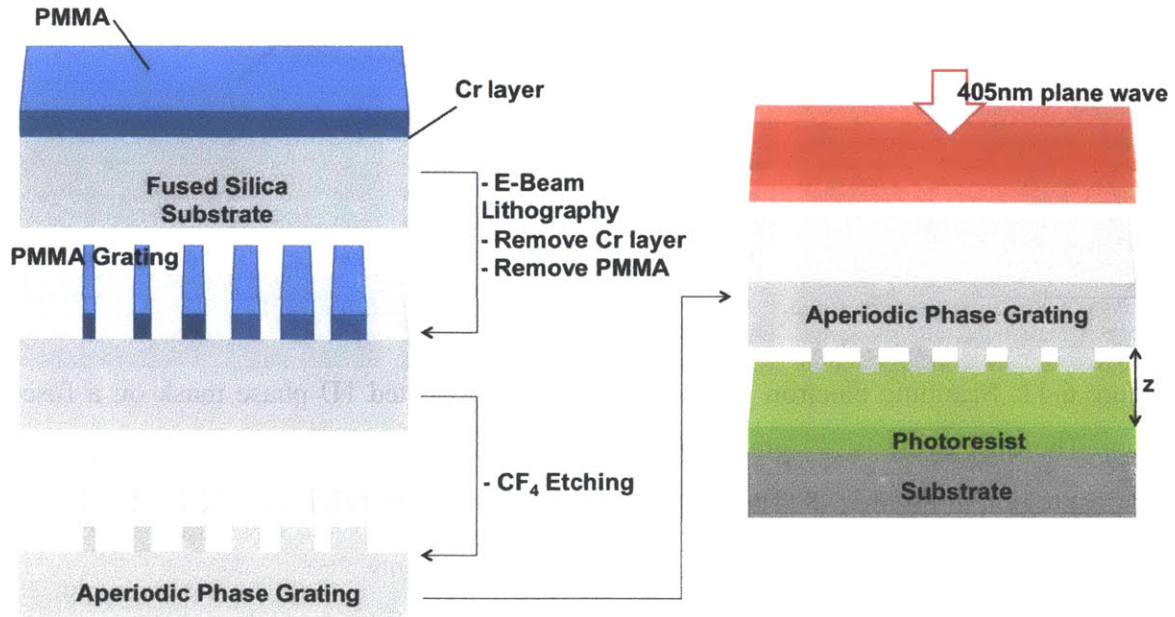


Figure 6-10. Schematic of the processes for fabricating aperiodic diffracted intensity pattern from aperiodic grating phase mask.

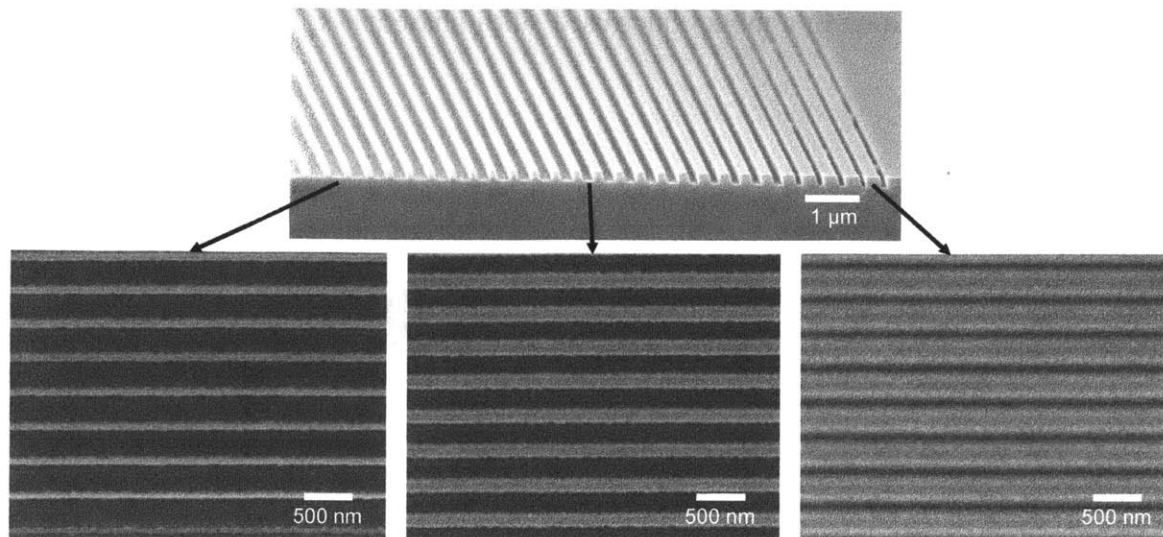


Figure 6-11. Scanning electron micrographs of the fabricated 1D phase mask on a fused silica. The duty cycle (w/P) gradually varies from 0.1 to 0.75, which covers the perfect contrast region in Figure 6-8. The period P is 390 nm, and the height $H = 220 \pm 5$ nm.

The sample for the 3D phase mask exposure is prepared on a silicon substrate. A layer of anti-reflection coating (ARC, Brewer Science BARLi) is used to reduce reflection from the substrate. A thick photoresist (Sumitomo PFi88A8, $\sim 1 \mu\text{m}$) is then spincoated on top of the ARC layer. The thickness of the ARC is optically simulated to minimize the reflection from the zeroth-order light. The phase mask is then brought together with the prepared substrate so that the aperiodic structure is in close contact with the photoresist. A laser ($\lambda = 405$ nm, h-line) then illuminates through the phase mask at normal incidence, generating the Talbot field and exposing the photoresist. The exposed photoresist can then be developed with ultrasonic agitation to yield 3D aperiodic nanostructures with spatially varying duty cycles.

Figures 6-12 and 6-13 shows the cross-section scanning electron micrographs of the preliminarily fabricated 3D nanostructures with an exposure dose of 32.15 mJ/cm^2 and 56.16 mJ/cm^2 , respectively. As expected in Figures 6-8 and 6-9, the fabricated photoresist nanostructures under the 1D phase mask with a low duty cycle (left) exhibit smaller feature size of the nanoholes and more defects due to the low contrast of the intensity

profile, compared to those under the mask with a large duty cycle (right). Again, these are the preliminary results, and results can be enhanced by using shorter wavelength laser source and non-absorptive photoresists, such as SU-8. The photoresist thickness is limited to $\sim 1.0 \mu\text{m}$ because the photoresist used in the experiments absorbs at the exposure wavelength ($\lambda = 405 \text{ nm}$).

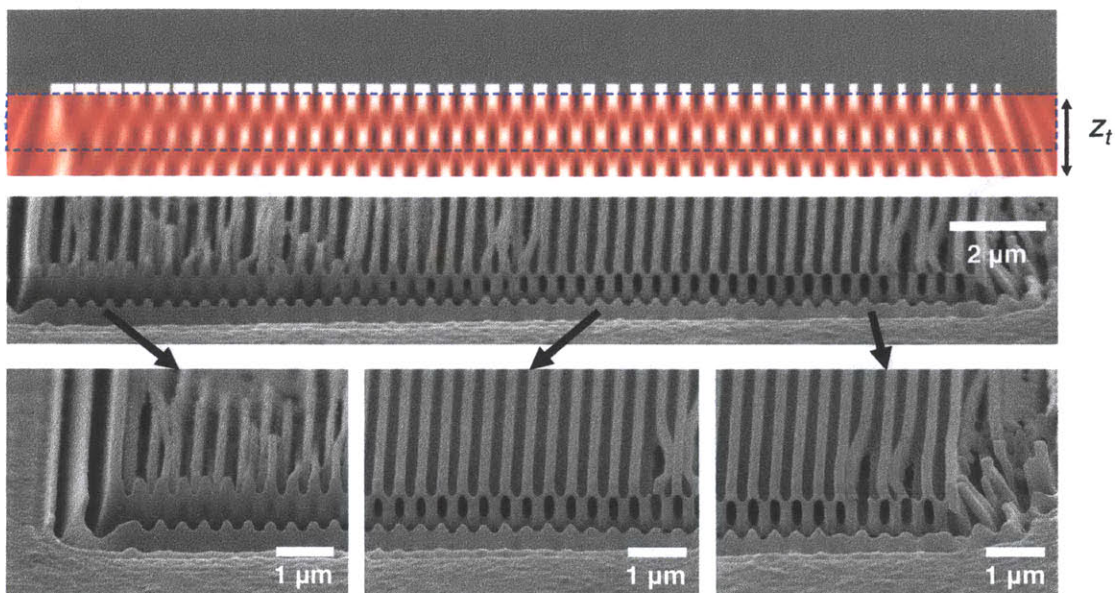


Figure 6-12. Cross-section scanning electron micrographs of the preliminarily fabricated 3D nanostructures with the simulated intensity profiles (exposure dose: 32.15 mJ/cm^2).

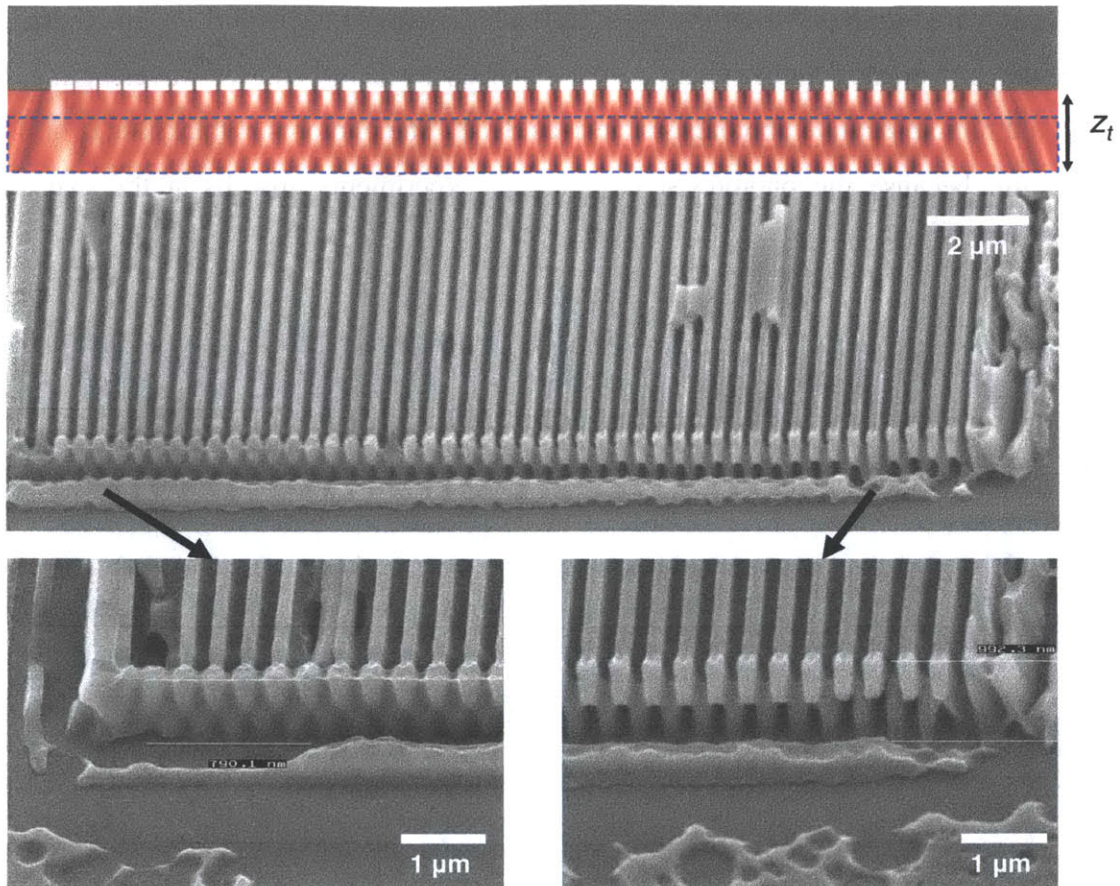


Figure 6-13. Cross-section scanning electron micrographs of the fabricated 3D nanostructures with the simulated intensity profiles (exposure dose: 56.16 mJ/cm^2).

In this work we utilize an aperiodic 1D phase grating with spatially varying duty cycle to generate an aperiodic 3D Talbot field. These preliminary results validate that the volumetric intensity pattern can be recorded by photoresist to form 3D nanostructures. We need to explore further utilizing 1D aperiodic phase grating with both varying duty cycle and periods, allowing more design parameters to control the resulting interference pattern. This approach would be a good candidate for generating desired 3D nanostructures with more flexibility due to the variation in the Talbot distances. Fabricating the 1D grating structure in polymer material can also result in flexible phase mask that is stretchable, and different 3D nanostructures can be fabricated by controlling the applied axial and shear strain.

6.2.3 Fabrication of multifunctional inverted nanocone arrays

The multifunctionality of the silica nanocone surfaces (introduced in Chapters 2 and 3) can be optimized and enhanced by increasing the aspect-ratio, since taller, narrow nanostructures contribute to lower reflection reflectance and more robust superhydrophobicity or superhydrophilicity [157]. However, it is inevitable that the high aspect-ratio of the tapered nanocones is also detrimental to the mechanical robustness of the nanostructured surface, which is a critical barrier when developing textured materials for practical applications or products [157].

Here, we propose an inverted nanocone structure to create improved nanostructured multifunctional materials with greater mechanical robustness [157, 158]. Whilst retaining the high aspect-ratio of tapered nanostructures for enhancing the optical and wetting performance, such as anti-reflection, self-cleaning, and anti-fogging effects, the inverted nanocone structure also provides high mechanical robustness regardless of its aspect-ratio, since the nanostructures are structurally supported by the matrix material around the neighboring structures [157, 158].

The inverted nanocone surface has been fabricated using a simple UV replication method. The master mold comprising of a large area periodic array of nanoconical features is the silica nanocone structure that have introduced in Chapters 2 and 3. It is replicated into UV curable polymer by a sequence of pressing, UV curing, and demolding steps. The fabricated inverted nanocone arrays have a pitch of 200 nm with an aspect-ratio of 5, while demonstrating a far improvement in mechanical robustness by the simulated and experimental results [157, 158].

The inverted nanocone surface can also be manufactured on a fused silica surface or a sapphire surface using negative photoresist. Negative photoresist can be easily utilized instead of positive photoresist in the fabrication processes shown in Figures 3-4, 3-9, and 3-11; thus this will lead to fabricating nanostructured multifunctional surfaces with low risk of mechanical damage.

Appendix A

Dimensionless measure of robustness $T^*(z/H)$ of the Cassie-Baxter state against an applied pressure difference across the water-air interfaces

For a slender tapered cone structure, transition from the Cassie-Baxter to the Wenzel state is due to the application of a sufficiently-large external pressure difference across the water-air meniscus that form the composite interfaces [72]. Typical high aspect-ratio pillar structures possessing a constant value for the critical pressure difference that the liquid meniscus can resist when the contact line is located on the vertical sidewall of pillars. In contrast, the pressure difference that the nanotaper structure can support varies as the liquid meniscus descends along the oblique sidewall because the spacing between nearby structures becomes increasingly narrow, as shown in Figure A-1. The dimensionless measure of robustness T^* compares this pressure difference as a function of penetration depth z/H into the microstructure with the reference pressure $P_{ref} = 2\gamma_{LV}/\ell_{cap}$, which characterizes the typical pressure difference across the liquid-air interface for millimetric-sized liquid droplets sitting at rest on the top of the posts [72]. Due to the high aspect-ratio of the nanocone structure and the small pitch, we can neglect the sagging of the liquid-air interface and this does not drive the wetting transition except when the meniscus is very close to the base of the structure [45].

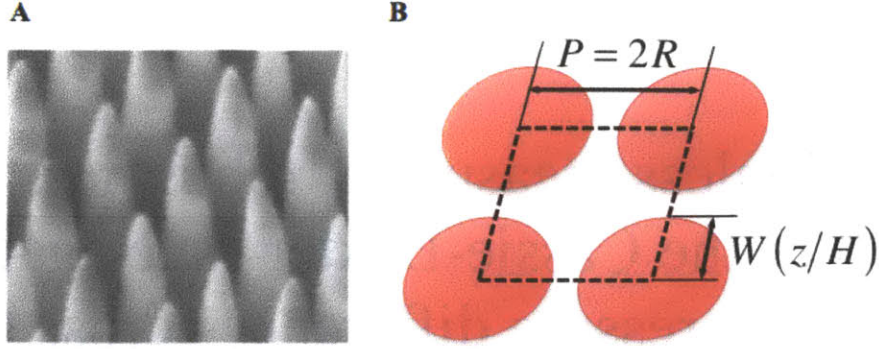


Figure A-1. a) SEM micrograph of slender tapered nanocone structure. b) Schematic diagram of horizontally cross-sectioned nanocone structure [45].

The general force balance on the liquid meniscus at equilibrium equates the pressure difference across the liquid-air interface (ΔP) multiplied by the area with the surface tension (γ_{LV}) multiplied by the total length of the contact line contained in the unit cell as shown in Figure A-1. Assuming that (i) the contact line is on the same horizontal plane and (ii) the angle between the direction of surface tension and axis of nanotaper is $\theta_{adv} - \varphi$ (see Figure 2-12) at all points along the contact line, we obtain

$$\Delta P \cdot (P^2 - \pi W^2) = \gamma_{LV} \cdot (2\pi W) \cdot \cos(\theta_{adv} - \varphi), \quad (\text{A.1})$$

where the column radius W as a function of the penetration depth z/H depending on the approximation of the shape of nanotaper structures (e.g., a truncated cone or a cubic paraboloid) [45].

The overall force balance (Eq. A.1) can be re-written as

$$\Delta P = \frac{2\pi\gamma_{LV} W \cos(\theta_{adv} - \varphi)}{P^2 - \pi W^2}. \quad (\text{A.2})$$

Therefore, the dimensionless robustness parameter T^* becomes

$$T^* = \frac{\Delta P}{P_{ref}} = \frac{2\pi\gamma_{LV}W \cos(\theta_{adv} - \varphi)}{(P^2 - \pi W^2)/(2\gamma_{LV}/\ell_{cap})} = \frac{\pi\ell_{cap}(W/P)\cos(\theta_{adv} - \varphi)}{P[1 - \pi(W/P)^2]}. \quad (\text{A.3})$$

We can approximate the slender tapered cone structure as a cubic paraboloid, $W = (P/2)\sqrt[3]{z/H}$, as discussed in Chapter 2, and Eq. A.3 can be rearranged by substituting the paraboloid profile to obtain

$$T^*(z/H) = \frac{\pi\ell_{cap}(z/H)^{\frac{1}{3}}\cos(\theta_{adv} - \varphi)}{2P[1 - (\pi/4)(z/H)^{\frac{2}{3}}]}. \quad (\text{A.4})$$

This dimensionless parameter (Eq. A.4) provides a measure of how robust the Cassie-Baxter state is when the contact line is located at a certain vertical position z/H and can be easily re-dimensionalized into a physical pressure difference $\Delta P = T^* \cdot P_{ref}$, which determines the equilibrium penetration distance of the liquid-solid-air three phase contact line into the microstructure, depending on the external pressure difference acting on the meniscus [45]. The values of T^* obtained for the nanocone structures are very large because the pitch P is only 200 nm and because the chosen scale for pressure $P_{ref} = 2\gamma_{LV}/\ell_{cap}$ for a static liquid droplet is very small [45].

Appendix B

Transparent Anti-fingerprint Surfaces

B.1 Quantification of lateral capillary imbibition of sebum over a thin porous layer of TiO₂ nanoparticles

In this section, we quantitatively analyze lateral capillary imbibition of human sebum on the nanoporous and oleophilic titania layer, which has been designed to minimize the required ultraviolet light exposure time for photocatalytic degradation of a deposited dactylogram. As shown in Figure B-1, as time increases from the moment the dactylogram is deposited ($t > 0$), the two adjacent sebum-air-titania contact lines (denoted by white dotted line, l_{front}) approach each other due to lateral capillary imbibition. The initially light blue (porous titania) region is progressively filled with light brown color (sebum).

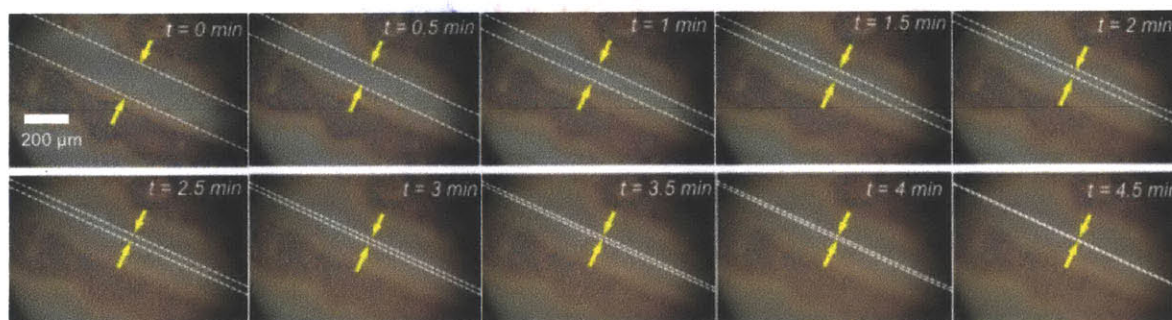


Figure B-1. Sequential microscope images of dactylogram. As time increases, the two adjacent sebum-air-titania contact lines (denoted by white dotted line) approach each other by lateral capillary imbibition. The initially light blue (porous titania) region is progressively filled with light brown color (sebum).

The spreading of a stripe of sebum deposited from a single friction ridge over a thin porous titania film layer can be modeled by considering wicking of a hemi-cylindrical droplet of sebum into a porous substrate (Figure B-2) [125]. To derive the differential equation that describes the time change of position ($l_{\text{front}}(t)$, in the x-direction) of sebum-air-titania interface through the thin porous layer, the volume inside the porous layer and outside the hemi-cylindrical droplet (colored in blue) is considered as a control volume of interest. Because the nanoporous film thickness ($d_{\text{film}} \sim O(10^{-1} \mu\text{m})$) is much smaller than the lateral spreading scale (the distance between two adjacent friction ridges is typically $O(10^2 \mu\text{m})$), wicking of the sebaceous liquid in the vertical direction (z direction) proceeds much more quickly than laterally; it is thus reasonable to simplify the problem as a quasi one-dimensional spreading problem supplied by a reservoir of fluid, as shown in Figure B-1.

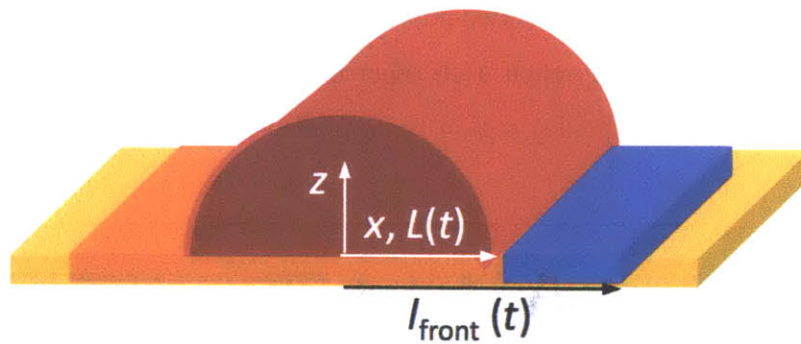


Figure B-2. Schematic illustration of hemi-cylindrical sebum on a partially wetted thin porous film of titania nanoparticles. The control volume of interest is represented by blue color.

Conservation of mass and Darcy's equation governing the motion of liquid through porous media [125, 159], result in two governing equations,

$$\frac{\partial v}{\partial x} = 0 \quad (\text{B.1})$$

$$v = -\frac{K_p}{\mu} \frac{\partial P}{\partial x} \quad (\text{B.2})$$

where v is the lateral velocity of sebum, K_p is the permeability of the porous layer, μ is the sebum viscosity, and P is the capillary pore pressure inside the porous layer. A solution can be obtained by integrating Eqs. B.1 and B.2

$$P = -\frac{A\mu}{K_p} x + B \quad (\text{B.3})$$

where A ($= v$) and B are constants of integration and can be determined by considering the following boundary conditions at the entrance and exit of the control volume in the x -direction.

$$P = P_g - P_c \quad \text{at } x = l_{\text{front}}(t) \quad (\text{B.4})$$

$$P = P_g - P_d \quad \text{at } x = L(t) \quad (\text{B.5})$$

where P_g is the gaseous pressure, P_c is the capillary pressure at the front of sebum ($x = l_{\text{front}}(t)$) inside the porous layer, and P_d is the capillary pressure of the deposited droplet at $x = L(t)$. It should be noted that according to [125], the inequality $P_c \gg P_d$ is satisfied since the characteristic radius of curvature inside the porous layer is much smaller than the radius of curvature of the deposited droplet. Therefore, we ignore the value of P_d and the following expression for $v|_{x=l_{\text{front}}} = dl/dt$ can be derived,

$$\frac{dl_{\text{front}}}{dt} = \frac{K_p P_c}{\mu} \frac{1}{l_{\text{front}} - L} \quad (\text{B.6})$$

or

$$(l_{\text{front}} - L)dl = \frac{K_p P_c}{\mu} dt \quad (\text{B.7})$$

From our assumption in Figure B-2, $L(t)$ can be approximated as a constant because the width of sebum deposited from friction ridge does not change with time ($L(t) = l_0$). By integrating both sides of the Eq. B.7, the equation becomes

$$\frac{1}{2}l_{front}^2 - Ll_{front} + C = \frac{K_p P_c}{\mu} t \quad (B.8)$$

or

$$l_{front} = \left[\frac{2K_p P_c}{\mu} (t - C') \right]^{1/2} + L \quad (B.9)$$

where C and C' are unknown constants and $K_p \sim 10^{-18} \text{ m}^2$, $P_c \sim 5 \times 10^6 \text{ Pa}$ and $\mu \sim 10^{-1} \text{ Pa}\cdot\text{s}$ according to order of magnitude values in [124, 125, 160].

Finally, we checked the order of magnitude of $2K_p P_c / \mu \sim 10^{-10} \text{ m}^2/\text{s}$ in Eq. B.9 by comparing the value determined from curve fitting the experimental data shown in Figure B-3 using the quadratic function $l_{front} = [D(t - E)]^{1/2} + F$ with curve-fitting coefficients D , E , and F . We find that the estimated value based on the first approximation is in good agreement with the value determined from curve-fitting that gives $D \sim 9.8 \times 10^{-11} \text{ m}^2/\text{s}$.

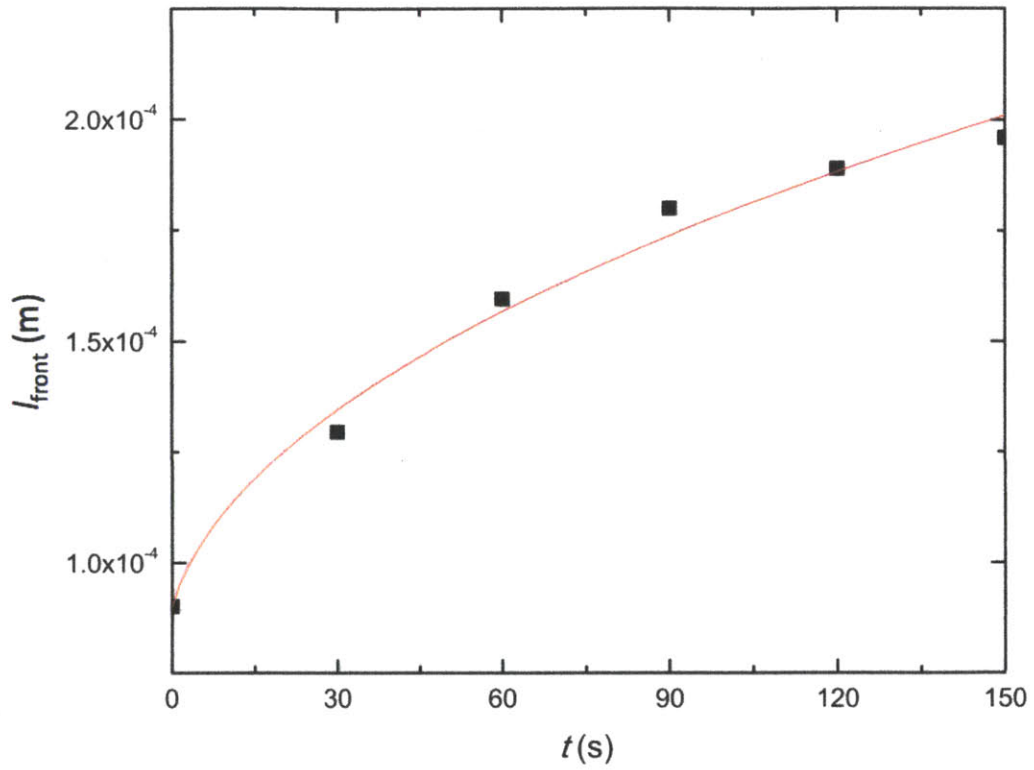


Figure B-3. Plot showing the time evolution of the sebum-air-titania contact line position as a result of lateral capillary imbibition. The red solid line represents a result of curve fitting with a quadratic function form $l_{front} = [D(t - E)]^{1/2} + F$ (represented by red solid line).

B.2 Porosity of the TiO₂ nanoparticle coating

To analyze the characteristics of the nanoporous TiO₂ coating prepared by Layer-by-Layer (LbL) coating method, parameters quantifying the capillary imbibition, surface area, and averaged refractive index are important. Because the physical properties of nanoparticles can differ from the bulk properties of the materials, in this section we calculate the porosity and the refractive index of the thin layer nanoporous coating using the method proposed by Lee *et al.* [109]. When the refractive index of the nanoparticle (n_p) and the porosity of the nanoporous media ($p = 1 - \varphi$, where φ is the packing density of the nanoparticles) are unknown, solving two equations containing two unknowns (n_p and p) is required to determine these values. Effective medium theory can be used to derive an expression for the effective refractive index of a nanoporous thin film deposited on a substrate [65, 66]. Measuring the effective refractive indices with two different fluids (of known refractive indices) imbibed into the porous nanotexture yields two equations that can then be solved simultaneously to give the pore volume fraction (p) and the refractive index of the nanoparticles (n_p). Among various effective medium approximations, Bruggeman's model has been selected, since it matches well with finite difference time domain (FDTD) simulations of random structures [65, 66]. The effective permittivity of the medium (ϵ_{eff}) is given by solving the following two equations

$$(1 - \varphi) \frac{\epsilon_{air} - \epsilon_{eff}}{\epsilon_{air} + 2\epsilon_{eff}} + \varphi \frac{\epsilon_p - \epsilon_{eff}}{\epsilon_p + 2\epsilon_{eff}} = 0 \quad (\text{B.10})$$

$$(1 - \varphi) \frac{\epsilon_{water} - \epsilon_{eff}}{\epsilon_{water} + 2\epsilon_{eff}} + \varphi \frac{\epsilon_p - \epsilon_{eff}}{\epsilon_p + 2\epsilon_{eff}} = 0 \quad (\text{B.11})$$

where ϵ_{air} is the permittivity of air, ϵ_{water} is the permittivity of water, ϵ_p is the permittivity of the particle, and φ is the packing density (*i.e.*, volume fraction) of the particles. In addition, refractive index n is approximately $\sqrt{\epsilon}$ at optical frequencies for most natural materials.

As shown in Figure B-4, the effective refractive indices ($n_{eff} = \sqrt{\epsilon_{eff}}$) measured by ellipsometry ($\lambda = 633$ nm) are 1.478 (with the air) and 1.633 (with the water). Since the refractive indices of air and water are known and the effective permittivity is measured on the same nanoporous textured film, two unknown values (ϵ_p and φ) can subsequently be calculated from Eqs. B.10 and B.11. The calculated packing density (*i.e.*, volume fraction, φ) of the particle is $\varphi = 0.504$ ($p = 0.496$), and the refractive index of the TiO₂ particle is determined to be $n_p = 2.001$ at $\lambda = 633$ nm.

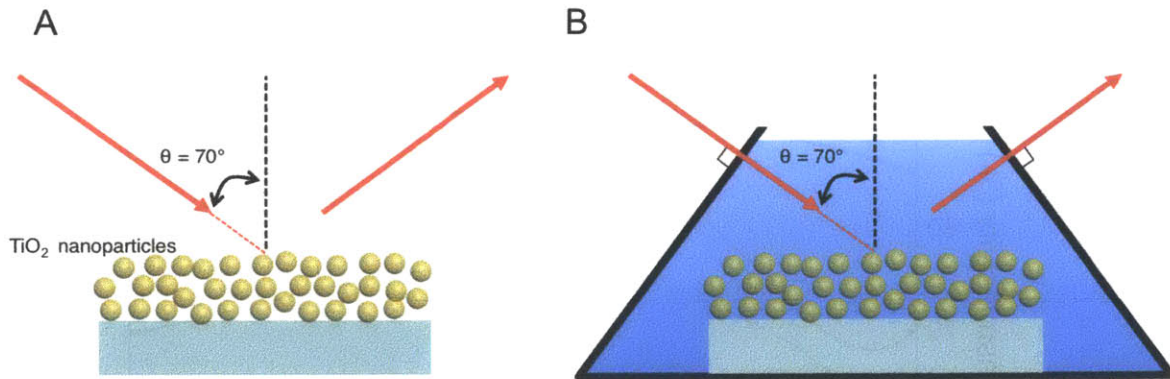


Figure B-4. Measurements of packing density and refractive index of the nanoparticle thin films in the air (A) and in the water (B) using ellipsometry.

B.3 Optical transmissivity and photocatalytic effect for the TiO₂ nanoparticle coating (50 dipping cycles), a flat TiO₂ film deposited by using electron beam deposition, and SunClean™ glass

The optical transmissivity values over the wavelength range of visible light for the TiO₂ nanoparticle coating (50 dipping cycle), a flat TiO₂ film, and SunClean™ glass (a commercially available glass coated with TiO₂) [161] are measured, as shown in Figure B-5. The layered nanoparticle structures with 50 dipping cycles ($d_{50} = 114.8 \pm 6.2$ nm) have the highest transmissivity over the wavelengths of $400 \text{ nm} \leq \lambda \leq 800 \text{ nm}$, compared to the flat TiO₂ film deposited on the microscope slide (thickness = 115 ± 10 nm) and SunClean™ glass. Figure B-6 shows surface topography of the three kinds of surfaces (oblique views, tilting angle = 70°).

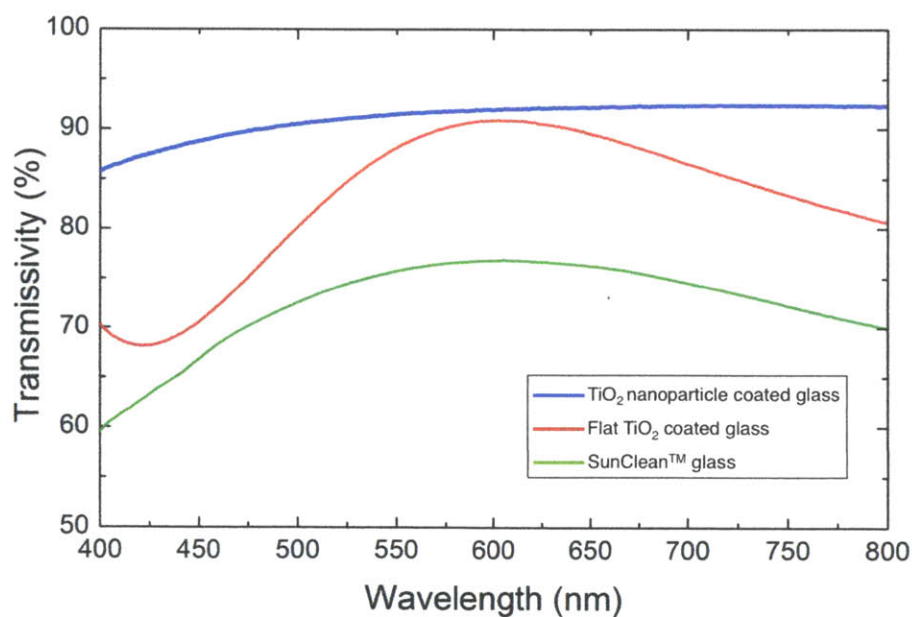
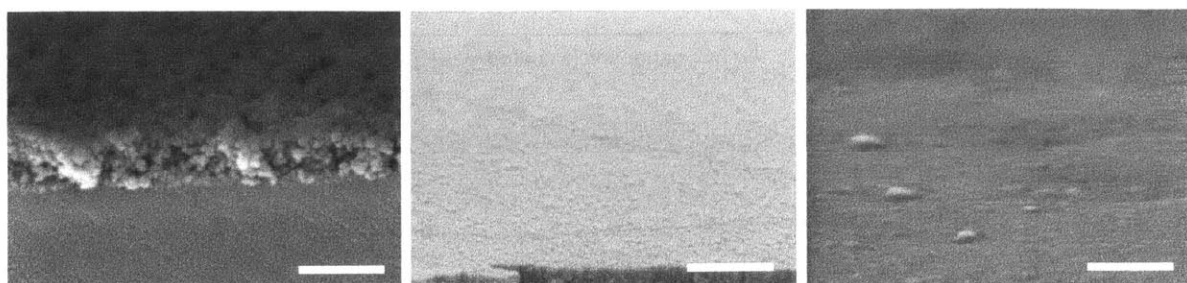


Figure B-5. Measured optical transmissivity over the visible range ($400 \text{ nm} \leq \lambda \leq 800 \text{ nm}$) for the three different surfaces



(a) TiO₂ nanoparticle coating

(b) Flat TiO₂ film deposited on a microscope slide

(c) SunClean™ glass

Figure B-6. SEM micrographs for the three different surfaces (oblique views, tilting angle = 70°). All scale bars represent 200 nm.

Figure B-7 shows the measured transmissivity of monochromatic light ($\lambda = 660$ nm from a diode laser) for the 50 dipping cycle film ($d_{50} = 114.8 \pm 6.2$ nm), the flat TiO₂ film, and SunClean™ glass with respect to UV exposure time after deposition of stamped artificial sebum. All the transmissivity values initially drop from the initial sebum-free values represented by the dotted lines, due to the stamped artificial sebum. As the nanoparticle coated surface is exposed to UV light (1.5 ± 0.1 mW/cm² at $300 \text{ nm} \leq \lambda \leq 400 \text{ nm}$) the transmissivity gradually recovers to its initial sebum-free value within 3 hours. In contrast, optical transmissivity values for the flat TiO₂ film and SunClean™ glass do not reach the sebum-free values within 15 hours because the artificial oils on both coatings are not completely degraded photocatalytically. The required UV light exposure time until the moment that the optical transmissivity through the artificial sebum-deposited region reaches 99% of the original transmissivity is also measured. The required UV light exposure time for the 50 dipping cycle porous TiO₂ nanoparticle coating and SunClean™ glass are 2.5 hours and 15 hours, respectively. In addition, the flat TiO₂ coating does not show any noticeable changes in transmissivity even after 24 hours of UV light exposure.

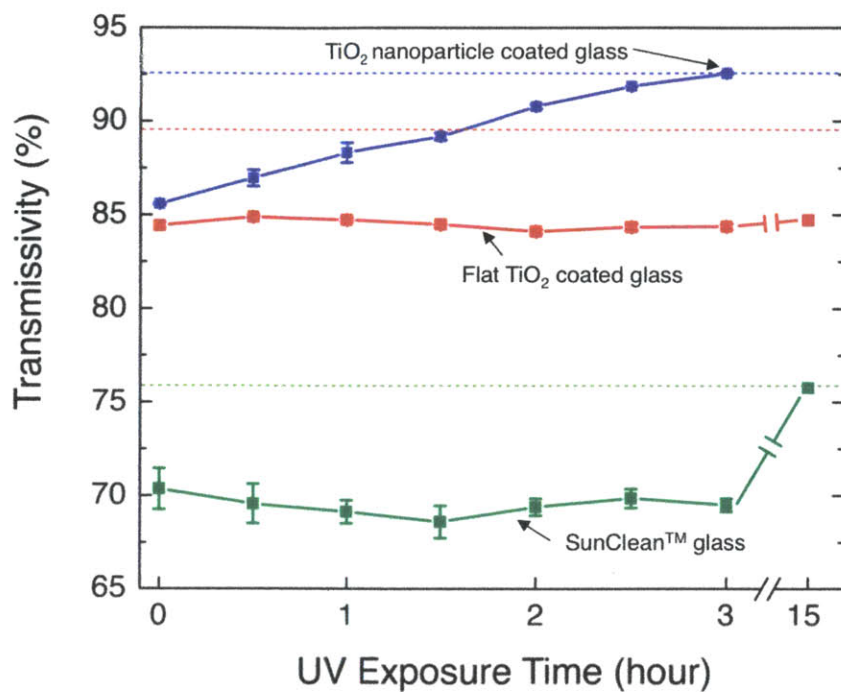


Figure B-7. Time evolution of measured transmissivity (incident angle = 0°, $\lambda = 660$ nm) through artificial sebum-stamped spots of the three different surfaces exposed to UV light (1.5 ± 0.1 mW/cm² at $300 \text{ nm} \leq \lambda \leq 400$ nm). The dotted lines represent the initial, sebum-free transmissivity values.

B.4 Mechanical robustness test results of the TiO₂ nanoparticle coating (50 dipping cycles) against repeated shear force

The mechanical durability of the nanoporous TiO₂ coatings constructed from calcinated TiO₂ nanoparticles against shear force is tested in consideration of applications such as touch screens. Equivalent shear forces in the range of the human finger shear forces measured on capacitive touchscreens (Figure B-8a) are applied onto the TiO₂ nanotextured coatings [102] by sliding different magnitudes of normal load.

In order to measure kinetic friction coefficient between the rubber pad and the TiO₂ nanoparticle coating, an inclined plane is utilized. By changing the tilting angle of the TiO₂ nanoparticle coated surface, we measure a specific angle at which the rubber pad slides down at a constant speed. The tangent value of the measured specific angle is determined to be the coefficient of kinetic friction between the rubber pad and the TiO₂ nanoparticle coating because the friction force and the sine of the gravitational force acting on the rubber pad are the same, and the force normal to the tilted surface is the cosine value of the gravitational force acting on the rubber pad when the rubber pad slides down at a constant speed.

As shown in Figure B-8, the TiO₂ nanoparticle coating shows approximately no change (< 1%) from the initial optical transmissivity, even after 50 times repeated contact sliding test with the maximum shear force value of 0.3 N. It should be noted that 0.3 N covers most of the range of measured friction shear force without electrostatic force.

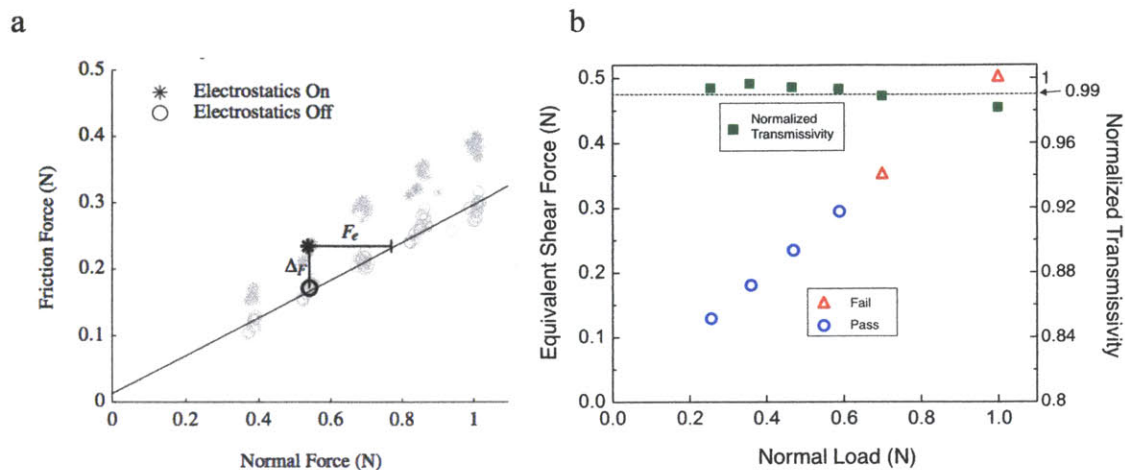


Figure B-8. a) Plot of averaged human finger touch force on capacitive touchscreens with or without electrostatic force F_e [102]. The standard error is 0.01 N. Reproduced from Ref. [102] with the permission of IEEE. b) Plot of estimated shear force with pass (represented as blue hollow circles) or failure (represented as red hollow triangles) results of the shear resistance test. Evolution of optical transmissivity (at $\lambda = 660$ nm) is measured after applying different shear force on the nanoporous TiO_2 surface through a latex rubber pad with area $A = 81 \text{ mm}^2$ (see Figure 4-27 caption for details of shear resistance tests). If transmissivity of the nanoporous TiO_2 coating after 50 times of tests with the magnitude of given shear force shows more than 99% of the initial transmissivity value, the result is marked as pass. The green solid squares represent normalized transmissivity values to initial transmissivity of the nanoporous TiO_2 values after 50 times of shear force tests.

References

1. Min, W.-L., Jiang, B., and Jiang, P., *Bioinspired self-cleaning antireflection coatings*. Adv. Mater., 2008. **20**(20): p. 3914-3918.
2. Zhu, J., et al., *Nanodome Solar Cells with Efficient Light Management and Self-Cleaning*. Nano Letters, 2010. **10**(6): p. 1979-1984.
3. Kanamori, Y., Sasaki, M., and Hane, K., *Broadband antireflection gratings fabricated upon silicon substrates*. Optics Letters, 1999. **24**(20): p. 1422-1424.
4. Lee, H.J. and Willis, C., *Dressed for combat*. Chem. Ind. (London, U. K.), 2009: p. 21-23.
5. Hu, X.L., Li, G.S., and Yu, J.C., *Design, Fabrication, and Modification of Nanostructured Semiconductor Materials for Environmental and Energy Applications*. Langmuir, 2010. **26**(5): p. 3031-3039.
6. Clapham, P.B. and Hutley, M.C., *Reduction of Lens Reflection by Moth Eye Principle*. Nature, 1973. **244**(5414): p. 281-282.
7. Barthlott, W. and Neinhuis, C., *Purity of the sacred lotus, or escape from contamination in biological surfaces*. Planta, 1997. **202**(1): p. 1-8.
8. Wilson, S.J. and Hutley, M.C., *The Optical-Properties of Moth Eye Antireflection Surfaces*. Optica Acta, 1982. **29**(7): p. 993-1009.
9. Parker, A.R. and Townley, H.E., *Biomimetics of photonic nanostructures*. Nature Nanotechnology, 2007. **2**(6): p. 347-353.
10. Vukusic, P. and Sambles, J.R., *Photonic structures in biology*. Nature, 2003. **424**(6950): p. 852-855.
11. Parker, A.R. and Lawrence, C.R., *Water capture by a desert beetle*. Nature, 2001. **414**(6859): p. 33-34.
12. Nosonovsky, M., Bhushan, B., *Roughness optimization for biomimetic superhydrophobic surfaces*. Microsyst. Technol., 2005. **11**(7): p. 535-549.

13. Xia, F. and Jiang, L., *Bio-inspired, smart, multiscale interfacial materials*. *Advanced Materials*, 2008. **20**(15): p. 2842-2858.
14. Zorba, V., et al., *Biomimetic Artificial Surfaces Quantitatively Reproduce the Water Repellency of a Lotus Leaf*. *Advanced Materials*, 2008. **20**(21): p. 4049-4054.
15. Huang, Y.F., et al., *Improved broadband and quasi-omnidirectional anti-reflection properties with biomimetic silicon nanostructures*. *Nature nanotechnology*, 2007. **2**(12): p. 770-774.
16. Choi, K., et al., *Nano-tailoring the Surface Structure for the Monolithic High-Performance Antireflection Polymer Film*. *Advanced Materials*, 2010. **22**(33): p. 3713-3718.
17. Brunner, R., et al., *Lessons from nature: biomimetic subwavelength structures for high-performance optics*. *Laser & Photonics Reviews*, 2012. **6**(5): p. 641-659.
18. Xi, J.Q., et al., *Optical thin-film materials with low refractive index for broadband elimination of Fresnel reflection*. *Nature Photonics*, 2007. **1**(3): p. 176-179.
19. Land, M.F. and Nilsson, D.E., *Animal Eyes, Second Edition*. *Animal Eyes, Second Edition*, 2012: p. 1-271.
20. Diao, Y.Y. and Liu, X.Y., *Mysterious coloring: structural origin of color mixing for two breeds of Papilio butterflies*. *Optics Express*, 2011. **19**(10): p. 9232-9241.
21. Ko, D.H., et al., *Biomimetic microlens array with antireflective "moth-eye" surface*. *Soft Matter*, 2011. **7**(14): p. 6404-6407.
22. Vukusic, P., et al., *Quantified interference and diffraction in single Morpho butterfly scales*. *Proceedings of the Royal Society B-Biological Sciences*, 1999. **266**(1427): p. 1403-1411.
23. Ben Amar, M., *New trends in the physics and mechanics of biological systems : École de physique des Houches, session XCII, 6-31 July 2009*. 2011, Oxford ; New York: Oxford University Press. xxi, 357 p.
24. Zheng, Y.M., Gao, X.F., and Jiang, L., *Directional adhesion of superhydrophobic butterfly wings*. *Soft Matter*, 2007. **3**(2): p. 178-182.
25. Hecht, E., *Optics*. 4th ed. 2002, Reading, Mass.: Addison-Wesley. vi, 698 p.

26. Kong, J.A., *Electromagnetic wave theory*. 2008, Cambridge, Massachusetts: EMW Publishing. xv, 1016 p.
27. Fowles, G.R., *Introduction to modern optics*. 2nd ed. 1989, New York: Dover Publications. viii, 328 p.
28. Dussan, E.B., *Spreading of Liquids on Solid-Surfaces - Static and Dynamic Contact Lines*. Annual Review of Fluid Mechanics, 1979. 11: p. 371-400.
29. Butt, H.-J., Graf, K., and Kappl, M., *Physics and chemistry of interfaces*. 2nd ed. 2006: John Wiley & Sons. xii, 386 p.
30. Hiemenz, P.C. and Rajagopalan, R., *Principles of colloid and surface chemistry*. 3rd ed. 1997, New York: Marcel Dekker. xix, 650 p.
31. Shafrin, E.G. and Zisman, W.A., *Upper Limits to the Contact Angles of Liquids on Solids*, in *Contact Angle, Wettability, and Adhesion*, F.M. Fowkes, Editor. 1964, American Chemical Society: Advances in Chemistry. p. 145-157.
32. Quéré, D., Lafuma, A., and Bico, J., *Slippy and sticky microtextured solids*. Nanotechnology, 2003. 14(10): p. 1109-1112.
33. Lafuma, A. and Quéré, D., *Superhydrophobic states*. Nature materials, 2003. 2(7): p. 457-460.
34. Degennes, P.G., *Wetting - Statics and Dynamics*. Reviews of Modern Physics, 1985. 57(3): p. 827-863.
35. Wenzel, R.N., *Resistance of solid surfaces to wetting by water*. Industrial and Engineering Chemistry, 1936. 28: p. 988-994.
36. Choi, W., *Micro-textured surfaces for omniphobicity and drag-reduction*, in *Massachusetts Institute of Technology. Dept. of Mechanical Engineering*. 2009, Ph.D. thesis, Massachusetts Institute of Technology.
37. Cassie, A.B.D. and Baxter, S., *Wettability of porous surfaces*. Transactions of the Faraday Society, 1944. 40: p. 0546-0550.
38. Marmur, A., *Wetting on hydrophobic rough surfaces: To be heterogeneous or not to be?* Langmuir, 2003. 19(20): p. 8343-8348.
39. Tian, Y. and Jiang, L., *WETTING Intrinsically robust hydrophobicity*. Nature Materials, 2013. 12(4): p. 291-292.

40. Bhushan, B., Jung, Y.C., and Koch, K., *Micro-, nano- and hierarchical structures for superhydrophobicity, self cleaning, and low adhesion*. Philos. Trans. R. Soc., A, 2009. 367: p. 1631-1672.
41. Biswas, A., et al., *Advances in top-down and bottom-up surface nanofabrication: Techniques, applications & future prospects*. Advances in Colloid and Interface Science, 2012. 170(1-2): p. 2-27.
42. Chou, S.Y., Krauss, P.R., and Renstrom, P.J., *Imprint lithography with 25-nanometer resolution*. Science, 1996. 272(5258): p. 85-87.
43. Ahn, S.H. and Guo, L.J., *Large-area roll-to-roll and roll-to-plate nanoimprint lithography: a step toward high-throughput application of continuous nanoimprinting*. Acs Nano, 2009. 3(8): p. 2304-10.
44. Park, H.S., et al., *Novel process to improve defect problems for thermal nanoimprint lithography*. IEEE Transactions on Semiconductor Manufacturing, 2007. 20(1): p. 13-19.
45. Park, K.C., et al., *Nanotextured Silica Surfaces with Robust Super-Hydrophobicity and Omnidirectional Broadband Super-Transmissivity*. ACS nano, 2012. 6(5): p. 3789-3799.
46. Haast, M.A.M., et al., *Reversal mechanism of submicron patterned CoNi/Pt multilayers*. Ieee Transactions on Magnetics, 1998. 34(4): p. 1006-1008.
47. Farhoud, M., et al., *Fabrication of 200 nm period nanomagnet arrays using interference lithography and a negative resist*. Journal of Vacuum Science & Technology B, 1999. 17(6): p. 3182-3185.
48. Campbell, M., et al., *Fabrication of photonic crystals for the visible spectrum by holographic lithography*. Nature, 2000. 404(6773): p. 53-56.
49. Ullal, C.K., et al., *Photonic crystals through holographic lithography: Simple cubic, diamond-like, and gyroid-like structures*. Applied Physics Letters, 2004. 84(26): p. 5434-5436.
50. Ritucci, A., et al., *Interference lithography by a soft x-ray laser beam: Nanopatterning on photoresists*. Journal of Applied Physics, 2007. 102(3): p. 034313.
51. Ferrera, J., Schattenburg, M.L., and Smith, H.I., *Analysis of distortion in interferometric lithography*. Journal of Vacuum Science & Technology B, 1996. 14(6): p. 4009-4013.

52. Gates, B.D., et al., *New approaches to nanofabrication: Molding, printing, and other techniques*. Chemical Reviews, 2005. 105(4): p. 1171-1196.
53. Lehn, J.M., *Supramolecular Chemistry - Scope and Perspectives Molecules, Supermolecules, and Molecular Devices*. Angewandte Chemie-International Edition in English, 1988. 27(1): p. 89-112.
54. Choi, H., *Fabrication of Anti-reflective and Imaging Nanostructured Optical Elements*, in *Massachusetts Institute of Technology. Dept. of Mechanical Engineering*. 2011, Master thesis, Massachusetts Institute of Technology.
55. Chang, C.-H., *Multilevel Interference Lithography - Fabricating Sub-wavelength Periodic Nanostructures*, in *Massachusetts Institute of Technology. Dept. of Mechanical Engineering*. 2008, Ph.D. thesis, Massachusetts Institute of Technology.
56. Ariga, K., Hill, J.P., and Ji, Q.M., *Layer-by-layer assembly as a versatile bottom-up nanofabrication technique for exploratory research and realistic application*. Physical Chemistry Chemical Physics, 2007. 9(19): p. 2319-2340.
57. Rubner, M.F. and Cohen, R.E., *Layer-by-Layer Processed Multilayers: Challenges and Opportunities*, in *Multilayer Thin Films*, in *Multilayer Thin Films: Sequential Assembly of Nanocomposite Materials, Second Edition*, G. Decher and J.B. Schlenoff, Editors. 2012, Wiley-VCH Verlag GmbH & Co. KGaA: Weinheim, Germany. p. 23-41.
58. Decher, G., *Fuzzy nanoassemblies: Toward layered polymeric multicomposites*. Science, 1997. 277(5330): p. 1232-1237.
59. Iler, R.K., *Multilayers of Colloidal Particles*. Journal of Colloid and Interface Science, 1966. 21(6): p. 569-594.
60. Quéré, D., *Wetting and roughness*. Annual Review of Materials Research, 2008. 38: p. 71-99.
61. Rayleigh, L., *On reflection of vibrations at the confines of two media between which the transition is gradual*. Proceedings of the London Mathematical Society, 1879. 1(1): p. 51-56.
62. Minot, M.J., *Single-Layer, Gradient Refractive-Index Antireflection Films Effective from 0.35 to 2.5-Mu*. Journal of the Optical Society of America, 1976. 66(6): p. 515-519.

63. Southwell, W.H., *Gradient-index antireflection coatings*. Optics Letters, 1983. 8(11): p. 584-586.
64. Hodgkinson, I.J., et al., *Measurement of the Principal Refractive-Indexes of Thin-Films Deposited at Oblique-Incidence*. Journal of the Optical Society of America a-Optics Image Science and Vision, 1985. 2(10): p. 1693-1697.
65. Choy, T.C., *Effective medium theory : principles and applications*. International series of monographs on physics. 1999, New York: Oxford University Press. xi, 182 p.
66. Sihvola, A.H., *Electromagnetic mixing formulas and applications*. IEE electromagnetic waves series. 1999, London: Institution of Electrical Engineers. xii, 284 p.
67. Bhushan, B., *Biomimetics: lessons from nature—an overview*. Philosophical Transactions of the Royal Society A: Mathematical, Physical and Engineering Sciences, 2009. 367(1893): p. 1445-1486.
68. Sainiemi, L., et al., *Non-Reflecting Silicon and Polymer Surfaces by Plasma Etching and Replication*. Advanced Materials, 2011. 23(1): p. 122-126.
69. Yu, Z.N., et al., *Fabrication of large area subwavelength antireflection structures on Si using trilayer resist nanoimprint lithography and liftoff*. Journal of Vacuum Science & Technology B, 2003. 21(6): p. 2874-2877.
70. Bhushan, B., Koch, K., Jung, Y. C., *Biomimetic Hierarchical Structure for Self-Cleaning*. Applied Physics Letters, 2008. 93: p. 093101-093103.
71. Tuteja, A., et al., *Design Parameters for Superhydrophobicity and Superoleophobicity*. MRS Bulletin, 2008. 33(8): p. 752-758.
72. Tuteja, A., et al., *Robust omniphobic surfaces*. Proceedings of the National Academy of Sciences of the United States of America, 2008. 105(47): p. 18200-18205.
73. Lau, K.K.S., et al., *Superhydrophobic carbon nanotube forests*. Nano Letters, 2003. 3(12): p. 1701-1705.
74. Deinega, A., et al., *Minimizing light reflection from dielectric textured surfaces*. Journal of the Optical Society of America a-Optics Image Science and Vision, 2011. 28(5): p. 770-777.

75. Grann, E.B., Moharam, M.G., and Pommet, D.A., *Optimal-Design for Antireflective Tapered 2-Dimensional Subwavelength Grating Structures*. Journal of the Optical Society of America a-Optics Image Science and Vision, 1995. 12(2): p. 333-339.
76. Grann, E.B. and Moharam, M.G., *Comparison between continuous and discrete subwavelength grating structures for antireflection surfaces*. Journal of the Optical Society of America a-Optics Image Science and Vision, 1996. 13(5): p. 988-992.
77. Liu, V. and Fan, S.H., *S-4: A free electromagnetic solver for layered periodic structures*. Computer Physics Communications, 2012. 183(10): p. 2233-2244.
78. Moharam, M.G., et al., *Formulation for Stable and Efficient Implementation of the Rigorous Coupled-Wave Analysis of Binary Gratings*. Journal of the Optical Society of America a-Optics Image Science and Vision, 1995. 12(5): p. 1068-1076.
79. Moharam, M.G., et al., *Stable Implementation of the Rigorous Coupled-Wave Analysis for Surface-Relief Gratings - Enhanced Transmittance Matrix Approach*. Journal of the Optical Society of America a-Optics Image Science and Vision, 1995. 12(5): p. 1077-1086.
80. Koch, K., Barthlott, W., *Superhydrophobic and Superhydrophilic Plant Surface: an inspiration for biomimetic materials*. Review of Phil. Trans. R. Soc., 2009. 367: p. 1487-1509.
81. Reyssat, M., Courbin, L., Reyssat, E., Stone, H. A., *Imbibition in geometries with axial variations*. Journal of Fluid Mechanics, 2008. 615: p. 335-344.
82. Cebeci, F.C., et al., *Nanoporosity-driven superhydrophilicity: A means to create multifunctional antifogging coatings*. Langmuir, 2006. 22(6): p. 2856-2862.
83. Nuraje, N., Asmatulu, R., Cohen, R. E., Rubner, M. F., *Durable Antifog Films from Layer-by-Layer Molecularly Blended Hydrophilic Polysaccharides*. Langmuir, 2011. 27: p. 782-791.
84. Paivanranta, B., Saastamoinen, T., and Kuittinen, M., *A wide-angle antireflection surface for the visible spectrum*. Nanotechnology, 2009. 20(37): p. 375301.
85. Kang, Y.H., et al., *Fabrication of antireflection nanostructures by hybrid nanopatterning lithography*. Microelectronic Engineering, 2010. 87(2): p. 125-128.
86. Kobrin, B., et al., *An Improved Chemical Resistance and Mechanical Durability of Hydrophobic FDTS Coatings*. International Memes Conference 2006, 2006. 34: p. 454-457.

87. Honda, A., et al., *Effect of temperature and irradiation on fused silica optical fiber for temperature measurement*. Journal of Nuclear Materials, 2007. **367**: p. 1117-1121.
88. Yang, B., et al., *Bioinspired Silica Surfaces with Near-Infrared Improved Transmittance and Superhydrophobicity by Colloidal Lithography*. Langmuir : the ACS journal of surfaces and colloids, 2010. **26**(12): p. 9842-9847.
89. Li, X., Ma, X., and Lan, Z., *Dynamic behavior of the water droplet impact on a textured hydrophobic/superhydrophobic surface: the effect of the remaining liquid film arising on the pillars' tops on the contact time*. Langmuir, 2009. **26**(7): p. 4831-4838.
90. Srinivasarao, M., et al., *Three-dimensionally ordered array of air bubbles in a polymer film*. Science, 2001. **292**: p. 79-83.
91. Llopis, F. and Tobias, I., *Texture profile and aspect ratio influence on the front reflectance of solar cells*. Journal of Applied Physics, 2006. **100**(12): p. 124504.
92. Sun, C.H., Jiang, P., and Jiang, B., *Broadband moth-eye antireflection coatings on silicon*. Applied Physics Letters, 2008. **92**(6): p. 061112.
93. Choi, H.J., et al. *Fabrication of ultra high aspect ratio silica nanocone arrays by multiple shrinking mask etching*. in *Optical MEMS and Nanophotonics (OMN), 2012 International Conference on*. 2012. Canada: IEEE.
94. Choi, H., et al., *PROCESS FOR MAKING NANOCONE STRUCTURES AND USING THE STRUCTURES TO MANUFACTURE NANOSTRUCTURED GLASS*. 2013, US Patent 20,130,025,322.
95. Rueger, N.R., et al., *Selective etching of SiO₂ over polycrystalline silicon using CHF₃ in an inductively coupled plasma reactor*. Journal of Vacuum Science & Technology a-Vacuum Surfaces and Films, 1999. **17**(5): p. 2492-2502.
96. Choi, H.J., Kim, J.-G., and Barbastathis, G. *Fabrication of aperiodic subwavelength nanostructures by Grayscale Interference Lithography (GIL)*. in *Nanotechnology (IEEE-NANO), 2013 13th IEEE Conference on*. 2013. Beijing, China: IEEE.
97. Cornago, I., et al., *Simple and Low-Cost Fabrication Process of High Aspect Ratio Periodic Nanocone Structures*, in *International Micro & Nano Engineering Conference*. 2012: Toulouse, France.

98. Lehr, D., et al., *Simulating different manufactured antireflective sub-wavelength structures considering the influence of local topographic variations*. Optics Express, 2010. 18(23): p. 23878-23890.
99. Scrutont, B., Robins, B.W., and Blott, B.H., *The deposition of fingerprint films*. Journal of Physics D-Applied Physics, 1975. 8(6): p. 714-723.
100. Thomas, G.L. and Reynoldson, T.E., *Some Observations on Fingerprint Deposits*. Journal of Physics D-Applied Physics, 1975. 8(6): p. 724-729.
101. Mori, K., *Photo-Functionalized Materials Using Nanoparticles: Photocatalysis*. Kona, 2005(23): p. 205-214.
102. Yao, X., et al., *Adaptive fluid-infused porous films with tunable transparency and wettability*. Nature materials, 2013. 12(6): p. 529-534.
103. Wang, G., Wang, H., and Guo, Z., *Robust transparent and anti-fingerprint superhydrophobic film*. Chemical Communications, 2013. 49(66): p. 7310-7312.
104. *The Global Market for Anti-Fingerprint, Anti-Bacterial, Anti-Fouling, Easy-To-Clean and Self-Cleaning Nanocoatings*. 2012: Future Markets, Inc. 200.
105. Mackenna, R.M.B., Wheatley, V.R., and Wormall, A., *The Composition of the Surface Skin Fat (Sebum) from the Human Forearm*. Journal of Investigative Dermatology, 1950. 15(1): p. 33-47.
106. Cheng, J.B. and Russell, D.W., *Mammalian wax biosynthesis - II. ERxpression cloning of wax synthase cDNAs encoding a member of the acyltransferase enzyme family*. Journal of Biological Chemistry, 2004. 279(36): p. 37798-37807.
107. Deng, X., et al., *Candle Soot as a Template for a Transparent Robust Superamphiphobic Coating*. Science, 2012. 335(6064): p. 67-70.
108. Kang, S.M., et al., *Robust superomniphobic surfaces with mushroom-like micropillar arrays*. Soft Matter, 2012. 8(33): p. 8563-8568.
109. Lee, D., Rubner, M.F., and Cohen, R.E., *All-nanoparticle thin-film coatings*. Nano Letters, 2006. 6(10): p. 2305-2312.
110. Shimomura, H., et al., *Layer-by-Layer-Assembled High-Performance Broadband Antireflection Coatings*. ACS Applied Materials & Interfaces, 2010. 2(3): p. 813-820.

111. Parlitz, D., Peschel, T., and Altenmuller, E., *Assessment of dynamic finger forces in pianists: Effects of training and expertise*. Journal of Biomechanics, 1998. 31(11): p. 1063-1067.
112. Mascaro, S.A. and Asada, H.H., *Measurement of finger posture and three-axis fingertip touch force using fingernail sensors*. IEEE Transactions on Robotics and Automation, 2004. 20(1): p. 26-35.
113. Tuteja, A., et al., *Designing superoleophobic surfaces*. Science, 2007. 318(5856): p. 1618-1622.
114. Butt, H.J., et al., *Design principles for superamphiphobic surfaces*. Soft Matter, 2013. 9(2): p. 418-428.
115. Im, M., et al., *A robust superhydrophobic and superoleophobic surface with inverse-trapezoidal microstructures on a large transparent flexible substrate*. Soft Matter, 2010. 6(7): p. 1401-1404.
116. Nosonovsky, M. and Bhushan, B., *Roughness optimization for biomimetic superhydrophobic surfaces*. Microsystem Technologies-Micro- and Nanosystems-Information Storage and Processing Systems, 2005. 11(7): p. 535-549.
117. Wu, Z.Z., et al., *Deformable antireflection coatings from polymer and nanoparticle multilayers*. Advanced Materials, 2006. 18(20): p. 2699-2702.
118. Krogman, K.C., et al., *Photocatalytic layer-by-layer coatings for degradation of acutely toxic agents*. Chemistry of Materials, 2008. 20(5): p. 1924-1930.
119. DeRocher, J.P., et al., *Layer-by-Layer Deposition of All-Nanoparticle Multilayers in Confined Geometries*. Acs Applied Materials & Interfaces, 2012. 4(1): p. 391-396.
120. Fujishima, A., Rao, T.N., and Tryk, D.A., *Titanium dioxide photocatalysis*. Journal of Photochemistry and Photobiology C: Photochemistry Reviews, 2000. 1(1): p. 1-21.
121. Hashimoto, K., Irie, H., and Fujishima, A., *TiO₂ photocatalysis: A historical overview and future prospects*. Japanese Journal of Applied Physics Part 1-Regular Papers Brief Communications & Review Papers, 2005. 44(12): p. 8269-8285.
122. Choi, J., *Development of visible-light-active photocatalyst for hydrogen production and environmental application*, in *Engineering and Applied Science*. 2009, Ph.D. thesis, California Institute of Technology.

123. Kozawa, E., et al., *Photocatalytic activity of TiO₂ particulate films prepared by depositing TiO₂ particles with various sizes*. Journal of Microencapsulation, 2001. 18(1): p. 29-40.
124. Starov, V.M. and Zhdanov, V.G., *Effective viscosity and permeability of porous media*. Colloids and Surfaces a-Physicochemical and Engineering Aspects, 2001. 192(1-3): p. 363-375.
125. Starov, V.M., et al., *Spreading of liquid drops over dry porous layers: Complete wetting case*. Journal of Colloid and Interface Science, 2002. 252(2): p. 397-408.
126. Maldovan, M., et al., *Validation of the effective-medium approximation for the dielectric permittivity of oriented nanoparticle-filled materials: effective permittivity for dielectric nanoparticles in multilayer photonic composites*. Applied Physics B-Lasers and Optics, 2003. 76(8): p. 877-884.
127. Joannopoulos, J.D., *Photonic crystals : molding the flow of light*. 2nd ed. 2008, Princeton: Princeton University Press. xiv, 286 p.
128. Yan, H., Jo, T., and Okuzaki, H., *Potential application of highly conductive and transparent poly(3,4-ethylenedioxythiophene)/poly(4-styrenesulfonate) thin films to touch screen as a replacement for indium tin oxide electrode*. Polymer Journal, 2011. 43(7): p. 662-665.
129. Chinga, G. and Syverud, K., *Quantification of paper mass distributions within local picking areas*. Nordic Pulp & Paper Research Journal, 2007. 22(4): p. 441-446.
130. Lee, H., et al., *Zwitter-Wettability and Antifogging Coatings with Frost-Resisting Capabilities*. ACS nano, 2013. 7(3): p. 2172-2185.
131. Meyer, D.J., Peshkin, M.A., and Colgate, J.E., *Fingertip Friction Modulation due to Electrostatic Attraction*. 2013 World Haptics Conference (WHC), 2013: p. 43-48.
132. Eversole, W.G. and Lahr, P.H., *The thickness of the rigid water film at a quartz-water interface from a measurement of Newton's rings*. Journal of Chemical Physics, 1941. 9(9): p. 686-689.
133. Fu, G.F., Vary, P.S., and Lin, C.T., *Anatase TiO₂ nanocomposites for antimicrobial coatings*. Journal of Physical Chemistry B, 2005. 109(18): p. 8889-8898.
134. Srituravanich, W., et al., *Plasmonic nanolithography*. Nano Letters, 2004. 4(6): p. 1085-1088.

135. Homola, J., *Surface plasmon resonance sensors for detection of chemical and biological species*. Chemical Reviews, 2008. 108(2): p. 462-493.
136. Fang, N., et al., *Sub-diffraction-limited optical imaging with a silver superlens*. Science, 2005. 308(5721): p. 534-537.
137. Barnes, W.L., Dereux, A., and Ebbesen, T.W., *Surface plasmon subwavelength optics*. Nature, 2003. 424(6950): p. 824-830.
138. Cao, L.Y., et al., *Tuning the Color of Silicon Nanostructures*. Nano Letters, 2010. 10(7): p. 2649-2654.
139. Seo, K., et al., *Multicolored Vertical Silicon Nanowires*. Nano Letters, 2011. 11(4): p. 1851-1856.
140. Xu, T., et al., *Plasmonic nanoresonators for high-resolution colour filtering and spectral imaging*. Nature Communications, 2010. 1: p. 59.
141. Kumar, K., et al., *Printing colour at the optical diffraction limit*. Nature Nanotechnology, 2012. 7(9): p. 557-561.
142. Dominguez, S., et al., *Simple fabrication of ultrahigh aspect ratio nanostructures for enhanced antireflectivity*. Journal of Vacuum Science & Technology B, 2014. 32(3): p. 030602.
143. Macadam, D.L., *Color Science - Concepts and Methods, Quantitative Data and Formulas, 2nd Edition - Wyszecki, G, Stiles, Ws*. Optical Engineering, 1983. 22(4): p. S116-S117.
144. Shevell, S.K. and Optical Society of America., *The science of color*. 2nd ed. 2003, Amsterdam ; Boston: Elsevier. ix, 339 p.
145. Yeh, P., *Optical waves in layered media*. Wiley series in pure and applied optics. 1988, New York: Wiley. x, 406 p.
146. Chen, C.G., et al., *Nanometer-accurate grating fabrication with scanning beam interference lithography*. Nano- and Microtechnology: Materials, Processes, Packaging, and Systems, 2002. 4936: p. 126-134.
147. O'reilly, T.B. and Smith, H.I., *Photoresist characterization using double exposures with interference lithography*. Journal of Vacuum Science & Technology B, 2008. 26(1): p. 128-131.

148. Walsh, M.E., *On the design of lithographic interferometers and their application*, in *Dept. of Electrical Engineering and Computer Science*. 2004, Ph.D. thesis, Massachusetts Institute of Technology.
149. Hunt, J., et al., *Planar, flattened Luneburg lens at infrared wavelengths*. *Optics Express*, 2012. **20**(2): p. 1706-1713.
150. Takahashi, S., et al., *Fabrication of Dielectric Aperiodic Nanostructured Luneburg Lens in Optical Frequencies*. 2011 Conference on Lasers and Electro-Optics (CLEO), 2011: p. 179-180.
151. Jeon, S., et al., *Fabricating complex three-dimensional nanostructures with high-resolution conformable phase masks*. *Proceedings of the National Academy of Sciences of the United States of America*, 2004. **101**(34): p. 12428-12433.
152. Jang, J.H., et al., *3D micro- and nanostructures via interference lithography*. *Advanced Functional Materials*, 2007. **17**(16): p. 3027-3041.
153. Isoyan, A., et al., *Talbot lithography: Self-imaging of complex structures*. *Journal of Vacuum Science & Technology B*, 2009. **27**(6): p. 2931-2937.
154. Jang, J.W., et al., *Arrays of Nanoscale Lenses for Subwavelength Optical Lithography*. *Nano Letters*, 2010. **10**(11): p. 4399-4404.
155. Chang, C.H., et al., *From Two-Dimensional Colloidal Self-Assembly to Three-Dimensional Nanolithography*. *Nano Letters*, 2011. **11**(6): p. 2533-2537.
156. Choi, H.J., et al. *Talbot lithography using aperiodic structures*. in *Optical MEMS and Nanophotonics (OMN), 2011 International Conference on*. 2011. Istanbul, Turkey.
157. Kim, J.G., et al., *Inverted Nanocone Arrays with High Aspect Ratio for Mass-producible Multi-functional Films*, in *MRS Spring Meeting*. 2013: San Francisco, California, USA.
158. Kim, J.G., et al., *Multifunctional Inverted Nanocone Arrays for Non-wetting, Self-cleaning Transparent Surface with High Mechanical Robustness*. *Small*, 2014.
159. Darcy, H., *Les fontaines publiques de la ville de Dijon*. Dalmont, Paris, 1856. **70**.
160. Butcher, E.O. and Coonin, A., *The Physical Properties of Human Sebum*. *Journal of Investigative Dermatology*, 1949. **12**(4): p. 249-254.

161. *Sunclean™ Self-Cleaning Glass from PPG Industries.* Available from:
[http://www.ppg.com/corporate/ideascapes/glass/products/sunclean/pages/suncleanglass.a
spx.](http://www.ppg.com/corporate/ideascapes/glass/products/sunclean/pages/suncleanglass.aspx)